

# **Investigation of Fundamental Elements for Active Nanooptics**

DISSERTATION

zur Erlangung des akademischen Grades

doctor rerum naturalium

(Dr. rer. nat.)

im Fach Physik

eingereicht an der

Mathematisch-Naturwissenschaftlichen Fakultät

Humboldt-Universität zu Berlin

von

Diplom Physiker Günter Kewes

Präsident der Humboldt-Universität zu Berlin:

Prof. Dr. Jan-Hendrik Olbertz

Dekan der Mathematisch-Naturwissenschaftlichen Fakultät I:

Prof. Dr. Elmar Kulke

Gutachter/innen:

1. Prof. Dr. Oliver Benson

2. Prof. Dr. Thomas Elsässer

3. Prof. Dr. Thomas Klar

Tag der mündlichen Prüfung: 10.11.2015



„One point twenty-one giga-watts!“

Doc Brown in *Back to the future*



---

## Zusammenfassung

---

Integrierte optoelektronische Anwendungen sind allgegenwärtig in moderner Technologie. Sie sind einerseits Schlüsselkomponenten in bekannten kommerziellen Produkten wie mobilen Geräten oder Flachbildschirmen, aber sie ermöglichen auch schnelle Netzwerke in Datenzentren. Um drängende Probleme im Zusammenhang mit dieser Technologie zu lösen, z.B. der hohe Energieverbrauch und die Verwendung und Rückgewinnung von seltenen Materialien, sucht die Forschung nach Alternativen. Insbesondere effiziente, nicht-lineare Prozesse werden benötigt, um Signale zu schalten. Einige vielversprechende Konzepte wurden in der Nanooptik vorgeschlagen. Diese basieren insbesondere auf plasmonischen Prozessen, die im Frequenzbereich von sichtbarem Licht stattfinden. Drei dieser Konzepte werden in dieser Arbeit diskutiert und untersucht.

Teil 1 der Arbeit handelt von der konkreten Umsetzung eines Konzepts, das eine starke Interaktion zwischen einzelnen Quantenemittern und dem geführten Lichtfeld an metallischen Wellenleitern ausnutzt. Hierdurch können prinzipiell extrem schwache Lichtsignale zum Schalten verwendet werden. In Teil 2 wird die Miniaturisierung von Lasern untersucht. Kleine Lasersysteme finden schon heute Anwendungen in verschiedensten Bereichen der Optoelektronik. Diese Arbeit behandelt die kleinstmögliche Realisierung von Lasern, sogenannte Nanolaser, und untersucht deren Anwendbarkeit. Teil 3 widmet sich dem relativ neuen Materialsystem Graphen. In dieser Arbeit wird untersucht, in wie weit sich Graphen zur Manipulation von sichtbarem Licht verwenden lässt, beziehungsweise, in wie weit Graphen plasmonische Eigenschaften aufweist.

Die Analyse der Konzepte liefert neue Erkenntnisse zu kontrovers diskutierten Themen bezüglich der Vorzüge und Nachteile der Miniaturisierung mit Hilfe der Plasmonik. Die Erkenntnisse geben des Weiteren klare Richtlinien zur Optimierung der Konzepte hin zu effizienteren und praktikableren Designs.

---

## Abstract

---

Integrated optoelectronic applications are omnipresent in modern technology. They are key constituents of familiar commercial products such as mobile devices and flat screens but also enable fast networks in data centers. In order to solve pressing problems induced by the technology, such as high power consumption and the use and recycling of rare materials, research tries to explore alternatives. In particular, there is a need for efficient, non-linear processes that could be employed for switching of signals. Some promising concepts have been proposed using nanooptics, especially based on plasmonic processes that take place at frequencies of visible light. Three of these concepts are discussed and investigated in this work.

Part 1 of this work is about a concrete realization of a concept which makes use of a strong interaction between individual quantum emitters and guided light-fields of metallic waveguides. With this approach, in principle extremely weak light-signals can be sufficient for switching. In part 2 the miniaturization of lasers is investigated. Small laser-systems are already used today for a broad range of applications in optoelectronics. This work examines the smallest possible realization of lasers, so-called nanolasers, and investigates their applicability. Part 3 focuses on the relatively young material graphene. In this work it is investigated in which way graphene could be used for the manipulation of visible light, and accordingly, whether graphene features plasmonic properties.

The analysis of these concepts provides new insights to controversial discussed topics with respect to the advantages and disadvantages of miniaturization with the help of plasmonics. Further, the findings give clear advice for the optimization of the concepts towards more efficient and practicable designs.

---

# Table of Content

---

<b>1</b>	<b>Introduction</b>	<b>1</b>
<b>2</b>	<b>Theoretical Basis: Matter &amp; Emitters, Modes and Methods for Modelling</b>	<b>6</b>
2.1	Basic Concept	6
2.2	Matter	8
2.2.1	Silver and Gold	10
2.2.2	Silicon, Gallium Phosphide and Silicon Nitride	12
2.2.3	Graphene	14
2.3	Dipole Emitters	18
2.3.1	Hertzian Dipole	18
2.3.2	Near-fields	19
2.3.3	LDOS	19
2.3.4	Quantum vs. Classical	20
2.3.5	Stokes Shift	23
2.4	Modes	25
2.4.1	Metals or Dielectrics Hosting Modes – on the Distinction between Photons and Plasmons	25
2.4.2	Guided Modes	27
2.4.3	Localized Modes	29
2.5	Methods to Quantify Light-Matter-Interactions	33
2.5.1	Analytic Approaches	33
2.5.2	Numerical Simulations with Finite Element Methode	34
2.5.3	Coupling of Emitters to Individual Modes	36

## Table of Content

---

<b>3 Experimental Basis: Preparation and Investigation</b>	<b>42</b>
3.1 Sample Preparation: Matter & Emitters	42
3.1.1 Chip Fabrication by Lithography	42
3.1.2 DBT in Anthracene	44
3.1.3 Synthesis of Core-Shell nanoparticles	45
3.1.4 Graphene exfoliation on Mica	46
3.2 Sample Investigation: Versatile Setup for Assembly and Analysis	48
3.2.1 Setups	48
3.2.2 Confocal Microscopy	49
3.2.3 Dark-field Microscopy	50
3.2.4 Atomic Force Microscopy	51
3.2.5 Pulsed Lasers	51
<b>4 An On-chip Platform for Active Nano optics based on Single Emitters</b>	<b>53</b>
4.1 Basic Concept	53
4.2 The Chip	54
4.2.1 Design and Analysis with FEM	56
4.2.2 Performance Tests of Fabricated Structures	68
4.3 Nanomanipulation and Photoluminescence Studies on DBT	73
4.3.1 Cutting and Nanomanipulation	73
4.3.2 Coupling to the Chip	74
4.4 Conclusion and Outlook	76
<b>5 Nanoscopic Lasers &amp; Spasers: Theory, Fabrication and Experiment</b>	<b>78</b>
5.1 An Analytic Model for Spasers	78
5.1.1 Mie-model: A Semi-Classical Laser Rate-Equation Model for Spherical Resonators	79
5.1.2 Prime Example: The Core-Shell Spaser of Noginov et al.	86
5.1.3 Optimization Concepts for Spasers	91
5.1.4 Minimum Gain and Heat Production in the VIS to NIR Range	93
5.2 All-dielectric Nanocavities for Nanolasers	102
5.3 Refined Gain-Medium Description	107
5.3.1 Four-level Gain Medium	107
5.3.2 Non-constant Inversion	109

## Table of Content

---

5.4 Experiments on Nanoparticle based Resonators	114
5.4.1 Core-shell Particles	114
5.4.2 Dye-film Coated Nanoparticles	118
5.5 Studies on Waveguide-like Resonators	121
5.6 Conclusion and Outlook	128
<b>6 Strategies to Probe Plasmons in Graphene and Graphene-like Materials</b>	<b>133</b>
6.1 Indications for Graphene Plasmons in the VIS	133
6.1.1 Motivation	133
6.1.2 Graphene Plasmons in the VIS: Current Status in Literature	134
6.2 Short-pulse Excitation of Graphene	138
6.3 Conclusion and Outlook	144
<b>7 Conclusion and Outlook</b>	<b>145</b>
7.1 Conclusion	145
7.2 Outlook	146
<b>8 Appendices</b>	<b>149</b>



---

# 1 Introduction

---

In 1989's Hollywood movie "Back to the future, part 2" the protagonist "Marty McFly" travels through time to visit the future of the 21th of October in 2015 – our today's present. Almost no futuristic invention shown in the movie (e.g., accurate weather forecast, nuclear fusion, self-drying clothes etc.) has made its way into real life. However, some inventions are nowadays present in everyone's living room: flat and large video-screens presenting interactive media contents and visual telephony. This technological achievement can be essentially ascribed to *optoelectronics*.

Many more applications like that have become possible and accessible to the broad public during the last decades. This progress is driven by the acceleration and miniaturization of processors and interconnecting networks. This technology has a strong impact on our contemporary society – people speak about the "era of information". At the same time this technology is polluting the natural environment significantly. The overall energy consumption of the internet, or more precisely of the "information-communications-technologies" (ICT) ecosystem, is rising with a higher rate than men's energy production and reached already 1,500 TWh per year (10%) in 2013 [1]. Rare materials integrated in miniaturized electronic and optoelectronic devices are virtually impossible to recover. This is because efficient recycle procedures are either not known or too energy costly [2,3]. Furthermore, current chip-technologies (e.g., CMOS-technology) are struggling with fundamental physical limitations which hinder further improvements, that are based on higher integration density [4–6]. Thus, motivation for various scientific projects (beyond pure curiosity) is to find ways to provide energy efficient alternatives for current technologies. At the same time these alternatives should be based on recyclable materials and allow for improved performance – without losing its high degree of integration density. In this context the Olympic motto "cuius, altius, fortius" (Latin for "faster, higher, stronger") may be translated into "faster, smaller, cleaner, more efficient". Promising attempts to tackle these issues have been proposed in nano optics.

## 1. Introduction

---

Nano optics or nanophotonics is a branch in science and engineering that combines optics, nanotechnology and optoelectronics. It is formally distinguished from optics by a natural frontier, i.e., the diffraction limit. This limit basically states, that two small objects, observed in an optical microscope, which are only separated by less than a half of a wavelength of light, cannot be resolved as two but will appear as one. The underlying reason is related to inherent near-fields that exist around any object [7]: as the name suggest, these are fields that cannot leave the object by radiating to the far field. Thus, not the complete information stored in the light field can reach a potential observer.

Nowadays, nano optics deals with various disciplines that can be divided into

- Analytic tools, e.g., near-field microscopy of sub-diffraction limited objects [8,9] and spectroscopy, e.g., surface enhanced Raman spectroscopy [10].
- Light harvesting, e.g., collecting and trapping of light in solar cells [11], but also sub-diffraction lithography [12] or miniaturized photo detectors [13].
- Active or novel functionality, e.g., miniaturized lasers [14–17] or metamaterials [18–20].

Some of the most impressive advancements in recent years have been accomplished in the field of microscopy, where nano optics is now capable of investigating and controlling individual quantum systems [9,21]. Also, various achievements already made a successful transformation from basic research to applied technology.

The term optoelectronics leads to the fact that various technical instruments use a combination of optics and electronics to provide specific functionality. For instance optics is frequently used for data transport but electronics for data processing. However a transformation from optical to electrical signals is accompanied by losses in efficiency and speed. An optically “active” process, i.e., a non-linear response of high speed and energy efficiency would render a further breakthrough in nano optics, a transformation could become faster or even obsolete. Summarized, nano optics scientists try to tackle two demands at the same time: increase of integration density and reduction of power consumption.

Nano optics often utilizes surface plasmon polaritons – from now on mostly called “plasmons” - to confine optical energy to nanoscales: to so-called “hot-spots”. Thus, the term “plasmonics” [22] is sometimes almost synonymously used for nano optics. Plasmons are described as being partly photon and electron-density oscillation (in a metal). Through this interaction of light fields with conduction band electrons in the metal, plasmons gain

## 1. Introduction

---

momentum with respect to photons, resulting in shorter wavelength than photons of the same energy (which interact only with bound electrons in dielectrics). Furthermore, on interfaces of metals and dielectrics, plasmons feature an evanescently decaying intensity distribution into both media. These properties usually yield a higher confinement than the one found for photons. However, advantages in confinement have to be paid up by relatively fast damping (due to Ohmic losses). Also quenching of fluorescence of near-by emitters can be a problem. This thesis shines light on various aspects of an often emerging discussion about pros and cons of plasmonics.

This discussion is held in parallel with the reports on three attempts to produce non-linear responses for “active” plasmonics or nanooptics that have been considered and investigated during this thesis:

- Non-linearities that arise from the interaction of individual quantum systems (emitters) with waveguide modes.
- Non-linearities that are associated with coherent amplification - switching from non-lasing to lasing state in a nanolaser or spaser.
- New plasmonic materials (2D-materials like graphene) that feature on-the-fly controllable optical properties by electrical tuning.

Figure 1 depicts a typical physical system discussed within the following chapters.

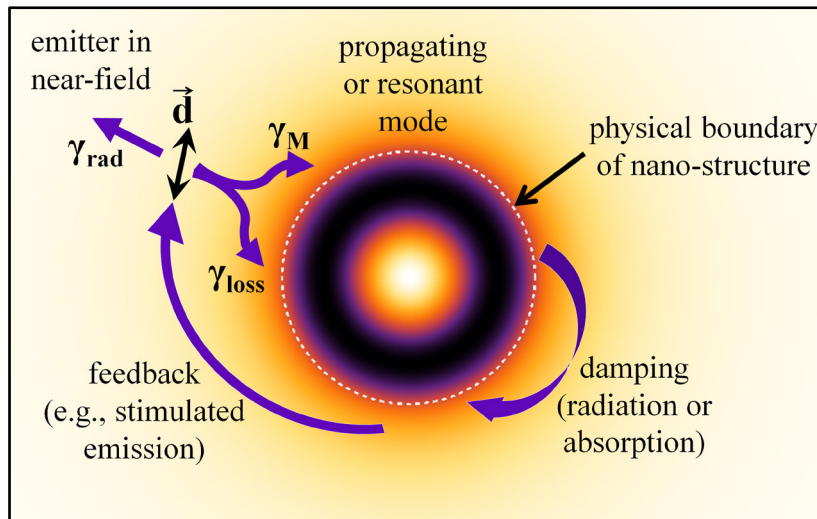


Figure 1: Scheme of a typical physical systems discussed throughout this thesis. A nanostructure hosts specific modes (that might be prone to losses). Emitters located in the near-field of these modes couple to these modes and other channels. The system may feature non-linearities when the feedback is of comparable strength to all the other optical processes or if the properties of the mode-hosting nanostructure change.

## 1. Introduction

---

Speaking of nano optics implies that the frequencies of interest are mainly in the visible spectral range (VIS), maybe up to the near infrared (NIR). This is a spectral range of electromagnetic radiation, which is not only interesting because it is visible to the human eye, but also for other reason: Highly efficient detectors and optics are available for the VIS and also the best emitters with good quantum efficiency and stability. Additionally, the larger the wavelength, the harder it will be to accomplish a high degree of miniaturization down to the nanoscale. This thesis is thus not dealing with infrared (IR) or even terahertz physics.

This thesis starts with a theory and experimental chapter (**chapter 2 and 3**) in which the underlying models are discussed and a short report on experimental tools and sample preparation is given. This is followed by chapters on the three aforementioned attempts to achieve a non-linear response in nano optics.

**Chapter 4** deals with integrated on-chip nano optics, by investigation and design of a platform utilizing waveguides and photon-to-plasmon couplers. The aim is here to provide an efficient chip design that enables the investigation of the interplay between individual quantum emitters with confined guided modes. Finite element methods are used to design a highly efficient coupler (Figure 2) and a high coupling strength to close-by emitters. On-chip structures fabricated by collaborators via e-beam lithography have been evaluated in experimental performance tests finding a good agreement with the predictions of the simulations.

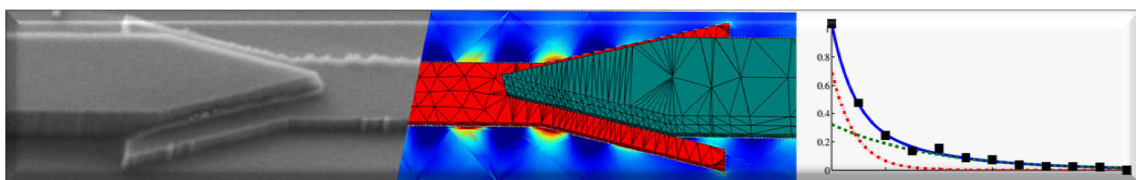


Figure 2: Scanning electron microscopy image, numeric simulation and experimental results for a photon-to-plasmon coupler.

## 1. Introduction

---

**Chapter 5** represents the main focus of this thesis. It reports on investigations of fully nanoscopic lasers, i.e., lasers with sub-diffraction limited dimensions in all spatial directions, both on theoretical and experimental grounds. Theoretical modeling was done using analytical methods based on Mie-theory. Experiments have been performed on chemically synthesized core-shell particles as well as on nanostructures combined with dye-doped films (Figure 3).

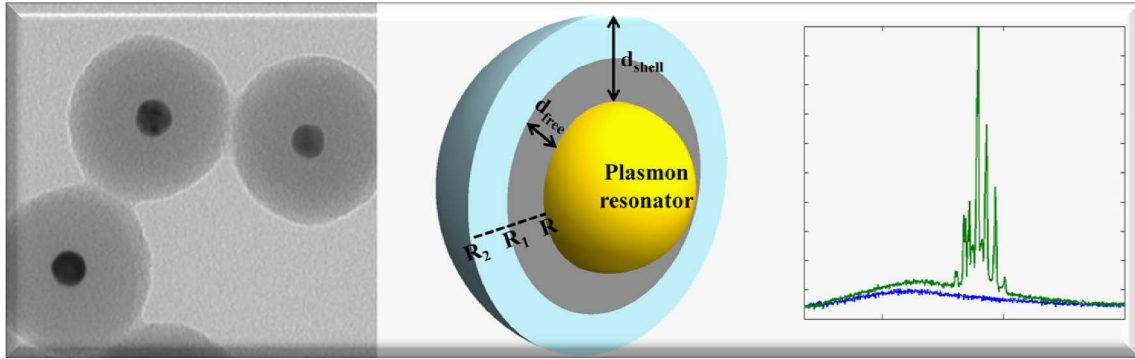


Figure 3: Scanning electron microscopy image, scheme of the analytic model and experimental results for plasmonic particles coated with dye-doped films.

**Chapter 6** presents the most fundamental research in this work. It reports on ways to investigate and understand the optical response of graphene. Especially potential routes to excite plasmons in graphene in the VIS are discussed, where graphene is widely considered to feature no plasmonic responses. In pulsed excitation experiments the broad photoluminescence of graphene and emerging potential second-harmonic generation (SHG) features are discussed (Figure 4).

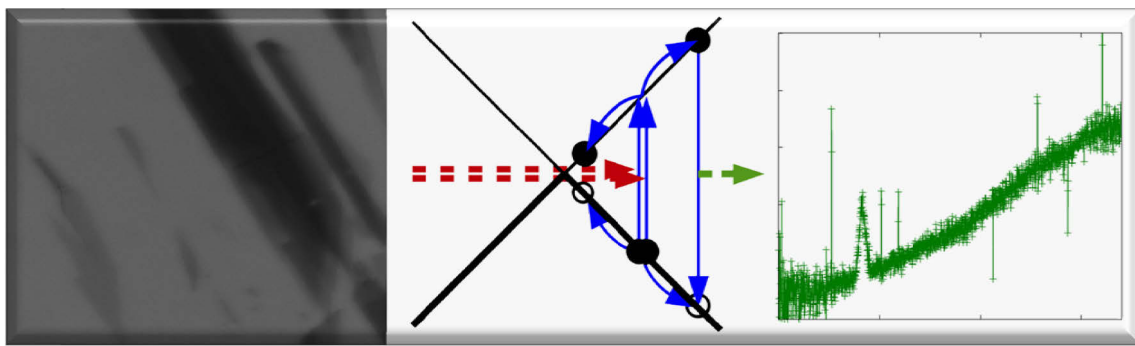


Figure 4: Optical microscopy image of multi- and monolayer graphene on mica, theoretical model for the broad photoluminescence and a corresponding spectrum with a potential SHG peak.

---

## 2 Theoretical Basis: Matter & Emitters, Modes and Methods for Modelling

---

This chapter introduces important conceptions that build the basis for the following chapters, i.e., the qualitative picture of physical processes and tools to quantify light matter interaction. Conceptually this chapter is divided into the description of matter (2.2) that hosts modes, emitters (2.3) that may “excite” (populate) modes and modes themselves (2.4). Beyond pure description, controversial aspects concerning the derivation of the Purcell effect in nanooptics (2.5) and the distinction of photons and plasmons (2.4.1) are discussed.

### 2.1 Basic Concept

The variety of possible material systems, frequency ranges and field strength captured by the phrase “light-matter interaction” is huge. Interactions with materials like inorganic or organic solids, fluids, gases or even plasmas are investigated in optical sciences and energy and length scales may differ by orders of magnitude. Depending on the effects of interest, light is often regarded as a stream of photons (e.g., photoelectric effect) or as a classical electromagnetic wave (e.g., non-linear effects like second-harmonic generation) with certain momentum and frequency.

The work presented here roughly deals with light as the visible part of the electromagnetic spectrum, i.e., with photon energies in the range of approximately 1-3 eV. Mostly a useful picture of optical modes (or quasi-normal modes [23]) is used. These modes may be populated by optical quanta, i.e., photons or plasmons. Physical bodies that are considered here may be divided into two main classes: matter and emitters. The objects summarized with “matter” are mainly regarded as *passive* objects, just reacting on an optical stimulus or hosting modes. Basically those objects like dielectrics or metals can be sufficiently described by frequency-dependent complex

## 2. Theoretical Basis

---

functions of their dielectric permittivity. Emitters are the fundamental constituents of *active* material. They are active in a sense, that they may store energy and release by luminescence (spontaneous or stimulated emission), e.g., organic emitters.

However this distinction into passive and active is sometimes becoming blurry when for instance solids like gold or graphene are excited to emit photoluminescence (PL) due to intrinsic optical interband or intraband transitions of the material [24,25]: the PL-producing processes can be regarded as dipole emissions from within the matter. Thus, modes hosted by passive objects may be populated by their own luminescence.

Further the assumption of passive matter objects may lose its validity when i) transient phenomena come into play or when ii) the absorption of the matter (and thus its dielectric permittivity) is changed via strong pumping. In these cases one faces a coupled system with non-linear feedback mechanisms. An example for i) could be a material that changes from dielectric to metallic electron distribution in a short time after an optical excitation. The matter is then able to host different modes than before or the quality factors of an excited cavity might be affected [26,27]. Laser-resonators that are made from the laser's gain medium feature case ii): the quality factors and central frequencies of the laser's eigenmodes might change during pumping and differ from that of the cold cavity ("frequency pulling") [28].

Consequently, the basis for a quantitative modelling of light matter interaction, will be the knowledge of band-structures, dielectric permittivities and energy levels. From its knowledge and the geometry of the problem optical modes can be computed that finally allow to describe the interaction with emitters, i.e., where the emitted power goes, how it is concentrated, how long it will be stored or how fast it might be damped. This model-construction is depicted in Figure 5.

## 2. Theoretical Basis

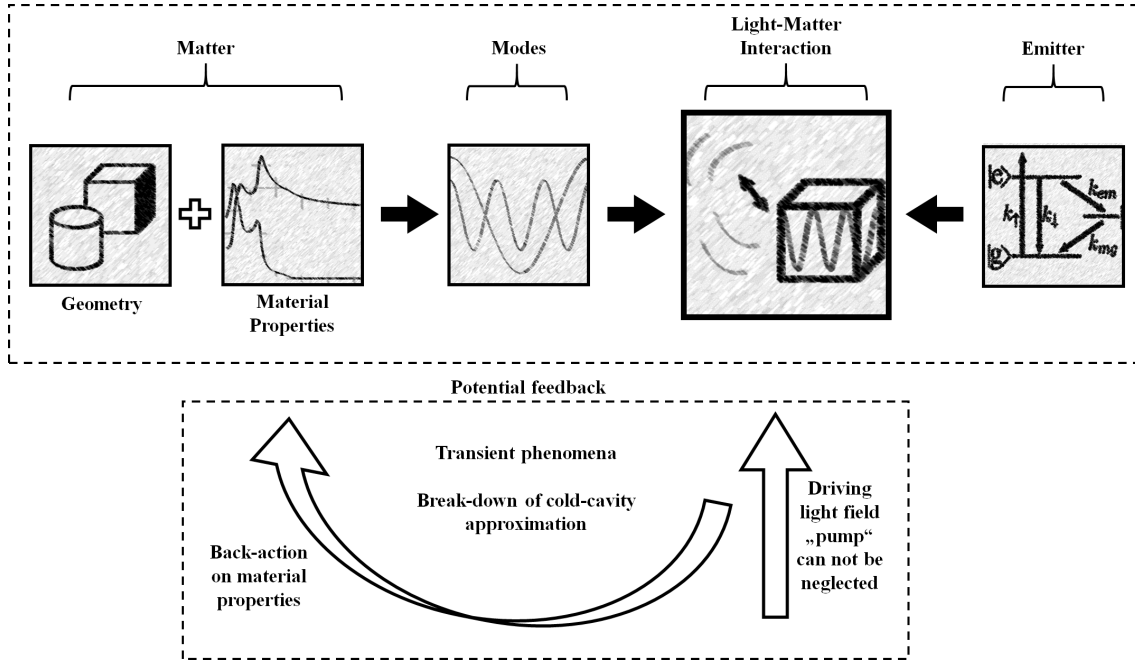


Figure 5: Scheme of multiscale models to describe light-matter interaction. Knowledge about material properties like dielectric permittivities or energy levels and of the geometrical arrangements are used to calculate guided or cavity modes. This information is used to predict the performance of envisioned systems, i.e., light-matter interaction of individual emitters with specific modes (upper dashed box). This static system may be altered when a feedback to the material properties is present.

## 2.2 Matter

The response of solid state materials on optical excitations is for reasonable low powers described by a linear dielectric permittivity. This is the case for most of the studied materials in this thesis. This means that the electric displacement  $D$  is a linear function of the applied electric field  $E$ :

$$D = \epsilon \epsilon_0 E \quad (2.1)$$

where the proportionality factor  $\epsilon = \epsilon' + i\epsilon''$ , the *relative dielectric constant* or *permittivity*, is a complex number that is usually a function of frequency (known as dispersion):  $\epsilon = \epsilon(\omega)$ ;  $\epsilon_0$  is the vacuum permittivity.  $\epsilon'$  is a measure of how polarization in a medium weakens the field inside the medium compared to the applied outer electric field.  $\epsilon''$  accounts for losses inside the material, i.e., processes that lead to dissipation of energy, which was initially stored in the electromagnetic field.  $\epsilon'(\omega)$  peaks when the frequency is scanned over a range that corresponds to the bandgap of a semiconducting material.

## 2. Theoretical Basis

---

This is only one example, where a strong relationship between the bandstructure of a solid with its dielectric permittivity is obvious. Relatively simple models such as the Drude-model, which basically describes kinetic movements of charge carriers, can be used as the fundament for material models describing optical properties [29]. Such models that render the complex dielectric permittivity are not only of academic interest but are explicitly needed for numerical Maxwell-equation solvers (“time-domain” methods section 2.5) but also in the fundamental task of (analytically) searching for the eigenfrequency or an eigenmode of a cavity: The eigenfrequency depends on both the design (geometry and material) of the cavity but at the same time on the dispersion of used materials [30].

The relevant materials studied in this thesis are gold (Au), silver (Ag), (crystalline) silicon (Si), gallium phosphide (GaP) and silicon nitride (SiN) as well as graphene. Therefore the dielectric permittivities and band structure diagrams will be depicted in the following. Subsequently some basic properties of graphene will be discussed briefly. Its quasi-two-dimensional character, being only 0.34 nm thick, introduces some problems to the description, as the use of a simple dielectric permittivity is in principle only well-defined for macroscopic objects. This is reflected by theoretical results which found a strong influence of the edges (armchair or zig-zag) of small graphene sheets on the hosted plasmonic modes [31,32].

Materials can be described and compared by either looking at their dielectric permittivities  $\epsilon$  or the refractive indices  $\tilde{n} = n + ik$  or sometimes even at their complex conductivities. These quantities are equivalent as they are connected via distinct relations. It is useful to compare the dielectric permittivities when it comes to considerations as in this thesis. Especially for the estimation of the losses due to quenching of emitters close to passive nanostructures,  $\epsilon''$  is the most intuitive number. The imaginary part of the refractive index  $k$  can be very small for some dielectrics and thus one might conclude that quenching effects are small, too.  $\epsilon''$  however can be relatively high at the same time, especially for high index media. As  $\epsilon''=2nk$ , it accounts for the way how light will penetrate the medium ( $\sim n$ ) *and* how it is absorbed ( $\sim k$ ), finally leading to more losses. As a matter of fact  $k$  can be very high for noble metals, but  $n$  is small – the free carriers shield the field and prevent it from entering the metal – so that the  $\epsilon''$  of metals can also be relatively small. However, there will be no metal that is absolutely free of losses ( $\epsilon''=0$ ), as there is no absorption-free metal (in the VIS) with  $k=0$  in contrast to dielectrics that can be effectively free of absorption.

### 2.2.1 Silver and Gold

Silver is widely regarded to be the best plasmonic material, i.e., the metal with the highest conductivity at frequencies of visible light. Noteworthy is however, that silver oxidizes relatively fast at ambient conditions. The resulting silver-oxide layer has turned out to alter silver's properties significantly [33]. This fact limits the application of silver even though it can be protected from oxidation with coatings.

The band-diagram of silver (Figure 6) shows only few features in a wide energy range around the Fermi-level. Consequently optical transitions that correspond to vertical arrows in such a band-diagram (due to the relative small momentum of photons) can occur only with low probability, i.e., silver is mainly free of absorption in the VIS. The same can be seen more directly from the dielectric permittivity for which a low imaginary part was found [34]. The permittivity of silver can be modeled with a simple Drude-model over a wide range.

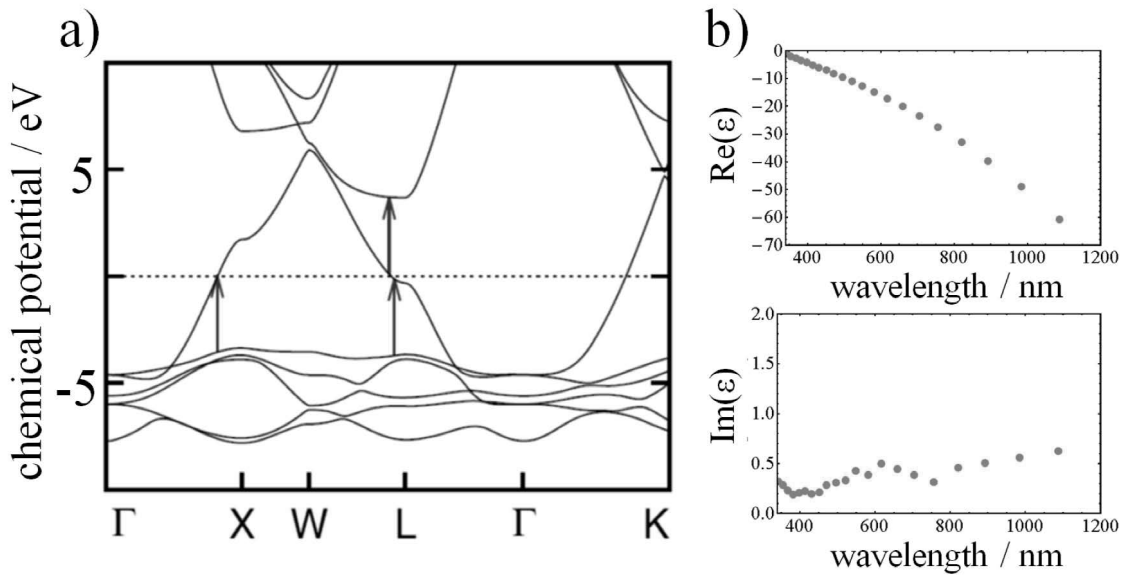


Figure 6: Band-diagram and dielectric permittivity of silver. a) Dotted line indicates the Fermi-level. Optical transitions are marked by vertical arrows (3.6 eV), that have to connect two bands of the diagram. If the distance between bands is too wide, only transitions from or to the Fermi-level can occur. The probability of possible transition rises with the density of electronic states, which is high for extremal points in the band-diagram (Figure taken from [177]). b) Real and imaginary part of silver's dielectric permittivity (upper and lower curve, respectively). The real part follows almost an ideal Drude-model, the imaginary part is small in the entire VIS and shows only weak features (data taken from [34]).

## 2. Theoretical Basis

---

In contrast to silver the 5d-band of gold is close ( $\sim 2$  eV) to the 6sp-band (Figure 7). Optical transitions can thus lead to significant absorption - or in the time-reversed process - to luminescence. Interestingly this luminescence was found to be increased by orders of magnitude in gold nanoparticles (NPs), which is explained by the increased density of modes (originating from the plasmon resonance) at the particle [25]. This effect can be used to detect gold nanoparticles with a laser that excites the particle with photon energies above the transition. Further it is possible to probe the corresponding localized plasmon resonance as the spectral response of the luminescence follows the plasmon resonance [25,35,36].

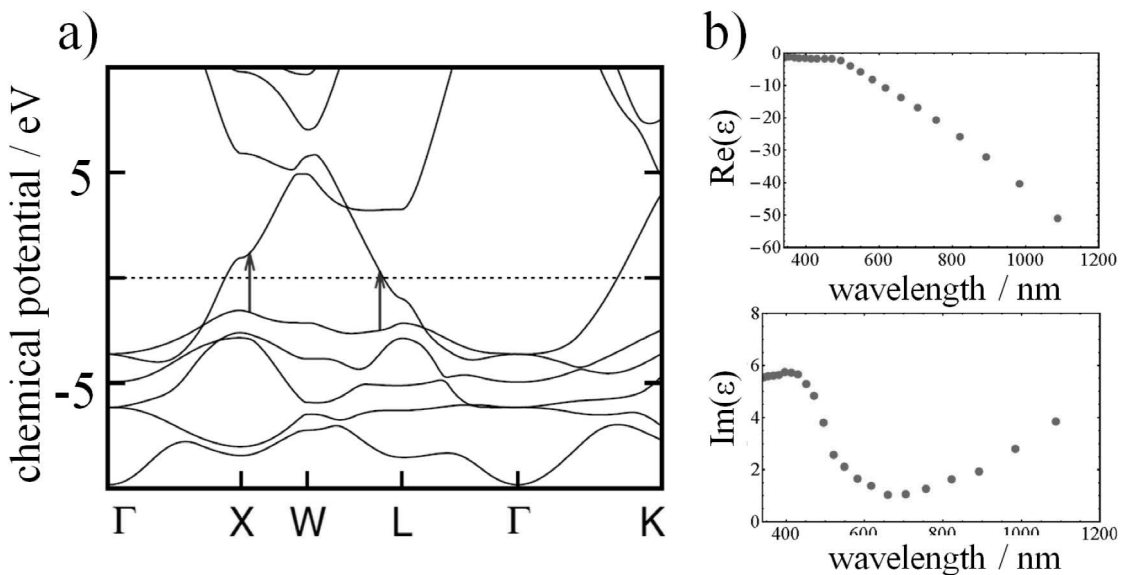


Figure 7: Band-diagram and dielectric permittivity of gold. a) Dotted line indicates the Fermi-level. The vertical arrows correspond to the allowed transitions at 2.8 eV (Figure is taken from [177]). b) Real and imaginary part of gold's dielectric permittivity (upper, lower curve, respectively). The real part follows almost an ideal Drude-model for wavelength beyond roughly 530 nm where significant intraband transitions set in that lead to absorption. Consequently an increase of the imaginary part is observed in that range. Permittivity data is taken from [34].

### 2.2.2 Silicon, Gallium Phosphide and Silicon Nitride

The banddiagram of silicon [37] exhibits a bandgap of 1.1eV, i.e., silicon is a semiconductor (Figure 8). Importantly this is an indirect bandgap. While a direct bandgap material usually shows strong absorption and luminescence silicon doesn't. This is due to the momentum mismatch between photons and the corresponding indirect bandgap transition.

The dielectric permittivity shows two noteworthy features. The real part is one of the highest known for materials in the VIS. The refractive index  $n = \sqrt{\epsilon}$  is high too, thus yielding a small wavelength of light in silicon. This fact allows for silicon nano-structures like waveguides or resonators for optics that are dimensioned well below the corresponding photon wavelength in air, e.g., nano-antennas with diameters around 100-200 nm [38]. Additionally the imaginary part is rather small for photon energies above the bandgap. Together with the high refractive index, silicon based nanostructures with relatively low losses or damping are possible.

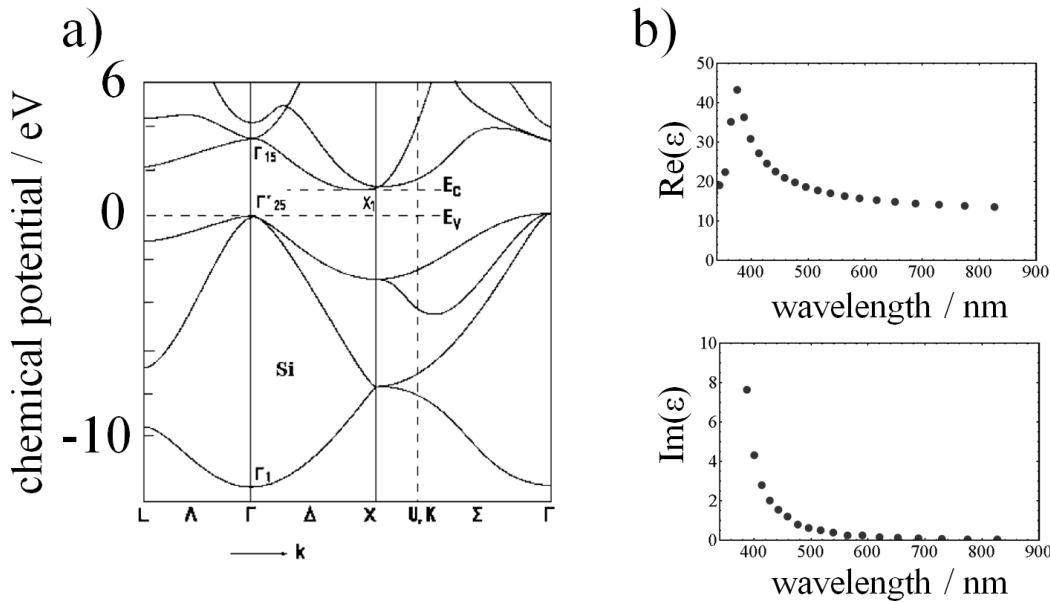


Figure 8: Band-diagram and dielectric permittivity of Si. a) The bandgap of Si is indirect, so that optical transition can only take place when additional momentum is provided, e.g., by phonons. b) Real and imaginary part of Si's dielectric permittivity (upper, lower curve, respectively). The real part is the highest for dielectrics in the VIS. Beyond roughly 500 nm more and more direct transitions set in that lead to increased absorption (rise of  $\text{Im}(\epsilon)$ ).

## 2. Theoretical Basis

Gallium phosphide is in many aspects comparable to silicon. It also exhibits an indirect bandgap and a high index of refraction in the VIS. Most valuable for nanooptics based on dielectrics is that the bandgap is relatively wide (at around 550 nm, 2.25 eV) and thus almost no losses are expected for longer wavelength. Figure 9 shows the banddiagram and dielectric permittivity of GaP.

Silicon nitride exhibits a relatively flat dispersion in the VIS featuring a refractive index of 2 and no absorption. This is because of its wide bandgap of around 5 eV. This material is considered here for on-chip waveguides. As silicon exhibits losses in the VIS, SiN is often considered as an alternative. Thin films of the material can be grown with high quality on glass and thus it can be used as a basis for lithography [39].

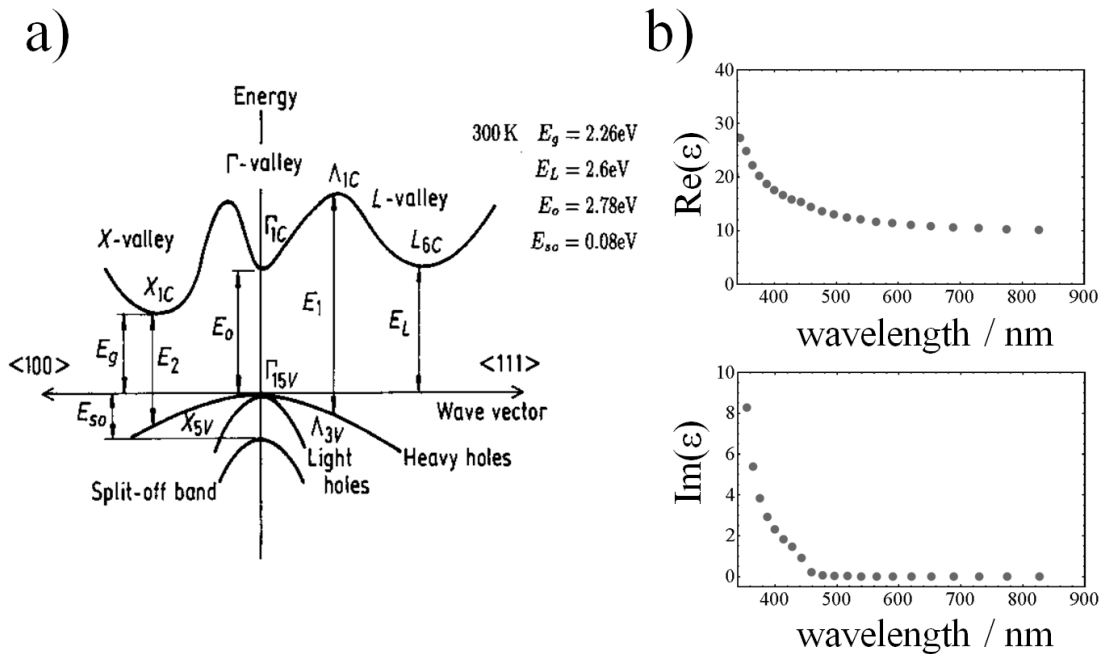


Figure 9: Band-diagram and dielectric permittivity of GaP. a) Relevant transitions (with high probability / at extremal points of bands) and corresponding energy differences are marked by vertical arrows (figure taken from [178]). b) Real and imaginary part of GaP's dielectric permittivity (upper, lower curve, respectively). The real part is relatively high for dielectrics in the VIS. Beyond roughly 550 nm transitions set in which lead to absorption (rise of  $\text{Im}(\epsilon)$ ), first only weak absorption is found due to an indirect band gap followed by a significant increase around 450 nm (2.78 eV). Permittivity data is taken from [179].

### 2.2.3 Graphene

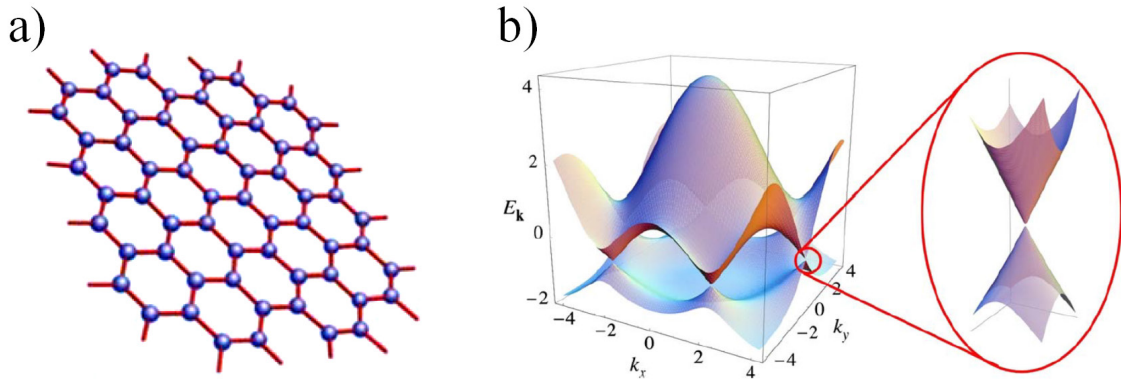


Figure 10: a) Honeycomb-like structure of graphene. b) Banddiagram of graphene with zoom-in to one of the Dirac-cones. Figures taken from [180].

In contrast to the aforementioned bulk materials that are well understood, graphene represents a relatively “young” material. It is a quasi-2D material, a fact that introduces various challenges to theory and experiment. The band-diagram of graphene shows some features that give rise to extraordinary physical properties. It is a semi-metal in its undisturbed state, i.e., the Fermi-level lies on a single point in the band-diagram. This single point is where the so-called Dirac-cones touch – the Dirac-point [40]. The Dirac-cones refer to regions around the Fermi-level where the band-diagram has a linear dispersion (Figure 10). A linear dispersion yields charge-carriers of zero effective mass  $m^*$  as this is inversely proportional to the second derivative of the band dispersion  $E(\mathbf{k})$  with respect to momentum  $\mathbf{k}$ . Thus charge-carriers in this region are said to behave photon-like – nevertheless they are still fermions. A direct consequence of the linear dispersion is an efficient carrier scattering, as energy and momentum conservation are fulfilled simultaneous in this situation [24,41].

An important feature of graphene is its electrostatic tunability: the chemical potential can be shifted away from its natural Fermi-level (Figure 11a) which acts like a doping with donors or acceptors (depending on the applied voltage) as in ordinary semiconductor science. Doping can be controlled in a relatively simple configuration (Figure 11c) that can be understood and quantitatively modeled via a simple capacitor model derived during this thesis. It yields a functional connection between applied voltage and doping (chemical potential  $\mu$ ). Here a doped silicon wafer and the graphene layer are the capacitor plates and a silicon dioxide layer acts as the dielectric. Well-

## 2. Theoretical Basis

---

known relations describing the capacity  $C$  are  $C=Q/U$  and  $C=\epsilon_0\epsilon_r d/A$ . Combining these two yields the equation:

$$U = \frac{d}{\epsilon_0\epsilon_r A} Q \quad (2.2)$$

with the charge  $Q$ , the permittivity of the dielectric  $\epsilon_0\epsilon_r$ , the distance between the plates  $d$  and the plates' area  $A$ . The ratio  $Q/A$  can be interpreted as the charge per unit cell size ( $Q_{EZ}/A_{EZ}$ ). The charge per unit cell is connected with the density of states  $\rho(E)$  via

$$Q_{EZ} = e \int_0^{\mu} \rho(E) dE , \quad (2.3)$$

i.e., an integration over the density of states yields a number of states or “charges”  $Q_{EZ}$ . A complicated analytic form of graphene’s density of states (Figure 11b) is known, but up to 1.5 eV a linear dispersion is a good approximation:

$$\rho(E) = \frac{2A_{EZ}}{\hbar^2 \pi v_F^2} |E| , \quad (2.4)$$

Where  $v_F$  is the Fermi-velocity of the electrons in graphene. This finally yields

$$U(d, \mu) = \frac{e}{\epsilon_0\epsilon_r \pi \hbar^2 v_F^2} \cdot \mu^2 \cdot d , \quad (2.5)$$

which is plotted for three different  $d$  in Figure 11d. The chemical potential is thus inversely proportional to the thickness of the dielectric and proportional to the square root of the applied voltage. Reaching high dopings by this method is in practice restricted to about 1 eV: The combination of relatively high voltages and thin dielectric layer runs the risk of having a breakdown of the dielectric.

## 2. Theoretical Basis

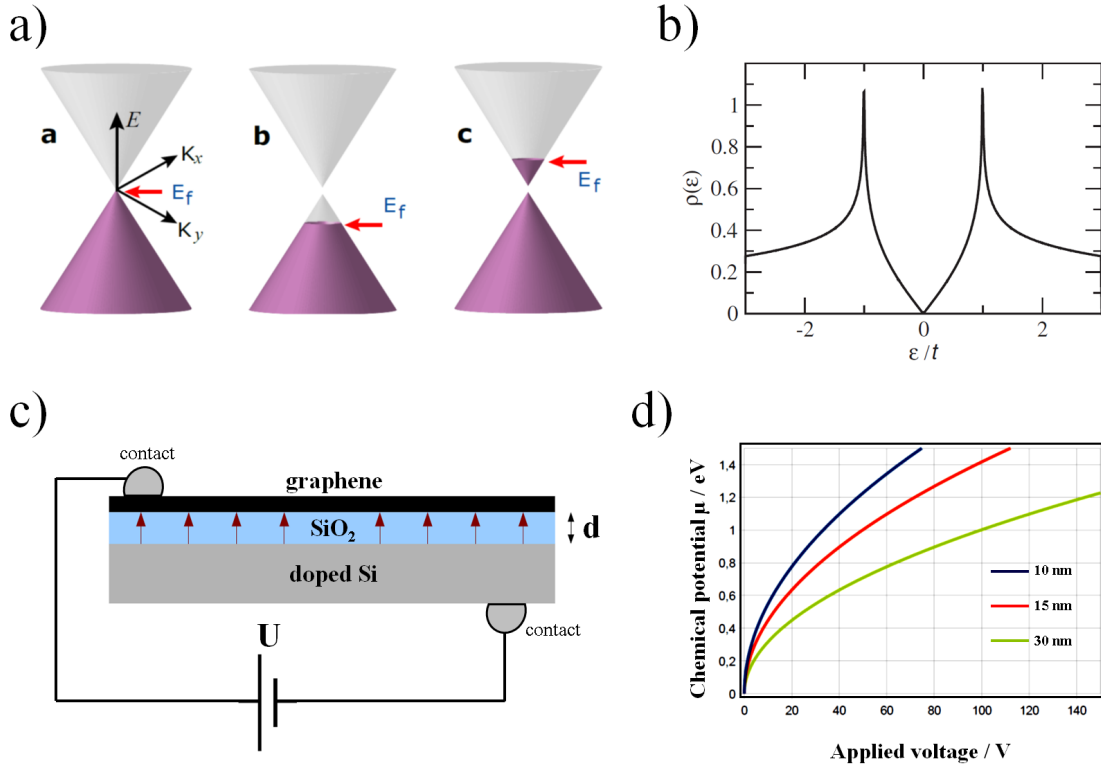


Figure 11: Electrostatic doping of graphene. a) Doping shifts the chemical potential  $\mu$  (or  $E_f$ ) away from the Dirac-point (figure taken from [160]). b) Density of states for graphene as calculated by tight binding modelling (TBM) with  $\epsilon$  in units of  $t=2.7\text{ eV}$  (figure adapted from [181]). c) Capacitor-like configuration for electrostatic doping of graphene with graphene acting as one of the capacitor plates and a thin  $\text{SiO}_2$ -layer as the dielectric. d) Chemical potential as a function of applied voltage for different thicknesses of the dielectric.

To describe graphene's (electromagnetic) properties, mostly the band-diagram is reduced to the Dirac-cone region, as the mathematical description is significantly simplified by this approximation - an approximation that starts to lose its validity when the energy range of the VIS is entered. Optical properties of graphene are computed based on the random phase approximation (RPA) that is applied on the band-diagram derived by TBM. Mostly the conductivity  $\sigma(\omega)$  is used, assuming no conductivity in out-of-plane direction. Thus, predicted optical properties are coupled to the method to derive the band-diagram as well as on the way to convert this into a conductivity. A direct measurement as it is done for ordinary bulky dielectrics or metals is more difficult. Finally the conductivity may then be transformed into a dielectric permittivity via

$$\epsilon(\omega) = 1 - i \frac{\sigma(\omega)}{\omega \epsilon_0 d}, \quad (2.6)$$

## 2. Theoretical Basis

---

where  $d$  is the thickness of graphene of around  $3.4 \text{ \AA}$  [42,43]. Whether the use of a macroscopic permittivity is an accurate way to describe a material in this ultimate thickness-limit, being quasi 2D, is questionable on principle grounds. However, in pioneering work graphene was handled like this within numerical simulations yielding results that qualitatively matched to measured data [44]. Specifically an *effective* thickness  $0.5 \text{ nm}$  of graphene was assumed with an isotropic and homogeneous dielectric permittivity, even though  $\epsilon(\omega)$  is a function of the thickness and in- or out-of-plane direction. Also the modelling of  $\sigma(\omega)$  already comprises some parameters with uncertainties, that can effectively act as fitting parameters.

Another open question is how to handle deviations from an idealized graphene sheet, e.g., finite graphene sheets. As soon as the infinite plane of the carbon lattice features an edge many theoretical calculations are in principle not valid anymore. Simulations including every single atom of small graphene islands found that the optical response would be significantly altered in some cases depending on the edges being in arm-chained or zig-zag configuration [31,32]. Whether such effects even out on realistic samples or not is still unclear, as well as the influence of roughness, substrates and solvent-layers on top or between graphene and substrate. Thus, as both theory and experiment are dealing with significant complications, graphene remains a very challenging subject of research.

As graphene was found to be an extraordinary good direct current (DC) conductor, showing ballistic transport at room-temperature [45], it is straightforward to think about potential plasmonic properties based on high frequency-dependent conductivity. First simulations predicted that graphene would behave like a metallic sheet at frequencies of IR or THz photons with low damping. This allows for plasmons controllable by electrostatic doping [42,46–48]. With scattering near-field microscopy (SNOM) it was possible to excite and visualize such plasmons [44,49]. These plasmons had faster damping rates than expected from theory but were indeed showing extremely short wavelengths (high momenta) and thus a very high degree of confinement. Whether these plasmons exist only in the IR region or can be excited also in the VIS is the topic of various theoretical publications and has been a controversial discussion. In chapter 6 experiments are presented that try to shine more light onto this topic.

## 2.3 Dipole Emitters

### 2.3.1 Hertzian Dipole

In classical electrodynamics a single fluorescent molecule can be described by an oscillating charge: a Hertzian dipole with a frequency-dependent polarizability. This dipole can absorb and emit electromagnetic energy continuously, basically acting as a resonator that stores energy for a time. Thus, such a structure is (in classical physics) fundamentally nothing else than the ultimate limit of a nanostructure hosting localized modes (2.4.3). Consequently a dipole has a far- and a near-field, as it represents a lossy (radiating) cavity (even though there is no inside for this cavity). That is exactly what is found, when the fields around a driven electric point-charge are analyzed as depicted in Figure 12 taken from Ref. [7].

The electromagnetic field around an oscillating point-charge can be decomposed into a series of components that decay proportional to  $(kr)^{-1}$ ,  $(kr)^{-2}$  and  $(kr)^{-3}$  [7]. Here  $k$  is  $\omega/c$  or  $2\pi/\lambda$  and  $r$  is the distance from the charge. Thus,  $kr$  is a normalized distance, where  $kr < 1$  is the near-field and  $kr > 1$  the far-field; fields decaying with  $(kr)^{-2}$  are denoted as intermediate-fields. Some basic features of this analysis are: i) the near-field contains much higher field strengths than the far-field, ii) in the near-field regions of high energy density (hot-spots) are found in the direction of the oscillating charge, in contrast to the far-field where no power is emitted in this direction, iii) near-, intermediate- and far-field can be associated to the position of the charge, its speed and acceleration, respectively [7].

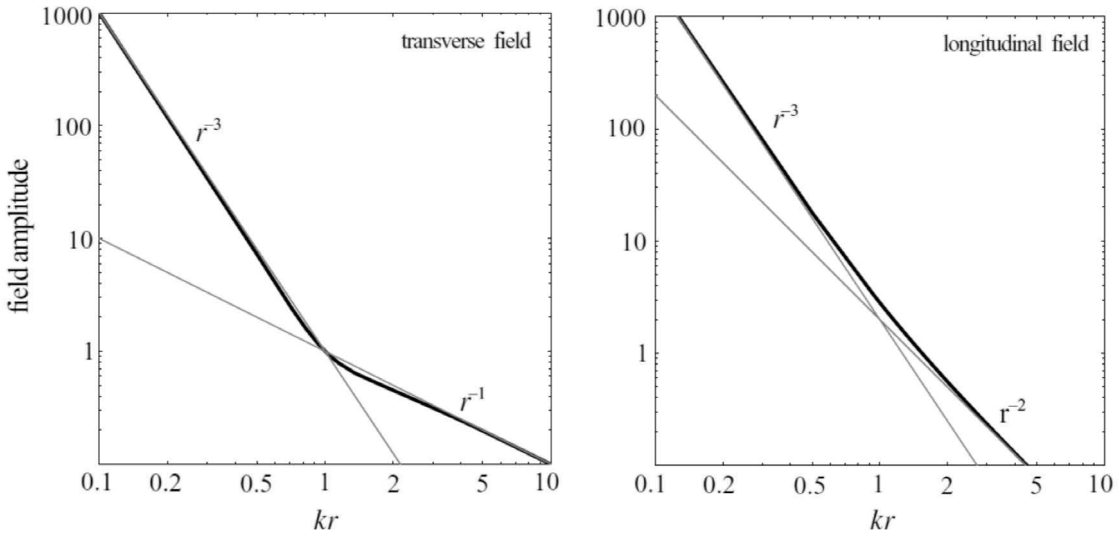


Figure 12: Field amplitudes (transversal and longitudinal) as a function of distance (normalized by the vacuum wavelength) from the dipole emitter. Different regimes (near-field, intermediate field and far-field) can be identified. A comparison of the longitudinal and transverse fields shows, that the highest near-fields are found in direction of the oscillating charge (longitudinal field), where no far-fields are present. Figure taken from Ref. [7].

### 2.3.2 Near-fields

As will be discussed later (2.4.1) the near-field must contain fields of higher momentum  $k_{\parallel}$  than that of the far-field (with  $k = \omega/c$ ), to compensate for the evanescent nature (imaginary momentum  $k_{\perp}$ ) away from the center:  $k = \sqrt{k_{\parallel}^2 + k_{\perp}^2}$ . Following energy ( $\hbar\omega$ ) and momentum ( $\hbar k_{\parallel}$ ) conservation, access to the energy stored inside the near-field of an emitter is possible, when modes with near-fields of high-momentum are “offered” to the emitter to emit into. This means that the power emission-rate of emitters can be significantly altered when the emitter is coupled to photonic/plasmonic structures by spatially overlapping the near-fields of the emitter and the optical mode.

### 2.3.3 LDOS

The change of the emitted power of a dipole mentioned at the end of the last section is described quantitatively with the changes in the local density of states (LDOS) sometimes also called local density of *modes* in order to prevent confusion with the density of states for electrons. The LDOS  $\rho$  is defined as the number of modes per volume at a specific frequency and location  $\rho = \rho(r, \omega)$ . Furthermore, the LDOS

## 2. Theoretical Basis

---

associated to individual modes can differ according to their degree of confinement and quality factor of the mode. The LDOS can usually not be measured directly. However, as mentioned before, changes in the emission rate  $\gamma$  of an emitter (with dipole moment  $\mu$ ) can. According to Fermi's Golden rule the quantities  $\gamma$  and  $\rho$  are related linearly via [7]:

$$\gamma = \frac{2\omega}{3\hbar\varepsilon_0} |\mu|^2 \rho_\mu(r, \omega) . \quad (2.7)$$

$\rho_\mu$  is the *partial* LDOS: as a dipole emitter has a specific orientation it can only react on a part of the LDOS [7]. Further, various physical processes can lead to a modified emission-rate (or modified LDOS) like Förster resonant energy transfer (FRET), pure quenching by an absorber or a Purcell-effect induced by a high-Q cavity. All these effects have to be taken into account for a correct identification of the underlying reasons for an enhanced emission rate (see discussion of Purcell effect in 2.5.3).

### 2.3.4 Quantum vs. Classical

#### *Emission and Absorption*

Without explicitly saying, the classical nature of energy dissipation (“emission rates”) and the quantum nature of spontaneous emission (“LDOS”) have been mixed in the last paragraph. That is only valid, as the equivalence of the classical and quantum picture have been mathematically demonstrated [7]. In classical physics the LDOS can be understood as the back-action to an emitter that stems from its own emission. The emission-rate (rate of energy dissipation) of a classical dipole is interpreted in quantum physics as a statistical probability of emitting a photon. The latter process happens randomly; photon-by-photon. When a pulsed excitation of a single photon emitter is performed, the arrival times of the emitted photons relative to the pump pulse can be recorded and fed into a histogram. An exponential decay is found (Figure 13). The time to decay to  $1/e$  of the initial amplitude is called the lifetime of the excited state of the quantum emitter. The inverse lifetime gives the same emission rate that was discussed before for classical dipoles. The equivalence is very valuable, as it allows computing of this important quantum physical quantity by relatively simple classical electrodynamics, i.e., by solving the Maxwell equations. While spontaneous and stimulated emission is quite clear to describe in classical electrodynamics by a damped or driven oscillator, spontaneous decay in quantum optics is interpreted by the stimulated emission induced

## 2. Theoretical Basis

---

by a virtual photon. The chance to interact with a virtual photon/plasmon is proportional to the LDOS.

However, there are more differences between a classical and a quantum emitter. As the latter has internal states with certain lifetimes it can be saturated. This means that the re-emission of power during excitation cannot be increased further and further by increasing the excitation. Thus, a strategy to produce many single photons, is to reduce the lifetime of the excited state by coupling the emitter to photonic structures that alter the LDOS. This is closely connected to another quantum effect, the photo-effect: a classical dipole may absorb or emit light continuously. This yields an in- or decrease in its amplitude of oscillation, while a quantum emitter can only absorb or emit photons in energy-packages of  $\hbar\omega$ . Additionally, allowed frequencies for excitation and emission are dictated by the energy levels of the internal quantum states and are not possible – no matter how strong the excitation power – when the photon energy is too low (except for non-linear interactions like two-photon absorption).

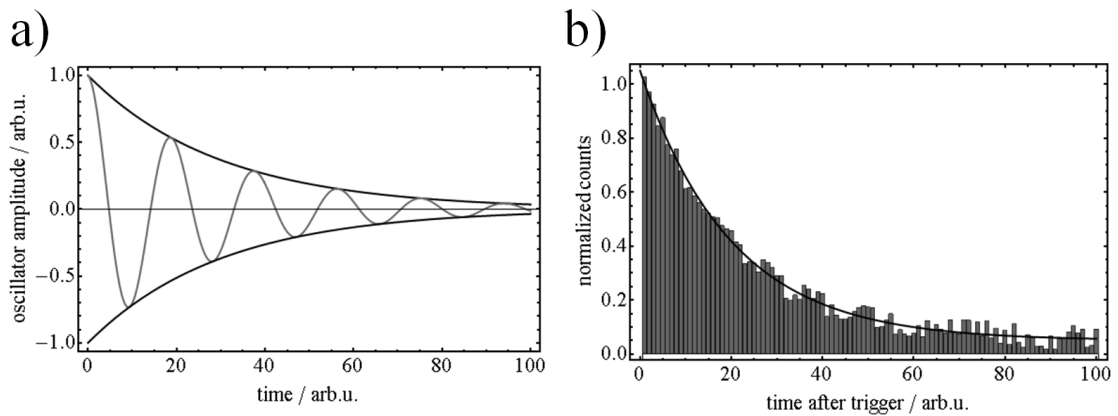


Figure 13: Schematic of classical and a quantum decay. a) Amplitude of a classical oscillator that is damped. The oscillator loses its energy with a rate corresponding to the exponential envelope. The decay constant is related to the rate of power emission. b) Histogram (with exponential guide-for-the-eye) of randomized numbers as in a typical lifetime measurement. Photon arrival-times of a spontaneous emission process are random but following an exponential probability distribution. Its decay constant is the emitter's lifetime (the inverse is the decay-rate).

### *Strong Coupling*

What was said before about the lifetime (or decay rates) is in principle only valid if the surrounding of the emitter does not give rise to a “strong” feedback. Such a surrounding with strong feedback is typically called a “cavity”. In case of a strong feedback the photon field and the emitter are said to become strongly coupled, creating a polariton. Thus, two regimes are distinguished: the weak coupling regime and the strong coupling regime. The strong coupling regime is entered when the decay rate into the cavity mode exceeds the loss rate of the cavity and the rate with which the emitter becomes decoherent. In optics this regime is typically described within a quantum mechanical description. However, it was pointed out by Novotny that various aspects of the strong coupling regime can be understood even within a classical toy-model of coupled oscillators [50] (see also section 2.5). In the typically applied quantum description, the decay rate of an emitter (at position  $\vec{r}$  and frequency  $\omega$ ) into a specific mode is described as a product of the dipolar coupling constant  $g$  and the density of states of that mode:

$$\gamma(\vec{r}, \omega) = 2\pi |g(\vec{r}, \omega)|^2 D(\omega). \quad (2.8)$$

In comparison to equation (2.7) here the density of states  $D$  is not local anymore but defined in a different way, depending only on the frequency. Consequently, it has to be expressed in different units which can lead to confusion. The spatial (local) character of the LDOS is here separated and included in  $g$ . However, the quantity of  $g$  cannot be measured directly and in some cases even not calculated. In principle it is only well defined for an emitter in a cavity. Nevertheless,  $g$  was also used to describe the interaction of emitters with guided photons or plasmons [51,52] (see chapter 4), which corresponds to an infinitely large cavity. The authors found a way to avoid the direct calculation of  $g$  but expressed their results with the help of decay rates (Purcell factor and total decay rate) following the usual definition of the local density of states of equation (2.7).

### *Photon Statistics*

The intensity auto-correlation of the light emitted by a single photon emitter is a prominent example where a classical description fails and a quantum description is needed. This kind of auto-correlation is called a  $g^{(2)}$ -function – a second order correlation. In this work it becomes important for the single photon transistor that is discussed in chapter 4.3.1. For this auto-correlation measurement the emitted photons

## 2. Theoretical Basis

---

are guided to a detector that allows to record the arrival times of the photons. As only a single photon is emitted at a time the correlation of two distinct photons will differ depending on the time delay  $\tau$  between two subsequent detections. The  $g^{(2)}$ -function is a way to quantify this correlation. It is defined as

$$g^{(2)}(\tau) = \frac{\langle I(t)I(t+\tau) \rangle}{\langle I(t) \rangle^2}, \quad (2.9)$$

where the  $\langle \rangle$  brackets denote an ensemble average. When expressing the intensities  $I$  in terms of the second quantization with field operators one can derive a quantum mechanical version of the  $g^{(2)}$ -function. This can be simplified for  $\tau=0$  and photon states of defined photon number  $n$  to:

$$g^{(2)}(0) = \frac{n(n-1)}{n^2} = 1 - \frac{1}{n}. \quad (2.10)$$

This yields a value of zero in case of a single photon light source whereas for classical light sources no value below unity is allowed at  $\tau=0$ . Thus, measurements of second order correlations are used to identify non-classical light sources.

### 2.3.5 Stokes Shift

Apart from cryogenic temperatures, realistic emitters like fluorescent molecules show rather broad absorption and emission spectra. Absorption and emission spectra are separated from each other: this spectral feature and the separation is known as Stokes shift. This effect is due to a multitude of energy levels that result from a coupling of the electronic energy levels with vibrational modes of the molecule. Photon emission will happen at energies somewhere between the lowest unoccupied molecular orbital (LUMO) and the highest occupied molecular orbital (HOMO) depending on the probability for this transition to take place. This probability follows the (frequency-dependent) LDOS but also the matrix element describing the electronic transition between two internal states of the molecule. The probability of the transitions and thus their intensities in spectroscopic investigations is described by the Franck-Condon principle. It basically states that a transition is the more likely to happen the larger the corresponding wave functions do overlap (Figure 14).

## 2. Theoretical Basis

---

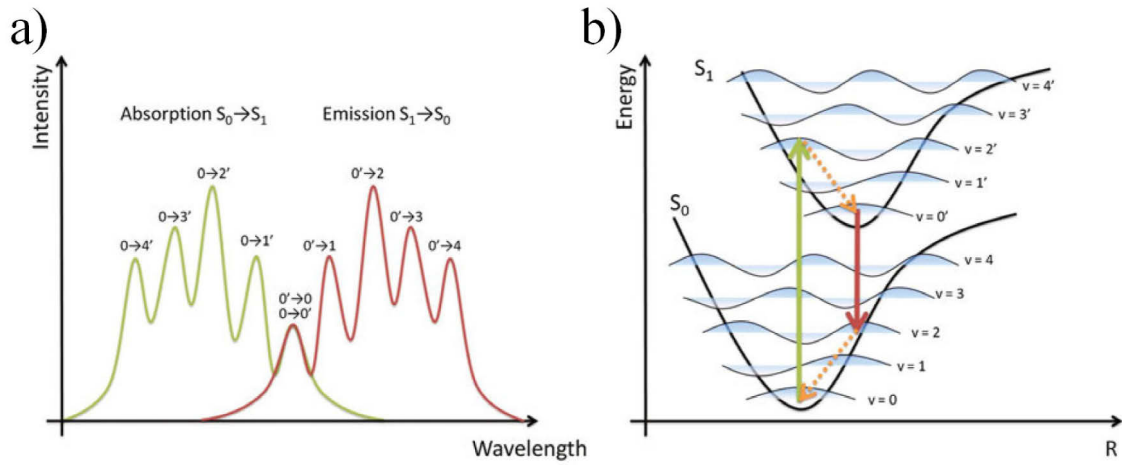


Figure 14: Correspondence of internal states and spectral response of an organic chromophore.  
 a) Absorption (green) and emission spectrum (red) showing various peaks that correspond to the main optical transitions. b) Multiple states exist in the ground and the upper potential ( $S_0$ ,  $S_1$ ) due to coupling to vibrational states ( $v=1\dots4$ ) of the molecule. An excitation (green arrow) and fluorescence (red arrow) process is accompanied by fast relaxation processes that include interaction with phonons. Figure taken from [182].

Further, the Stokes shift is important to consider, when organics are used as a gain medium in a laser. Despite the Stokes shift, absorption and emission overlap spectrally. The highest gain will be found where self-absorption is already very weak, i.e., at a frequency which is usually red shifted to the maximum of the emission spectrum. The effect is well-known from amplified spontaneous emission (ASE) [53,54].

## 2.4 Modes

### 2.4.1 Metals or Dielectrics Hosting Modes – on the Distinction between Photons and Plasmons

As mentioned in the introduction the term “plasmon” is a short name for surface plasmon polariton or localized plasmon polariton. A polariton is a coupled excitation of light and a solid-state excitation. Figure 15 shows a dispersion diagram of an exciton-polariton. In a quantum picture the polariton is a quasi-particle. It is said to become more and more “photon-like” the closer it is to the photon line on its dispersion. On the other hand, the classification of electromagnetic excitations into photons and plasmons seem to be somehow arbitrary since both are solutions of Maxwell’s equations. These solutions are called modes. Especially Mie-theory [55] describes modes hosted by spheres. These modes are sometimes called localized plasmons, sometimes whispering gallery modes, depending on the material and the size of the sphere – however Mie-theory treats all these modes equally.

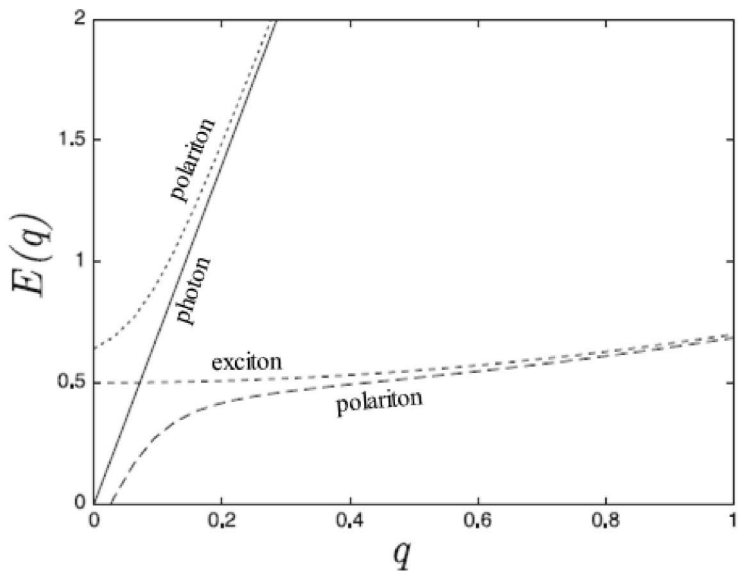


Figure 15: Dispersion (energy vs. momentum) of photons, excitons and the corresponding exciton-polaritons. Figure adapted from [183].

## 2. Theoretical Basis

---

Another way to define a plasmon is by its localization on a metallic surface, or to be more precise on an interface where the sign of the real part of the dielectric permittivity does change. The distinction between metallic or dielectric materials is in a microscopic picture mainly a distinction between freely movable and bound electrons. In both cases deflection of the material's electrons by an electromagnetic excitation is the underlying process of its response. A photon travelling through a dielectric could also be regarded as a polariton with bound electrons. Experiments have confirmed that important quantum properties of photons like coherence time, wave-particle dualism and indistinguishability do not change when they were transformed into plasmonic excitations and back again [56,57].

Khurgin and Sun comment on this in a paper related to nanolasers that are discussed in chapter 5 : “*In the case of a solid-state laser, the electronic oscillations are those of bound electrons, while for a spaser [surface plasmon laser] they are the oscillations of free electrons in the metal. For a VCSEL [vertical cavity surface emitting laser] operating near the bandedge of a semiconductor, up to 60% of energy is contained in the oscillations of bound electrons. In a spaser, this value can be as high as 85%, which is a quantitative and not a fundamental difference.*” [58].

In any case the conceptual discrimination into plasmon and photon causes many discussions considering the relatively vague physical difference. More relevant properties are the oscillator strength of the electrons (free or bound) together with the speed of energy dissipation (damping). The ultimate limit of this problem is a single oscillating charge bound to some potential – a Hertzian dipole – which exhibits an intense near-field, but a classification into being either metallic or dielectric is of little use. Another example for this is the discussion about nano-sized graphene islands and whether they feature plasmonic responses or not (“molecular plasmons” [59]).

However, it seems to be of higher importance to distinguish between near- and far-fields as both do not differ in frequency but in momentum, which is essential in many cases. As a matter of fact, near fields appear at boundaries of metallic *and* dielectric nanostructures, intensity and damping rates will depend on the individual nanostructure and the exciting light source but qualitatively they behave the same.

### 2.4.2 Guided Modes

The way to route optical energy or information carried by light beyond free-beams is to use waveguides. Optical waveguides can be formed by any material with higher refractive index than the surrounding or by metallic materials. The simplest waveguide is a “slab” or “film” waveguide formed by uniform media that are separated by clear edges in only one dimension. Light can be trapped inside these waveguides by total internal reflection. A set of specific guided modes can exist in a waveguide for a fixed frequency.

Guided modes are computed assuming a transversal symmetry, meaning that a cross-section is elongated to infinity. Although this approach turns out to be extremely useful and accurate, such a structure can of course never exist. Usually guided modes are distinguished from leaky modes that are damped during propagation by radiative losses [60,61]. However, only the mathematically idealized waveguide, e.g., free of bending, can be absolutely free of leakage. Moreover, guided modes can have propagation losses, i.e., when the waveguide material suffers from absorption ( $\kappa$  or  $\epsilon'' \neq 0$ ). The higher the order of the guided mode, the more field will evanescently leak out of the waveguide until a cut-off appears and no higher modes can be guided. Thinning down the waveguide reduces the number of possible modes. Only a single

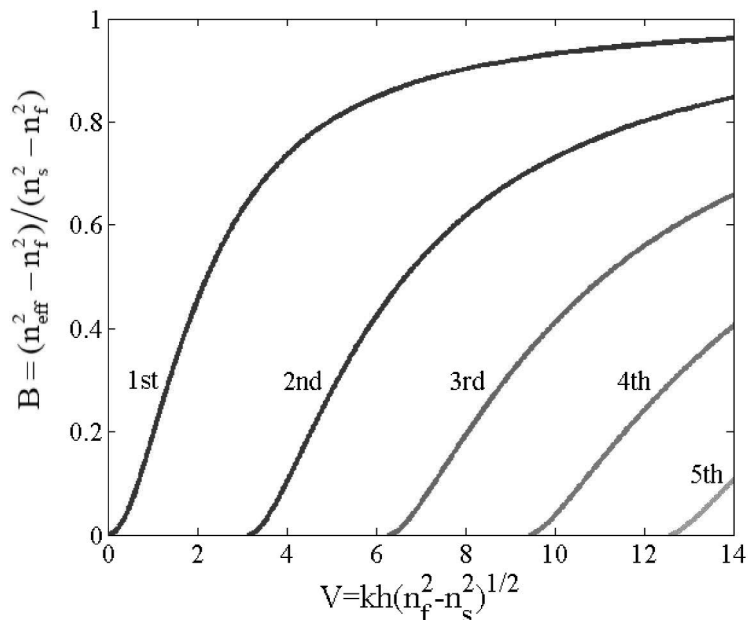


Figure 16: Five lowest order guided modes in a slab-waveguide consisting of an infinite film with a thickness of  $h=400$  nm and a refractive index of  $n_f=2$  in vacuum ( $n_s=1$ ) represented by dimensionless, normalized parameters  $B$  and  $V$ .  $B$  is the normalized propagation constant,  $V$  the normalized frequency.

## 2. Theoretical Basis

---

fundamental mode will always “survive” irrespective of how thin the enclosed material is (as long as it can be described by a dielectric permittivity).

Guided modes in simple slab geometries can be computed analytically (Figure 16) [62]. Even though their technological relevance might be limited as they only confine light in one dimension, they may appear in various configurations as an important side effect. For instance solar cells or (organic) light emitting diodes are often composed of numerous layered films of different materials. Slab waveguides can thus either limit the performance (e.g., limited light out-coupling) or be used to improve it (e.g., by light-trapping in solar cells).

The most prominent waveguide is the optical fiber as it is one of the basic elements for today’s broadband communication. A fiber is basically a very long thin cylinder of a glassy material. Again, without a break of symmetry a fundamental mode will always exist independent of the cylinder diameter. Both in slab waveguides and in cylindrical fiber-like waveguides purely “TE” (transversal electric) or “TM” (transversal magnetic) modes can be identified. In such a guided mode the denoted field (electric or magnetic) is purely orthogonal (transversal) to the direction of propagation [60,62].

This purity is lost when the symmetry is broken and only so-called TEM modes are found, i.e., a mixture of pure TE and TM modes. Waveguides “on a chip” for integrated optical structures represent such waveguides. Due to chip fabrication processes they usually have a rectangular cross-section. Guided modes in such waveguides cannot be computed on analytical grounds anymore due to the discontinuities at edges and corners but can be analyzed with numerical Maxwell solvers [62,63] as it was done during this thesis (chapter 4.2.1).

Beyond pure light guiding, distribution and connecting of optoelectronic elements, waveguides may be used to “focus” light. As mentioned above confining the light in a small waveguide leads to intense evanescent near-fields. For instance these near-fields can be used for trapping of atoms [64] or to enhance the interaction between near-by emitters and the photons/ plasmons that are passing by [65]. This strategy to enhance the light-matter interaction is explored in chapter 4.

### 2.4.3 Localized Modes

In this section basic features of modes in nanoresonators are discussed. They are especially important for the theoretical model of nanolasers that is discussed in chapter 5.1. Localized modes can be envisioned when guided modes are forced to bounce back and forth in-between at least two steps in the dielectric permittivity profile (leading to reflection) or by bending the waveguide to a closed loop. In both cases - if sufficient coherence is present - interference will lead to resonance conditions. So, electromagnetic energy can be stored (or localized) by the structure. Corresponding frequencies and field distributions are called eigenfrequencies and eigenmodes (or eigensolutions), respectively. The quality factor  $Q$  is a measure for the damping of the energy that is stored in a resonator. It is defined by the complex eigenfrequency via  $Q = -\text{Re}(\omega)/(2 \text{Im}(\omega))$ . Similar to waveguides, two main loss channels of the bare optical resonator are thinkable: damping via absorption or by leaking radiation. Losses due to scattering at imperfections within the resonator material such as variations in the refractive index may also reduce the quality factor but are more relevant for high-Q cavities rather than for the low-Q particle-based cavities considered in this thesis. Every

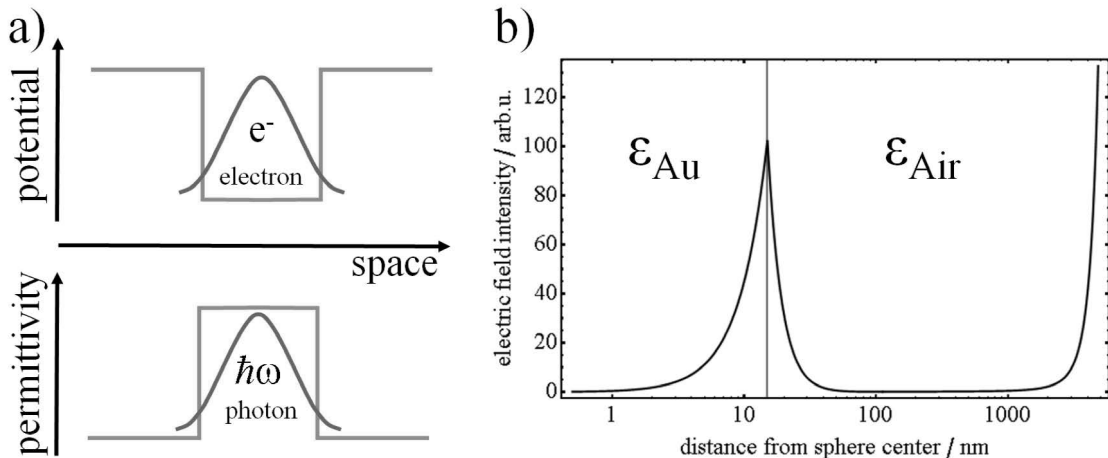


Figure 17: Electronic states vs. localized photonic modes. a) Scheme of an electronic wavefunction in a potential well and a photonic mode in a resonator. Both are often assumed to represent almost equivalent problems. b) Electric field intensity of a resonant quasi-normal Mie-mode (a plasmon) as a function of distance to the sphere's center. The vertical line marks the radius (15 nm) of a spherical cavity ( $\epsilon_{\text{Au}}$ ) in air ( $\epsilon_{\text{Air}}$ ). Characteristic for a plasmon, the field intensity is peaking at the surface and decays exponentially away from the interface. However, as this Mie- mode radiates, the field intensity does not converge to zero but increases again and diverges for larger distances.

## 2. Theoretical Basis

---

practical resonator, even those with no absorption, will suffer from losses by leakage, i.e., radiate to the far-field (Figure 17) [66]. Otherwise no optical interaction with the outside would be possible. Due to the losses modes of a resonator are *not* power-orthogonal (modes will exchange power). Consequently, any localized mode in optics should be called “quasi-normal” mode [23,66] in order to distinguish them from ideal orthogonal eigenmodes.

Photonic modes are often equated with electronic states, e.g., an electron in a potential well (Figure 17a). The latter can be usually normalized as the probability to find the electron far away from the well tends to zero. As any optical cavity will radiate, a similar normalization does not work out for photonic modes, so that no normalization can be used that yields orthonormal modes. Consequently, Hermitian mathematics cannot be applied to photonic eigenmodes in principle. The lower the Q-factor the more any conclusion based on the orthonormal relations will be violated. Specifically the coupling of such eigenmodes to emitters, mostly described with the Purcell effect may be overestimated [23,66,67]. The violated power-orthogonality relation also has to be considered for waveguides, especially when absorption losses as in plasmonic waveguides are present.

Apart from the well-known Fabry-Pérot resonator, basically set up by two parallel mirrors, spheres are very simple and well describable cavities for light. Gustav Mie used spherical harmonics to describe all possible electromagnetic modes in spherical objects. As mentioned earlier, various names are used for these modes, depending on the ratio of size to wavelength, the material or the physical community, such as “whispering gallery modes”, “particle plasmons” or simply “Mie-modes”. Due to the intrinsically high symmetry of these modes numerous physical problems can be tackled on analytic grounds giving fundamental insight into otherwise complex problems such as scattering and absorption of plane waves and modified dipole emission, or computation of eigenfrequencies and eigenmodes.

### *Mie-Theory*

Gustav Mie derived solutions for the wave-equation in spherical coordinates yielding all possible eigenmodes of spherical objects [55]. Similar to the orbitals and corresponding quantum numbers of a hydrogen atom, these modes depend on integer numbers. Often the terms “order”  $n$  and “angular momentum” number  $m$  are used (with  $m \leq n$ ), which stem from associated Legendre polynomials and spherical Bessel functions that appear

## 2. Theoretical Basis

---

in the solution. Furthermore the solutions are distinguished by being either “even” or “odd”, so that in the relevant cases there are at least  $2n+1$  solutions for a fix  $n$ :  $n=1$  corresponds to a dipolar eigenmode,  $n=2$  to a quadrupole and so forth. That is, a mode of order  $n$  is also  $2n+1$ -times energy-degenerated. Each mode is either a transversal magnetic (TM) or a transversal electric (TE) mode.

Based on the eigensolutions Mie derived the so-called scattering coefficients  $a_n$ ,  $b_n$ , (for the outer field) as well as  $c_n$  and  $d_n$  (for fields inside the sphere), for an excitation via a plane wave. These coefficients are typically more useful than the general solution itself. They read:

$$a_n = \frac{N^2 j_n(Nx)[xj_n(x)]' - j_n(x)[Nxj_n(Nx)]'}{N^2 j_n(Nx)[xh_n^{(1)}(x)]' - h_n^{(1)}(x)[Nxj_n(Nx)]'}, \quad (2.11)$$

$$b_n = \frac{j_n(Nx)[xj_n(x)]' - j_n(x)[Nxj_n(Nx)]'}{j_n(Nx)[xh_n^{(1)}(x)]' - h_n^{(1)}(x)[Nxj_n(Nx)]'}, \quad (2.12)$$

$$c_n = \frac{j_n(x)[xh_n^{(1)}(x)]' - h_n^{(1)}(x)[xj_n(Nx)]'}{j_n(Nx)[xh_n^{(1)}(x)]' - h_n^{(1)}(x)[Nxj_n(Nx)]'}, \quad (2.13)$$

$$d_n = \frac{Nj_n(x)[xh_n^{(1)}(x)]' - Nh_n^{(1)}(x)[xj_n(x)]'}{N^2 j_n(Nx)[xh_n^{(1)}(x)]' - h_n^{(1)}(x)[Nxj_n(Nx)]'}, \quad (2.14)$$

where potential magnetic permeabilities have been ignored for simplicity,  $N$  is the ratio of the inner to the outer refractive index,  $j$  and  $h$  are the Bessel or Hankel functions, respectively and  $x$  is the “size parameter”, i.e., the ratio of the sphere’s radius  $R$  and the photon wavelength in the outer medium ( $x=2\pi R/\lambda \cdot n_{out}$ ). As suggested by the name “scattering coefficients”, they can be used to derive absorption and scattering cross-sections for a plane wave excitation of a sphere by summing up over a series of those coefficients [55].

From the denominator of the scattering coefficients, characteristic equations for the (complex) eigenfrequencies can be derived, i.e., when the denominator becomes zero, the scattering coefficient will diverge. Putting this eigenfrequency into general solution yields the fields of a pure eigenmode.

Actually, even more solutions can be found than the  $2n+1$ : Due to the oscillatory behavior of the Bessel function there is a discrete set of roots. These roots are numbered and named radial mode number  $r$  as they have  $r$  field maxima in radial direction. These modes are often neglected (apart from the first root) as they are usually shifted towards higher photon energies.

### *Quasi Static Limit*

In the quasi static limit the description of small plasmonic particles of diameter  $d$  can be simplified significantly with respect to Mie-theory. This can be very helpful to estimate for instance the quality factors resonances in plasmonic particles or even for the needed gain-factors in nanolasers (see chapter 5.1.4). When  $d$  is much smaller than the wavelength of the light  $\lambda$  that interacts with the particle ( $d \ll \lambda$ ) the field amplitude does not change significantly over the sphere. Therefore a way to describe the response is, to assume a static potential that polarizes the sphere and adding a harmonic time dependence afterwards [29]. It can be shown, that the scattering of a plane wave by such a particle behaves like the emission of a dipole. Another way to get to this result is an expansion of the Bessel functions that appear in the scattering coefficients of Mie-theory in a power series. For very small spheres the dipolar coefficient  $a_1$  dominates for the outer field. However, a similar simplification cannot be derived for the internal coefficients.

This result seems to be a source of misinterpretation as was pointed out by Moroz [68] when it comes to the description of decay rates of emitters close to the sphere. The strength of light-matter interaction scales with  $\vec{d} \cdot \vec{E}$  (dipole moment  $d$  and field strength  $E$ ). However, when estimating the spontaneous decay rate of an emitter in the presence of a metallic particle it is generally not precise to take only the field of the dipole-like response of the particle into account. In contrast a dipole emitter is able to excite numerous higher-order modes in the sphere [68] when its near-field penetrates the sphere. There is in principle an infinite number of higher order modes that can be regarded as additional decay channels. Thus, the total decay rate can be substantially higher than the decay rate that is found when only assuming a dipole-dipole interaction. For the nanolaser model discussed in chapter 5.1 a rigorous approach is used, that is based directly on Mie-theory.

## 2.5 Methods to Quantify Light-Matter-Interactions

As mentioned earlier (2.3) a classical description, i.e., solving Maxwell's equations, is sufficient to describe many effects in nanooptics. This allows to predict processes even though the quantum nature is expected to play a major role, e.g., decay rates of individual quantum emitters. At least classical calculations help to decide whether a more detailed description with quantum mechanics is necessary. Three classes of problems are most relevant to describe most of the problems: scattering and absorption of a specific light source by a structure, the eigenmodes (localized modes) of a cavity and propagating eigenmodes, i.e., guided modes.

### 2.5.1 Analytic Approaches

Analytic solutions are of high value, as they reveal the underlying physical principles. At the same time they allow separating various effects that would be intermixed in a numerical study or an experiment. However, only few problems of high symmetry have been solved analytically. As mentioned in section 2.3, the field around an oscillating point-charge was analytically solved, making it possible to separate contributions of the near- and far-field. Furthermore a way to decompose the dipolar field into plane waves was found [7], which makes it possible to use a dipole emitter as a source for other highly symmetric problems. Three of these symmetric problems are especially the one of two separated half spaces, Mie-scattering, as well as infinitely long cylinders.

A possible route to analyze the light-matter interaction is to compute a set of supported localized or guided modes in a structure. In a second step possible sources may interact with these modes. Accordingly, Ruppin [69] used the expansion of a dipole into plane waves. This was then used to compute the scattering and absorption cross-sections of each plane wave with the spherical harmonics that describe the modes in spherical particles. Finally he was able to derive the modified decay rates of a dipole close to a sphere and separate contributions into radiated and absorbed power [69]. Ruppin's description is the basis for the theoretical model of nanolasers described in chapter 5.1.

### 2.5.2 Numerical Simulations with Finite Element Method

Only a little number of mostly highly symmetric problems in optics can be treated analytically. Efficient numerical solvers are thus frequently used to study and design nanostructures. Especially in chapter 4 where on-chip structures are discussed, various numerical calculations are presented. Numerical solvers are basically divided into two classes, those working in the time-domain and those working in the frequency-domain. In this work the finite element method FEM (JCMwave) was used, in which solutions of the Maxwell's equations are computed for a fixed frequency, thus FEM belongs to the frequency-domain solvers.

Each FEM solver splits the computational domain, which represents a model of the physical system, into finite elements. These are predominantly triangles in two-dimensional problems or tetrahedrons in three-dimensional problems. These elements can be of non-uniform size and shape, enabling a relatively smooth mesh with a small number of elements (Figure 18) of the considered physical system. Maxwell's equations are reformulated and adapted for the specific solver and then solved on the whole computational domain. A solution consists of polynomials of variable degree existing on the elements. These polynomials line up to the overall solution [70].

A major strength of FEM is the adaptivity (based on error-estimation) and the possibility to increase the degree of freedom, i.e., increasing the polynomial degree of the ansatz-functions on the individual elements or to increase the number of elements (refinement) [71]. With the use of adaptivity the accuracy of the solution can be increased where it is necessary, i.e., where the estimated error is high. Increasing the degrees of freedom allows for relatively fast convergence tests. Stepwise increasing these degrees should lead to new results with decreasing difference to the corresponding latest result and to decreasing estimated errors. In any case a numerical method should be tested whenever possible against an analytic solution.

Just like described above (2.5), also JCMwave allows for the solution of three problem classes named self-explanatory (i) Scattering, (ii) Propagating-Mode and (iii) ResonanceMode. Depending on the applied boundary conditions one can search for different solutions.

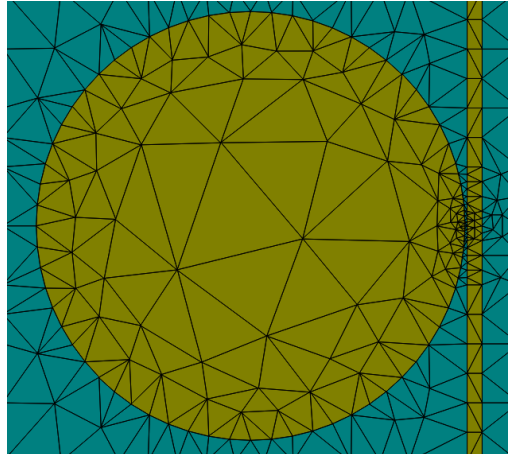


Figure 18: Example of an adaptive two dimensional finite element grid. A straight waveguide passes a whispering gallery resonator (circle). Light may couple evanescently from the waveguide to the resonator. Especially due to smaller and thus denser triangles the round surface of the circle can be approximated relative good even though the triangles are constructed from straight lines. Small features like the gap between waveguide and circle where essential physical processes will take place, are resolved automatically more accurate than the rest of the computational domain.

For scattering problems mostly transparent or periodic boundaries are used. Transparent boundaries are represented by perfectly matched layers (PML) that act like an infinitely large computational domain, meaning that no light will be reflected at borders of the domain. To obtain such a behavior the PML act like a material with absorption, i.e., that damps the entire outgoing field very fast. Additionally it is designed in way, that its permittivity gives no rise to any reflection, i.e., it starts at the border to the computational domain with the same permittivity as inside and only gradually evolves towards a more and more absorptive medium [72–74]. Guided modes are calculated with boundaries, on which the field has to vanish, leaky modes are found when transparent boundaries are used, as these boundaries “allow” for solutions that radiate. As basically all resonators radiate some power to the far-field, transparent boundaries have to be applied when cavity-eigenmodes are computed. The light source for scattering problems may be constructed from plane waves, coming from the outer domain, or dipole emitters inside the computational domain. Also propagating modes that were computed before in one or two dimensional problems can be fed to two or three dimensional problems, respectively.

### 2.5.3 Coupling of Emitters to Individual Modes

This section describes ways to calculate the interaction of dipole emitters with optical modes. What is meant by this interaction is the Purcell effect. It is quantified by the Purcell factor  $\Gamma$ , that is a measure for the exchange of energy between emitters and nanostructures in terms of rates normalized to the decay rate in vacuum.  $\Gamma$  sorts out the interaction of individual modes with emitters from the total LDOS.  $\Gamma$  is an important number in physical systems that depend on a *feedback* mechanism. Especially  $\Gamma$  can play an important role for effects like lasing and strong coupling that may yield a non-linear optical response.

Strong coupling is usually discussed in a quantum mechanical framework while the Purcell-effect is mainly considered in the weak coupling regime. However, as discussed by various authors, many features of strong coupling can be accurately described within a classical description with the help of the Purcell-factor. Dowling even notes: “*This present work proves, then, that the effect of spontaneous emission changes in cavities is about as classical as one can possibly get*” [75]. Tanji-Suzuki et al. review this topic [76]. The authors present for instance a formula for the reflectance and transmittance (including Rabi splitting) through a cavity with a strongly coupled atom. The formula only depends on detuning from the transition frequency of the atom, the cavity losses and the Purcell factor. The Purcell factor coincides in their description with the cavity cooperativity. The classical description only loses its validity when saturation effects of the atom start to play a role. [76]

In Purcell’s original work the altered emission rate  $\gamma_M$  ( $M$  stands for individual mode) normalized to the unaltered emission rate  $\gamma_0$  (in vacuum or air,  $\Gamma = \gamma_M/\gamma_0$ ) was defined for a dipole that oscillates resonantly to a cavity mode positioned at the maximum and oriented along the major polarization of the mode. As mentioned before, the Purcell effect is thus caused by a modified LDOS stemming from a single mode, so to say the mode-selective partial LDOS.

However, results from Purcell’s original work are based on the assumption of orthogonal modes, which can be an approximation for high quality resonators at most (see 2.4.3). This is found to be basically always violated in plasmonics due to intrinsic material losses but also often when lossless dielectrics are used in nanooptics [23,66,67]. Thus, in these cases a careful theoretical analysis is necessary to avoid misinterpretation of experimental results and for accurate predictions that allow

## 2. Theoretical Basis

---

for a successful design of experiments. In the following it is discussed how a computation of the Purcell-factor can be performed for guided and localized modes.

### *Guided Modes*

When one strives for efficient coupling of an emitter to a guided mode again the term Purcell factor is used. However, as there is no resonance whatsoever in an infinitely long waveguide, in principle the term could be completely misleading. Nevertheless it is used, as again the mode-selective effect of the LDOS is meant.

No analytic solution is known for this problem when waveguides with absorption losses are employed even for the highly symmetric problem of an infinitely long cylinder in a homogeneous surrounding. To derive quantitative estimates the quasi static limit of very thin waveguides has been used [65,77] or numerical simulations have been used. Several papers are published that come to fundamentally different results [78,79]. Basically, problems arise due to the absorption in the waveguide: The guided modes can no longer be expanded into a set of orthogonal modes which would allow for a rigorous decomposition of the decay processes. Close to a metallic nanowire an emitter may emit light to the far-field when decaying by direct emission of photons, or by excitation of leaky plasmons. Non-radiative decay channels stem partially also from leaky plasmons, but also from guided plasmons and localized plasmons (oscillation along the cross-section of the waveguide). A decomposition of all these contributions is difficult. It was concluded [77] that the problem can be solved in the limit of very thin nanowires – in the quasi static limit – where the non-radiative channels would only stem from a single guided mode. This is however a misinterpretation of the meaning of quasi static, as various higher-order localized modes that can exist along the short-axis of the nanowire cannot be neglected (see discussion 2.4.3). However, a reasonable solution for the coupling to guided modes seems to be presented by Barthes et al. [79] for waveguides of arbitrary cross-sections.

## 2. Theoretical Basis

---

As depicted in Figure 19 the density of states can be analyzed with respect to the momenta of the electromagnetic field. Processes with momenta up to that of a free space photon  $k_0$  belong to the radiative decay rate  $\gamma_{\text{rad}}$ , everything above that value is bound to the waveguide and yields nonradiative processes  $\gamma_{\text{nrad}}$ . The pole around the effective refractive index  $n_{\text{eff}}$  of the guided mode represents the density of states associated with the actual guided mode  $\gamma_M$ . It was found that the coupling to a lossy guided mode can be calculated just like in the lossless case even though mode orthogonality is no longer given. Barthes et al. state: “*this simply reveals that the emitter couples to the guided mode, no matter whether the energy is dissipated by losses during propagation or propagates to infinity*” [79]. In this thesis this method was compared to a more heuristic approach [52] and confirmed by fully three-dimension numeric simulations, resulting in good agreement. The method is especially important

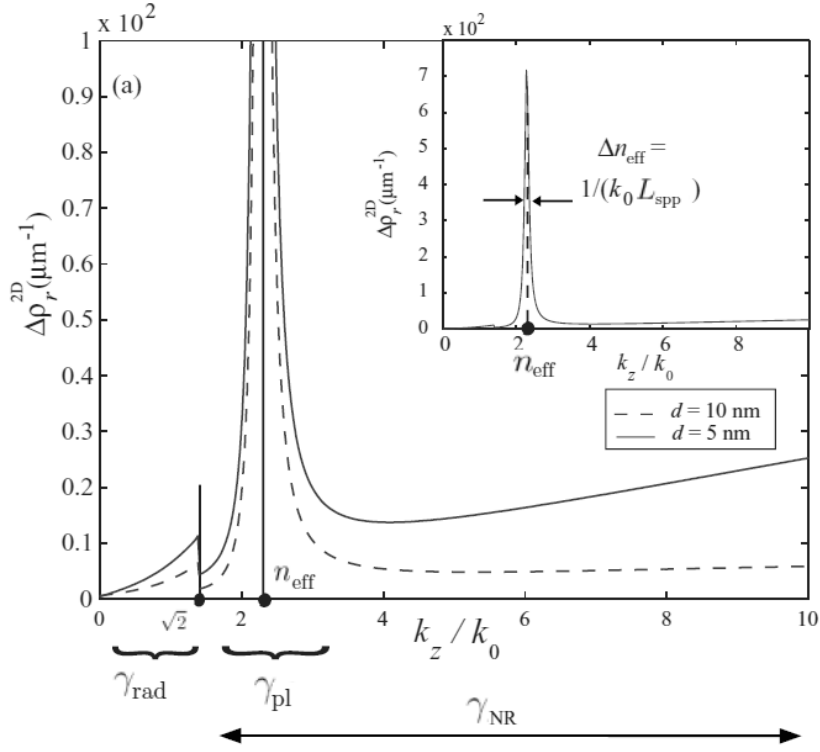


Figure 19: Density of states  $\rho$  of an infinitely long waveguide as a function of the associated momentum  $k_z$  (normalized by  $k_0$ ). All processes up to a momentum of  $k_0$  belong to radiated photons – thus to the radiative decay rate  $\gamma_{\text{rad}}$  – everything else are consequently non-radiative processes ( $\gamma_{\text{nr}}$ ). The pole around the guided mode’s momentum  $n_{\text{eff}}$  is the density of states associated with the actual guided mode. The rest belongs to unwanted quenching processes stemming from modes associated with the short axis of the waveguide.  $\rho$  is plotted for two distances (5 and 10nm) to the wire’s surface (full and dashed line, respectively). Figure taken from [79].

## 2. Theoretical Basis

---

for the design of on-chip structures that are discussed in chapter 4.2.1. Thus, it will be described in more detail in the following.

Two calculations have to be performed to derive the so-called  $\beta$ -factor, i.e., the ratio of plasmons emitted into the waveguide to the overall emission:

$$\beta = \frac{\gamma_M}{\gamma_{\text{tot}}} = \frac{\gamma_M}{\gamma_0} \cdot \frac{\gamma_0}{\gamma_{\text{tot}}} = \Gamma \frac{\gamma_0}{\gamma_{\text{tot}}} . \quad (2.15)$$

One calculation is to derive  $\Gamma$ , another has to be performed to derive the total decay rate  $\gamma_{\text{tot}}$ . Here,  $\gamma_0$  is the decay rate in vacuum/air. First the Purcell factor  $\Gamma$  is calculated using the result found in [79]:

$$\Gamma = \frac{\gamma_M}{\gamma_0} = \frac{3\pi c E_u(r) [E_u(r)]^*}{k_0^2 \int_{A_\infty} (\vec{E} \times \vec{H}^*) \cdot \hat{z} dA} , \quad (2.16)$$

where,  $\hat{z}$  is the normalized vector pointing in the direction of propagation and standing orthogonal on  $A$ .  $k_0$  is the photon momentum in air.  $E_u$  denote the electric field components parallel to the direction of the emitter. The only input needed for this computation is the solution of the guided mode field pattern, which can be exported on a two dimensional Cartesian grid. The field is represented by three-dimensional complex field-vectors at each point. For each independent dipole orientation along  $u$  (e.g.  $x,y,z$ ) the Purcell factor is now straightforwardly calculated by taking only the projections of the fields on the corresponding orientations ( $\vec{E} \rightarrow E_u$ ). The denominator represents a normalization by the flux along the waveguide direction  $\hat{z}$ . As all the  $\beta$ -factors are computed just based on the guided mode solution which is a single FEM-calculation (that can be reduced to a two-dimensional one), this evaluation is very fast. However, computation of the total decay rate is time-consuming as for each position and orientation of interest a full three-dimensional calculation has to be performed. Such calculations further need rather strong refinement especially close to corners of metals as high moments occur in the near field of a dipole. The total decay rate can only be computed, as the ratios of emitted power and decay rates are equal:

$$\frac{\gamma_{\text{tot}}}{\gamma_0} = \frac{P_{\text{tot}}}{P_0} , \quad (2.17)$$

where  $P_0$  is the power radiated by a dipole in vacuum and  $P_{\text{tot}}$  that close to the nanostructure [7]. A pragmatic way to tackle the problem of calculating  $P_{\text{tot}}$  for all interesting positions is to make use of the knowledge about strong quenching close to metals. In this case  $P_{\text{tot}}$  is a continuously increasing function when the distance to the

## 2. Theoretical Basis

---

metal is reduced. Thus, for numeric simulations it is not necessary to check convergence for very small distances, but convergence is only needed up to distances where unacceptable strong quenching sets in anyway, i.e., as a rule of thumb below a distance of 5 nm in the VIS.

### *Localized Modes*

Various publications report on experiments where high Purcell factors were found when emitters have been coupled to nanoscopic resonators. Experimentally this is then mostly supported by lifetime measurements and numerical simulations are performed to support the results. This was done even though a rigorous way to calculate the Purcell factor was only reported very recently in 2013 [23]. Further, lifetime measurements can only be used to probe changes in the total LDOS, i.e., various decay process sum up and not only the effect stemming from the resonator. Work in this field has to be treated with caution as it was demonstrated that the outcome of numerical calculations that were used to determine the Purcell factor can lead to overestimations: The result is a function of the used domain-size if not performed in the correct way. Thus, theory could (accidentally) yield results – especially overestimations - that fit to the observed lifetime reduction, when this was simply caused by ordinary quenching.

A major problem of defining the Purcell factor for individual leaky cavity modes arises from the complex eigenfrequency  $\omega_{\text{res}}$  and accompanied normalization of the modevolume  $V_M$ . The quality factor is defined by  $Q = -\text{Re}(\omega_{\text{res}})/(2\text{Im}(\omega_{\text{res}}))$ , so that only for unphysical cavities with infinite Q there is no imaginary part of the eigenfrequency. This imaginary part however leads to an exponentially increasing field intensity of the leaking fields away from the cavity as shown in Figure 17 in section 2.4.3. An integral over the usual energy density that is needed for normalization will thus diverge. Furthermore, not all the modes in the cavity are orthogonal to each other. As mentioned earlier, for low Q cavities, especially in plasmonics this is problematic [67].

Sauvan et al. [23] present a solution for the normalization. They use a coordinate transform, that damps the leaking field very fast – this transformation is nothing else than a PML (0). A modified energy density (with respect to the original formalism by Purcell) can then be integrated inside the computational domain and inside the PML. The formalism is constructed such, that diverging parts of these integrals cancel out irrespectively of the size of the computational domain. They show that for a specific

## 2. Theoretical Basis

---

choice of energy density the normalization can be computed, as it is an invariant of the coordinate transform.

The derived modevolume  $V_M$  is a complex quantity, but its imaginary part only comes into play, when the emitter is detuned from being perfectly resonant to the cavity's eigenfrequency or when the effect of two or more cavity modes interfere. More importantly it is not a global number characterizing a cavity but it depends on the position and orientation of the emitter.

An analytic counterpart of the numeric approach found by Sauvan et al. is the analytic solvable case of a spherical particle that was analyzed by Ruppin [69]. This formalism was used in this thesis to describe nanolasers and spasers (chapter 5.1).

---

## 3 Experimental Basis: Preparation and Investigation

---

This chapter contains predominantly technical information about the samples and applied experimental methods that would possibly obscure a clear view on the relevant physical discussion in the main chapters 4 to 6. This chapter starts in 3.1 with description of the sample preparation and sample properties regarding the on-chip structures and the designated quantum emitters, the synthesis of the core-shell particles for spasing as well as some details on the exfoliation of graphene. This is followed in section 0 by a description of the main experimental tools and the setups in total.

### 3.1 Sample Preparation: Matter & Emitters

#### 3.1.1 Chip Fabrication by Lithography

The on-chip structures that have been designed and simulated during this thesis (chapter 4.2) have been fabricated at the Helmholtz-Zentrum Berlin (HZB) by e-beam lithography performed by Max Schoengen and Jürgen Probst. The process includes several masking and etching steps and will be briefly and simplified described here. As mentioned earlier (2.2.2) silicon nitride is available with high quality (pure, crystalline, thin and flat) on chips. Thus, such chips have been the starting point for the processing. Figure 20 shows a sketch of important fabrication steps. The major difficulty comes from the usage of two different materials, i.e., Au and SiN for the waveguides, especially from the fine alignment of these structures to each other.

### 3. Experimental Basis

Often applied strategies in lithography are “subtractive” or “additive”, here both strategies have been combined. A subtractive method has to be applied to the SiN, as most of this material has to be removed to leave thin stripes that act as waveguides. To this end a positive mask has to be used, i.e., a resist was used that remains after e-beam exposure and processing (Figure 20b). Only then etching will lead to waveguides. On the other hand, as no Au is on the chip in the beginning, it has to be deposited there. Therefore a negative mask has to be used, i.e., a mask with gaps and slots in which Au is deposited into. This task is solved by putting a second resist on top of the first positive mask. This resist is however washed away where it was exposed by e-beam (Figure 20c). Now Au is deposited (Figure 20d), before the second (negative) mask is removed (Figure 20e) and the SiN that is not protected by the first mask is etched away. After a final removal of the first mask the designated on-chip structure is accomplished (Figure 20f).

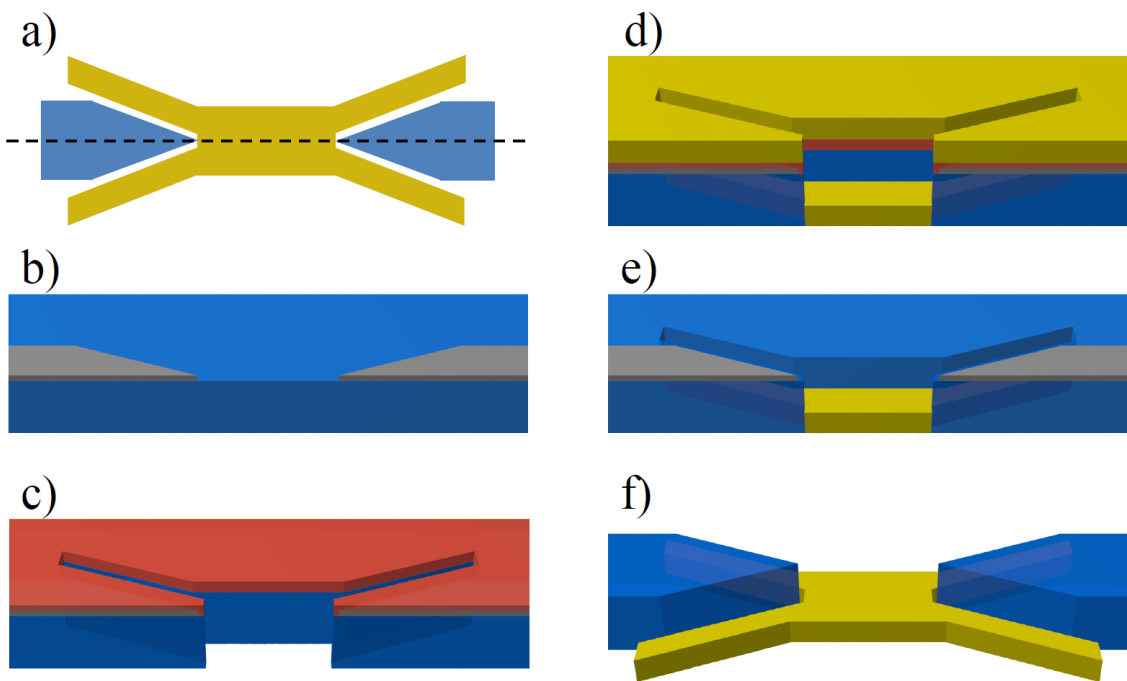


Figure 20: Schematics of main fabrication steps of the on-chip structures with focus on the photon-to-plasmon coupler. b)-f) Cut along the waveguide axis as indicated in a) by the dashed line. b) SiN (blue) chip is decorated with a positive mask (grey) for the SiN waveguides, c) Negative mask (red) is deposited on top, d) Au is deposited, e) Negative mask is removed and f) residual SiN is etched away.

### 3. Experimental Basis

---

This is the basic strategy to fabricate the on-chip structures. However many tests have to be performed until satisfying results are found. For instance etching never leads to perfectly straight side walls. Further, here an adhesion layer made from Cu had to be used to make the Au stick to the substrate and an additional Ni layer had to be used to protect the Au during the etching of the SiN. More details of the process can be found in Ref. [80].

#### 3.1.2 DBT in Anthracene

An essential constituent of the non-linear on-chip device as discussed here is a quantum system, i.e., a single photon emitter (chapter 4.1). The performance of the device sensitively depends on the quality of the emitter. Especially a high quantum yield and a narrow spectral width – at best Fourier limited emission – is preferred [51]. For practical reasons the emitter should be as stable as possible and emit significantly red shifted to the increasing absorption of gold around 530 nm to reduce plasmon damping but also accidental excitation of gold photoluminescence (that can be very broad) by laser light [25,35].

Dibenzoterrylene (DBT) in anthracene (AC) host crystals is a promising candidate, as it fulfills the requirements in principle. The molecular structure is shown in Figure 21. Notable, when cooled to cryogenic temperatures, DBT exhibits a very narrow absorption and emission linewidth, so that individual emitters can be addressed even for high DBT concentrations by scanning the laser frequency. AC crystals can be grown out of a gas phase, i.e., AC crystals will form on cool surfaces like the chip with waveguide structures. Furthermore it can be spin-coated, which leads to relatively thin crystals of roughly 30 nm thickness [81]. A drawback appears for very thin AC crystals, where the line width was found to be broadened even when cooled down, presumably, as the surrounding AC host is not that pure as in thicker samples.

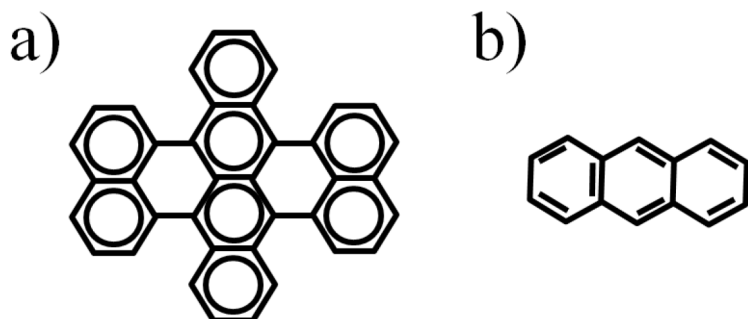


Figure 21: Structure of a) DBT and b) anthracene.

### 3. Experimental Basis

---

Especially the narrow line width features potentially easy combination of waveguide structures with DBT-doped AC that is free of any alignment: An AC crystal could be grown directly on the chip resulting in crystals with various DBT emitters close to the designated nano-structures. By scanning the excitation laser those DBT molecules that are well positioned and oriented would show up as the brightest peaks, others that are badly positioned would be quenched or only weakly excited.

#### 3.1.3 Synthesis of Core-Shell nanoparticles

Core-shell particles were fabricated by Andreas Ott at the HZB, by wet chemistry approaches. Some basic techniques and results are briefly described here for completeness. Core-particles are grown by standard approaches to get on purpose rod-shaped or spherical particles. The particle shape can be controlled by add-on of specific molecules which feature sensitive adhesion properties. These depend on the crystalline facets of the gold particles, thereby inhibiting growth in certain crystallite directions. Such methods can be extended to synthesize micrometer-sized but nanometer-thin gold flakes [82]. All fabricated cores are synthesized from gold as it is free of oxidation and thus its conductivity is conserved.

Subsequently, the gold cores are covered with a dye-hosting shell, which is either a silica-shell fabricated via Stöber method or a layer-by-layer polymer shell. Mostly organic laser-dyes like Rhodamin were used. Other gain-media like colloidal quantum dots would provide less gain-factor due to the limited achievable density caused by the relative large size of quantum dots compared to dyes [83].

Core-shell particles have been pre-characterized during and after synthesis by UV-VIS and fluorescence spectroscopy, yielding fluorescence and extinction spectra like shown exemplarily in Figure 22.

Using this technique, it was verified that the resonance of the metallic cavities was well-aligned with respect to the dye's emission band. Extinction measurements can also gain rough insight into the degree of dye-doping when the pure particle extinction is modified according to the absorption of the dye's absorption band. Precise estimation of the dyes-concentration incorporated into the shell is in general difficult. At the beginning of the chemical synthesis a defined amount of dyes is fed to the synthesis solution. However, it is delicate to separate and thus to measure precisely what is left behind after the synthesis.

### 3. Experimental Basis

A common problem in particle synthesis is agglomeration. Signatures of this effect are fast accumulation at the bottom of the solvent cuvette. Furthermore, transmission electron microscopy (TEM) was used to check for such effects and for the quality of the particles in general.

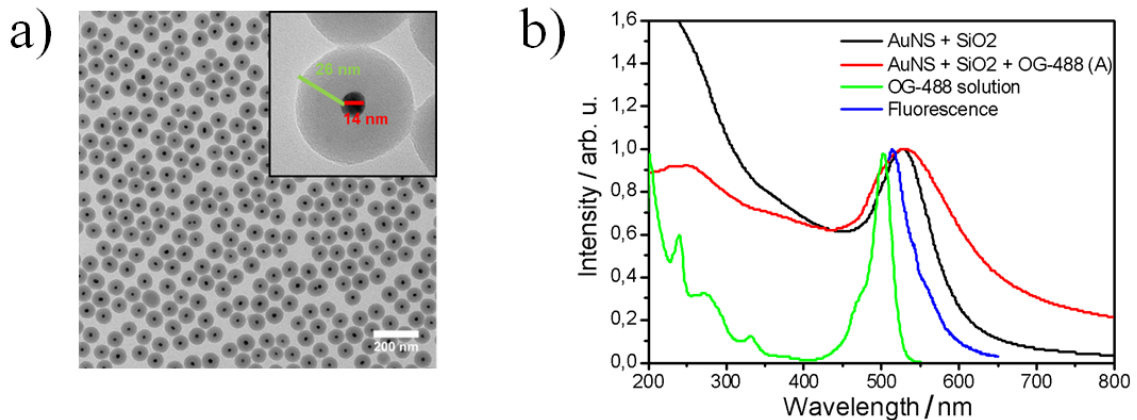


Figure 22: Core-shell particles as synthesized by Andreas Ott. a) TEM image, b) UV-VIS and luminescence spectra showing that the fluorescence maximum of the organic emitters (OG 488, blue line) matches with the resonance of the particles (black and red line).

#### 3.1.4 Graphene exfoliation on Mica

The first successful graphene deposition was done via adhesive tape [45]. Graphene can however also be deposited just by gently pushing a piece of graphite to a substrate. Thereby unwanted molecules stemming from glue of the tape are avoided that might influence the properties of the graphene sheets. The chance to deposit large graphene sheets rises when highly oriented pyrolytic graphite (HOPG) is used. Also the use of ultra-flat and clean substrates is helpful as this yields a high van-der-Waals interaction between graphene and substrate. Samples investigated during this thesis have been exfoliated onto mica. Mica can be split into sub-crystals revealing fresh surfaces that are atomically smooth. Furthermore mica features a birefringence which allows for an optical detection of individual graphene layers with simple microscopic tools [84]. This exfoliation method leads to significantly cleaner and smoother graphene samples than the ones produced by chemical synthesis, however control over sample size and position accuracy is very low.

### 3. Experimental Basis

---

Figure 23 shows graphene and graphite deposited on mica by the aforementioned exfoliation technique. It was found that exfoliated graphene samples on mica exhibit mono-layers of water (or sub-mono-layers with lateral holes in the water film) when fabricated or stored under ambient conditions [85].



Figure 23: Exfoliation of graphene and graphite on mica. Thin layers (few to multi-layer graphene) appear darker than the mica substrate. Thick graphite pieces appear brighter. A relatively large single layer is marked with the black ellipse (long axis of ellipse  $\sim 50 \mu\text{m}$ ).

## 3.2 Sample Investigation: Versatile Setup for Assembly and Analysis

### 3.2.1 Setups

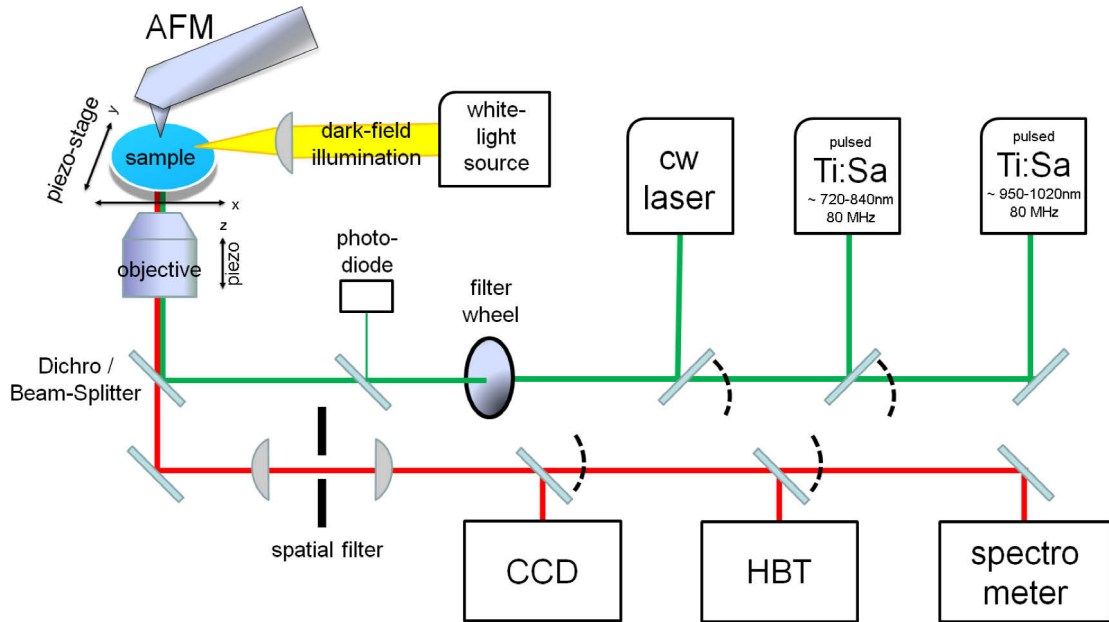


Figure 24: Setup I to assemble and analyze hybrid nanostructures. Basic ingredients are a confocal microscope and an AFM. Various light sources like cw- or pulsed lasers or white light sources are used to excite luminescence or to probe samples by light scattering. Detection of optical signals can be performed via camera (CCD), APDs – potentially in a Hanbury-Brown and Twiss configuration (HBT) - or spectrometer.

During this thesis two setups (Figure 24 and Figure 25) for the investigation of nanooptical systems were established. Apart from a well-defined excitation of fluorescence or photoluminescence via lasers, the detection with low background is mandatory to collect data with good signal-to-noise ratios. This was the main reason to set up a confocal microscope composing the basis of the first setup. The microscope was subsequently combined with a bright white-light source to illuminate nanoparticles in a dark-field excitation scheme. Optical resonances supported by the nanostructures can be identified when the scattered light is spectrally analyzed. Furthermore the microscope was equipped with an atomic force microscope (AFM) to analyze the topography of the nanostructures or manipulate them.

### 3. Experimental Basis

The experimental tools can be aligned with respect to each other so that luminescence, scattering spectra and topography information can be collected for individual particles. The second setup was established at the Max Born Institut (MBI) in cooperation with Dr. Ingo Will, where access to a Nd:YAG laser was given. This setup was basically used to pump nanostructures in order to excite lasing.

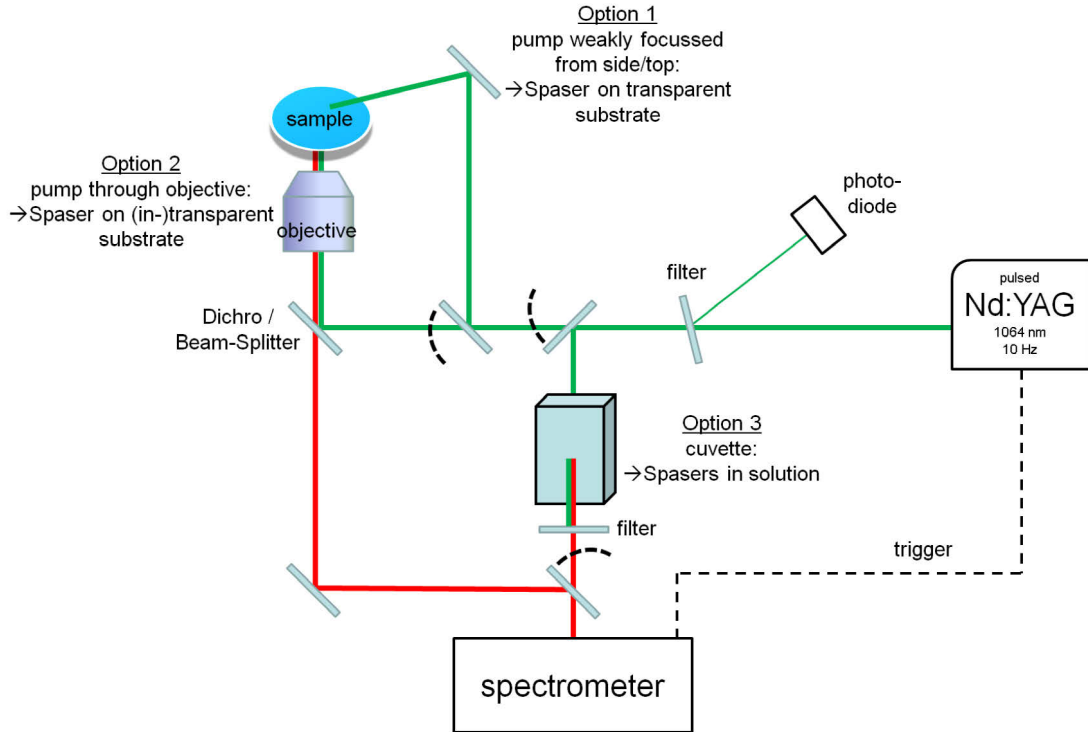


Figure 25: Setup II predominantly to investigate nanolasers. Intense laser pulses ( $\sim 25$  ps) of low repetition rate ( $\sim 10$  Hz) are used to reach maximum inversion and to protect the gain medium from fast bleaching and trapping in dark intermediate states. This setup was established at the MBI in cooperation with Dr. Ingo Will.

#### 3.2.2 Confocal Microscopy

The confocal microscope consists of various beam paths for different lasers that are coupled via a beamsplitter or a dichroic mirror into an upwards (z-axis) mounted objective. The objective focuses the laser light onto a sample that can be mounted on a (x-y) piezo stage. Luminescence excited by the laser is collected through the same objective, passes a beamsplitter or a dichroic mirror and is guided through a spatial filter (two lenses and a pinhole) and filters to block the laser light until it is guided onto avalanche photo diodes (APDs), into a spectrograph or to a camera. The pinhole is

### 3. Experimental Basis

---

attached to a foldaway mount so that a full camera picture can be seen, but also to detect more luminescence for instance stemming from fluids in cuvettes.

When guided to the APDs a map of the sample's luminescence can be recorded when the piezo stage is scanned in x-y and correlated with the signal of the APDs. APDs produce a short electric signal, a “click”, for each detected photon. Thus, binning the outgoing signals yields a voltage proportional to the detected intensity of the luminescence. In contrast to that, also single clicks can be recorded. When they are plotted in a histogram in reference to a trigger signal of a pulsed laser, i.e., in a start-stop measurement, the characteristic exponential decay and thus the lifetime of the luminescence can be analyzed.

The luminescence can also be auto-correlated (correlated to itself), when the light is split by an additional beamsplitter and detected by two APDs. This is done to measure the so-called  $g^{(2)}$ -function (the second order auto-correlation), which yields the “intensity correlation” or “photon-statistics”. This analysis allows to distinguish between classical, coherent and quantum light sources. The latter could be a single quantum emitter, e.g. a quantum dot (see chapter 2.3.4).

#### 3.2.3 Dark-field Microscopy

Nanoobjects can be analyzed by their ability to scatter and absorb light, especially when specific resonances exist, that can be excited by light. In a dark-field microscope this effect is utilized, specifically the scattering of light. A sample is illuminated in general with a broad light source that covers the spectral range in which the resonances of the considered nanoobjects are expected. Illumination and detection are arranged such, that no light is detected whenever the sample is free of any scattering object other than the sample substrate, e.g., a flat glass substrate. This is to achieve a good signal-to-noise ratio, as the scattering signals might be of weak intensity.

The dark field microscope set up during this thesis uses the already mentioned detection (objective, spatial filter with foldaway pinhole, APDs, spectrometer, camera) as used for the confocal microscope setup. The broad light source has been either a halogen or a Xenon-gas white light source. The light source was illuminating samples either under a flat-angle from the side or through a dark-field condenser to which the transparent sample substrate was attached with immersion oil.

### 3. Experimental Basis

---

#### 3.2.4 Atomic Force Microscopy

The confocal microscope was additionally equipped with an atomic force microscope (AFM). As the confocal setup uses an upwards standing objective, the AFM (NT-MDT) can be mounted on top of the sample and luminescence and topography can be recorded at the same time. As the AFM has its own x-y-piezo tube, sample and AFM can be moved independently. This allows alignment of the laser focus to the AFM tip, to take AFM scans of optically pre-characterized nanoobjects. The topography measurements are mostly taken when the AFM runs in a mode in which the tip is oscillating free of concrete contact to the sample. Nanoobjects can be manipulated (moved, picked-up and placed) when the AFM is switched to a contact mode, in which the tip is pushed to the sample until the cantilever reaches a certain value of bending.

#### 3.2.5 Pulsed Lasers

Pulsed lasers have been a key element for experiments with nanolasers (chapter 5). First of all they allow for measuring of emitter lifetimes but more importantly, they are used to generate high intensities and consequently a strong pump of the nanolaser's gain medium.

Two different versions of Titan-Sapphire Lasers (Coherent) have been set up. The mirrors and other optical components inside the lasers differ, so that they generate different colors: the first one produces laser light of around 800 nm wavelength, the second of around 1000 nm. The Tsunamis can be run in both, continuous wave (cw) and pulsed mode. The pulsed mode can be optimized and checked when the laser light is focused inside a frequency doubling element, e.g., a barium borat (BBO) crystal: the brighter the emission of the frequency doubled light, the shorter, more intense and purer (less cw content) the pulsed mode is running. Puls-lengths produced by the Tsunami are in the range of 80 - 150 fs with a repetition rate of roughly 80 MHz and a mean output power of around 800 mW of direct emission and around 100 mW when frequency doubled.

### 3. Experimental Basis

To generate even higher pump rates of the nanolaser's gain medium, a Neodyn YAG laser (in-house construction at MBI) was used. It generates 25 ps long pulses providing up to 1 mJ of power per pulse at 532 nm. The low repetition rate of 1 to 50 Hz promises a slow bleaching of the sample during experiments. Furthermore the gain medium will be fully relaxed and available for the lasing process, in contrast to pumping with high repetition, where the gain medium consisting of organic emitters could be trapped in a dark intermediate state.

## 4 An On-chip Platform for Active Nanooptics based on Single Emitters

---

In this chapter optical on-chip structures are discussed. These nanostructures composed of dielectric and plasmonic waveguides and couplers are designed to perform investigations on the interaction of single emitters with single photons or plasmons. Here the design of the on-chip structures and performance tests of fabricated chips (4.2) are described together with room-temperature studies on individual emitters (4.3). The results presented here have been published partly in Ref. [86] and Ref. [80].

### 4.1 Basic Concept

A proposal from 2007 [51] discusses the possibility to build a single-photon transistor, i.e., a non-linear optical device that is able to switch weak optical signals (few to single photons) with the help of a single emitter (see Figure 26). To this end, a quantum emitter is coupled to a plasmonic waveguide, so that a passing plasmon will interact with the emitter with very high chance (high  $\beta$ -factor see chapter 2.5.3). The plasmon will be either absorbed, reflected or transmitted, sensitively depending on the internal state of the quantum emitter. The proposal is based on estimations of the coupling strength between emitter and guided mode combined with a quantum mechanical description of the emitter. The proposal works without the need of a high-quality cavities. Thus no spectral alignment of the emitter to the cavity has to be accomplished as the working-principle is intrinsically very broadband.

As losses in the plasmon waveguide would heavily limit the throughput of this device, since only few plasmon quanta are guided, the design proposal suggests to use an almost lossless dielectric waveguide that couples to a short plasmon waveguide just for the interaction with the emitter and then back to a dielectric waveguide like depicted in Figure 26.

Section 4.2 will discuss design and performance studies of a possible realization of such a device that is integrated on a chip, section 4.3 presents studies on a potential emitter (quantum system) for which the on-chip structures are optimized and section 4.4 discusses open tasks.

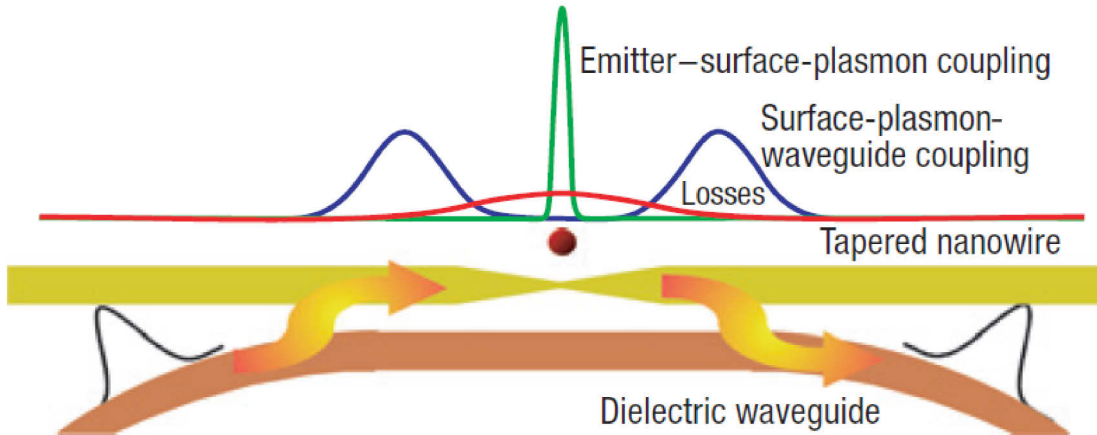


Figure 26: Scheme of the photon-to-plasmon coupler to minimize propagation losses for the single photon transistor (Figure adapted from [51]).

## 4.2 The Chip

The choice of materials for the chip and the on-chip nanostructures complies with the choice of quantum emitter, which is DBT in AC throughout this study (see sections 3.1.2 and 4.3). Obviously the materials have to have as little intrinsic losses as possible at the emission frequency of the emitter (emission wavelength around 785 nm). Furthermore they should not introduce strong Raman scattering or photoluminescence signals when the emitter is excited with a laser. As mentioned in section 3.1 silicon-nitride (SiN) on oxidized silicon wafers (silicon-dioxide ( $\text{SiO}_2$ ) on silicon (Si)) was chosen as a basis, since SiN on  $\text{SiO}_2$  comprises a natural waveguiding layer with almost no losses at 785 nm. The materials are also chosen for reasons of stability at ambient conditions, i.e., gold is preferred over silver for the plasmonic part of the structure, as it is more noble and does not oxidize.

#### 4. On-chip Nanooptics

---

The basic chip concept comprises in- and out-coupling ports to feed optical signals from the far-field to dielectric waveguides on the chip and extract them from the chip. So far, grating couplers have been employed. Dielectric waveguides guide photons to the plasmonic waveguides, where a specifically designed coupler (4.2.1) provides an efficient photon-to-plasmon conversion. A short straight plasmon waveguide connects two of these couplers. The emitter is supposed to be coupled to this short plasmonic waveguide (Figure 27).

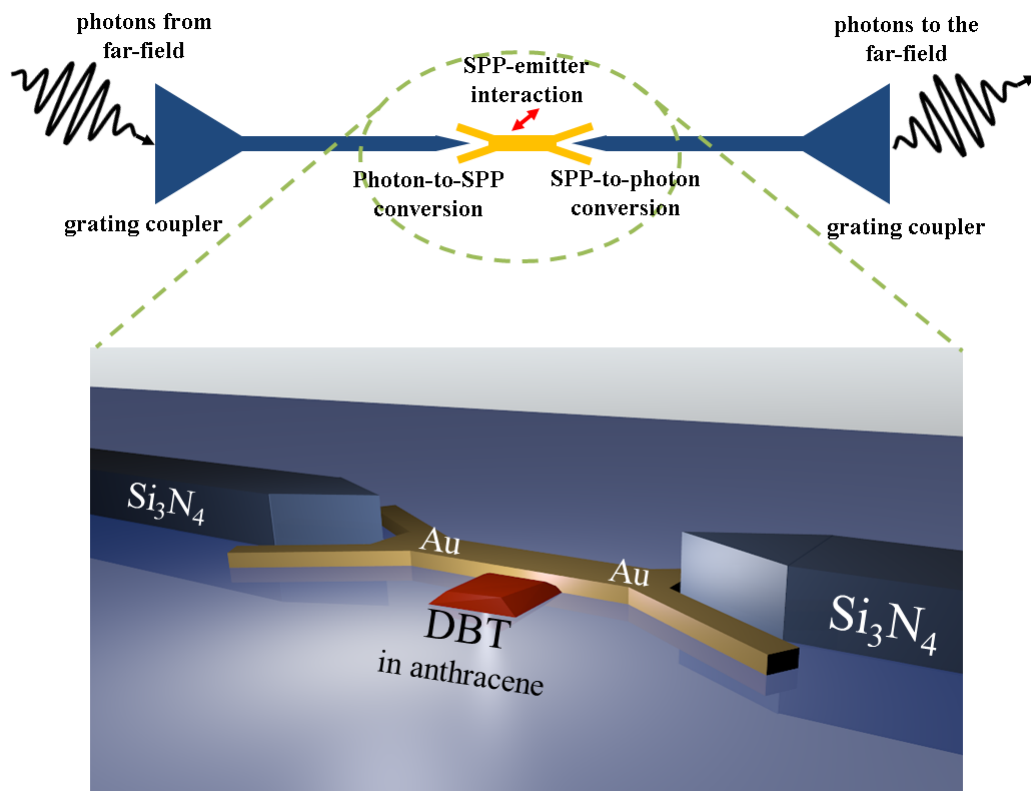


Figure 27: Basic chip design with far-field grating couplers, low-loss dielectric waveguides, photon-to-plasmon converters and emitters.

### 4.2.1 Design and Analysis with FEM

#### *Design Recipe*

The photon-to-plasmon coupler was designed, optimized and analyzed numerically using FEM (see chapter 0), based on a few basic design ideas. These ideas are summarized like this: (i) the dielectric waveguide is tapered at the end, which leads to an increasing evanescent field along the waveguide; (ii) two short metal stripes running parallel to the side-walls of the taper “catch” these fields, finally funneling the energy into a straight plasmon waveguide (Figure 28). These basic ideas for the design are especially compatible with restrictions placed by the fabrication, i.e., actual producibility (straight side walls etc.).

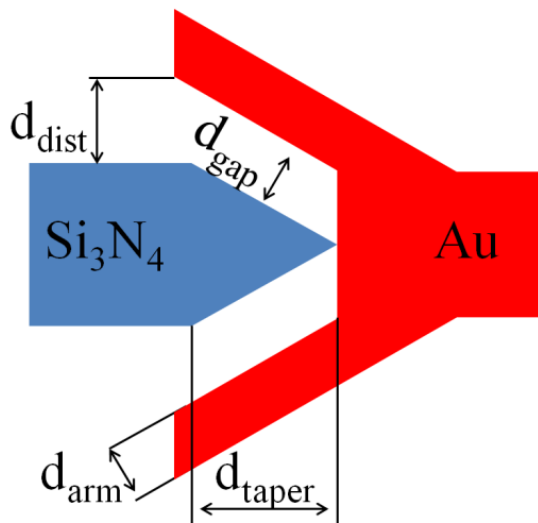


Figure 28: Basic design principle of the photon-to-plasmon coupler with four free parameters that were modified to find the maximum coupling efficiency.

The numerical studies start with the waveguides. In principle a single guided-mode operation is desired to avoid decay of the emitter into more channels than absolutely necessary, i.e., to achieve a high  $\beta$ -factor (2.5.3). This means that the cross-section of the waveguides are reduced so far, that the waveguide support only two modes which is usually the minimum number of guided modes in a waveguide with broken symmetry (deviation from cylindrical waveguide in homogeneous surrounding). Further, for the plasmon waveguides the cross-section has been chosen such, that the propagation loss is relatively weak, i.e., a not too small cross-section.

#### 4. On-chip Nanooptics

---

A further rough design guide for the coupler has been the principle of momentum conversation ( $\hbar k_{\text{ph}} = \hbar k_{\text{pl}}$ ). Concretely, the waveguides are matched to each other with respect to their effective refractive indices  $n_{\text{eff}}$  ( $k_{\text{ph}} = k_{\text{pl}} = k_0 \cdot n_{\text{eff}}$ ), which is a number that is directly derived by FEM calculations. This is however no strong restriction, as the tapering and the coupling of evanescent fields to the plasmonic parts introduces light fields of various momenta. Beyond the basic properties of the guided modes, the actual field-plots of the guided modes, i.e., their polarization, is another “parameter”. This is probably the most important aspect of pre-adjustment of the waveguides: Coupling of modes in the dielectric and metallic waveguide will be more efficient if their polarizations fit to each other. Indeed, the study presented in Ref. [86] revealed, that only one mode of the dielectric waveguide can couple efficiently to the plasmon waveguide. Moreover, only one mode in the plasmon waveguide was predominantly excited (Figure 29).

Based on this recipe an optimization procedure was performed to find parameters that maximize the coupling efficiency. To reduce the parameter-space and consequently the effort of the numerical calculations during the optimization, the waveguide cross-sections were fixed. During the subsequent calculations four parameters were left free to change (Figure 28): the width of the arms  $d_{\text{arm}}$ , the taper length  $d_{\text{taper}}$ , the gap width  $d_{\text{gap}}$  between arms and taper, as well as the arm length (which was indirectly controlled by the distance of the arms at their ends to the dielectric waveguide  $d_{\text{dist}}$ ).

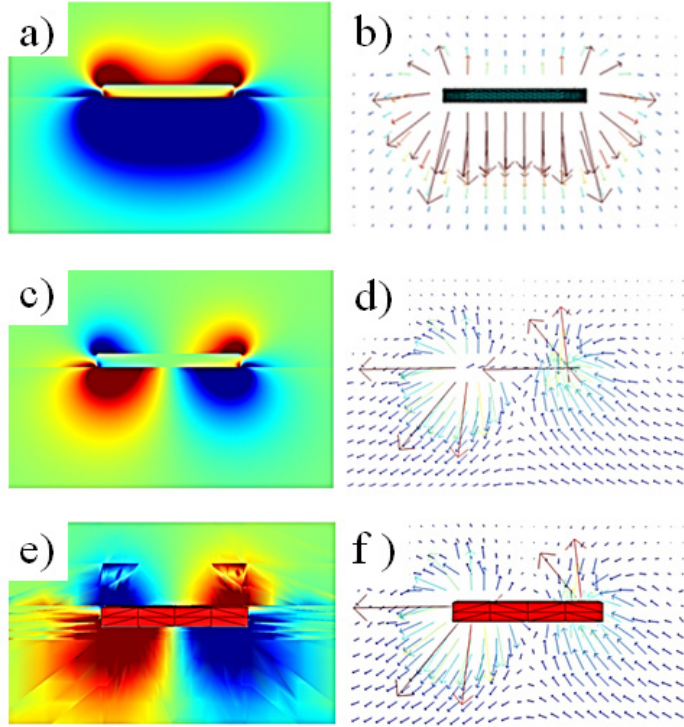


Figure 29: Guided modes of the plasmonic waveguide. a), c) and e) Electric field strength of the vertical field component. b), d) and f) Corresponding field vectors, that reveal the polarization. a), b) Lowest order guided mode with the highest effective refractive index. c), d) Second mode of the plasmonic waveguide. Modes are calculated with the propagating mode solver. e), f) Guided field intensity after the coupler in a 3D calculation, demonstrating that predominantly the second guided mode is excited.

Still, with four free parameters, the possible parameter-space is relatively large. Thus, the so-called Taguchi method was chosen to find an optimum for the coupling efficiency [87]. This method works with specific predefined arrays that dictate which parameter configurations to use for a small set of (virtual) test-experiments. In order to optimize the coupler with this method, a quantifiable number is needed: here it is the coupling efficiency. Based on the results of the test-experiments a set of parameters that could lead to a maximum performance is predicted. A final experiment to prove this prediction completes the optimization run. The design recipe is summarized and sketched in Figure 30.

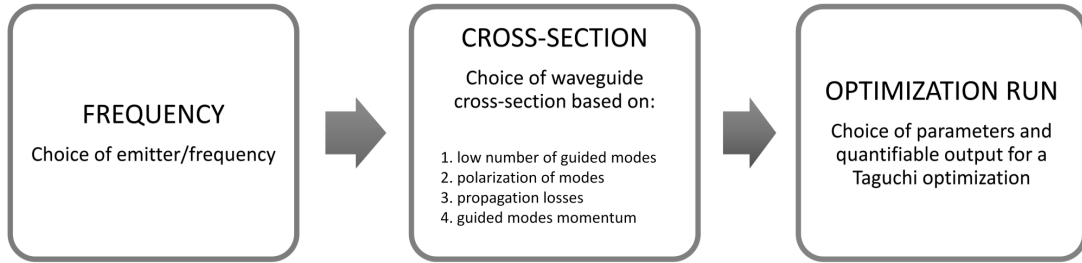


Figure 30: Schematic design recipe for the on chip-structures and optimization.

#### *Numerical Evaluation of the Coupling Efficiency*

A reliable quantitative evaluation of the coupling efficiency is the key to a useful optimization. The guided modes in both the dielectric and the plasmonic waveguide were investigated with a guided mode solver together with full 3D scattering calculations in which one of the dielectric waveguide modes was used as a source. Based on the knowledge about the guided modes, a straightforward framework to study the coupling structures would be the coupled mode theory (CMT) [88]. As a matter of fact, this was also the first approach during this work. However, this approach turns out to be not accurate enough. The basic concept is, that the light field behind the coupler can be decomposed into three contributions: the two possible guided modes in the plasmon waveguide and residual stray fields. By computing a mode-overlap integral of the light field behind the coupler and the guided mode solutions one would then be able to derive the coupling efficiency to the two guided modes right away. However, very high coupling efficiencies were found using this approach. In some cases the sum of the power guided by the two modes was exceeding the inserted power. Obviously, CMT leads to an overestimation of the coupling efficiency.

The origin of the overestimation is a prerequisite of the CMT, i.e., the modes have to fulfill a power-orthogonality relation which is not the case for a lossy waveguide [88,89]. In other words, this means that the overlap-integral of the two different guided plasmon modes amongst each other does not vanish.

As a consequence, no CMT analysis but a self-derived method based on the characteristic damping of propagating modes was performed to evaluate the coupling efficiency [86].

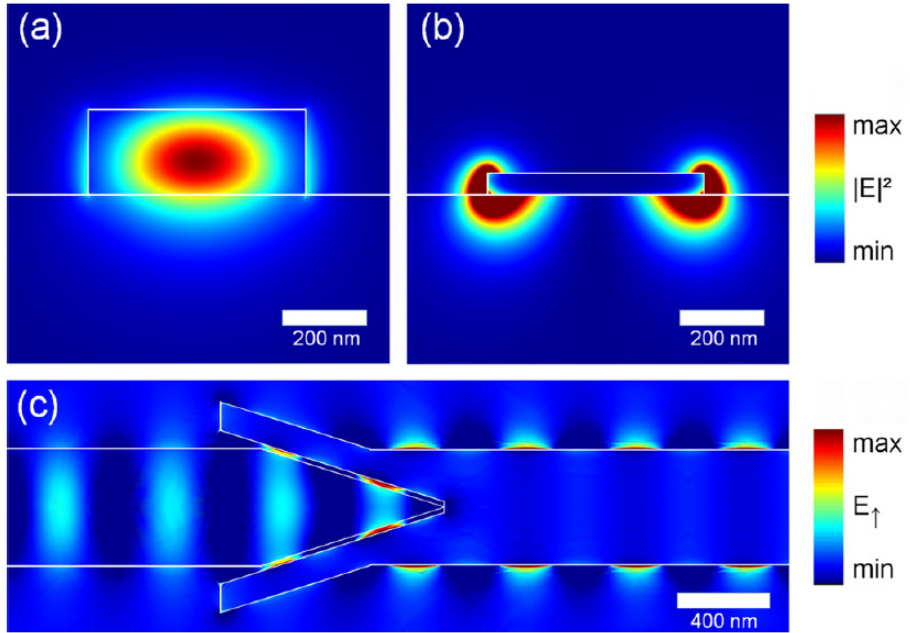


Figure 31: Guided modes (intensity) and 3D FEM calculation (electric field). a) Guided mode of the dielectric waveguide, that acts as a light source in the 3D numerical scattering experiment. b) Plasmonic mode, that is excited after the photon-to-plasmon coupler (Figure as also presented in [86]), c) Numerical simulation of the whole structure in 3D (top view showing the electric field strength) where the guided mode (a) is used as a source.

Again the guided mode of the dielectric waveguide was used as a source field in a full 3D calculation of the photon-to-plasmon coupler (Figure 31). The electromagnetic energy flux along the plasmon waveguide was extracted and recorded through various cuts (planes) perpendicular to the waveguide as a quantitative measure. Further the field-pattern and polarizations of the guided field in the plasmon waveguide was compared qualitatively to the ones calculated with the guided mode solver. Both, the quantitative and the qualitative results support the conclusion that the coupler leads only to the excitation of one of the two possible plasmon modes (Figure 29). This is further supported by the characteristic decay of the flux along the plasmon waveguide. This decay fits to the one predicted from the guided mode calculation. The guided mode solver yields a complex effective refractive index and thus a damping of the mode along the waveguide. To derive the coupling efficiency, the decaying flux along the waveguide is normalized to the input flux and fitted with an exponential decay. The amplitude of that fit at the position where the straight plasmon waveguide begins, yields the coupling efficiency. More flux, especially found directly after the coupler, can only stem from stray-fields.

The fit to the decaying fluxes is not influenced by these stray-fields as the fit is only based on data points that are a few microns away from the coupling structure (Figure 32). The only free parameter of the fit is its amplitude as the decay constant is taken from the propagating mode solver.

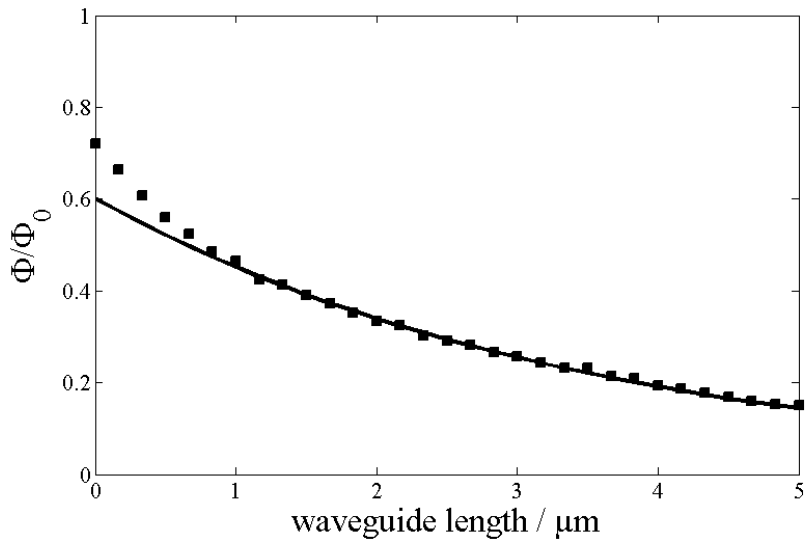


Figure 32: Calculated flux  $\Phi$  in waveguide direction through equidistant planes. Zero waveguide length corresponds to the onset of the straight plasmon waveguide. The series of fluxes follows an exponential damping with a decay constant as predicted by the propagating mode solver. A fit to this data (ignoring the first data points) using a normalization to the flux entering the computational domain  $\Phi_0$  yields the coupling efficiency (amplitude at zero waveguide length).

#### *Reaching High $\beta$ -factors: Stripe and Slot Waveguides*

Chronologically, after the numerical optimization of the coupler, fabrication and experimental performance tests have been carried out. It was only in following studies when the actual coupling of emitters to the plasmonic waveguide got into the focus of interest.

To achieve a high  $\beta$ -factor and Purcell-factor it is quite intuitive to taper the plasmon-waveguide towards smaller cross-section as it was already proposed by Chang et al. [51] for cylindrical plasmon waveguides. As a metallic waveguide of smaller cross-section also introduces higher propagation losses, a relatively wide waveguide was used

for the optimization of the coupler to gain useful test on-chip structures with only moderate damping.

The mode that was efficiently excited via the coupler finally turns out to experience a cut-off when reducing the waveguide width, while the second mode reveals to be evolving into what is the fundamental mode. This is in contrast to what is said in Ref. [90], where the first four modes are named fundamental modes. In any case, here we will refer to the fundamental mode as the one that does not suffer from a cut-off at all. Nevertheless, the effect that only a single mode “survives” the tapering is intuitively clear: Any mode without a cut-off, even that of an asymmetric waveguide like here, will gain more and more localization and momentum during the tapering. Thus, the overlap with the outer decreases. This mode will be less affected by spatial jumps in the outer media (sub- to superstrate) and the actual shape of the waveguide, finally yielding a mode that looks almost like that of a small cylinder in a homogeneous medium (Figure 33, compare with Figure 29). In other words such a mode evolves towards a mode that can be described within the quasi static regime, well-known for its statements that are insensitivity to shape [65].

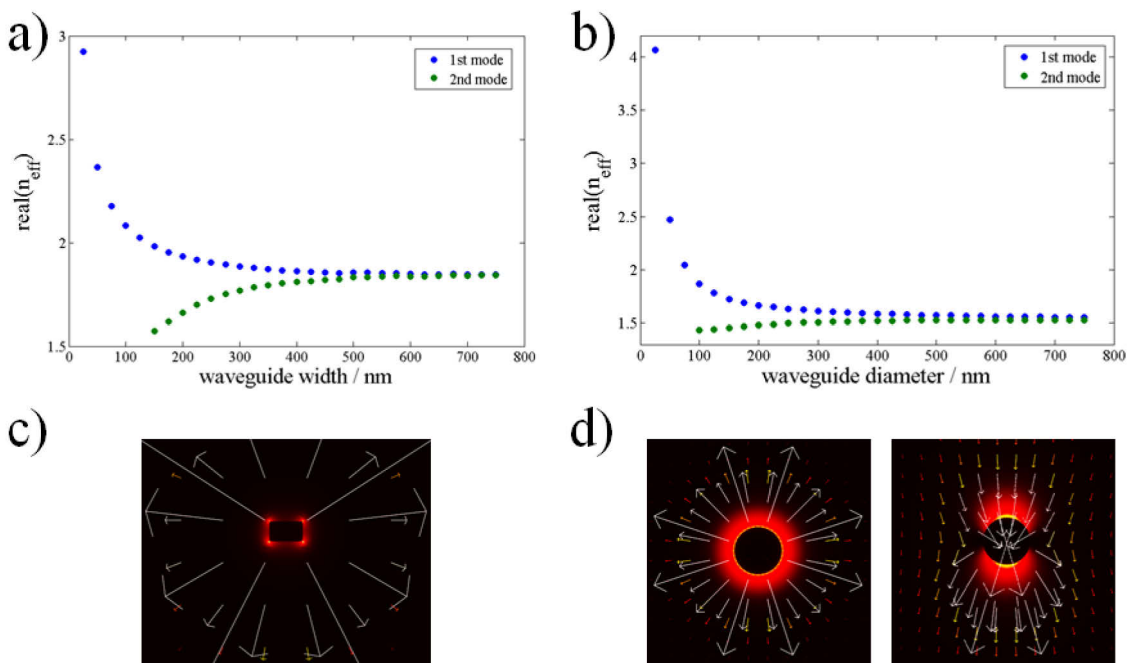


Figure 33: Guided modes of a cylindrical and a stripe waveguide. a), b) Effective refractive indexes (real parts). c), d) Intensity profiles and polarization. Numerical result are obtained for  $\lambda_0=780\text{nm}$  and gold in an  $n=1.4$  surrounding. The smaller the cross-section of plasmonic waveguides, the more the guided mode resembles the properties of the fundamental mode of a cylinder.

At first glance, this problem fundamentally questions the so-far developed method of coupling. A high  $\beta$ -factor of a simple stripe waveguide is not accessible with this photon-to-plasmon coupler. It even remains unclear how to excite the fundamental mode within a compact and simple coupler device and high efficiency at all: The fundamental mode happens to have an almost starlike or breathing-mode-like polarization as shown in Figure 29 and Figure 33 while a dielectric waveguide guides almost pure TM or TE modes.

Nevertheless, there is a practical solution for this issue that works without changing much of the coupler design: utilization of a slot-stripe waveguide (Figure 34). Specifically the mode with the maximum intensity inside the slot shows a useful polarization symmetry similar to that of the formally used simple stripe waveguide.

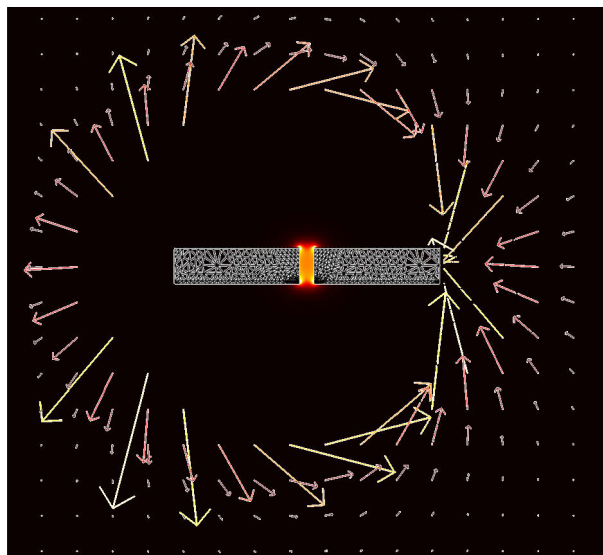


Figure 34: Field intensity and polarization of a plasmonic slot-stripe waveguide mode with high energy density guided in the slot. The polarization's symmetry fits in principle to the exciting mode in the dielectric waveguide.

Apart from the option to use a stripe waveguide as before with a slot, also a simple slot in a full metal-film could be used. A full film would be simpler to fabricate as the metal arms would become dispensable. These arms have been basically used to excite modes with hotspots at the outer edges of the waveguide. Further, the minimal number of modes would be smaller compared to the number in a slot-stripe waveguide. However, it was found in this thesis that a multitude of lossy film-modes are excited in the taper-region, an effect that significantly reduces the overall transmission through the coupler and plasmon waveguide. This is not the case for the slotted-stripe waveguide, where a high transmission and coupling efficiency is found, although a mode-beating effect

appears (Figure 35). The mode-beating between the guided modes leads to an oscillation of high power-density from the outer waveguide edges to the slot and back during propagation. As a consequence, an emitter placed inside the gap that is supposed to be efficiently excited has to be placed at the right distance from the taper-tip.

Now, that a mode with high field confinement and good coupling efficiency ( $>50\%$ ) to the dielectric waveguide is found, it is reasonable to compute the actual  $\beta$ -factors for this mode. First the Purcell factor  $\Gamma$  ( $\Gamma = \gamma_M/\gamma_0$ ) is computed (Figure 36) for all potential positions of a dipole around the waveguide and for each of the three linearly independent dipole orientations (here x,y and z). More important than  $\Gamma$  is however the  $\beta$ -factor, i.e., the ratio of power emitted into the guided mode to the total emission (chapter 2.5.3). To this end the normalized total decay rate has to be calculated (normalized to the decay in vacuum) which is possible when a dipolar point source is used within FEM. The total emitted power of the dipolar point source can be directly derived with a post-process, which basically sums up over the absorbed power in all absorbing media and the radiated power that leaves the computational domain. Relatively “expansive” full 3D calculations have to be performed in principle for each

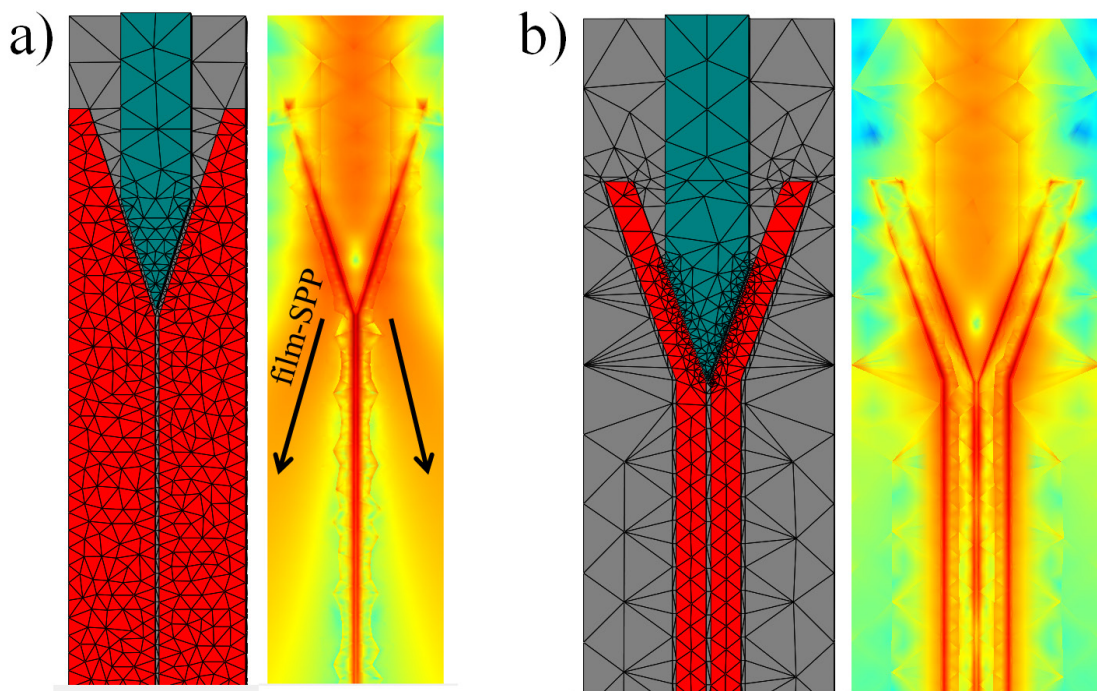


Figure 35: 3D meshes and corresponding numeric simulations (showing logarithm of electrical field intensity). a) Dielectric waveguide couples to a plasmonic slot waveguide in a gold film. b) Dielectric waveguide couples to a slot-stripe waveguide. A slot waveguide in a film might be easier to fabricate but plenty of unwanted modes exist in the gold film resulting in poor coupling efficiency to the designated slot mode.

emitter position and orientation.

Here however, obviously the best Purcell factor is expected for a dipole oriented along the x-axis (Figure 36) and positioned inside the slot. Additionally, the best  $\beta$ -factor will be found in the center of the slot, as any further approach towards the metal will lead to more quenching but only marginally improve the Purcell factor. Thus, the total decay is only calculated for a dipole oriented along x and for various steps along a line through the center of the slot. The result is shown in Figure 37 together with the corresponding  $\beta$ -factor ( $\beta = \gamma_0 \cdot \Gamma / \gamma_{\text{tot}}$ ).

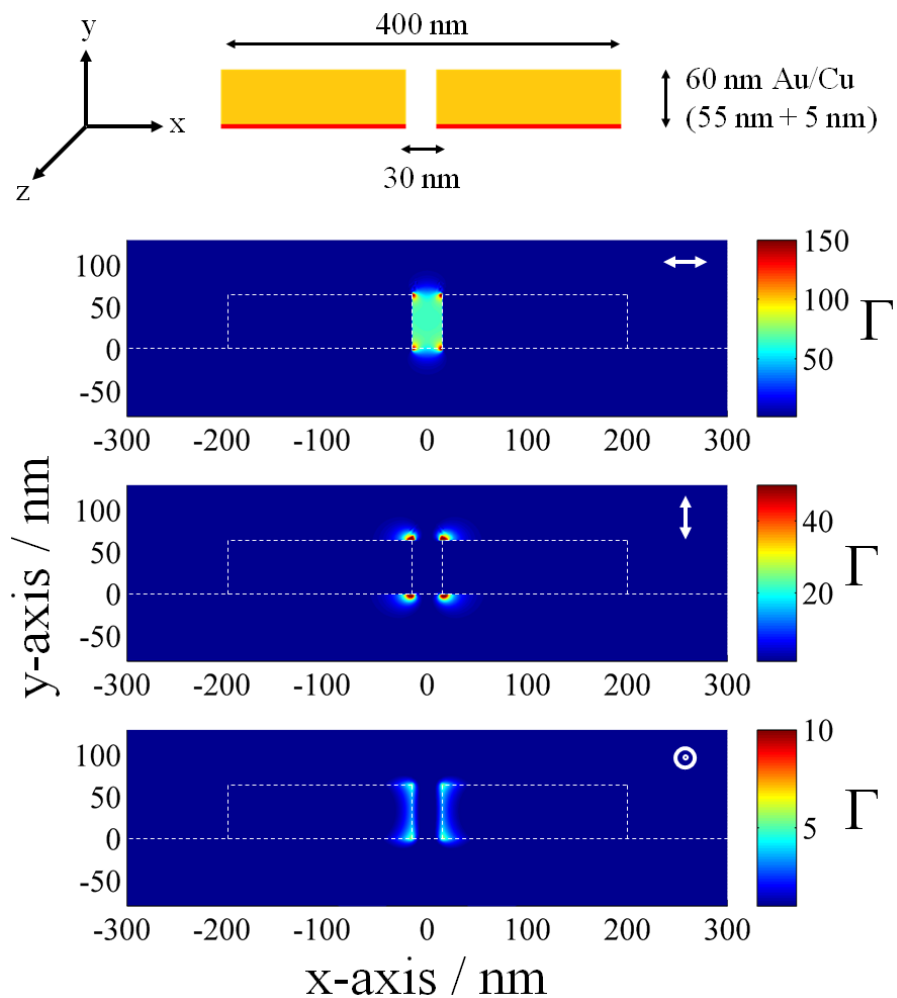


Figure 36: Purcell factors  $\Gamma$  with respect to the guided slot waveguide with a cross section as shown in the upper panel.  $\Gamma$  is shown for three linearly independent dipole orientations (indicated by the white arrows).  $\Gamma$  was calculated according to Barthes et al. [79] (see chapter 2.5.3).

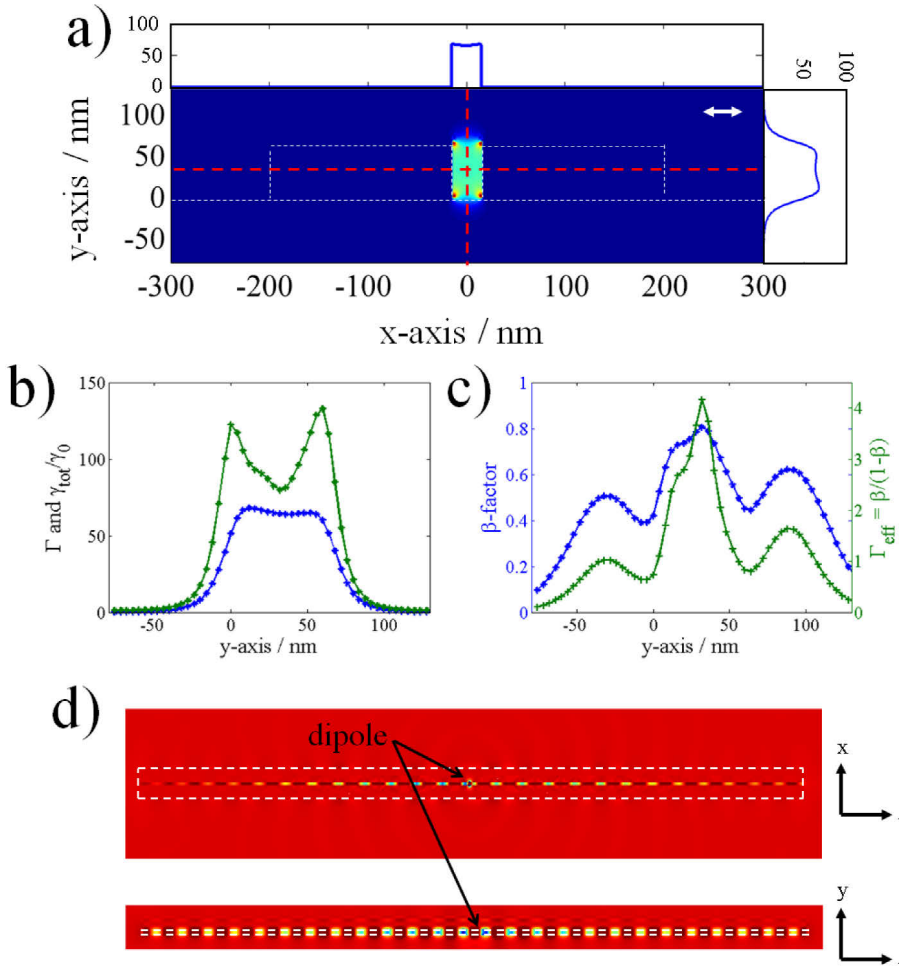


Figure 37: Coupling of an *ideal* emitter to a slot-stripe waveguide mode. a) Purcell-factor  $\Gamma = \gamma_M/\gamma_0$  for an emitter oriented along the x-direction with line scans along the red dashed lines. b) Purcell-factor  $\Gamma$  (blue) and normalized total decay rate  $\gamma_{\text{tot}}/\gamma_0$  (green) scanned along the y-axis through the middle of the waveguide's slot. c) Corresponding  $\beta$ -factor (blue) and *effective* Purcell-factor  $\Gamma_{\text{eff}}$  (green). d) Top- and side-view on the 3D configuration that was used for the computation of the total decay rate: a 10  $\mu\text{m}$  long slot-stripe waveguide with a dipole emitter in the slot. The corresponding electric fields (top- and side-view; E-field component along dipole axis) show that most of the power is emitted into the guided mode.

For a convenient comparison with Chang et al. [51] also the “effective Purcell factor”  $\Gamma_{\text{eff}}$  is shown, which was defined by the authors as  $\Gamma_{\text{eff}} = \gamma_M/(\gamma_{\text{tot}} - \gamma_M) = \beta/(1 - \beta)$ , a number that can diverge for high  $\beta$ -factors. The 3D structure chosen to compute the total decay has been a 10  $\mu\text{m}$  long slot-stripe waveguide with the emitter in the center. This is a trade-off between accuracy and computational effort: a potential Fabry-Pérot cavity effect of the 10  $\mu\text{m}$  long waveguide will only weakly influence the total decay. The decay constant (damping to 1/e) corresponds to a propagation length of the slot-plasmon

of  $L \sim 6.2 \mu\text{m}$ , so that a plasmon is mostly damped when it comes back to its origin. The actual waveguide structure with two couplers would have been even better for this computation, but again this would lead to more computational effort. It is more important to be able to check for convergence, thus a simplified structure as shown in Figure 37 was used.

### *Nonlinear Response*

As mentioned in the theory chapter (section 2.3.4) the expected nonlinear response – also related to strong coupling - can be calculated directly from the Purcell-factor and the total decay rates. Especially, Chang et al. [51] calculated the reflection coefficient  $r$  (or the reflectance  $R = |r|^2$ ) caused by a single emitter (two level system) depending on the detuning  $\delta$  between the incoming plasmons and the transition line of the emitter:

$$r(\delta) = -\frac{1}{1 + 1/\Gamma_{\text{eff}} - 2i\delta/\gamma_M}. \quad (4.1)$$

The transmission coefficient is then given by  $t(\delta) = 1 + r(\delta)$  and the transmittance by  $T = |t|^2$ . Losses  $\kappa$  can be computed with  $\kappa = 1 - R - T$ . Figure 38 shows the reflectance, transmittance and losses as a function of detuning. The reflectance must not be calculated from the decay rates and Purcell-factors as shown in Figure 37. These correspond to the ideal situation of an emitter that emits all the power into its zero phonon line. For DBT in AC the branching ratio  $\eta$  of this emission to the phonon-assisted emission will be around 0.5 according to Hwang and Hinds [52]. This reduces the decay rate into the guided mode by this factor ( $\gamma_M = \eta \cdot \Gamma \cdot \gamma_0$ ) but not the total decay rate. Consequently the  $\beta$ -factors are also reduced yielding an corrected effective Purcell-factor of  $\Gamma_{\text{eff}} = \eta\beta/(1 - \eta\beta)$ .

The relevant parameters to compute the reflectance are  $\beta = 0.8$  and  $\Gamma = 64$  (found by the numerical simulations for the optimum position of the emitter),  $\eta = 0.5$  and a vacuum decay rate of  $\gamma_0 = 1/(\tau \cdot n_{AC}) = 1.45 \cdot 10^8 \text{ s}^{-1}$  [81] where  $\tau$  is the lifetime of DBT molecules measured in AC with a refractive index of  $n_{AC} = 1.434$ . Figure 38 shows the reflectance, transmittance and losses for these values.

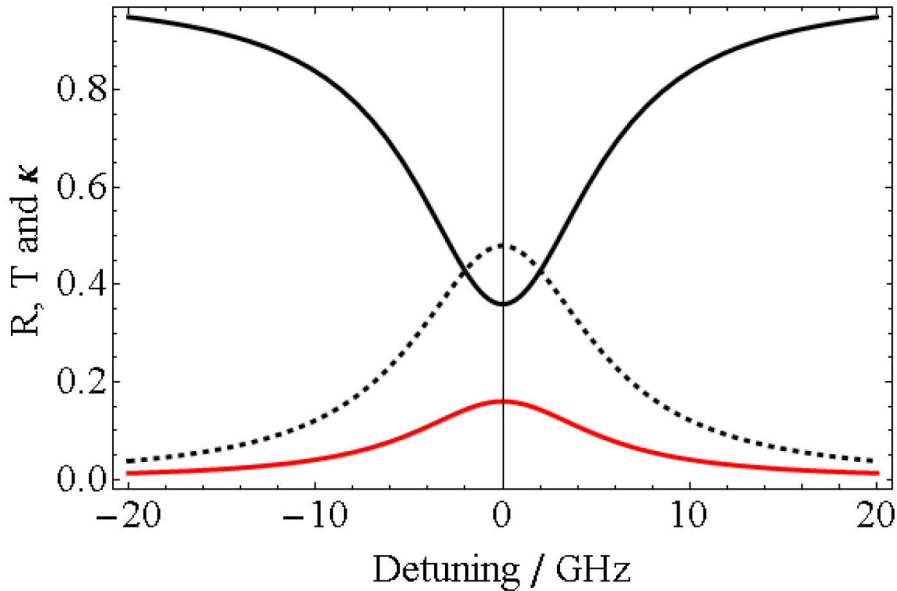


Figure 38: Estimated reflectance  $R$  (solid red), transmittance  $T$  (solid black) and losses  $\kappa$  (dashed) of a single DBT molecule optimally positioned and oriented in the slot-stripe waveguide as a function of detuning between single guided plasmons and the transition frequency of the molecule. Two or more incident plasmons would saturate the emitter yielding a significantly enhanced transmission.

#### 4.2.2 Performance Tests of Fabricated Structures

Coupler structures have been fabricated according to the simulations shown in Figure 31 (plasmonic stripe waveguide) at the Helmholtz Zentrum in Berlin Adlershof by Max Schoengen and Jürgen Probst. The alignment of metallic and dielectric components with respect to each other has been accomplished by a relatively complicated method, which is described in chapter 3.1 and in greater detail in Ref. [80]. The structures have been directly equipped with dielectric far-field grating-couplers. The couplers have been experimentally optimized by producing a chip with various grating coupler-pairs connected with a simple dielectric waveguide. Without quantification of the actual efficiency the best grating coupler was then used throughout subsequent chip-designs. The basic design has been taken from a PhD thesis [91]. It consists of two gratings in a funnel like design as shown in the scanning electron microscope (SEM) image in Figure 39: the first grating is for the far-field coupling itself, while the second, finer grating is supposed to act as a Bragg-mirror to reflect light towards the waveguide and thereby enhance the overall coupling efficiency.

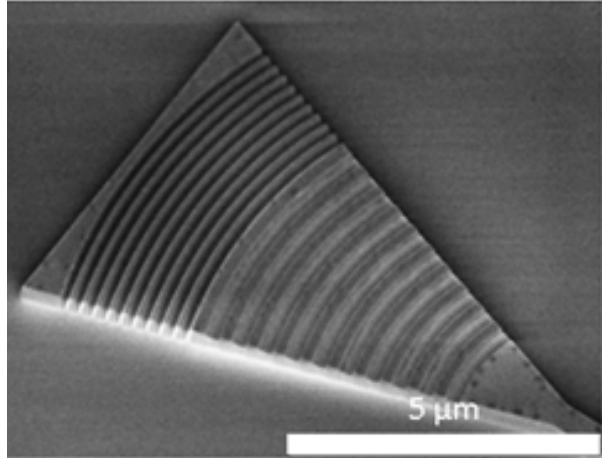


Figure 39: SEM image of the grating coupler with two different grating periodicities. The finer grating is supposed to act as a Bragg-mirror to reflect in-coupled photons into the direction of the attached dielectric waveguide.

Recently also the in-house optimization of such couplers started, as it was found, that such couplers are very sensitive to the waveguide thickness and should thus not simply be adapted from sources that used a different waveguide thickness.

Even though the photon-to-plasmon coupler was designed to obtain a scheme that would be much easier to fabricate than several others presented in literature [86], the yield of the first processing attempts had been low as still the fabrication process is relatively complicated. Thus, one of the best samples that was actually tested was an experimental design, which had not been simulated before: the metallic waveguide is lifted by a residual SiN base of the same shape as the plasmon waveguide to bring the plasmon waveguide vertically to the center of the higher dielectric waveguide. That is where the guided intensity is maximal. During the coupler-design, it was believed, that this degree of freedom would not be available during fabrication. Although this lifted plasmon-waveguide design seems to lead to an advanced coupling efficiency at first glancy, the opposite is actually correct, as was found in subsequent simulations including the changes. This is, because several physical processes are coupled and thus various aspects change at the same time when lifting the metallic waveguide. Most importantly the effective refractive index of the guided mode changes. Nevertheless, still the coupling efficiency was found to be reasonably good. So, this design was tested experimentally and compared to an adapted simulation. A very good agreement was found that allows for the conclusion, that the simulation technique is a reliable tool to quantitatively predict the actual performance of the chip. The measurement of the

coupling efficiencies, both for the photon-to-plasmon coupler as well as for the grating coupler will be described below.

### *Photon-to-Plasmon Coupler*

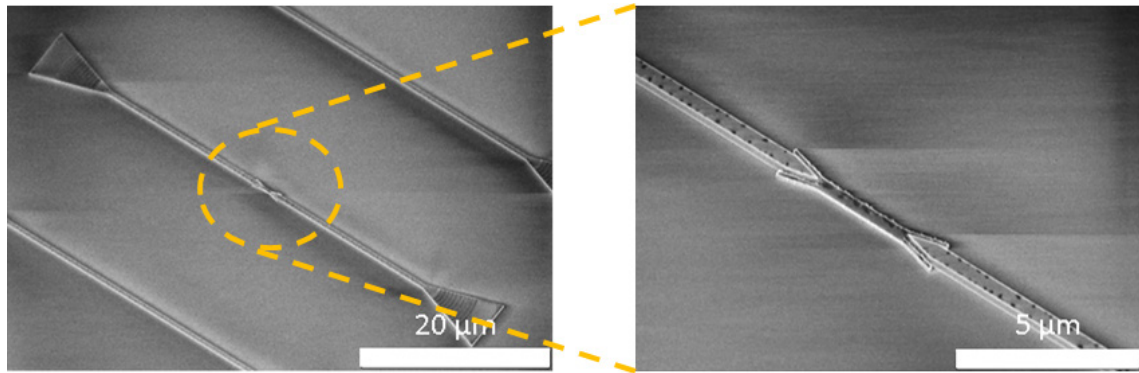


Figure 40: SEM images of a symmetric waveguide structure consisting of grating couplers, dielectric waveguides, photon-to-plasmon couplers and a plasmon waveguide in the center.

In the following a combination of two grating couplers that are connected with a dielectric waveguide - potentially with a photon-to-plasmon coupler pair and a plasmon waveguide in the middle - is simply denoted as a “waveguide structure” (see Figure 40).

Pairs of such waveguide structures were fabricated right next to each other: always one structure with and one without the plasmonic part. The second waveguide structure acts as a reference to check for quality-variations on the chip as well as to normalize the following efficiency measurements.

The grating couplers were illuminated with a large laser-spot, to make sure, that variations in positioning of the laser spot from one waveguide structure to another only weakly influence the result of the measurement. Excitation on the first grating coupler and re-emission from the other was recorded with a CCD camera, i.e., a series of images was recorded.

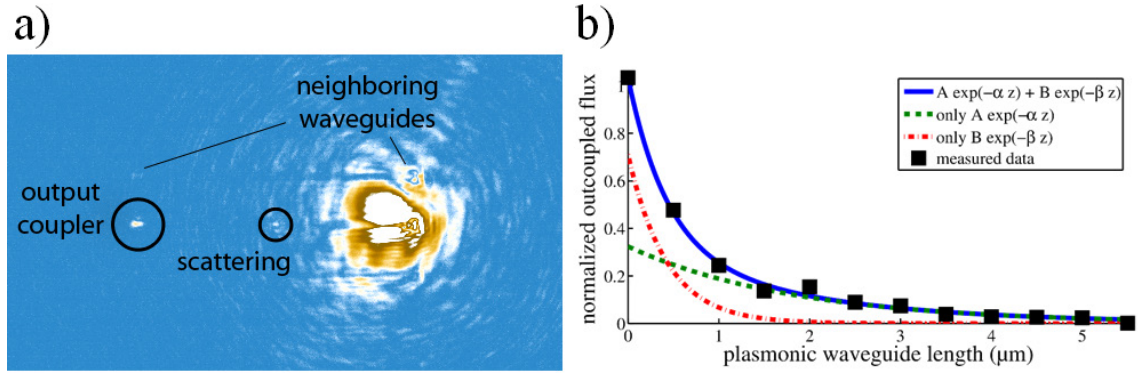


Figure 41: Evaluation of the coupling efficiency of the photon-to-plasmon coupler. a) CCD image of a single test-measurement. A widened laser spot is used to illuminate one of the grating couplers (right bright spot). This is done to provide a comparable excitation of all grating couplers on the chip. The relative position of chip to laser is optimized for maximum out-coupling on the second grating coupler. Also weak scattering is observed from the photon-to-plasmon coupler. b) Out-coupled intensities normalized by reference waveguide structures with exponential fits. Figures as presented in Ref. [80].

In a series of waveguide structures the length of the plasmonic waveguide was changed. Thereby, the intrinsic plasmon-damping is varied and recorded, which represents a measurement that is analogous to the numerical estimation of the coupling efficiency (section 4.2.1). As for the numerical simulations it is expected that stray light is present just after the coupler which may lead to an overestimated coupling efficiency for short plasmon waveguide length. Thus, a double exponential decay is fitted to the distance (or waveguide length) dependent damping (normalized by the transmission through the reference waveguide structures). The first decay with the higher damping constant corresponds to coupling via stray-light fields. The slower decay corresponds to the actual coupling to the plasmon waveguide. Again, the amplitude at the start of the plasmon waveguide gives the coupling efficiency. Note, that each waveguide structure is symmetrically constructed and thus the coupling efficiencies of two subsequent photon-to-plasmon couplers are effectively multiplied. To reveal the actual coupling efficiency of a single coupler, the root of the fit's amplitude has to be taken (Figure 32 section 4.2.1 and Figure 41). A coupling efficiency of  $57 \pm 21\%$  was found.

*Grating Coupler*

To measure the efficiency of the grating couplers, a largely widened spot for excitation like before cannot be used because this approach would contradict the experimental situation in the designated experiments. The experiments are planned to be done with only weak signals, potentially coming from another single photon source. A large laser spot would lead to significant signal loss. Thus, we use a focused laser spot coming from an objective with a numerical aperture (NA) of  $NA=0.4$ , that illuminates less than the total grating coupler. A relatively small NA is a realistic value for the planned experiments with actual DBT molecules as emitters. This is because DBT will be cooled in a cryostat in which either a lens or fiber facets - both with relatively low NAs - will be used to couple light to the grating couplers.

For the measurement of the photon-to-plasmon coupler, reference waveguide structures were used to estimate the coupling efficiencies leading to a series of relative measurements. In contrast, for the grating couplers absolute values need to be known in principle. To this end, the reflection of the laser spot from a flat silver mirror (assumed to be almost 100% reflective) was used to determine the absolute incoming power (measured in counts on a CCD camera). During the measurements on the chip, the reflection of the laser on a flat chip area was repeatedly performed to track the laser's power stability. The actual in- and out-coupling to and from the waveguide structures

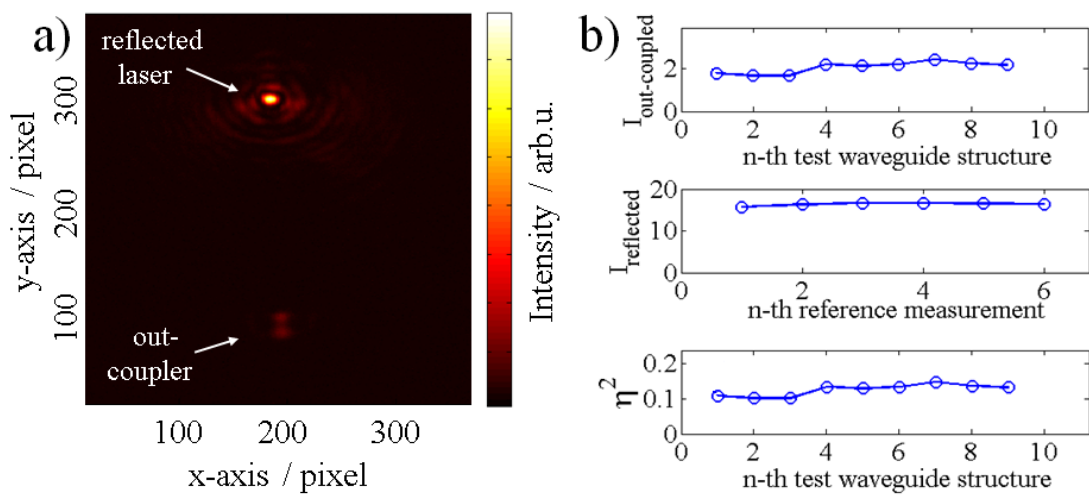


Figure 42: Performance analysis of grating couplers. a) CCD image of a test measurement showing reflected laser at the first grating and out-coupled intensity from the second grating. b) Reflected and out-coupled intensities of nine test-measurements on different waveguide-structures (without plasmonic elements) as well as overall-efficiencies  $\eta^2$  (mean of  $\eta^2=12.4\pm1.7\%$ ) yielding  $\eta=35.2\pm2\%$  (efficiency of a single grating coupler  $\eta$ ).

was adjusted with micrometer screws and an x-y piezo stage until the out-coupling was optimized. Just as for the photon-to-plasmon coupler we have two subsequent grating couplers – their efficiencies multiply – so that the root of the result gives the coupling efficiency of a single grating coupler. The procedure was performed for a series of waveguide structures (Figure 42) and an efficiency of  $35 \pm 2\%$  was found.

## 4.3 Nanomanipulation and Photoluminescence Studies on DBT

### 4.3.1 Cutting and Nanomanipulation

First experiments with AC crystals of low DBT concentration were performed at room-temperature under the leading supervision of Dr. Rolf-Simon Schönfeld. It was found that even at room temperature many of DBT molecules are long-term stable. Furthermore it turns out that AC crystals are very soft crystals, so that they are suited for nanomanipulation attempts for the assembling of hybrid nanoarchitectures: AC crystals can be cut or carved with an AFM tip, when the AFM is used in contact mode. Thus, DBT molecules could potentially be pre-characterized optically and afterwards cut out and pushed to a designated nanostructure. Similar nanomanipulation procedures have been established in the research group for nanodiamonds hosting nitrogen-vacancy centers [80]. However, it was revealed that a successful pick-and-place procedure [92] with tiny AC crystals would have a very low yield, as the AC crystals are relatively adhesive and placing of picked-up crystals is very difficult. Nevertheless, the crystals can be moved on a flat surface in a controlled way. As an example, a fluorescing spot, that showed antibunching in an autocorrelation measurement ( $g^{(2)}$ -function) with moderate dip depths (the deeper the dip, the lower the number of emitters), was cut into pieces via AFM resulting in two fluorescent spots, where one was identified to host presumably only a single emitter, as the normalized  $g^{(2)}$ -function went below 0.5 as shown in Figure 43.

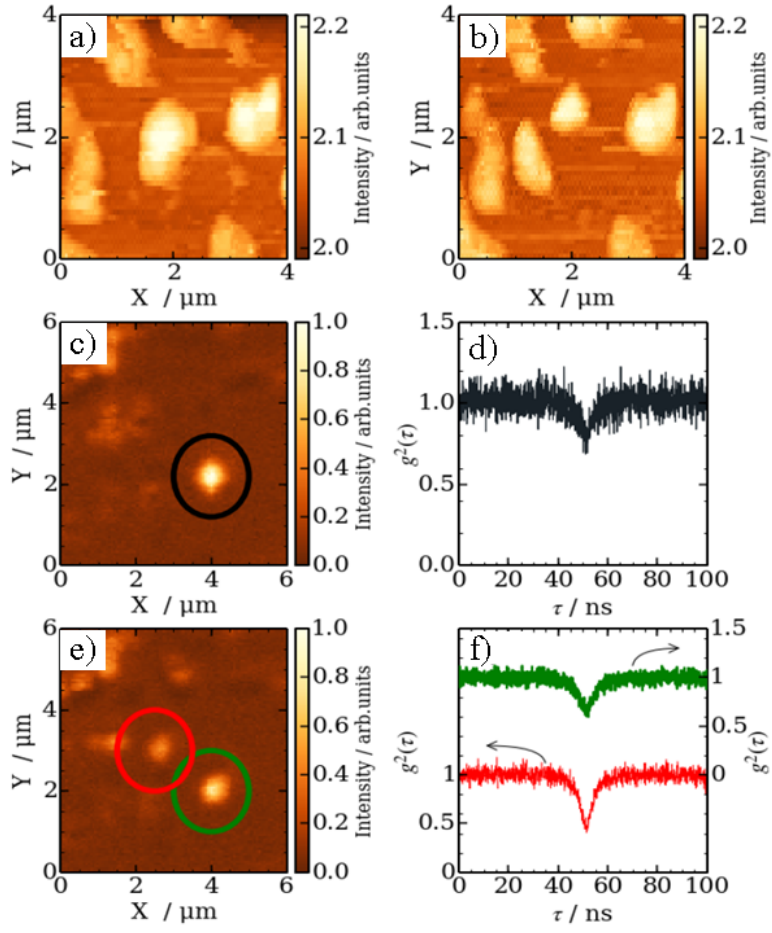


Figure 43: Cutting of AC crystals with individual DBT molecules. a), b) Subsequent AFM-scans of a typical AC crystal. In-between the scans a micron-sized crystal was cut into two pieces via AFM tip. c), e) Confocal images showing individual DBT molecules in AC. d), f)  $g^{(2)}$ -functions corresponding to the encircled spots of DBT in AC crystals as in c), e). The crystal hosting the DBT molecules in c) was cut via AFM leading to two spots as shown in e). The corresponding  $g^{(2)}$ -functions changed, indicating that the smaller crystal-parts host less emitters.

### 4.3.2 Coupling to the Chip

The measurements mentioned in the previous section were performed with AC crystals on glass, where it is straightforward to perform AFM measurements and luminescence studies on one and the same AC crystal. That is different for AC crystals on the chip with the waveguide structures as it is opaque. This fact was mainly limiting the progress of the approach of nanomanipulation and nanopositioning of single DBT molecules to designated positions on the chip.

#### 4. On-chip Nanooptics

---

Several depositing techniques were tested. Figure 44 shows AC crystals on the waveguide structures fabricated by spin-coating. With this technique only a random and loosely controlled crystal positioning was achieved. Secondly the quality and the thickness of the crystals varied on the chip. Crystal growth out of a gas phase would lead to thicker crystals which is impractical when a low in-plane density of emitters is required. Thus, a pre-characterized and well-controlled flat AC crystal that was fabricated via spin-coating on glass has been transferred by contact-printing onto the chip. It was found that this technique works quite well in principle, although some of the waveguide structures were destroyed in the process. With AFM measurements and subsequent confocal scans (after flipping of the chip) it was revealed that some DBT hosting AC crystals very placed right next to the waveguides. However, in order to achieve an efficient coupling to the plasmonic structures a time-consuming iterative of chip-flipping with a sequence of AFM nanopositioning and confocal scanning would have been necessary in principle.

Concerning nanomanipulation attempts of individual DBT molecules, a drawback of the current chip is its opaque substrate. However, when working within the cryostat and with high DBT concentrations any AFM manipulation would become obsolete. A much more severe principle limitation is the use of a simple stripe plasmon waveguide that does not allow for high  $\beta$ -factors. Switching from a stripe to a slot-stripe waveguide is however straightforward and as simulation and experiment were fitting very well to

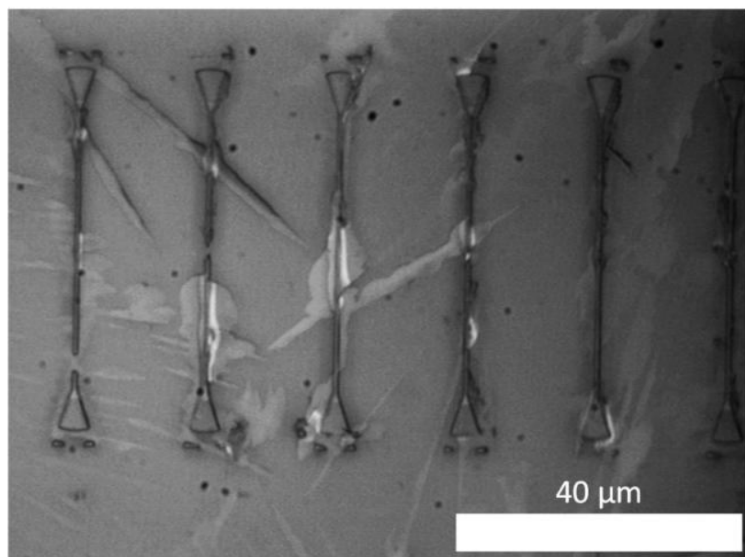


Figure 44: AC crystals on waveguide-structures fabricated by direct spincoating. Various crystal sizes and especially thicknesses are found.

each other, there is no reason to believe that an adapted chip-design would not perform as predicted by numerical simulations with FEM.

A severe fundamental problem for the experiment could arise from another effect. Even though various groups are trying to observe a plasmonic enhancement of Fourier limited line width emitters since years, no such papers are in press. A potential reason could be, that whenever such cooled emitters come close to metallic surfaces (roughly into the 5 nm halo, i.e., the very near-field), a broadening is induced due to i) a disturbance of the host crystal or ii) spectral diffusion induced by near-by moving charges and resulting Stark-shifts as known for other systems [93]. It is yet unclear, whether missing reports in press are indicating concrete experimental problems, unforeseen physical effects or just coincidence. In any case, it was decided to consider also alternative all-dielectric structures for the next steps of the ongoing project, especially as they are simpler to fabricate.

## 4.4 Conclusion and Outlook

In this section an on-chip platform for active nano optics was discussed. During this thesis various essential details of the concept have been analyzed and partly optimized, e.g., the photon-to-plasmon coupler. First milestones have been achieved, i.e., the fabrication of a working on-chip structure as well as the quantitative agreement with numerical simulations is a crucial step. The methods of evaluating the coupling efficiency are essential to understand and predict the chip's performance. Shortcomings have been identified and are partly solved, e.g., the limitations concerning the Purcell-factor of a simple (tapered) stripe waveguide was fixed by introducing a slotted stripe waveguide to the coupler scheme. Fixing the limitations of the used grating-couplers is subject of current numerical and experimental investigations.

Complementary, improvements on handling of the DBT-doped AC crystals and establishment of the analytic tools and setups combined with a cryostat is content of another PhD project currently in progress.

Recently alternative designs were discussed and will be fabricated that are based on purely dielectric on-chip structures, namely SiN waveguides on glass. Even though such structures do not promise as high Purcell factors as plasmonic nanostructures they can still provide an efficient coupling of emitters to guided modes with a high  $\beta$ -factor. Most importantly they feature various pros: fabrication is simpler (the yield of samples

will be higher) as less steps are needed and the chips are more robust especially for cleaning purposes (e.g., gold structures are easily removed in ultra-sonic baths). Furthermore, almost no quenching is expected, which will simplify the interpretation of lifetime measurements and improve the yield of emitters that efficiently couple to the waveguides. Also, a purely dielectric system may not suffer from the potential issue of emitter linewidth broadening mentioned above. All-dielectric stripe-slot waveguides (that would also be used here to gain a high Purcell factor) could be fabricated with wider slots, thereby allowing for AC crystals of higher quality and DBT molecules further away from interfaces where potentially fluctuating trapped charges give rise to Stark shifting.

All-dielectric waveguide structures would only consist of two grating coupler ports and a connecting waveguide. Two possible strategies to excite the mode in a slot-stripe waveguide are obvious: i) direct connection of the grating couplers to a slotted stripe waveguide. This would necessitate a complete time-consuming optimization of grating couplers (by numeric simulations in 3D) for such waveguides. ii) An ideally adiabatic transformation from a stripe to slot-stripe waveguide by cutting a fine slot into the stripe waveguide that widens during propagation. It is however unclear how to achieve this with current fabrication techniques, i.e., reflections will appear where the slot begins.

However, this route is worth going, as – in contrast to plasmonics - dielectric waveguide structures also allow for easy-to-implement extensions like mirrors and cavities of high reflectivity or quality factors. To this end a simple structuring of the waveguide boundaries, will be sufficient. For instance, Kuramachi studied numerically the quality factors of simple bars that form a cavity [94]. Even more promising is the recent result from Yu et al., where a slotted ‘alligator’ cavity integrated in a waveguide made from SiN is demonstrated as shown in [95] (see Figure 45).

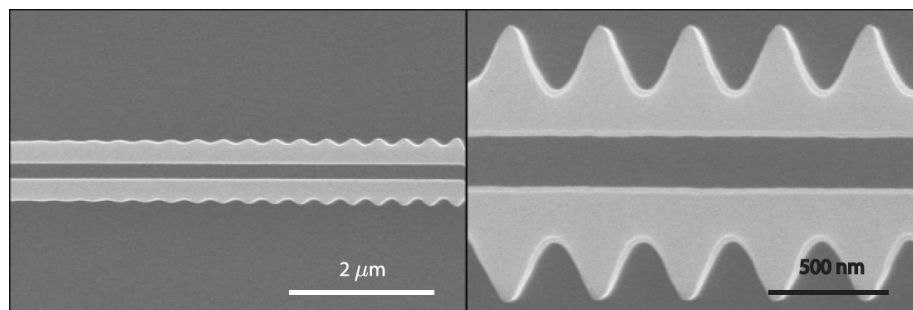


Figure 45: SEM image of an ‘alligator’-cavity integrated into a slot-stripe waveguide. Left figure shows the almost adiabatic transition from the waveguide to the cavity. Right figure shows a zoom-in to the cavity’s center. The cavity is made from SiN. Figure adapted from [95].

## 5 Nanoscopic Lasers & Spasers: Theory, Fabrication and Experiment

---

This chapter deals with the main focus of this thesis, which is the ultimate limit of laser miniaturization, i.e., surface plasmons lasers (spasers) and nanolasers. Here mainly the highest degree of localization is considered, namely a size reduction to less than the wavelength of free space photons in all three spatial dimensions. This chapter is divided into theory (5.1 - 5.3), experiment (5.4) and studies on nanowire based designs (5.5). Results of the theoretical work have already been published in Ref. [96] and Ref. [97].

### 5.1 An Analytic Model for Spasers

The proposal of the spaser is relatively young and experimental results are rare [98]. With only a single experimental paper on spasing from core-shell spasers [99], this project was initiated within the DFG collaborative research center SFB 951. While it was planned to reproduce the experimental results from others and continue with optimization of spasers, it was realized, that it is already extremely difficult to synthesize spasers (see chapter 3.1.3) and to achieve spasing at all.

Based on this experience the need for an own theory was deduced, as papers addressing this topic were complicated to use for concrete predictions on the system at hand. Furthermore, the origin of some parameters fed into the models have been unclear or the values were doubted to be realistic. So was the description of the coupling of emitters (building up the gain-medium) to the cavity mode as well as the quenching. These are parameters, which are known to behave most sensitively on slight position changes of emitters with respect to the cavity. Such effects have been roughly estimated and described by a simple number (rate). Also, potential problems arising from the violated orthogonality relations (see discussion in chapter 2.4.3) had been ignored to this point. Mostly the quasi static approximation was used as a starting-point of theoretical work, yielding a quantization condition that leads to orthonormal modes. This contradiction

was a further motivation to set up an own model. To summarize, a theoretical model was targeted that gives actual quantitative estimates for the experiments, e.g., on gain medium requirements, pump power, etc. in order to fix minimum requirements for the experiments. Further, the theory should be free of approximations that have been doubted.

### 5.1.1 Mie-model: A Semi-Classical Laser Rate-Equation Model for Spherical Resonators

#### *Basic Ansatz*

It was pointed out by the inventors of the spaser that this concept represents a “quantum amplifier”, which leads the reader to the conclusion, that such a device has to be described within quantum theory [100,101]. However, no forceful reason was given that one cannot establish a spaser model of less complexity, especially as it is also a typical procedure in laser physics to use models of different complexity depending on the specific questions one strives to answer. A starting point in laser textbooks is often a rate-equation model. It successfully describes various features of a laser, especially those most relevant for the basic performance [102]. Most valuable, in the steady-state solution, the photon/plasmon number per excitation rate – from now on called “input-output curve” – and the inversion per excitation rate can be plotted. While the steady-state solution can be derived analytically (for single- and two-mode operational systems), multi-mode operation and time-dependent solutions can be calculated numerically.

Thus, it was concluded to start with the relatively simple and consequently transparent rate equation model as it is capable to deliver the most relevant numbers for experimental purposes. The task of describing a spaser accurately now mainly becomes the task of determining rates that have to be fed to the rate-equation model. These rates basically describe how fast the gain medium is relaxing from the excited state to the ground state and how fast the cavity is losing energy. Excitation rates can be used as a control parameter and converted into actual pump powers for given gain media parameters and pump lasers.

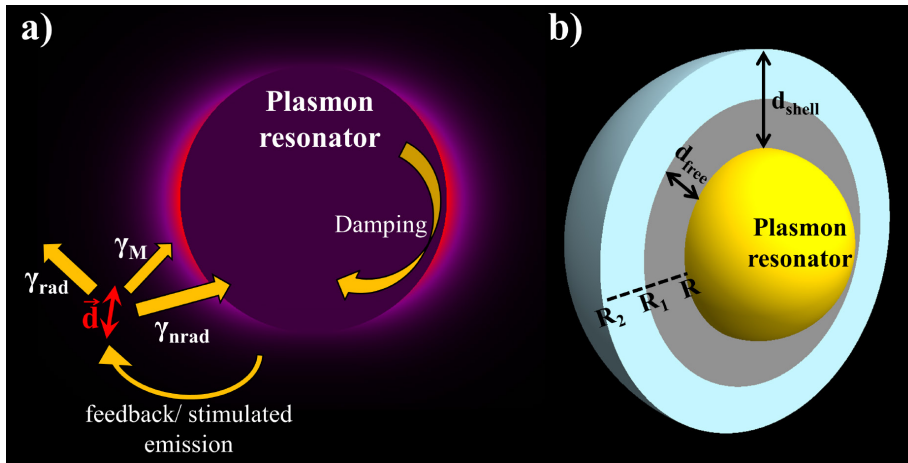


Figure 46: Schematic of the Mie-model. a) Energy emitted by a dipole  $d$  can go to various channels: to the far-field, it can be quenched or populate the cavity (a specific mode in the spherical resonator) described via corresponding rates ( $\gamma_{\text{rad}}$ ,  $\gamma_{\text{nrad}}$ ,  $\gamma_M$ ). The energy in the cavity can be damped or lead to a feedback to the emitter by stimulated emission. b) Geometry of the core-shell particle with a metallic particle as a core and an emitter-doped shell ( $d_{\text{shell}}$ ) around the core. The shell may be partly free of emitters ( $d_{\text{free}}$ ).

It was realized, that all the necessary rates can be calculated analytically within a single theoretical framework, i.e., Mie-theory, which is basically applying Maxwell's equation on spherical coordinates. Thus, the phrase "Mie-model" is used for the model presented here from now on. The pieces of theory used in the Mie-model are well established, partly known for a whole century, tested experimentally and basically free of approximations. A scheme of the model is shown in Figure 46.

### Approximations

The model is however in the end not totally free of approximations. These come into play when the gain medium is constructed, which is consisting of an ensemble of dipole emitters. To keep the model analytically solvable it is restricted to a spherical symmetry. For the gain medium this means, that a homogeneous density of emitters is used, which is surrounding the spherical cavity in a spherical shell. Furthermore a random orientation of dipole-moments (of identical strength) is assumed. At this point this simple but experimentally realistic and relevant construction is free of additional approximations.

However, yet not incorporated are *direct* (not mediated by the cavity) optical interactions of emitters with each other. Such interactions are however rarely done in

laser physics. Effects like self-quenching of the emitters which limit gain-factors (or equivalently the effective inversion-density) have to be kept in mind and results of the model have to be examined critically with respect to realistic inversion densities. When doing so, there should be no severe problem emerging from this approximation.

Further, the inversion density is approximated within a mean-field like approximation, i.e., assuming that the inversion density is constant inside the gain-medium hosting volume (it does not depend on the spatial position). This approximation is in principle not necessary, but is made to drastically simplify the system of equations. The approximation has to be undone, if one is interested in mode-competition processes or hole-burning. The next better approximation would be the use of a layered shell, like in an onion. In this case each layer has a separate inversion. The results of this onion-like gain-medium is examined in section (5.3.2)

Finally, we are doing any approximation that is inherent of rate-equation approaches. For instance we are considering the system to run at a single frequency: the emitters are perfectly in resonance with the cavity and the actual shape of the fluorescence spectrum or the cavity's resonance are ignored.

Please note, that the results are also heavily influenced by the used gain-medium level scheme. A two-level system is attractive due to its simplicity. However, it can intrinsically not be saturated, as the pump directly populates the upper level from which stimulated and spontaneous decay populate the cavity. In this level-scheme the stimulated emission due to the pump is ignored. Therefore, also results for a four-level system are discussed in section (5.3). However, many results use a simpler two-level model that is sufficient to gain basic insights.

### *Effective Single-Mode Rate Equations*

Here, the averaging process over the gain-medium is described, which finally leads to an effective single-mode rate equation. The model-situation at hand is as follows: a spherical cavity interacts with  $N$  emitters that compose the gain medium. In general the interaction may differ for each emitter, or at least will for various sub-groups of them. Consequently, each of these sub-groups will experience different decay rates and different inversion. On top of that there are multiple energetically degenerated cavity modes, for the  $n$ -th order (first order: dipolar, second order: quadrupolar, etc.) there are  $X=2n+1$  modes, that compete for the gain medium. Thus, one can write down a rate-

equation for each mode-population  $n$  with index  $\lambda$  (3 for a dipolar cavity mode), and  $\mu$  ( $\mu \leq N$ ) further equations for the different inversions  $D$  of the emitters:

$$\begin{aligned}\frac{dn_\lambda}{dt} &= \left( n_\lambda + \frac{1}{2} \right) \sum_\mu D_\mu \gamma_{\lambda\mu} + \frac{1}{2} \sum_\mu N_\mu \gamma_{\lambda\mu} - \frac{\omega_\lambda}{Q_\lambda} n_\lambda \\ \frac{dD_\mu}{dt} &= N_\mu (\gamma_{p\mu} - \gamma_{t\mu}) - D_\mu \left( \gamma_{p\mu} + \gamma_{t\mu} + 2 \sum_\lambda \gamma_{\lambda\mu} n_\lambda \right).\end{aligned}\quad (5.1)$$

Here,  $\gamma_t$  denote the total decay rate,  $\gamma_\lambda$  the decay rates into individual modes,  $\gamma_p$  the pump rate,  $\omega$  and  $Q$  are the realpart of the cavity's eigenfrequency and the quality-factor, respectively. In principle, this system of equations can be solved right away. However, to gain more insight and simplicity it is useful to average this system. To do so, the actual emitter and inversion numbers are replaced by constant densities and integrated over the gain-medium hosting shell. Due to the assumption of a homogeneous emitter distribution this transfer is most accurate for the emitter number. However, as mentioned earlier, the assumption of a constant inversion density represents a mean-field like approximation. When a further average over the decay rates is performed and when a potential feedback of off-resonant modes is ignored one ends up with effective single-mode rate equations:

$$\begin{aligned}\frac{dn}{dt} &= \left( n + \frac{1}{2} \right) D \bar{\gamma}_M + \frac{1}{2} N \bar{\gamma}_M - \frac{\omega}{Q} n \\ \frac{dD}{dt} &= N (\bar{\gamma}_p - \bar{\gamma}_t) - D (\bar{\gamma}_p + \bar{\gamma}_t + 2X \bar{\gamma}_M n)\end{aligned}\quad (5.2)$$

Here,  $X$  modes will start lasing simultaneously. In a concrete realization, slight variations of the emitter distribution (or ultimately random quantum fluctuations) would result in a lasing that is dominated by population in a single mode. Thus setting  $X=1$  features a rate-equation for a realistic situation above the laser threshold. However, the hole-burning associated with this symmetry break is not included in the mean-field approximation.

### *Eigen-Frequencies and Quasi-Normal Modes of the Cavity*

The photon/plasmon number in the cavity is reduced according to the rate equation (5.2) by a loss-rate  $\omega/2Q$  per plasmon in the cavity. It is intuitive, that this loss-rate is directly connected to the quality factor of the cavity. In experimental studies (but also in time-domain simulations), a quality factor is often deduced by a frequency-dependent transmission or scattering measurement. A peak or dip in the spectral response is then

used to evaluate the quality factor by dividing the (energetic) position by the full-width at half maximum. This approach is problematic as extinction spectra do depend on the nature of the light source, i.e., its polarization and its momentum composition (e.g., angle of incidence). As an example, a metallic nanorod exhibits two resonances, one devoted to the longer axis and the other to the shorter axis and relatively blue-shifted. In an scattering experiment it might be possible to excite and detect selectively one of these resonances (and the corresponding modes) [35]. This excitation scheme is especially insensitive to dark modes – that is why such modes are called “dark”. In the case of spherical particles this would be similar.

A more rigorous way is to calculate the complex eigenfrequency  $\omega$  directly, rather than to compute scattering spectra. Then the quality factor can be deduced very easily by

$$Q = \frac{\text{Re}(\omega)}{2|\text{Im}(\omega)|}. \quad (5.3)$$

The imaginary part of the eigenfrequency  $\text{Im}(\omega)$  turns out to be the loss-rate that is needed in the rate-equations. In the concrete case here, one has to find the maxima for the individual Mie-scattering coefficients. A characteristic equation can be deduced which has to be solved for complex frequencies, i.e., the roots of the equation in the complex plane are searched – for each mode of order  $n$  separately [103]. These characteristic equations are the roots of the denominators of the scattering coefficients  $a_n$  and  $b_n$  of the Mie-theory (equations (2.11) and (2.12), chapter 2.4.3). Figure 47 shows the characteristic equation plotted in the complex plane.

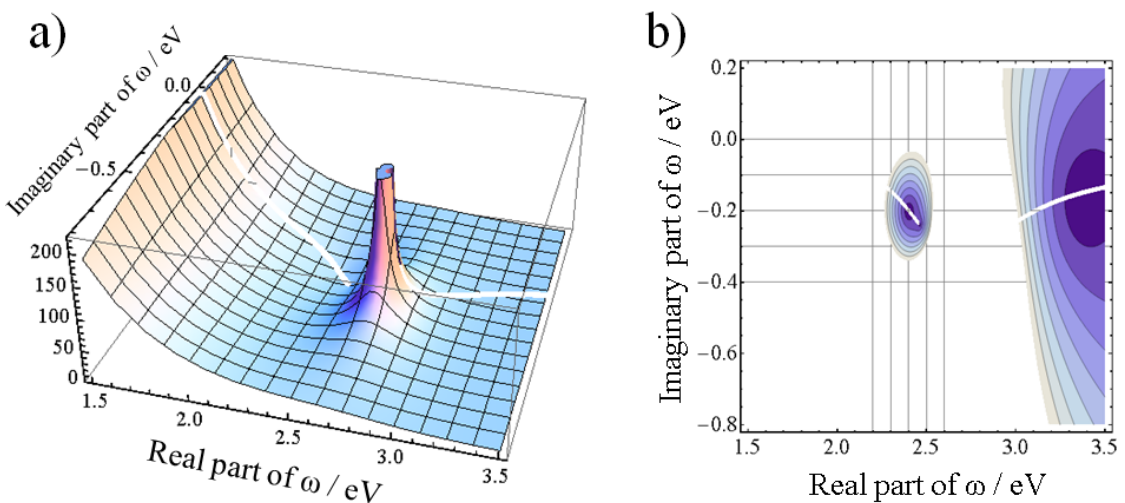


Figure 47: Eigenfrequency as root in the complex plane in a) a surface plot and b) a contour plot. These plots can be used to check the results from numeric root-finders/solvers that sometimes feature instabilities.

When a complex eigenfrequency is computed, it can be inserted into the solution for the electric and magnetic fields of a spherical particle. Only at these frequencies one deals with a pure (quasi-normal) eigenmode.

### *Decay Rates inside the Gain Medium*

In his work from 1982, Ruppin investigated the emission of a dipole close to a sphere [69]. He found a complete, analytic solution when he combined the analytic solution known for a Hertzian dipole with Mie-theory. He then applied this to a specific case, in which a single radiating dipole is influencing its own emission through the mediation of the sphere. This very problem has been studied later also by many others based on Ruppin's approach [68,104–108]. As the excitation-spectrum of any resonance behaves similar to a Lorentzian peak, i.e., broad and never reaching zero also far away from the maximum, in this specific case the dipole is interacting with a large number or continuum of modes. Ruppin's computation thus results in the total decay rate that is needed in the rate-equations. Furthermore, it was shown that the decay rate is only a function of emitter-to-sphere distance (for a fixed sphere material and frequency) and the choice of two dipole-orientations, i.e., orthogonal or parallel to the sphere's surface. The mean total decay of an emitter in the gain-medium is thus a weighted sum of these two decays: there are three linear independent orientations possible in space, two parallel and one orthogonal, yielding

$$\bar{\gamma}_{\text{tot}}(r) = \sum_n \frac{1}{3} \gamma_{\perp}(r) + \frac{2}{3} \gamma_{\parallel}(r) . \quad (5.4)$$

This is the distance dependent decay rate which can be calculated for any order  $n$  independently. By summing up over a series of orders (until convergence appears) the total decay rate can be calculated (Figure 48).

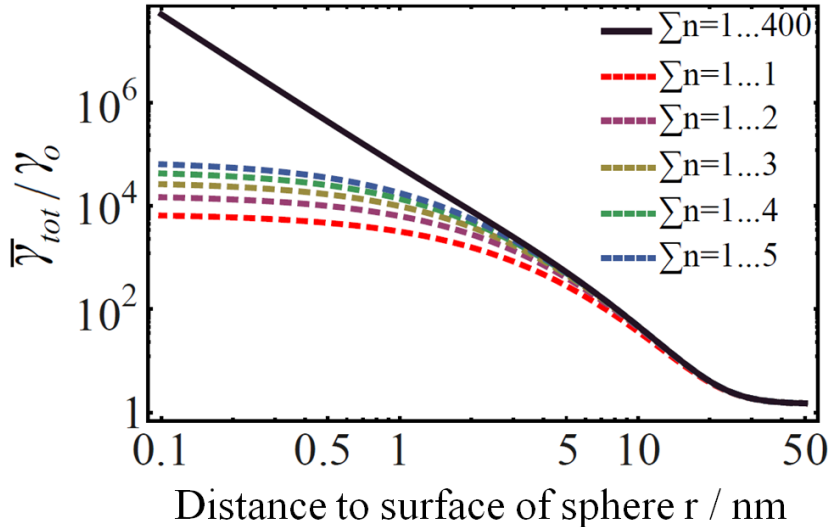


Figure 48: Orientation averaged, distance dependent decay rate of an emitter close to a spherical Au particle. The emitter is in resonance with the dipolar mode ( $n=1$ ). The rates are normalized to the vacuum decay rate  $\gamma_0$ . The result depends on the number of contributing orders  $n$  that are summed up. In this example a convergence was found after  $n=400$ . Even if a specific mode is in resonance, the corresponding contribution to the decay is not dominating for short distances but the total decay is orders of magnitude higher. This feature is an essential effect of the well-known quenching.

The solution found by Ruppin is even more general. For the total decay, the emitter is polarizing the sphere along a certain direction aligned with the emitter-to-sphere axis. To calculate the coupling of an emitter to a specific mode – here the (lasing) cavity mode this would be inaccurate, as an emitter might be positioned right in the hotspot of the mode or somewhere, where almost no interaction is going to happen. Even though this seems to be much more difficult, this evaluation can be performed with Ruppin's solution [69]. Although this situation seems to be very complicated, averaging over all possible positions and orientations leads to a very intuitive result, similar to the mean decay rate found before. Again the parallel decay and orthogonal decay's are weighted as before, but this time the sum over all Mie-scattering coefficients only goes over an individual summand – that of the cavity mode – and the sum has to be divided by the degeneracy  $X$  of that very mode.

$$\bar{\gamma}_M(r) = \frac{1}{X} \left( \frac{1}{3} \gamma_{\perp}(r) + \frac{2}{3} \gamma_{\parallel}(r) \right) \quad (5.5)$$

The coupling to a single mode (normalized by  $\gamma_0$ ) is nothing else than the Purcell factor  $\Gamma$  (2.5.3). To derive single rates ( $\gamma_M$  and  $\gamma_{tot}$ ) from  $\bar{\gamma}_M(r)$  and  $\bar{\gamma}_{tot}(r)$  for the effective

single-mode rate equation, the distance dependent decay rates are averaged over the shell in a last step. With this, all rates are found, that are needed to solve the rate equations.

### 5.1.2 Prime Example: The Core-Shell Spaser of Noginov et al.

Now, that the model is composed, concrete calculations can be performed. It seems likely to compare the theory with an experiment that resembles conditions that can be met by the Mie-model. Namely, such an experiment was published in “Demonstration of spaser-based nanolaser” by Noginov et al., where a 14 nm diameter gold sphere was

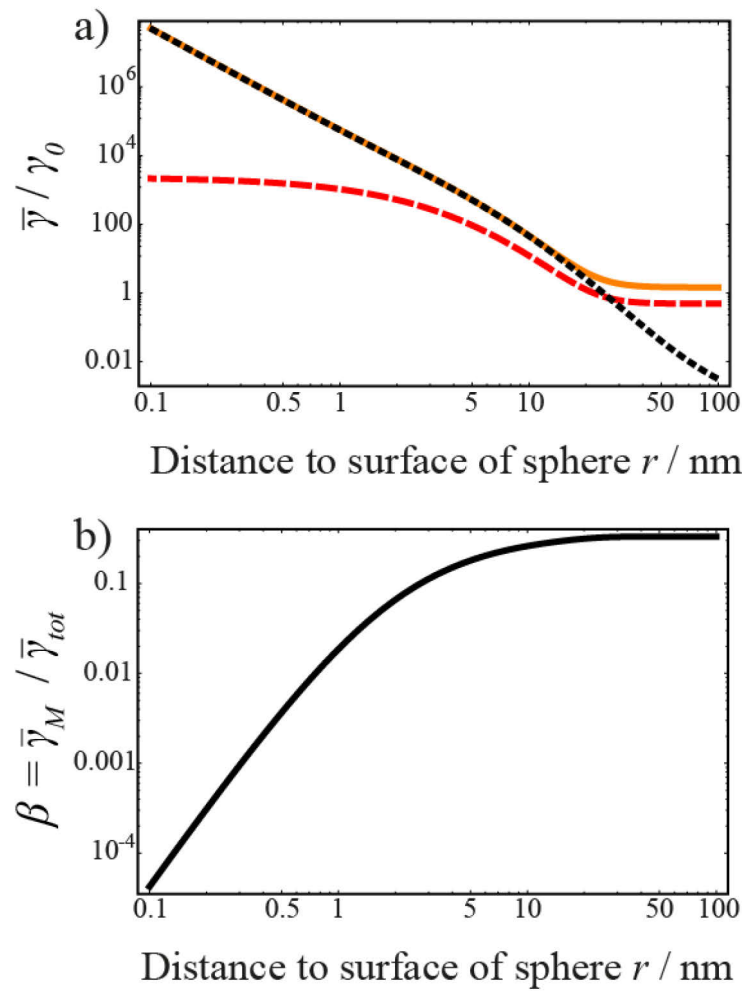


Figure 49: Normalized decay rates and  $\beta$ -factor of a dipolar emitter close to a gold sphere.  
 a) Orientation averaged decay rates  $\Gamma = \bar{\gamma}_M / \gamma_0$  (Purcell-factor, red dashed),  $\bar{\gamma}_{\text{tot}} / \gamma_0$  (total decay, orange) as a function of distance for the configuration described by Noginov et al. [99]. Additionally the black dashed curve shows the contribution of non-radiative decay rate  $\bar{\gamma}_{\text{eh}} / \gamma_0$ .  
 b) Corresponding  $\beta$ -factor ( $\beta = \bar{\gamma}_M / \bar{\gamma}_{\text{tot}}$ ) which shows that emitters in close proximity to the sphere can only provide a small fraction of their emitted power to the cavity mode.

coated with a silica shell of 15 nm thickness, doped with roughly 2700 OG-488 emitters, i.e., an organic gain medium [99]. These nanoparticles were diluted in an ethanol bath in which they were pumped optically with 5 ns long laser pulses. From the fabrication processes it can be concluded, that the emitters will be presumably oriented randomly and homogeneously in the shell, just as in the theoretical model. Although layered spheres can be handled within Mie-theory, it is a good approximation to ignore the change in refractive index at the interface between silica shell and ethanol as both refractive indexes are relatively close to each other. The decay rate of the pure emitters in ethanol and their absorption cross-section is known, thus actual decay rates and pump rates (related to the pump laser) can be calculated.

For this specific configuration we find the distance dependent decay rates as shown in Figure 49, yielding average decay rates in the shell of  $\gamma_M = 1.32 \cdot 10^{10} \text{ s}^{-1}$  and  $\gamma_{\text{tot}} = 6.81 \cdot 10^{12} \text{ s}^{-1}$ . In this case the vacuum decay rate of  $\gamma_0 = 1/(\tau \cdot n_{\text{EtOH}}) = 1.75 \cdot 10^8 \text{ s}^{-1}$  is used, showing, that the plasmonic cavity indeed alters the decay rates significantly. The average  $\beta$ -factor is poor:  $\beta = 0.0019$ , i.e., two out of a thousand spontaneous emission processes populate the designated spaser cavity. The resonance of the cavity is centered at  $\lambda_{\text{res}} = 537.7 \text{ nm}$  with a quality factor of  $Q = 9.29$ .

## 5. Nanolasers & Spasers

When these values are plugged into the rate-equation model the remarkable result is found, that a lasing behavior is not reached, no matter how hard the system is pumped. Obviously there is not enough gain-medium present. As the number of 2700 emitters is surely differing for different core-shell particles, we increase the number more and more until the input-output curve finally shows a typical laser curve with threshold. However, this is not until we reach a value of  $N=3396$  emitters (Figure 50).

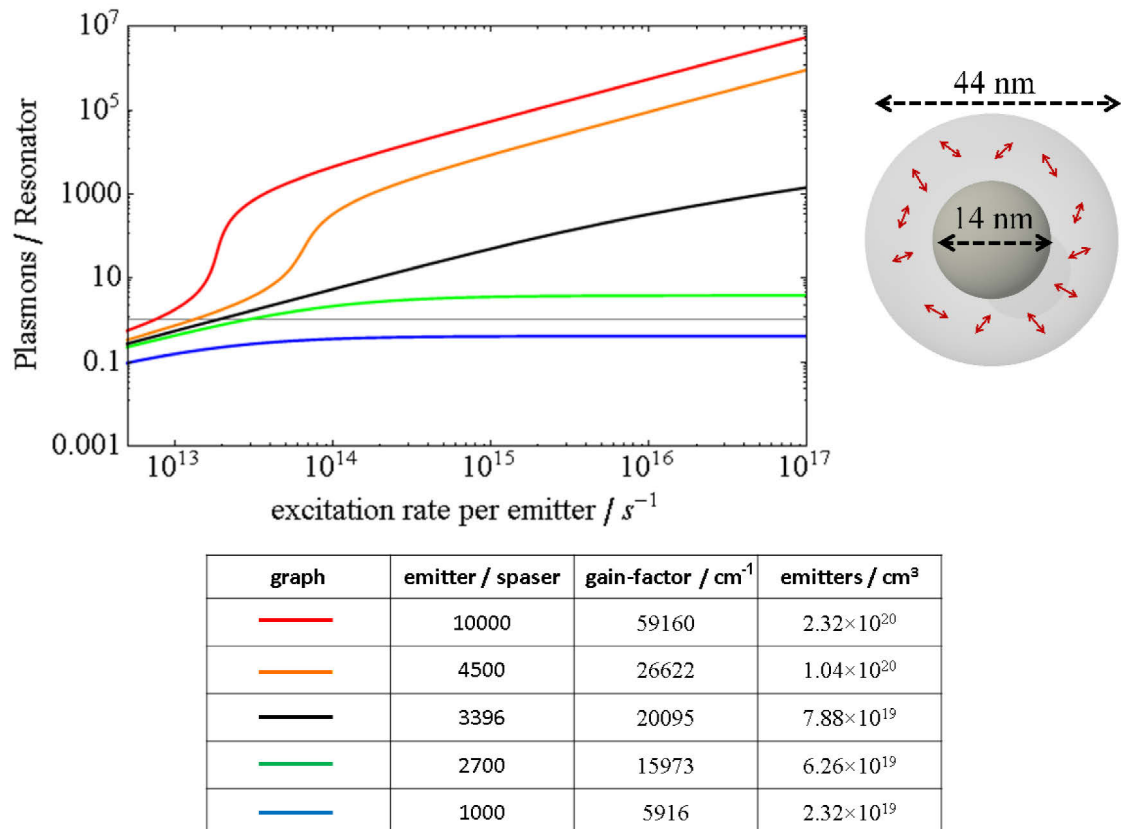


Figure 50: Input-output curve for various emitter densities and parameters as reported by Noginov et al. [99]. The absolute emitter numbers per spaser  $N$ , corresponding gain-factors and emitter-densities are tabulated.

Furthermore – and this is the key message here - when the inversion, that is reached during lasing is translated into a gain-factor, values are found that are definitely extreme for organic gain-media. The 2700 emitters reported by Noginov et al. in the volume of the shell yield already an inversion density  $\rho$  of  $\rho=6.26\times 10^{19}\text{ cm}^{-3}$  (if all emitters are excited). When this is multiplied with the absorption cross-section  $\sigma_{\text{abs}}$  of the emitters given by the authors, this yields a gain-factor  $g$  ( $g=\sigma_{\text{abs}}\cdot\rho$ ) of almost  $16,000\text{ cm}^{-1}$ . Organic gain media, however, are known to be limited to values of less than  $100\text{ cm}^{-1}$  [109]; this limitation is actually a well-known effect attributed to self-quenching [110]. This means that it is unrealistic to assume, that the emitters can contribute to the gain medium irrespectively of their density in the shell. Actually, it is already unrealistic to assume that for only 2700 emitters. This problem is discussed in more detail in section (5.1.4). Figure 51 shows the stationary solution for the inversion  $D$  and the corresponding gain-factor as a function of pump rate. A gain of  $100\text{ cm}^{-1}$  would be already reached for low pump-rates that correspond only to roughly a single plasmon in the resonator which can hardly be called spasing or lasing.

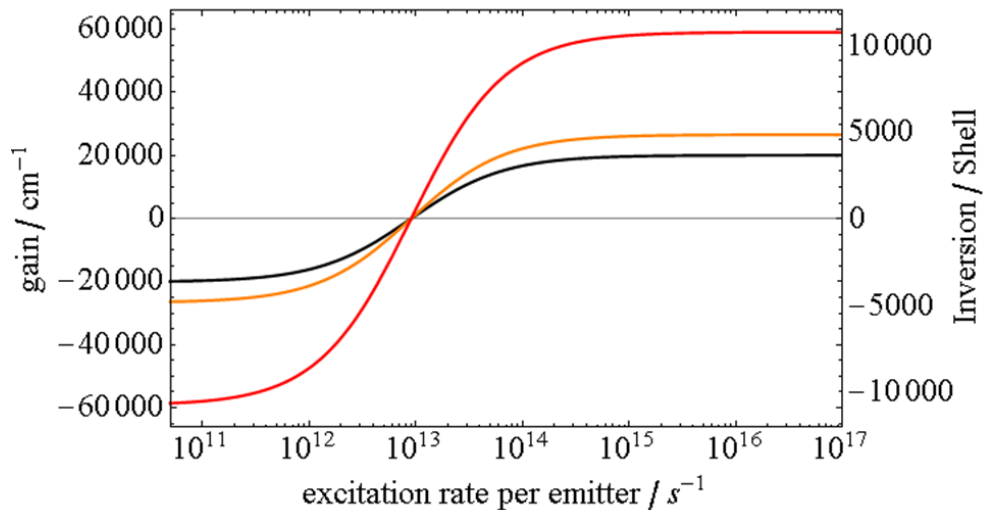


Figure 51: Inversion and gain achieved during pumping for the three potentially spasing configuration as depicted in Figure 50 (same color-code). The vertical line corresponds to a gain-value of  $100\text{ cm}^{-1}$ . At the crossing of the curves with this gain-factor an excitation rate per emitter of around  $9.1\cdot 10^{12}\text{ s}^{-1}$  is reached which corresponds to  $\sim 1$  plasmon in the resonator. For spasing unphysically high gain-factors are needed.

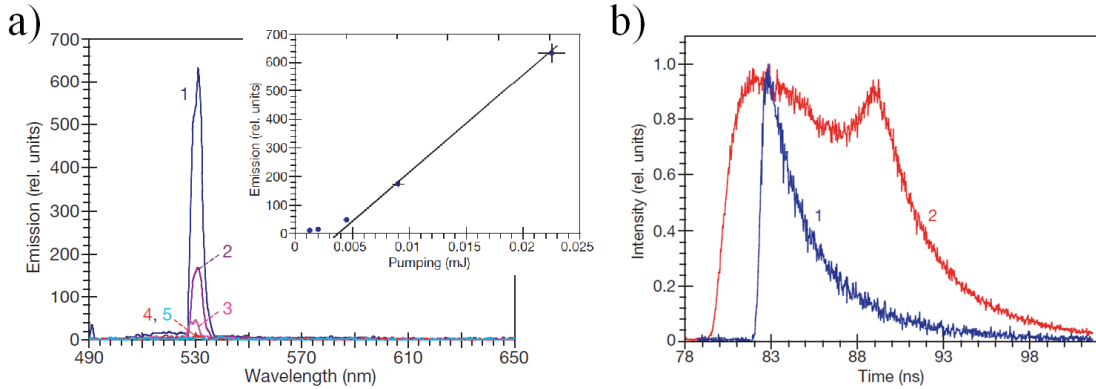


Figure 52: Measurements taken by Noginov et al. adapted from [99]. a) Five spectra of the core-shell particles (ensembles in solution) excited with increasing pump-powers (5 ns laser pulses weakly focused into a cuvette). The inset shows the peak heights as a function of pump power. b) Lifetime measurements of the core-shell particles illuminated through an objective with 90 ps pulses for two different pump powers.

Consequently, the Mie-model predicts that Noginov's core-shell spaser is clearly incapable of spasing. In order to discuss this discrepancy of theory and experiment, the experimental findings are briefly repeated here. The actual data set shown in the paper consists of 5 spectra at different pump powers, which are basically flat apart from a peak that emerges from a noisy background floor. To evaluate this data, the authors plot the peak intensities as a function of pump power. A kink in the curve connecting the five points was interpreted as a lasing threshold. The data presented in the work by Noginov et al. [99] is shown in Figure 52.

All the spectra were taken from an ensemble, however, to demonstrate that the observed effect is not a collective effect, but stemming from the individual core-shell particles, it was discussed that different concentrations of this solution with core-shell particles showed the same threshold curves. This data is not shown in the paper. One can conclude, that the best looking data was presented, i.e., the data of the higher concentrated samples, which was already of relatively poor signal-to-noise ratio. Therefore, the significance of this mentioned additional data has to be doubted. Secondly, lifetime measurement were presented (Figure 52b), that show a modified lifetime curve for high pump power, which does very much differ from ordinary ones: instead of a typical exponential decay the intensity rises shortly after the pulse before it decays. It is then argued, that this behavior is similar to random lasing, leading the authors to the conclusion that this is a signature of spasing. A more direct connection

could however lead to the conclusion that this typical random lasing signature actually belongs to random lasing rather than spasing.

Beyond criticism on earlier experimental work, theoretical findings by others about the minimum gain requirements (based on the quasi static limit) will be discussed in section (5.1.4). These findings perfectly support the pessimistic predictions of the Mie-model [100,111].

### 5.1.3 Optimization Concepts for Spasers

Although relative pessimistic results were found in the last section, general ways to optimize the system can be explored and analyzed. The performance of the core-shell spaser is mainly limited, as the relaxation of the gain-medium is very fast (high  $\gamma_{\text{tot}}$ ), making it hard to reach inversion. Additionally only a small fraction of the power provided by the emitters in the gain medium is feeding the cavity but only heating the core (poor  $\beta$ -factor). The high Purcell factor is not helping here, as the total decay rate is dominating. As a matter of fact, the gain medium close to the core is involved into a process of efficient reabsorption of eventually excited plasmons, thereby prohibiting spasing. This interpretation holds true when a 4-level gain medium is considered (section 5.3.1) and especially when the Mie-model with a non-constant inversion is investigated (section 5.3.2).

Thus, an emitter-free spacing layer between cavity and gain-medium is introduced (see Figure 46 section 5.1.1) to remove the emitters with the worst  $\beta$ -factors. This is possible within the model by simply adjusting the limits when computing the average decay rates. The effect is interesting to explore, since it shines light on a contradictory point: Stockman, who is one of the authors that proposed to build a spaser [98,100], argues that the strong Purcell effect experienced by emitters in the near-field of the plasmon resonator is the source of a very strong feedback between cavity and gain-medium, making the spaser a very efficient device [100]. On the other hand, very strong quenching is expected close to the cavity. The input-output curves for various configurations reveal that a 5 nm spacing layer leads to a significant reduction of the threshold pump-rate by roughly 3 orders of magnitude (Figure 53).

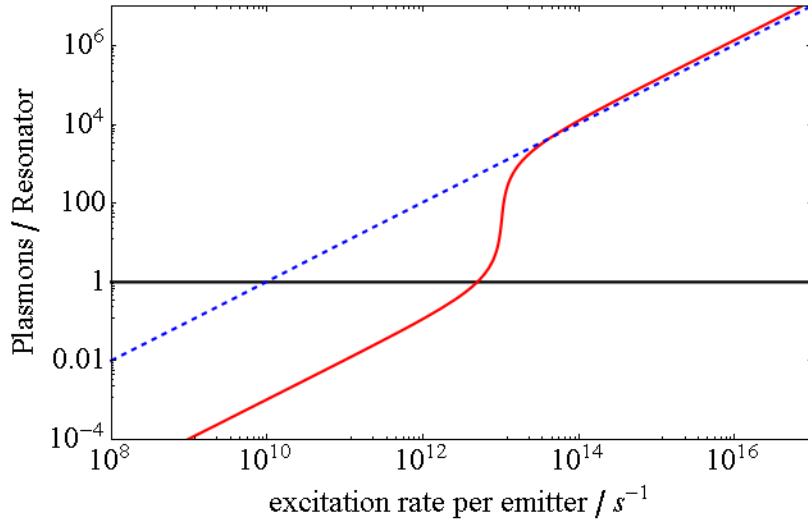


Figure 53: Input-output curves for the design of Noginov et al. [99] with (dashed blue line) and without (red line) an emitter-free spacing layer of 5nm. Calculations are done for an extremely high gain-factor.

However, the minimum gain needed is rising when doing so ( $\sim$  by a factor of 5). We can conclude from this, that a good ratio of cavity-to-gain coupling ( $\gamma_M$ ) to the total decay rate ( $\gamma_{\text{tot}}$ ) dominated by quenching, i.e., the  $\beta$ -factor, is an important number to optimize. This is a well-known fact from laser physics. A strategy to improve the  $\beta$ -factor is needed *and* a strategy to reduce the needed gain-factor. Both strategies have to work out at the same time. Obviously, using silver instead of gold leads to an improved  $\beta$ -factor and lower cavity losses (better Q-factors), however still the quenching is very strong and oxidation of silver is a practical issue as the conductivity can be severely reduced. For gold the high decay rates can be reduced, when the frequency is shifted to the red away from the interband transition around 520 nm (2.2.1). Shifting of the eigenfrequency of a sphere into the red is possible by increasing the radius, which leads to drastically reduced quality factors as radiative cavity-losses rise significantly. Another route is to increase the outer refractive index or to use modified shapes, e.g., rods [112]. With this tricks the quality factors are preserved and do even rise, since not only the quenching but also the quality factors are negatively affected by material losses. Figure 54 shows the quality-factors and eigenfrequencies of the dipolar mode of Au and Ag spheres with a radius of 5 nm when the outer refractive index is shifted from  $n=1$  to  $n=4$ . The result is compared to predictions based on the quasi static approximation [111].

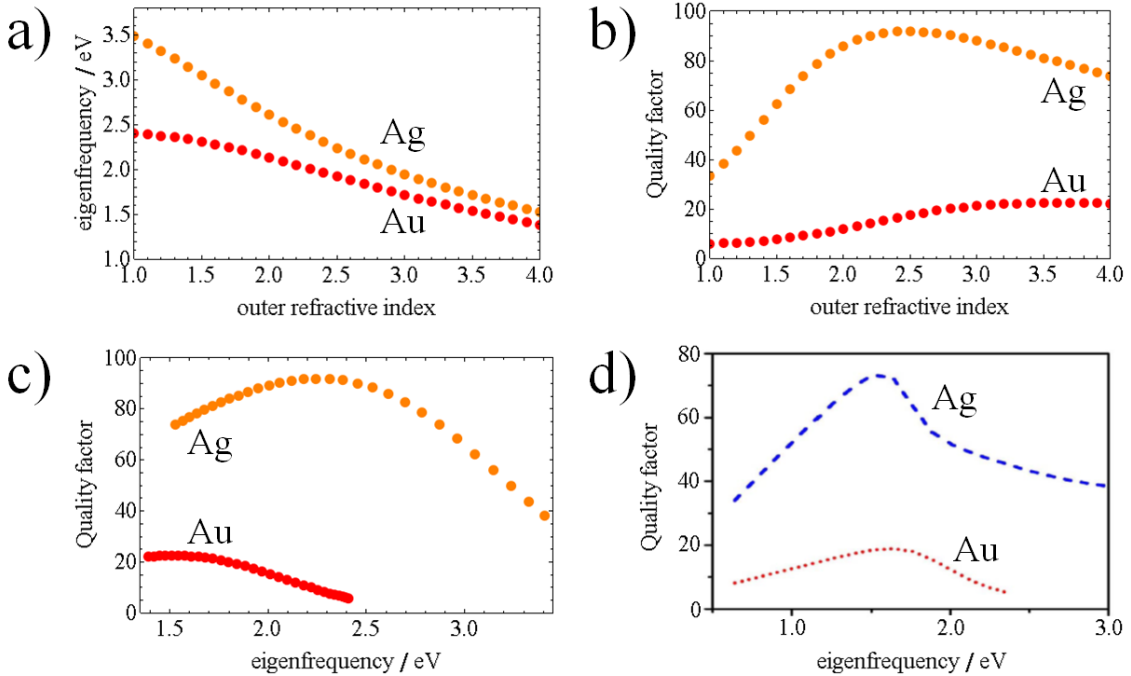


Figure 54: Resonances of small plasmonic spheres ( $R=5\text{ nm}$ ). a) Real part of the eigenfrequencies of Au (red) and Ag (orange) spheres as a function of outer refractive index. b) Corresponding Q-factors and c) Q-factors as a function of eigenfrequency. d) Q-factors as a function of photon energy (eigenfrequency) as predicted by the quasi-static approximation (adapted from [111]).

Concluding, both factors, strong quenching and low quality factor are directly connected to the imaginary part of the cavity's dielectric permittivity, i.e., the intrinsic material losses. Reducing losses even further might be possible with dielectric resonators. This option is discussed in section (5.2). Before that, a route to scan the performance of spasers over the entire VIS and beyond is discussed in the next section (5.1.4), in order to find optimum conditions for core-shell spasers.

### 5.1.4 Minimum Gain and Heat Production in the VIS to NIR Range

#### *Results of Quasi Static Approximation*

Earlier work studied the optimum conditions for spasing on the basis of very general considerations using the quasi static approximation [111,113]. It was found in section (5.1.2) that results shown in published experiments [99,114,115] have most likely been misinterpreted for spasing, as the gain-factors of organic gain-media are too small. It is

interesting to check the predictions for this system given by the quasi static approximation. Furthermore the model presented here should coincide with the quasi static case if we consider small spheres in the Mie-model. Such a test is especially interesting, as both models have rarely something in common with respect to their ansatz.

The quasi static approximation yields a very simple connection between the quality factor of a small particle and the real and imaginary parts of the metal's dielectric permittivity  $\epsilon_m(\omega)$ :

$$Q(\omega) = \frac{\omega^{\frac{d\epsilon_m}{d\omega}}}{2\epsilon_m''} , \quad (5.6)$$

the result is shown in Figure 54d [111]. For a *negative* imaginary part of the surrounding gain-medium  $\epsilon_g''$ , i.e., an amplifying medium, a simple equation is derived for the situation in which the quality factor diverges, which can be interpreted as the onset of spasing:

$$\frac{|\epsilon_g''|}{\epsilon_g'} \geq \frac{\epsilon_m''}{|\epsilon_m'|} \quad (5.7)$$

The imaginary part of the dielectric permittivity can be connected to the gain-factor  $g$ , which is defined as the negative absorption  $\alpha = -g = 2k_0\kappa$  by the well-known relations between permittivity and refractive index ( $\tilde{n} = n + ik$ )

$$\epsilon' = n^2 - \kappa^2 , \text{ and} \quad (5.8)$$

$$\epsilon'' = 2nk , \quad (5.9)$$

yielding

$$g = -2k_0n(\tilde{Q} - \sqrt{\tilde{Q} + 1}) \quad (5.10)$$

with the “quality” of the metal  $\tilde{Q} = |\epsilon_m'|/\epsilon_m''$ . Thus, minimum gain requirements can be plotted simply based on the permittivity data of the noble metals and the surrounding refractive index (Figure 55).

It can be seen, that the required gain-factor rises very fast, when approaching the frequency of the interband transition in gold. The necessary gain-factor for a spaser working at a photon energy of 2.34 eV as presented by Noginov et al., which is small enough to be described in the quasi static limit, needs a gain-factor of  $16,000 \text{ cm}^{-1}$ , which is way beyond anything known. So, the huge discrepancy between theory and experiment is also found here.

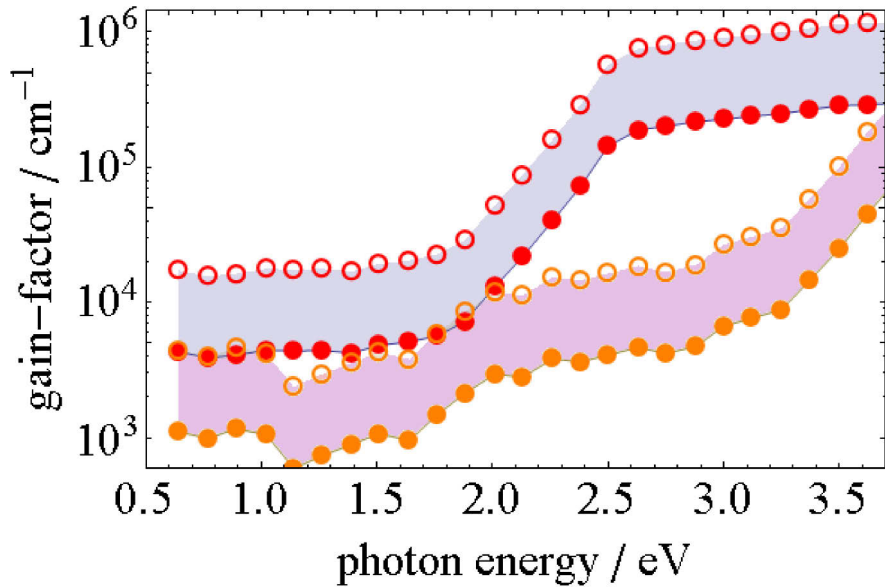


Figure 55: Logarithmic plot of the minimum gain requirement for a spaser predicted by quasi static approximation as a function of photon energy for Au (red) and Ag (orange). The filled regions mark the gain-factor for outer refractive indexes ranging from  $n=1$  (filled circles) to  $n=4$  (hollow circles).

#### *Quasi static approximation vs Mie-model*

The quasi static approximation and the Mie-model differ so much, that it is not a priori clear how to compare them. This is a short summary of what will follow in this section: In order to provide a fair comparison between the models, first a condition for the minimum gain has to be defined for the Mie-model. From this an analytic formula for the laser threshold and for the minimum inversion density is derived directly from the laser rate-equations. Then this formula will be fed by concrete rates. To this end a small sphere of 5 nm radius (which can be considered to fulfill the requirements of the quasi static limit) with a fixed shell-thickness of  $d_{\text{shell}} = 15$  nm is considered throughout this comparative study. The outer refractive index is swept from  $n=1$  to 4, which shifts the eigenfrequencies of the dipolar mode over the entire VIS up to the NIR. For the found frequencies the average decay rates ( $\Gamma$ -factors and  $\beta$ -factors shown in Figure 56) and the quality factors (Figure 54) are computed; the emission-frequency of the gain-medium is assumed to follow the eigenfrequency. Finally, the inversion density is converted into a gain-factor to compare with the quasi static approximation.

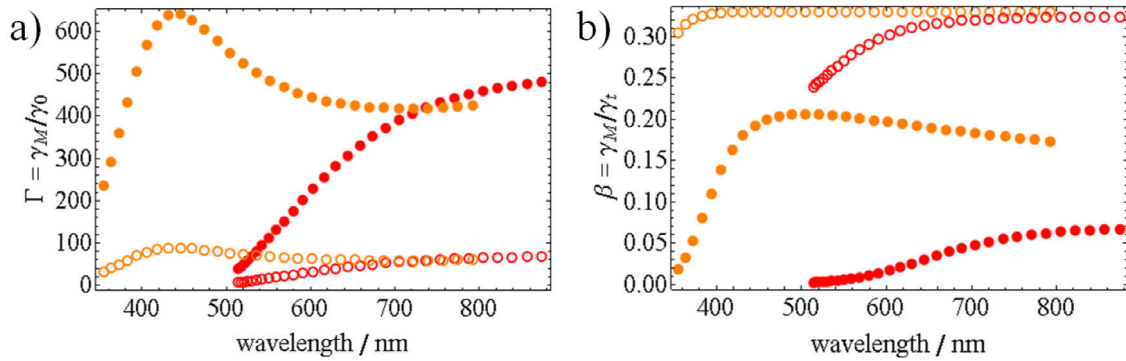


Figure 56: Purcell- and  $\beta$ -factor of small metallic spheres in the VIS. a) Purcell-factor  $\Gamma$  as a function of wavelength associated with the dipolar mode of an  $R=5\text{ nm}$  Au (red) and Ag (orange) spheres. Hollow circles show the result with a 5 nm emitter-free spacing layer, the full circles without. b)  $\beta$ -factor as in a)

A condition for the minimum necessary gain for a laser with a two level-gain medium can be found when plotting a series of input-output curves for different numbers of emitters, e.g. as in Figure 53. Two different regimes become obvious: one where the photon/plasmon number in the cavity is never saturated, one regime where it saturates. In the lasing state this laser never saturates. Thus, by constructing a condition for saturation yields a condition for the minimum necessary number of emitters  $N_{\min}$ . This condition is simply, that the gradient of the input-output curve  $n(\gamma_p)$  is larger than zero for a pump-rate that tends to infinity:

$$\lim_{\gamma_p \rightarrow \infty} \frac{dn}{d\gamma_p} > 0 \Rightarrow N_{\min} = \frac{\omega'}{Q \cdot \gamma_M} , \quad (5.11)$$

with the complex eigenfrequency  $\omega = \omega' + i\omega''$ . With this condition those input-output curves are extracted from the possible solutions that actually represent spasers (core-shell particles with enough gain-medium), especially the spaser, that is the limiting case with the minimum gain-medium  $N_{\min}$ .

However, in the following a slightly different condition is used that is more general and thus allows for a better comparison with the four-level model that will be discussed later (section 5.3.1). This condition is fulfilled when the losses of the cavity are compensated by stimulated emission processes of the gain-medium:

$$\frac{\omega'}{Q} n = (N_2 - N_1) \cdot n \cdot \gamma_M \Rightarrow D_{\min} = \frac{\omega'}{Q \cdot \gamma_M} . \quad (5.12)$$

This condition is only slightly harder to fulfill than the one in Equation (5.11). The same condition is found for the four-level gain medium rate-equations.

Now, a laser-condition is formulated. It defines at which position (pump-rate  $\gamma_p$ ) on an input-output curve actual lasing sets in. This point is reached when stimulated relaxation processes of the excited gain-medium equals the spontaneous processes. This is fulfilled when

$$N_2 \gamma_{\text{tot}} = N_2 \gamma_M n \quad . \quad (5.13)$$

$$\Leftrightarrow n = \beta^{-1} \quad .$$

The same holds again for the four-level rate equations. To derive a more useful laser-condition that relates the pump-rate  $\gamma_p$  with parameters that depend on the spaser design equation (5.12) is equalized with the inversion D that can be derived directly from the basic rate equations:

$$D_{\min} = N_2 - N_1 \quad .$$

$$\Leftrightarrow \frac{\omega'}{Q \cdot \gamma_M} = \frac{N(\gamma_p - \gamma_t)}{\gamma_p + \gamma_t + 2\gamma_t n} \quad . \quad (5.14)$$

$$\Leftrightarrow \gamma_p = \gamma_t \frac{NQ + 3\omega'/\gamma_M}{NQ - \omega'/\gamma_M} =: \gamma_{\text{th}} \quad .$$

This pump-rate is the threshold-pump-rate  $\gamma_{\text{th}}$ . To connect the inversion density D/V (in units of  $\text{cm}^{-3}$ ) with the gain-factor (in  $\text{cm}^{-1}$ ) one simply has to multiply with the absorption cross-section (in  $\text{cm}^{-2}$ ) of the corresponding gain medium - or more precise – with the emission cross-section:

$$g = \frac{D_{\min}}{V_{\text{shell}}} \cdot \sigma_{\text{em}} = \frac{\omega'}{QV_{\text{shell}}} \frac{\gamma_0}{\gamma_M} \cdot \frac{\sigma_{\text{em}}}{\gamma_0} \quad . \quad (5.15)$$

The minimum inversion  $D_{\min}$  is inversely proportional to  $\gamma_M$  (equation (5.12)) and thus also to the specific lifetime  $\tau = 1/\gamma_0$  of the used gain-medium. The cross-section is also a characteristic number of each gain-medium like the lifetime. It is thus convenient to separate parameters that can be calculated ( $\beta = \gamma_M/\gamma_0$ ) and parameters that are specific for the gain-medium ( $\sigma_{\text{em}}/\gamma_0$ ).

The Strickler-Berg relation connects both parameters  $\sigma_{\text{em}}$  and  $\gamma_0$  [116,117]. According to this relation the radiative decay rate in vacuum is proportional to the emission cross-section, folded with a frequency dependent expression that accounts for the change in the density of states in vacuum. Further an emitter-dependent characteristic spectral function  $f(\lambda)$  is needed to account for the specific spectral details that can differ significantly from emitter to emitter:

$$\frac{\sigma_{\text{em}}}{\gamma_0} = \frac{\lambda^4 f(\lambda)}{8\pi n^2} \quad (5.16)$$

The left-hand side of this formula gives  $1.45 \cdot 10^{-28} \text{ m}^2$  for the values of OG488 which was used by Noginov et al. [99] and a similar result is found for Rhodamin 6G. The latter is a widely used laser dye with an almost unity quantum efficiency. Thus, these values can be regarded to represent an efficient gain-medium. For simplicity we use here  $\sigma_{\text{em}}/\gamma_0 = 1.5 \cdot 10^{-28} \text{ m}^2$  instead of the formula by Strickler and Berg for the gain-medium. With this everything is given to compute the minimum gain-factors as a function of frequency with the Mie-model. The gain-factor is plotted together with the result of the quasi static approximation in Figure 57. While both models yield similar trends, the Mie-model predicts smaller minimum gain-factors.

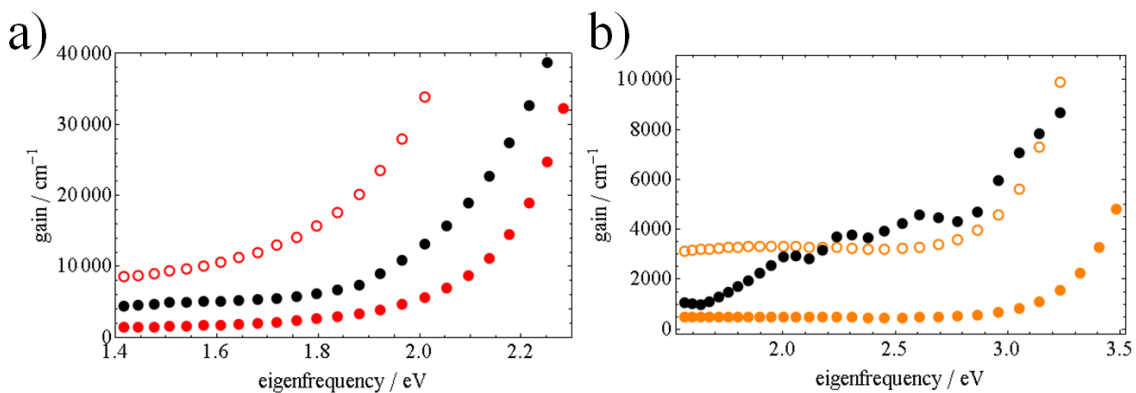


Figure 57: Comparison of minimum gain requirements found by the quasi static approximation and the Mie-model. a) Gain requirements for Au. Circles show results for a core-shell system with a 5 nm emitter-free spacing layer, full disks for the system without spacing layer. b) Results for Ag. Some of the differences between Mie-model and quasi static approximation stem from the Drude-Lorentz-Model used for the Mie-model while for the quasi static approximation the experimental data of the refractive indices [184] was used directly.

#### *Power Consumption and Core Temperature*

In this section the minimum power consumption and associated heat production is discussed for the small spaser discussed in the previous section. Both numbers are important when one wants to estimate the potential use of spasers in devices such as sensors or optical switches on a chip. Stockman predicted the spaser to be extremely efficient, consuming only a few quanta of energy [100,118]. However, as he used a model as described in the beginning of this chapter with various approximations, e.g. neglecting quenching, such an outstanding performance must be doubted. The analysis

that follows goes beyond the possibilities of the simple description via the quasi static approximation and features an advantage of the Mie-model.

The power consumption in the stationary case can be formulated with a threshold-pump-rate and the corresponding inversion, using  $P = \hbar\omega \cdot N_1 \cdot \gamma_{th}$ , where  $P$  is the power that excites the  $N_1$  emitters in the ground state with the threshold pump-rate  $\gamma_{th}$ . No concrete excitation technique is examined, but the fundamental limit is of interest, i.e., a perfect efficiency for the excitation is assumed.

No general analytic minimum for  $P$  was found yet during this study, i.e., only trivial solutions were found for  $dP/d\gamma_p = 0$ . Presumably this is due to the fact that the minimum threshold-pump-rate per emitter is decreasing while the number of emitters in the gain medium is rising. However, so far it was found by numerical tests, that there is no smaller power consumption than for the case of the minimum inversion  $D_{min}$  and the corresponding threshold-pump-rate  $\gamma_{th}$ . Until no better analytic proof is found this is used as an estimate. The minimum power consumption finally reads

$$\begin{aligned} P_{min} &= \hbar\omega \cdot N_1 \cdot \gamma_{th} \\ &= \hbar\omega \cdot \frac{(N - D_{min})}{2} \cdot \gamma_t \cdot \frac{N + 3D_{min}}{N - D_{min}} \\ &\stackrel{N=D_{min}}{\Rightarrow} P_{min} = 2\hbar\omega \cdot \beta^{-1} \cdot \frac{\omega'}{Q} \end{aligned} \quad (5.17)$$

which is shown in Figure 58 as a function of frequency and lies in the range of micro- to milli-watts per spaser. These are very high values when compared to former predictions [100]. Especially, this is a significantly higher power consumption than that of state-of-the-art transistors in computer chips, thus the spaser cannot replace the transistor as a switch. A typical chip with three billion transistors exploiting spasers with gold-cores operating at 2 eV would consume about three MW of power.

Note, the concrete power consumption can be much larger when typical optical excitation schemes are used that will hardly reach 100% efficiency. This finding is in agreement with a recent paper by Khurgin and Sun [58,119]. They discuss, that pumping of the spaser via electrical injection in a diode-like configuration with a gold particle core would hardly be possible. They argue that fast recombination processes stemming from the altered local density of states in close proximity to the metal core (fast decay rates) would necessitate unrealistically high injection currents. They found this result even though they did ignore any quenching processes.

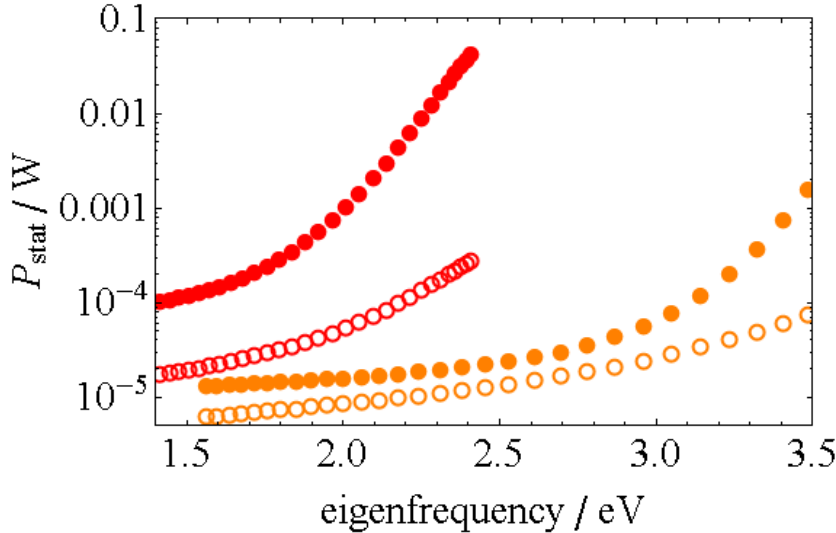


Figure 58: Power consumption of a *single* small core-shell spasers with an Au-core (red) or Ag-core (orange). Spasers with a 5 nm thick emitter-free spacing layer are plotted with empty circles. Even though spasers with a spacing layer need significantly higher gain-values (see Figure 57) they would consume less energy.

With the results for the minimum power consumption it is possible to estimate the heat production and the temperature of the metallic core. With Ruppin's framework [69] at hand it is straightforward to separate how much power is radiated by the gain medium from what is finally absorbed in the core. However, a good approximation is already, that the power is almost exclusively non-radiatively funneled into the core for the small spaser, that is considered here, as can be seen from Figure 49a (section 5.1.2). Thus, the power consumption can directly identified with a heating power. To model the core temperature, differential thermal diffusion equations are used as introduced by others [35,120]. These equations take into account the specific heat capacities, the densities and the thermal conductivities. In the stationary case the solution is independent of the heat capacities and densities and reads:

$$T(r, \omega) = T_0 - P(\omega) \frac{r^2}{6\kappa_p} + P(\omega) \frac{R^2}{3} \left( \frac{1}{\kappa_f} + \frac{1}{2\kappa_p} \right), r < R \quad , \quad (5.18)$$

$$T(r, \omega) = T_0 + P(\omega) \frac{R^3}{3\kappa_f r}, r \geq R$$

with the core-radius  $R$ , the Temperature of the surrounding  $T_0$ , the heat conductivities inside the core  $\kappa_p$  and outside  $\kappa_f$ , the radial position  $r$  and the heating power  $P(\omega)$  as computed before (Figure 58). Finally, a radial temperature profile can be plotted,

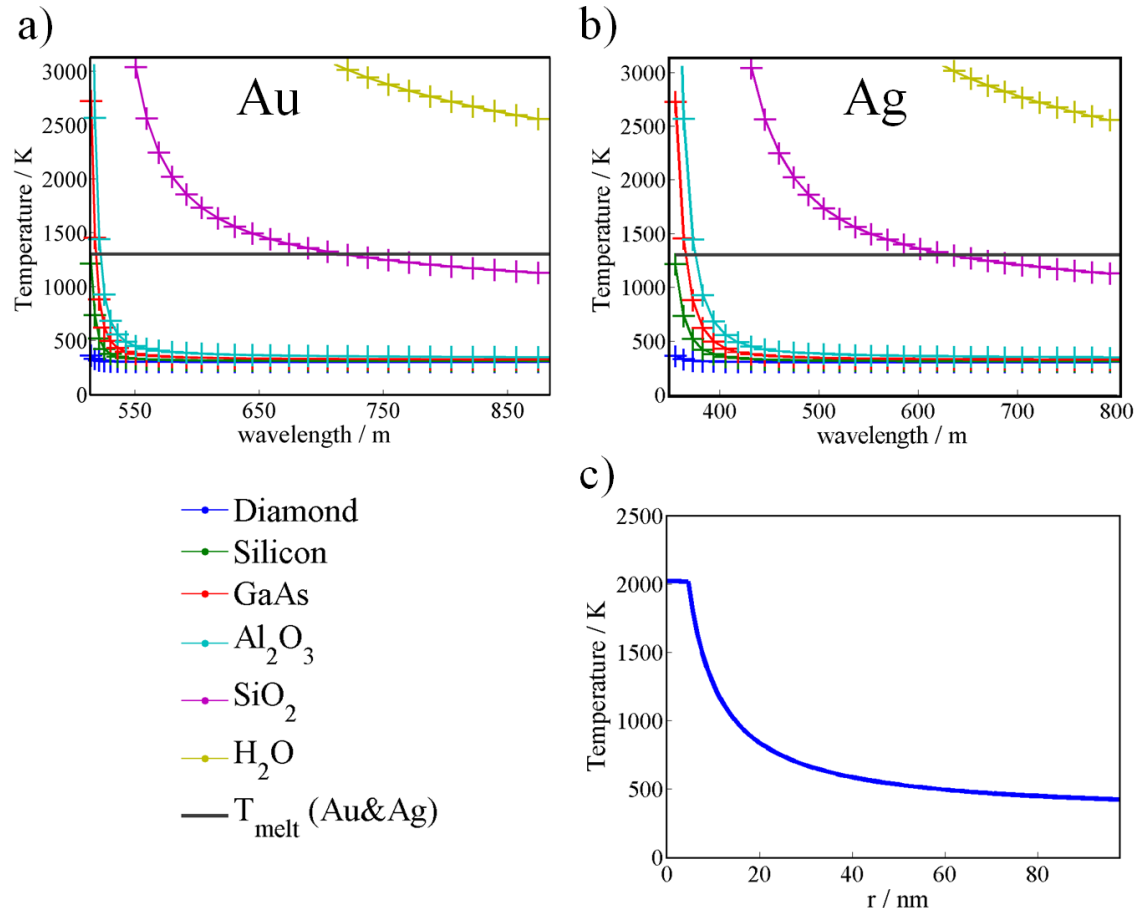


Figure 59: Temperature of spaser cores. a) Au cores in host media like listed in the legend. b) Results for Ag cores. Based on a thermal diffusion model the radial temperature profile can be computed. The maxima (at  $r=0\text{ nm}$ ) are the temperatures that are plotted in a) and b). The heating powers are the minimum powers required for spasing as plotted in Figure 58. The vertical lines in a) and b) mark the melting temperature of Au and Ag, respectively.

which heavily depends on the specific heat conductivity of the surrounding. The maximum Temperature, which is found in the center of the core, is plotted in Figure 59 for different outer materials. The fact, that each material would have a fix outer refractive index and thus determine the eigenfrequency etc. is ignored here to produce frequency dependent graphs. A horizontal line marks the melting temperature of the core which is actually reached for some of the host media, like ethanol or glass. Interestingly this is another severe limitation for the prime example of Noginov's spaser: in case of sufficient gain-medium, the spaser would have been melted.

To summarize this section, *minimal* conditions have been derived for the threshold pump rate and the power consumption. This was applied to small particle spasers ( $R=5\text{ nm}$  core). High power consumption was found ranging from milliwatts to tenth of

watts for *single* spasers which is significantly more than predicted so far (just a few quanta) [118]. Consequently, also the heat production in the core was analyzed with a thermal diffusion model. For some experimentally relevant host media with low heat conductivities like usual liquids (water, ethanol) or glassy materials, the core would melt.

It has to be noted again, that the estimations consider best-case scenarios: The spasers are running at low plasmon population numbers (just at the threshold) and a perfectly efficient excitation of the gain-medium. In a realistic experimental situation in which an optical excitation is used to pump the spasers the heating power would be significantly higher as the cores are efficient absorbers. Furthermore, high photon flux rates associated with high pump rates could reduce the quality factors of the metallic cavities [26]. This happens when the metal enters a kind of a transient regime, in which the electronic Fermi-distribution is significantly altered leading to losses by enhanced electron-electron scattering.

## 5.2 All-dielectric Nanocavities for Nanolasers

In the last section various results led to the conclusion that a particle-based spaser is of almost no practical use, as it is hard to provide the necessary gain and the power consumption is very high. The high loss rate of the cavity (poor Q-factor) and strong quenching are the main reasons. However, the Mie-model that was initially employed to handle spasers is actually capable of handling any core-material that can be described with a bulk dielectric permittivity. In Mie-theory no distinction between plasmons and other modes is made. From this it can be concluded, that there is no fundamental difference between a spaser and a nanolaser. Consequently, the core material can be replaced by any dielectric in the Mie-model.

Recent work discusses the use of silicon nanoparticles or nanostructures to enhance the coupling of light into solar cells [121] or for nanoantenna purposes in general [38]. Experimental results show, that particles as small as 100 nm up to 200 nm in diameter exhibit resonances all over the VIS with quality factors similar to plasmonic nanoparticles or higher. Therefore, such a small silicon nanoparticle can act as a nanoresonator for a nanolaser as well. The higher the refractive index of a dielectric resonator the smaller the resonator can be. Silicon benefits not only from its high refractive index but also from its low losses in the VIS, which stem from the indirect

bandgap (2.2.2). Another promising cavity material is gallium phosphide which also features a high refractive index but almost no losses beyond a wavelength of roughly 550 nm.

The eigenfrequencies and quality factors of Si and GaP nanospheres are studied in Figure 60 as a function of radius in comparison to gold and silver cavities. An obvious advantage is that high quality factors are preserved all over the VIS for the different modes, whereas the high-Q modes of the metallic counterparts condense around a fix frequency. As discussed before, this weakness of spherical metallic cavities can be lifted when the outer refractive index is tuned.

Doing the same for dielectric cavities unmasks their weakness, i.e., the quality factors are strongly reduced when the refractive of the outside increases. However, a realistic design of a dielectric nanolaser could be composed of a cylinder on a substrate with a thin gain-medium-capping surrounding the cavity. The main mode would only be slightly affected by the substrate and the thin gain-layer. Thus it is not artificial to study the input-output characteristic of spherical gain-coated GaP and Si cavities in vacuum/air.

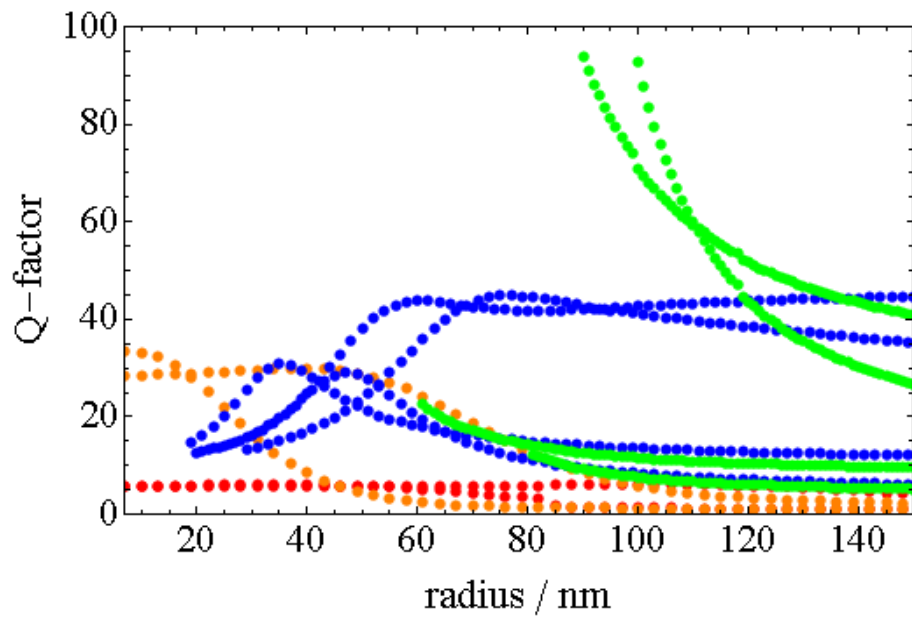


Figure 60: Quality factors of high index dielectric spheres (blue Si, green GaP) in comparison to plasmonic nanospheres (red Au, orange Ag). For Au and Ag the Q-factors for the dipolar (TM1) and quadrupolar (TM2) mode are shown, for the dielectrics, where also “magnetic” modes can exist, also TE1 and TE2 are plotted. The range of the curves in this plot are mainly limited by the region of trust for the analytic fits of the permittivities.

The results for the decay rates resonant to quadrupolar modes at 2 eV are shown in Figure 61 where indeed GaP exhibits a significantly improved  $\beta$ -factor compared to the other core materials. Consequently a GaP nanocavity based nanolaser could outperform the others with respect to the threshold. Also shown in Figure 61 are be Purcell-factors  $\Gamma$  which are much smaller for the dielectric spheres as the field is mainly localized inside the high index spheres. However, the effect on the laser performance might be counterbalanced by the higher Q-factors. The Purcell-factors for silver and gold are poor at 2 eV in air, as only poor Q-factor resonances are found at that frequency.

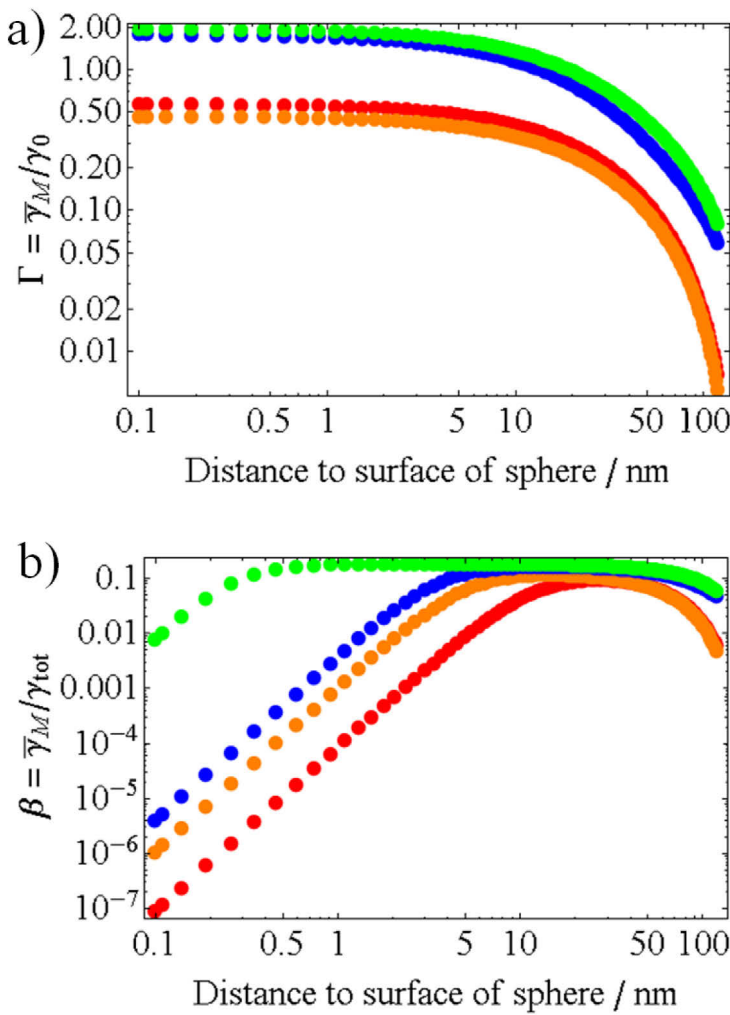


Figure 61: Comparison of the coupling of emitters to dielectric and metallic spheres, respectively. a) Purcell-factors  $\Gamma$  of quadrupolar TE modes in nanospheres of GaP (green), Si (blue), and quadrupolar TM modes in Au (red) and Ag (orange) with corresponding radii of  $R_{\text{GaP}} = 127 \text{ nm}$ ,  $R_{\text{Si}} = 110 \text{ nm}$ ,  $R_{\text{Au}} = 177 \text{ nm}$  and  $R_{\text{Ag}} = 176 \text{ nm}$ . b) Corresponding  $\beta$ -factors. All sphere sizes have been tuned to an eigenfrequency of 2 eV. As GaP exhibits almost no losses at this frequency, the  $\beta$ -factor is at its maximum ( $\beta_{\max} = 1/X = 1/5$ ) almost over the entire shell.

When plotting the corresponding input-output curves indeed the threshold of the GaP-based nanolaser is significantly reduced with respect to the other nanolasers (Figure 62).

Here it is worth to look at the time-dependent response as this has been a major selling point for spasers. As a matter of fact, the dielectric counterparts do represent the slightly quicker “switches”. Conclusively, dielectric nanocavities represent an alternative to spasers. They promise better performance at only slightly increased size, especially when considering the necessary gain-shell that would effectively double the size of the spaser (as in the example presented by Noginov et al.). The main problem of dielectric nanolasers is however the same as for spasers, the needed gain-factors are hard to reach. On the other hand there has to be a transition to a working laser when increasing the sphere’s size as lasing from dye-doped polystyrene or coated  $\text{SiO}_2$  micro-spheres has already been reported frequently [122–124]. Indeed, when going to higher order modes in GaP significantly higher Q-factors are found. For an  $R=180\text{ nm}$  sphere a Q-factor of 1116 is found for the TE4 mode at  $\lambda_{\text{res}}=565\text{ nm}$ . When coated with a 7 nm shell doped with 1000 emitters, which corresponds to a gain-factor of  $86\text{ cm}^{-1}$ , lasing is found (Figure 63). As this design is just on the edge of what is possible predicted by the idealizing conditions within the theory, presumably slightly larger spheres will actually be able to support lasing based on organic gain-media. Those lasers should then be rather called “sub-micron lasers” than nanolasers, as they are not smaller than the corresponding diffraction-limit in diameter.

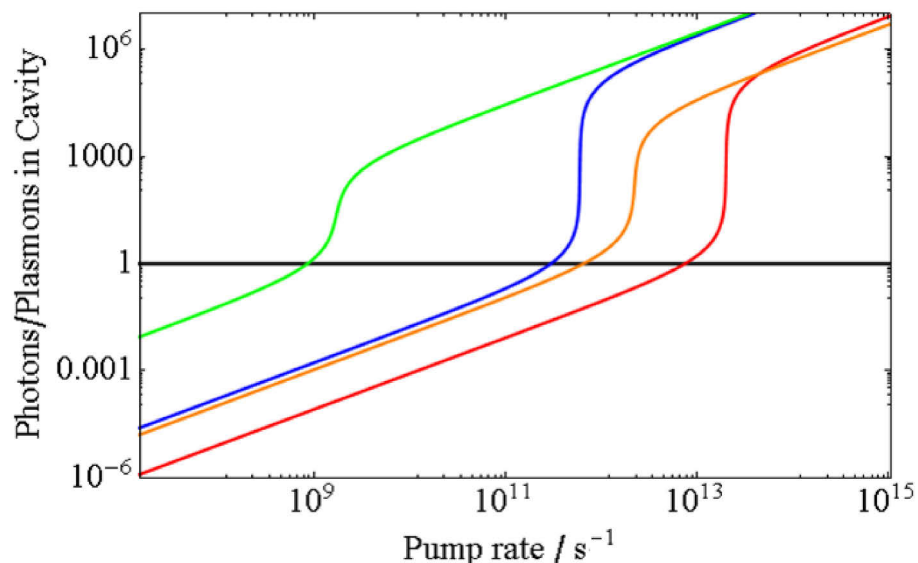


Figure 62: Input-output curves for nanolasers and spasers working at the quadrupolar resonance at 2 eV. Color code GaP (green), Si (blue), Au (red) and Ag (orange). As for the spaser (Figure 50), also here unrealistic high gain-factors are assumed.

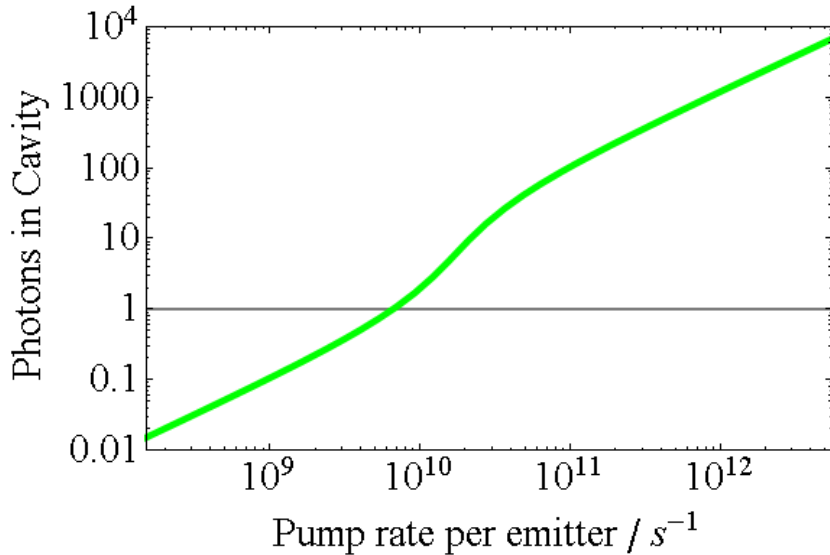


Figure 63: Input-output curve for an  $R=180\text{ nm}$  GaP nanosphere coated with a  $7\text{ nm}$  coating of 1000 emitters.

To achieve smaller lasers, thus better gain-media are necessary which are typically found in direct band-gap semiconductors that usually exhibit high refractive indexes themselves. This insight leads directly to the idea to use high gain-factor media like GaAs directly as nanoresonators – just like it has actually already been demonstrated for nanowires made of such materials [14–16] and recently also with very good performance from perovskite-based nanowires [125,126]. However, the description within the present model would be hardly of use, as the cavity material itself is changing both its real and imaginary part of the dielectric permittivity while the pump-rate is changed. Consequently the eigenfrequencies and recombination rates of electron hole-pairs would change at every pump-rate. Presumably the core would have to be described like a transient metal if the pump-wavelength would be far from the band-edge, leading to a broad electron distribution in the conduction band [27]. The Mie-model can only be used in its current state as long as it is a good approximation to assume that the cavity is not affected by the pump. In any case, from a principle point of view, it might be more interesting to keep cavity and gain-medium decoupled (to use a passive cavity), as the nanolaser could potentially be optimized towards low energy consumption, whereas a nanocavity with intrinsic gain has to be pumped at least so hard, that inversion is reached. A practicable design could consist of two thin ( $\sim 50\text{ nm}$ ), superimposable GaP disks on a chip of roughly  $250\text{ nm}$  diameter, that sandwiches a thin semiconductor gain-film, potentially as thin as a quantum well.

## 5.3 Refined Gain-Medium Description

### 5.3.1 Four-level Gain Medium

Usually a laser gain-medium is excited to energetic levels from where the charge carriers relax fast in a band or a multitude of closely lying energy levels (“intraband”) until they arrive at a certain level. From here the optical transition takes place that produces a further photon or plasmon. This underlying physical process is modeled quite accurately as long as the intraband relaxation (again modeled by rates) is much faster than the rate of the cavity related optical transition. This however is especially questioned for spasers, as the local density of states is huge in close proximity of the cavity, i.e., where the gain medium is located. Furthermore, the so-far applied 2-level gain-medium description is not accurate enough to foresee all important aspects of a nanolaser’s performance. Its main disadvantage is, i) that it can never saturate and ii) that it will always act as an absorber as depopulation from the ground state of the 2-level system is ignored.

Thus, here we examine the impact of a 4-level gain medium. As a consequence, a new set of rate-equations has to be solved, leading to modified equations for inversion and photon/plasmon number. An excitation rate that depopulates the ground state, pumps charge carriers to the uppermost level. However, now this excitation rate gives also rise to stimulated decay. Additionally decay of excited charge carriers via intraband transitions populates the cavity-associated upper level for lasing. After the optical transition another intraband relaxation brings the carriers back to the lowest level from where they might be re-excited. Relatively slow intraband transitions can lead to saturation or prevent lasing at all, if a hard pump is needed to keep pace with fast optical transitions. The underlying rate equations of the 4-level system are schematically depicted in Figure 64.

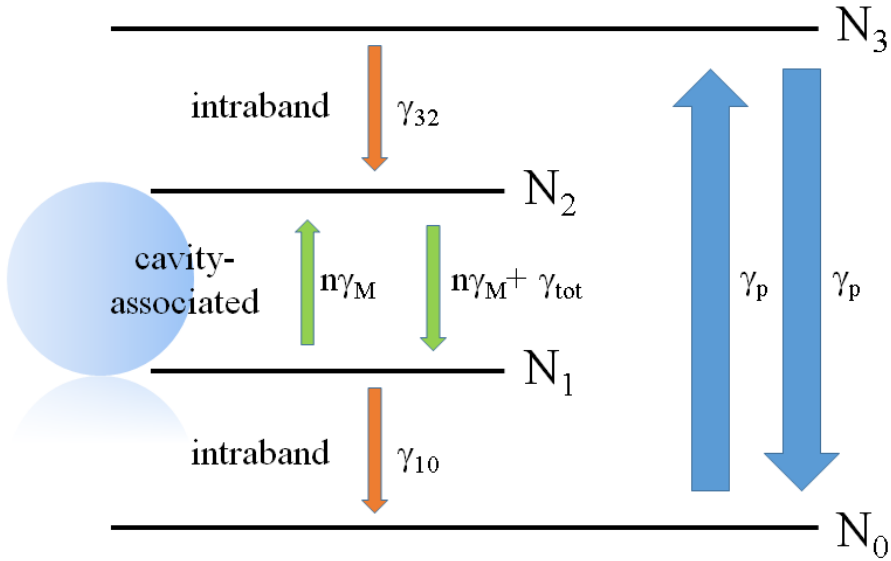


Figure 64: Scheme of the 4-level gain medium description. In contrast to a 2-level system the pump-rate  $\gamma_p$  can also lead to stimulated relaxation between the outer levels (lowest and the upmost level). The actual interaction with the cavity light-field takes place at the levels with the occupation numbers  $N_1$  and  $N_2$ . These levels are connected via intraband relaxation processes with the outer levels.

Input-output curves are shown in Figure 65 for the prime example of Noginov et al. [99] for some typical intraband relaxation rates of  $\gamma_{32} = \gamma_{10} = 10^{11} \text{ s}^{-1}$  ( $10^{13} \text{ s}^{-1}$ ) and, as before, an unrealistically high gain factor. The result is disenchanting, as even for this unrealistic gain-medium conditions the output (plasmon population number) saturates at a very low level of only 1-200 plasmons. For the spaser without emitter-free spacing layer no threshold occurs at all. This is due to the fast quenching processes and the poor cavity Q-factor: these loss channels inhibit an inversion of the gain-medium.

The two-level system was predicting a severe effect of the fast quenching of emitters close to the core due to reabsorption of plasmon (and subsequent quenching). As the carriers in this model would stay in the ground state until they eventually reabsorb a plasmon, the effect of quenching might be overestimated in this model. However, the four-level system shows only weak changes on the threshold behavior, in contrast, the spaser with emitter-free spacing layer is still performing better with respect to this point.

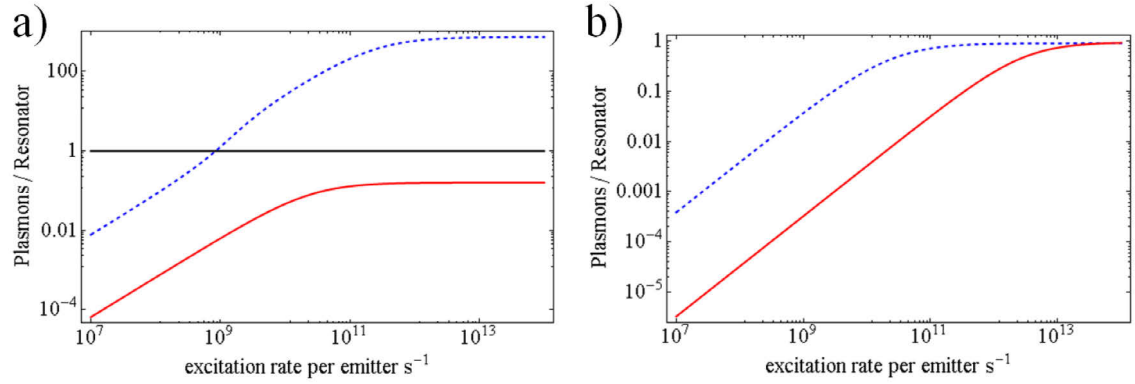


Figure 65: 4-level gain model applied on the configuration presented by Noginov et al. [99]. Red solid line marks the spaser without emitter-free spacing layer, the dashed blue curve shows the design with a spacing layer. a) Results for inter-band transition rates of  $\gamma_{32}=\gamma_{10}=1 \text{ ps}^{-1}$  and 27,000 emitters (gain-factor  $\sim 160,000 \text{ cm}^{-1}$ ), b) Results for  $\gamma_{32}=\gamma_{10}=10^{13} \text{ s}^{-1}$  and 2,700 emitters (gain-factor  $\sim 16,000 \text{ cm}^{-1}$ ). Even at this unrealistic high gain-factors almost no plasmons populate the cavity. Q-factor and quenching processes are so fast, that it is not possible to reach inversion for the spaser without spacing layer.

### 5.3.2 Non-constant Inversion

#### *Two-level system*

So far a constant inversion inside the gain medium was considered to simplify the rate-equations. Obviously the inversion will depend on the actual position with respect to the sphere, especially as there is a strong distance-dependent quenching. Thus, here the next more accurate gain-medium description is introduced in which the gain-hosting shell is subdivided into onion-like shells. In each sub-layer of the shell the inversion is assumed to be constant. The number of these shells can be adjusted at will without introducing long computation times. Each layer has an individual number of emitters  $N_i$ , a different  $\gamma_M$  and  $\gamma_t$ . In the stationary case one can write down an adjusted rate equation that can be solved numerically:

$$\frac{dn}{dt} = 0 = \sum_i \frac{(\gamma_p - \gamma_{i,t})N_i}{(\gamma_p + \gamma_{i,t} + 2\gamma_{i,M} n)} (n + \frac{1}{2}) + \frac{1}{2} \sum_i \gamma_{i,M} N_i - \frac{\omega'}{Q} n. \quad (5.19)$$

In the case of non-constant inversion the threshold condition now reads slightly more complicated (compare to equation (5.12)):

$$\sum_i D_i \gamma_{i,M} = \frac{\omega'}{Q}. \quad (5.20)$$

The left hand side can be understood as the sum of inversions of each layer that are weighted with the individual coupling rates. This sum will be denoted from here on as effective inversion  $D_{\text{eff}}$ . When dividing both sides by the averaged coupling rate of the whole shell  $\gamma_M$ , the result can be rewritten using equation (5.12):

$$\frac{\sum_i D_i \gamma_{i,M}}{\gamma_M} = \frac{\omega'}{Q \cdot \gamma_M} .$$

$$\Leftrightarrow \frac{D_{\text{eff}}}{D_{\text{min}}} \geq 1$$
(5.21)

Figure 66a shows the difference between the ordinary 2-level gain-medium with a constant inversion and the onion-like refinement in an input-output curve. The threshold-region in which the transition between non-spasing and spasing occurs becomes broader. This can be understood when investigating the inversion along the sub-shells as depicted in Figure 66b. Inversion is reached for outer regions of the gain-hosting shell for much smaller pump-rates as for the layers close to the cavity.

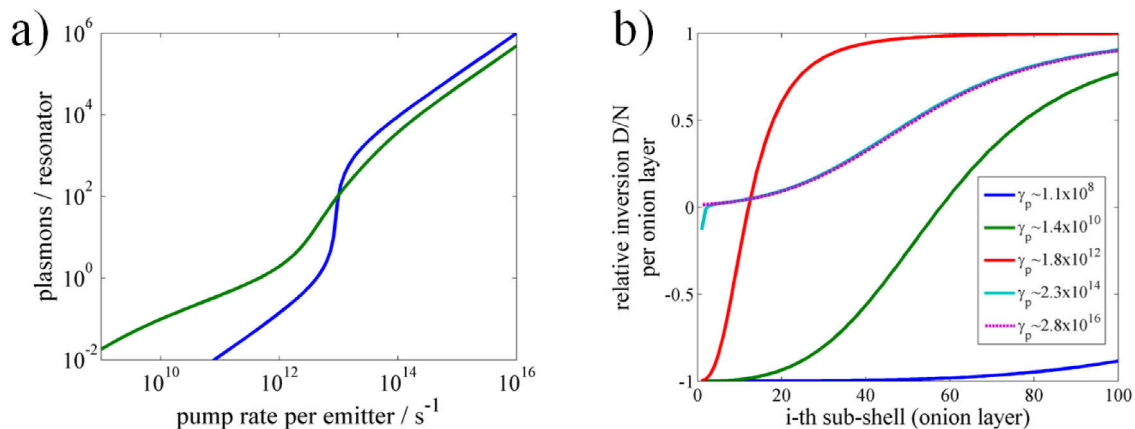


Figure 66: Comparison of a two-level rate-equation model with constant inversion to non-constant inversion (gain-shell subdivided into 100 layers) exemplarily shown for the design presented by Noginov et al. [99] but with 40,500 emitters (gain-factor of  $240,000 \text{ cm}^{-1}$ ). a) Input-output curves (blue: constant inversion, green: non-constant inversion). b) Inversion for 5 different pump-rates as a function of onion-layer. For pump-rates below threshold no inversion is established for regions close to the core: strong reabsorption prohibits the onset of spasing which leads to a high threshold.

*Four-level system*

Similar rate equations as for the two-level system with non-constant inversion can be also derived for a four level system. This represents the most accurate level of description for spherical nanolasers and spasers that has been derived during this thesis. As for the four-level system with constant inversion the results are again strongly influenced by the intraband relaxation times. Now it is more complicated to identify actual lasing systems. First, in contrast to the two level system saturation is found for both lasing and non-lasing systems. Secondly, the simple condition for the minimum inversion as for the model with constant inversion is lost. Thus, the ratio of  $D_{\text{eff}}/D_{\text{min}}$  (equation (5.21)) is used to identify lasing systems and plotted in Figure 67 and Figure 68 together with input-output curves and the relative inversion per layer in the shell. The latter reveals an interesting feature. Even though inversion is established already for lowest pump-rates in a four-level gain medium the minimum inversion to achieve lasing cannot be reached in many cases. For high pump rates the inversion is lost in gain-hosting layers close to the cavity. The relaxation due to optical transitions is faster than the intraband relaxation. For gain-layers close to the cavity this behavior is similar to a basin with a blocked drain where more water is entering than leaving.

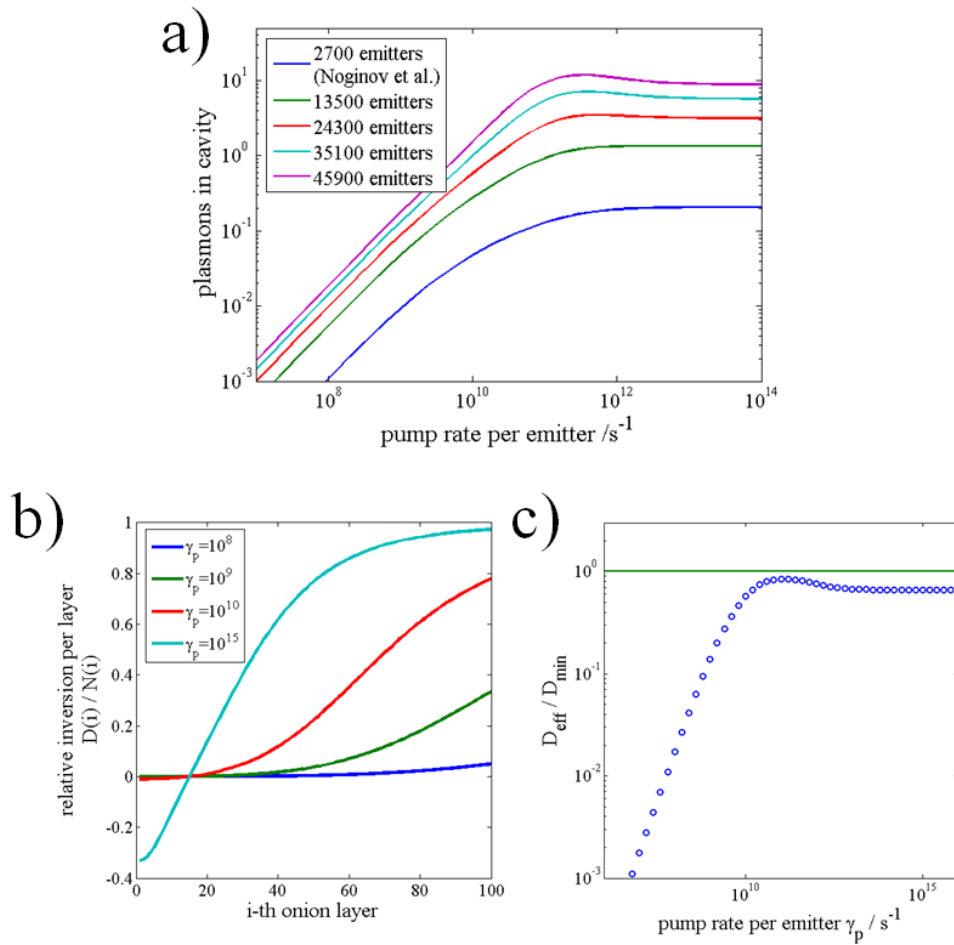


Figure 67: Spaser performance (Noginov design) within a 4-level model with non-constant inversion and intraband relaxation rates of  $1 \text{ ps}^{-1}$ . a) Input-output curves for various emitter numbers in the gain-hosting shell. Only few plasmons populate the cavity mode and a slight reduction with increasing pump power is found. b) Relative inversion as a function of gain-hosting layer for four different pump powers. Beyond a certain pump-power the inversion is lost for layers close to the cavity. c) Effective inversion normalized by the minimum inversion vs. pump power shows that lasing is never achieved.

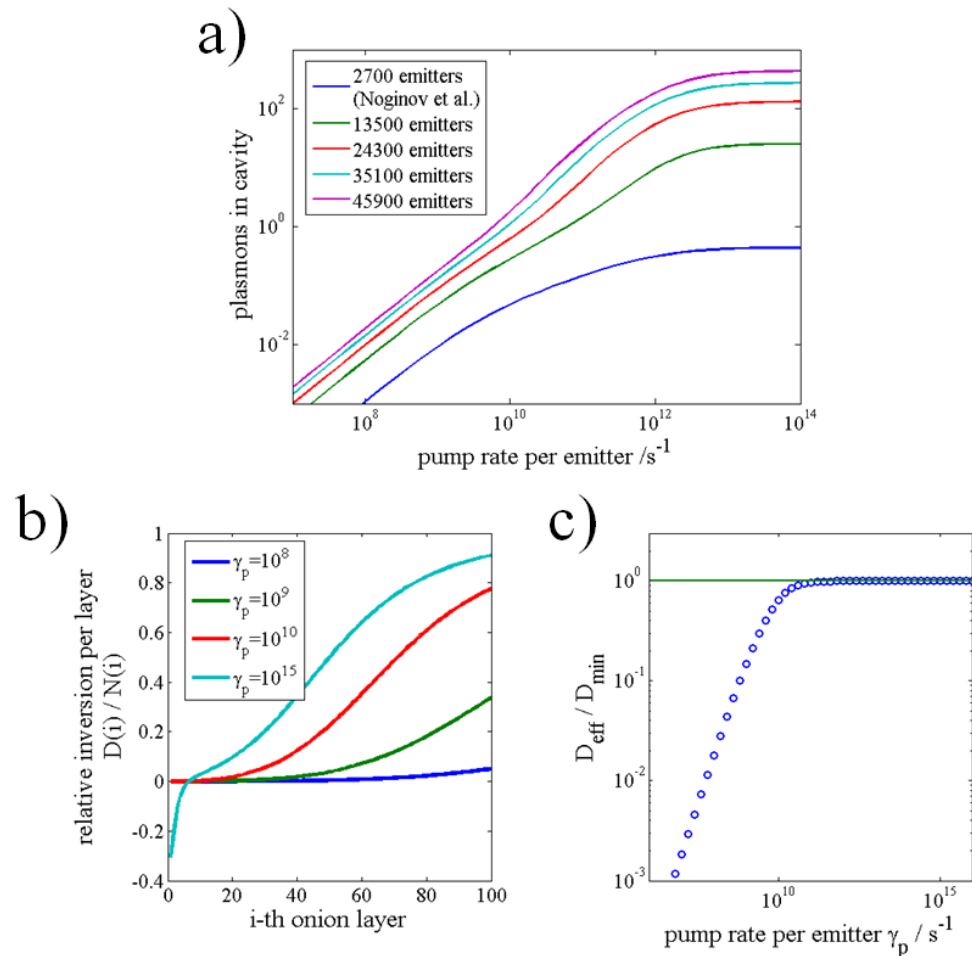


Figure 68: Spaser performance (Noginov design) within a 4-level model with non-constant inversion and intraband relaxation rates of  $10^{13} \text{ s}^{-1}$ . a) Input-output curves for various emitter numbers in the gain-hosting shell. For high gain-factors (many emitters) a few hundred plasmons populate the cavity mode when the population saturates. b) Relative inversion as a function of gain-hosting layer for four different pump powers. Beyond a certain pump-power the inversion is lost for layers close to the cavity. Compared to the case of slower intraband relaxation (Figure 67) the effect is less pronounced. c) Effective inversion normalized by the minimum inversion vs. pump power shows that lasing is achieved, i.e., the effective inversion converges to the minimum inversion.

## 5.4 Experiments on Nanoparticle based Resonators

In this section experiments on potential nanoparticle-based spasers are described that have been performed during this thesis. No laser-like signatures have been found for any sample type, when Ti:Sa lasers where used for pumping. Only towards the end of the thesis, when a Nd:Yag Laser system was employed, several samples, especially those featuring dye-doped films, produced signatures of lasing. It will be discussed why those signatures cannot be attributed to spasing.

### 5.4.1 Core-shell Particles

Most of the experiments on spasers during this thesis have been performed with chemically synthesized core-shell particles (see section 3.1.3), either suspended in ethanol or spincoated onto glass substrates. A setup like depicted in Figure 24 (section 3.2.1) was used utilizing a femtosecond pulse laser to pump the gain-medium. Besides samples that have been synthesized closely following the guide given in the paper by Noginov et al. [99], i.e., using OG488 as gain-medium, also samples with emitters further in the red have been investigated. Thus, two Ti-Sa Lasers with different emission ranges have been used in the experiments to be able to pump various emitters with high efficiency.

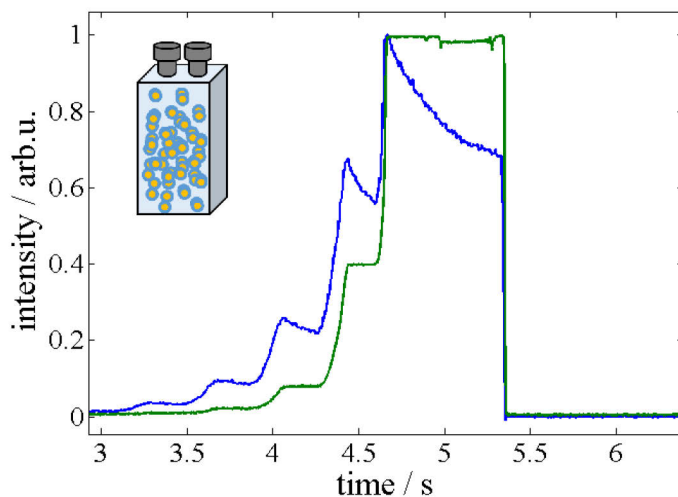


Figure 69: Laser (green) and fluorescence (blue) intensity. While the laser is increased in steps (controlled with a filter-wheel) the fluorescence follows this increase, however superimposed by a fast bleaching. Here core-shell particles suspended in solution in a cuvette are excited.

In these experiments it was searched for signatures of lasing: peaks emerging from the ordinary luminescence spectra, modified lifetime responses or non-linear increase of luminescence intensity with increasing pump power. To this end a photodiode illuminated with a part of the laser light that has passed through the beamsplitting optics right before the objective. The detected signal on the photodiode was thus always proportional to the actual pump-power at the sample. With this on-the-fly measurement of input and output power a high resolution for input-output curves is possible in contrast to what was shown elsewhere [99,115]. However, no data indicating a non-linear or lasing behavior was found, no matter whether the cores have been rods or spheres, no matter which laser dye has been used. Figure 69 shows luminescence intensity recorded in parallel with the pump laser intensity: The pump can be continuously increased with a filter-wheel, but was here for demonstrational reasons moved in steps. Thus, the pump intensity reaches steps and the luminescence follows this intensity, together with an exponential decrease due to bleaching of the organic gain medium. This fast bleaching was mainly observed for spincoated samples but also in weaker form for particles suspended in ethanol where a steady exchange of particles in the laser focus is expected. The fast bleaching is obviously induced by the intensive pump pulses of high repetition rate of around 80 MHz of the Ti:Sa laser which makes it difficult to study these systems, especially on a single particle level.

Experiments on individual particles have been performed next to ensemble measurements even though they are more complicated. The luminescence spectra in suspension could be in principle dominated by residual individual organic emitters in solution that were not removed after synthesis. This background could potentially obscure spasing signatures.

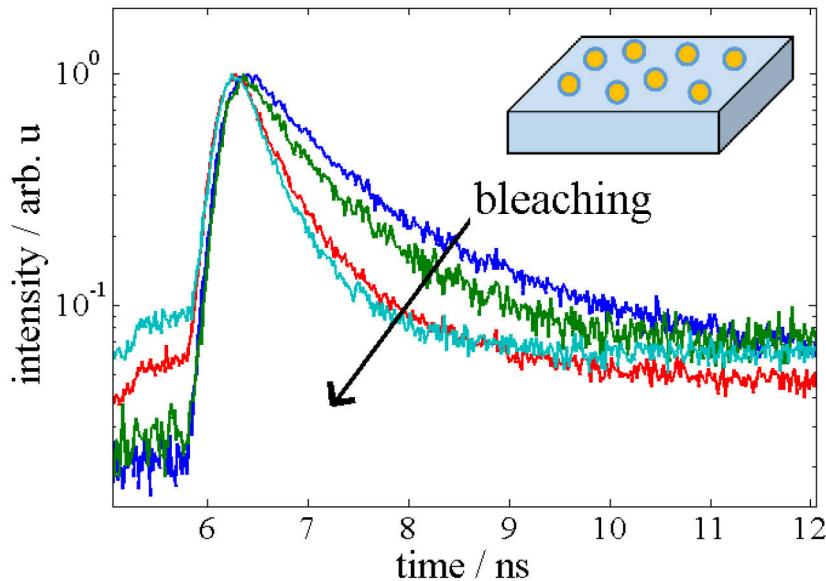


Figure 70: A series of lifetime measurements on a single core-shell particle. Reduction upon bleaching (indicated by the arrow) is observed. Core-shell particles are spincoated on a glass coverslide.

Figure 70 shows a series of lifetime measurements on an individual particle addressed by confocal microscopy. Each measurement corresponds to a different degree of bleaching and shows, that the lifetime is reduced during this process. One may conclude from this data that long living emitters are those with shorter luminescence lifetimes (faster decay rates). Thus this result could be regarded as a proof for an actual coupling between the emitters in the shell and the core. However, it cannot be excluded that a significant amount of luminescence stems from gold photoluminescence which is known to exhibit an extremely fast decay rate. In any case, various clearer studies on photo-physics of organic emitters in combination with plasmonics can already be found in literature [127].

As a potential problem of the setup used here (Figure 24, section 3.2.1), the high repetition rate of the Ti:Sa lasers was identified. As this excitation lead to fast bleaching, which could in principle destroy a potentially working spaser it was considered to switch to a pump laser with significantly reduced repetition rate. Further, it was suspected, that the gain-medium could be trapped inside an intermediate dark state when the next pump pulse arrives.

Thus, within a different setup a Nd:Yag laser with only 10Hz was used in the setup (shown in Figure 25, section 3.2.1). For detection only a spectrograph was available at that time. To increase the signal-to-noise ratio the spectrograph was triggered by the

laser. Measured spectra from dispersed particles in ethanol revealed only ordinary luminescence. Spincoated particles showed only a very weak luminescence becoming apparent on the background. However, when the pump power was increased, a sharp peak appeared slightly red shifted to the luminescence spectrum (Figure 71).

This behavior is similar to what was reported in earlier work [99] (see also Figure 52 in section 5.1.2) and as it is expected for a gain-medium in which absorption- and emission band overlap and thus the maximum of maximum net gain is red shifted to the peak of the emission band. In order to improve the detection efficiency the air objective was replaced by an oil immersion objective. The sharp peak was found to be significantly increased afterwards. However, in a reference measurement with a fresh and clean glass substrate the same peak appeared although no core-shell particles were present.

This finding lead to the conclusion, that the pump intensity reached values where ionization of the  $\text{SiO}_2$  substrate takes place, leaving a plasma of silicon and oxygen ions. During recombination of electrons with such ions a characteristic luminescence is produced with peaks that correspond to the elements found in the ionized material.

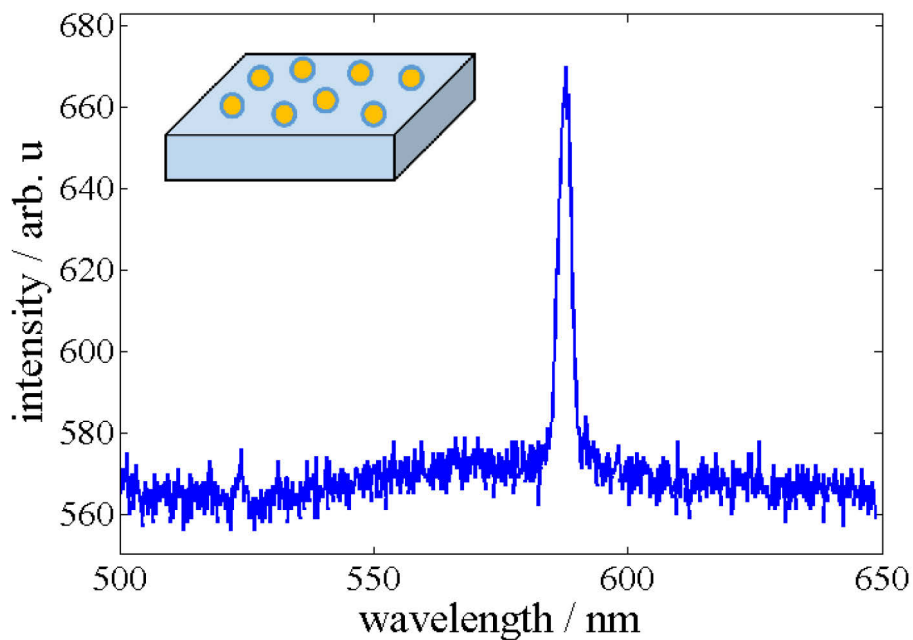


Figure 71: PL spectrum from spincoated core-shell particles on glass excited through a high NA objective. A laser-like peak emerged from a poor signal-to-noise signal (background) very similar to what has been presented by Noginov et al. [99] (compare with Figure 52 section 5.1.2). Reference samples free of core-shell particles showed the same signals. It can be concluded, that the peak is no signature of spasing but presumably from ablation of the glass substrate.

Concluding, this experiment was not detecting signatures of spasing but mimicking a technique called laser-induced breakdown spectroscopy (LIBS) [128].

### 5.4.2 Dye-film Coated Nanoparticles

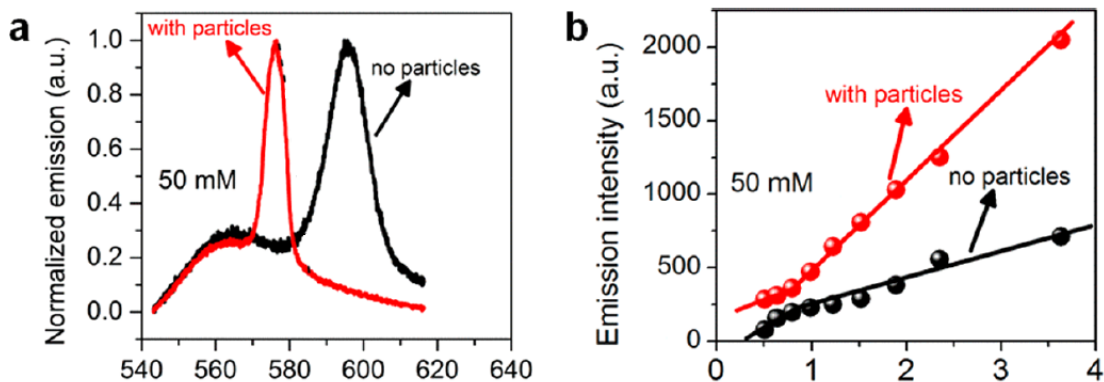


Figure 72: Measurements taken by Meng et al., figure adapted from [115]. a) Spectra of samples with and without particles. b) Peak heights of the spectra as a function of pump power. The peaks stemming from samples with particles are interpreted as signatures of spasing while peaks from samples without particles are interpreted as ASE features.

During the project a paper about nanoparticle based spasing was published by Meng et al. [115] using a drastically simplified fabrication. Here the plasmonic cavities simply were spincoated onto a glass substrate and then coated with a PVA-film doped with different laser dyes of various concentration. Modifications from the usual spectra - basically broad peaks of various heights - were found and attributed to amplified spontaneous emission (ASE) for bare films and to spasing when plasmonic particles were embedded. For an easier comparison with the results observed here, measurements taken by Meng et al. [115] are shown in Figure 72.

Similar samples were fabricated during this thesis following the paper by Meng et al. [115] and similar results have been found, however the conclusion is different.

Fabrication of the samples was performed in-line with Ref. [115]. It was found, that the spectra depend sensitively on the position on the sample and also on the PVA-film thickness. This effect has been at least as strong as any effect due to the incorporation of metal particles. The samples with strong spatial-depended features were found to be contaminated with what looks like small crystals or inclusions (Figure 73).

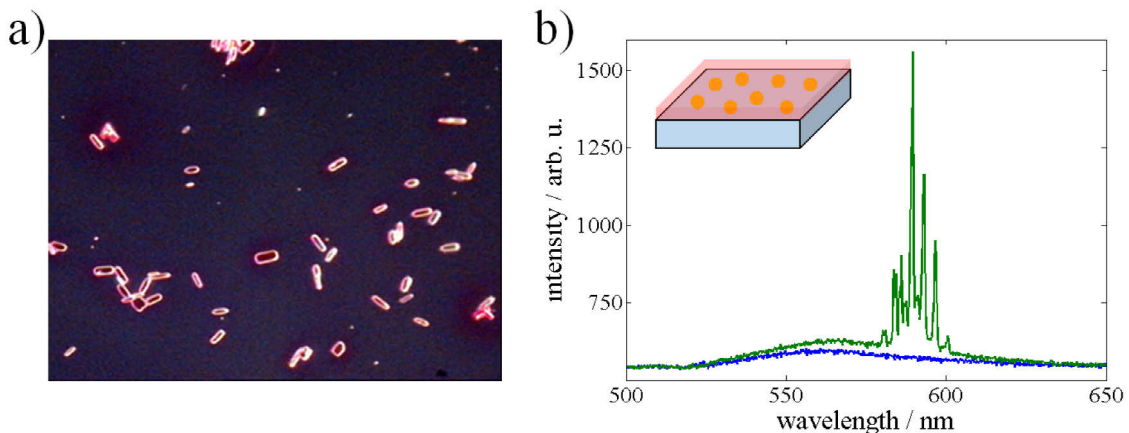


Figure 73: Random lasing in dye-doped PVA films. a) Microscope image of a dye-doped PVA-film. Inclusions are very likely to appear at high dye concentrations. b) Typical random lasing signatures are observed when structures with inclusions are pumped optically. Blue line shows ordinary PL from the dyes, the green line shows sharp spectral features.

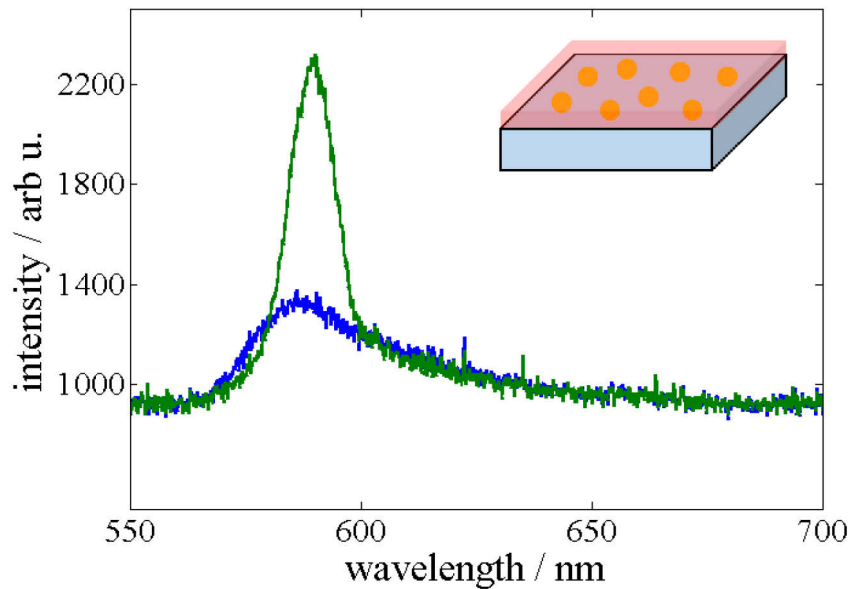


Figure 74: Plasmonic particles spin-coated onto glass and coated with a dye-doped PVA film. For high pump powers ASE-effects (green line) appear. The blue line shows ordinary PL for comparison. The peak position depends sensitively on film-thickness, state of bleaching, and inclusions.

Some of these samples showed clear features of random-lasing, i.e., various sharp peaks, which varied in time or which were extremely sensitive on the position of the pumping laser spot. It must be concluded, that the inclusion acted as small (several micrometer sized) resonators. The number of inclusions could be reduced up to

complete avoidance by either reducing the amount of laser dyes in the PVA host or by slightly increasing the PVA temperature for some minutes before spin-coating.

The now inclusion-free samples showed ASE peaks similar to those found in Ref. [115] that were sensitive to the film thickness (Figure 74). Especially the ASE peaks disappeared for relatively thin films. Not only the appearance but also the peak position acted sensitive on the film thickness no matter whether particles have been embedded or not.

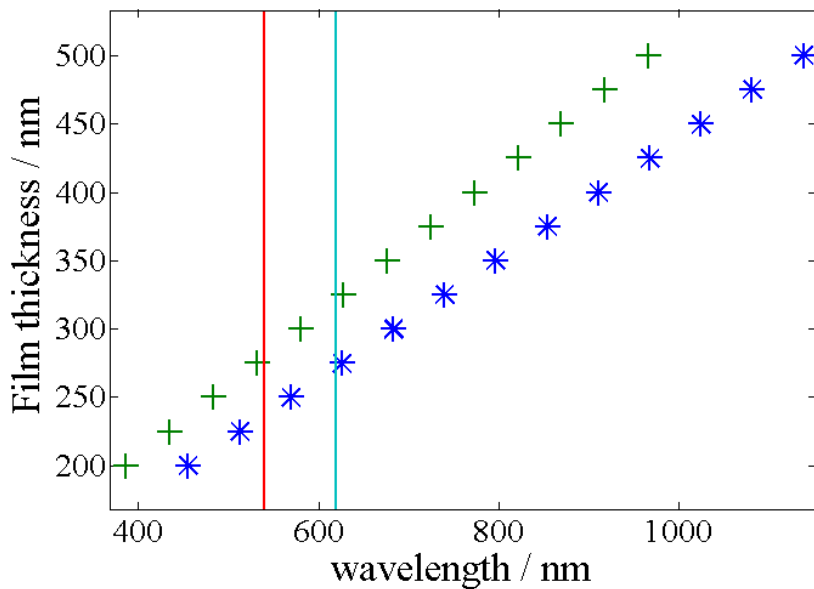


Figure 75: Cut-off for guided modes in slab-waveguides (films). When the film thickness is reduced the cut-off is found for shorter wavelength. Meng et al. [115] reported about Rhodamin-doped films of 200 nm thickness. The emission band of Rhodamin, is indicated by the two vertical lines. Even above cut-off for purely guided modes, leaky modes can lead to ASE features.

Meng et al. used gold nanorods with a short axis of around 20 nm and a porous silica shell of roughly 10 nm, thus the flatly lying rods have a height of 40 nm [115]. The dye-doped PVA films had a thickness of 200 nm according to the paper. Therefore, it is likely that the PVA film was way thicker than the particles height, even though it was not described how this thickness was determined. Especially, almost all dyes in the PVA film were out of reach of the rods near-field. In principle this is not desired, as those emitters will lead to a strong background of ordinary luminescence which overlaps and masks potentially interesting spectral effects.

These considerations and the experimental findings in this thesis, lead to the conclusion, that none of the observed broad peaks can be “unambiguously attributed” with spasing, in contrast all of them represent ordinary ASE peaks. The excitation of ASE effects in dye-doped films is a common way to study organic gain media, basically to study their gain-factor and other details [53]. The method explicitly exploits the effect of waveguiding in a dye-doped film. Just like in ASE experiments Meng et al. pumped a relatively large area (spot of 1.6 mm diameter). In Figure 75 the cut-off free-space-wavelength for the first two purely guided modes in an asymmetric slab-waveguide are plotted, like in the work by Meng et al. with  $n_{\text{Air}}=1$ ,  $n_{\text{PVA}}=1.52$  and  $n_{\text{SiO}_2}=1.46$  for a series of waveguide thicknesses. A film thickness of 200 nm is too thin to guide the emission of the used dyes. However, also leaky modes can travel along the film and lead to ASE effects – obviously they do, as they have been observed by the authors from the top side even without embedded particles [115]. However, when particles are embedded in the film, they will surely affect the guiding properties of the leaky modes, e.g., the waveguide may appear effectively thinner. Whatever, the ASE peak position can be explained by simple modification of the guiding properties. To put it clearly, it is much more likely to be a waveguiding effect than a signature of spasing because the same effects were found during this thesis at samples without particles when the film thickness was modified.

## 5.5 Studies on Waveguide-like Resonators

The spasers discussed so far in this thesis have been solely utilizing organic gain media and have been based on fully nanoscopic particle cavities, i.e., in these spasers one tries to populate a *localized* plasmon mode. Another approach, which has been much more successful (at least in terms of number of publications in press) is to exploit a Fabry-Pérot-like resonator that uses propagating plasmons that are confined in a small structure by total-internal reflection [129–134]. The simplest version of such a spaser is a (luminescent) semiconductor nanowire on a metallic film, separated by a small gap. The nanowire is not only defining the waveguide-like mode but is also the gain-medium.

This approach has some advantages over the fully nanoscopic version, foremost more gain-medium can be incorporated due to the softened degree of localization. This relaxes the high requirements on the gain-factor (or inversion density). The design of the cavity requires a thin (low index) dielectric film to separate wire and metallic film.

Note, that this separating layer was initially introduced to improve the propagating properties of the waveguide [135]. It “accidentally” also acts as a natural emitter-free spacing layer, that limits associated quenching and unwanted threshold boosting effects. The gain-factors of semiconductors are usually significantly higher than that of organic media and they do not bleach. However, the utilization of organic gain-media would represent a significant progress, as this would expand the flexibility of lasers, especially on their wavelength tunability.

In principle the fabrication of a spaser based on a passive waveguide (without intrinsic gain) should be easy, as the waveguide supports a huge bandwidth of propagating modes. Thus, no complicated alignment is needed to make the resonances overlap with the emission spectrum of the gain. Lastly, nanowire cavities will allow easier interpretation of experimental results, as they can be identified by bare eye with a usual light microscope. Especially it can be decided whether the surrounding area features additional particles or agglomerates that might give rise to spectral features that could interfere with the desired examination.

Thus, a nanowire cavity design was targeted that allows the use of organic gain-medium. Literature already provides studies on attractive cavity designs, where the gain-medium was sandwiched in-between a silver film and a silver nanowire or a silver film and a ZnO nanowire [136,137]. Both studies did not observe lasing, potentially because the separating layer was doped with emitters, i.e., no emitter-free spacing layer was apparent between silver and the gain-medium. However, a very interesting feature was reported in one of the studies, which is a Fabry-Pérot-like modulation of the fluorescence. In contrast to core-shell particles, where there are no unambiguous signatures known that may act as a quality criteria for well-synthesized core-shell particle – either it is lasing or not - nanowire-based spasers could be checked and optimized by detection and further strengthening of Fabry-Pérot-like modulations of the luminescence.

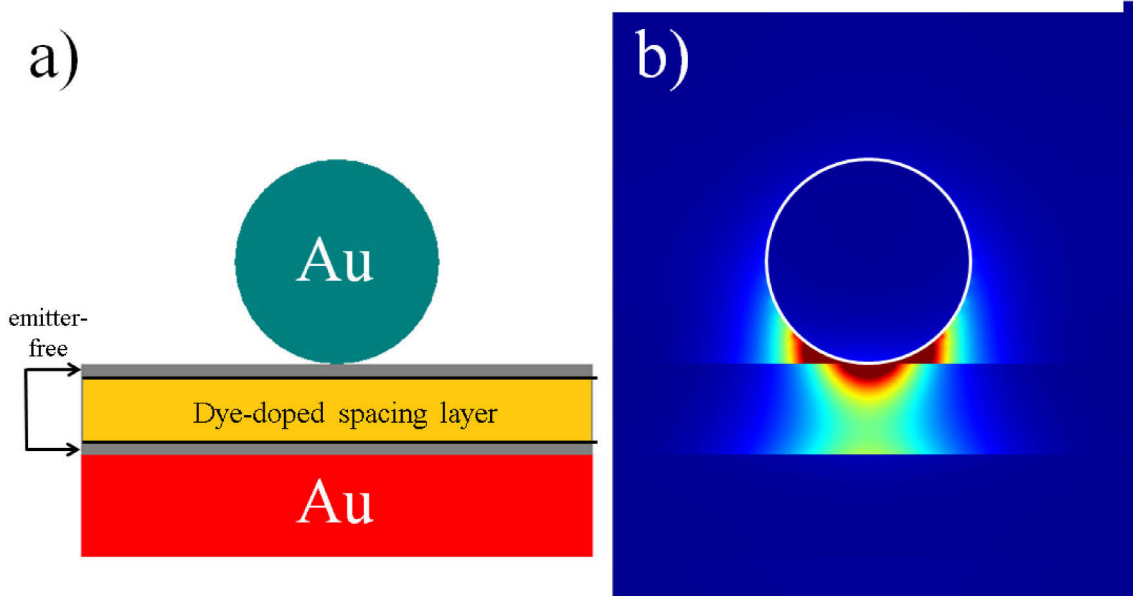


Figure 76: Spaser design based on a nanowire-film waveguide. a) Scheme of the cross section: three layers separate an Au film and nanowire. The central layer hosts the gain medium. b) Intensity of the guided mode. Diameter and gap thickness have to be designed such, that a significant amount of flux is guided inside of the gap and that propagation losses are small.

As mentioned the cavity design in Ref. [137] has been adapted. The cavity is based on a gap mode between metal film and a finite metal nanowire where the end facets act as mirrors. Just like for the core-shell spasers, emitter-free spacing layers are needed to reduce the threshold. Thus, a cross-section of the cavity looks like depicted in Figure 76: a metallic film is capped with three thin layers and finally with the nanowire. The inner of the three layers is doped with emitters, the outer ones are emitter-free. The metal of choice is gold as it does not suffer from oxidation.

#### *Numerical Optimization via FEM*

The cavity design is a trade-off between desired effects and unwanted side-effects. A high field confinement in the gain-hosting gap is preferred to achieve a good coupling of the cavity mode with the gain-medium. This confinement increases with reduction of gap width. However, at the same time the mean propagation length of the guided plasmon is reduced. Also, increased confinement reduces the volume of the gap with gain-medium, thereby boosting the gain-factor requirements.

Most of the cavity design can be done with relatively simple and especially fast propagating mode simulations. Thereby the plasmon damping can be calculated and the actual field distributions can be analyzed with respect to their overlap with the gain medium. As described earlier the emitter-to-waveguide coupling can be estimated just like in chapter 4.2.1. In fact on top of this the cavity related Purcell effect of suppressed and increased decay rate (following the standing wave pattern in the Fabry-Pérot cavity) will add up. However, the propagating mode solution will yield results that are close to the average of decay rates. Also most easily, different working frequencies and different nanowire diameters can be tested. A full description of the actual Purcell effect could be performed by implementation of the method reported by Sauvan et al. [23]. Figure 77 shows the real part of the effective refractive index  $n_{\text{eff}}$  (proportional to the plasmon momentum) and the decay length  $L$  to  $1/e$  of the initial power ( $L = \lambda / 4\pi \text{Im}(n_{\text{eff}})$ ) as a function of gap thickness for different frequencies (or vacuum wavelength  $\lambda_0$ ). Again, a negative effect of gold's intraband transition around 530 nm can be seen, here on the decay-length. Figure 78 shows the Purcell-factor of the waveguide mode as a function of emitter position in the x-y-plane.

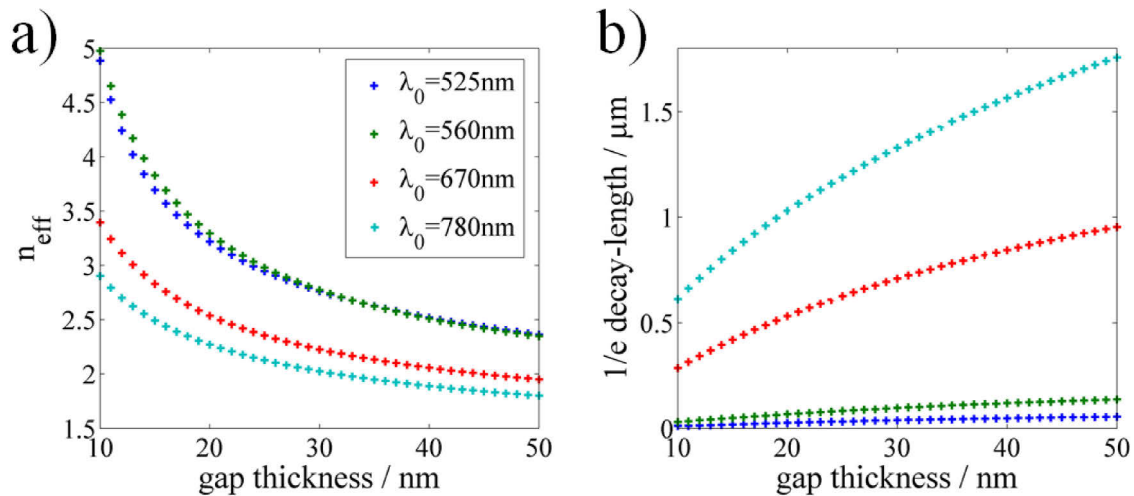


Figure 77: Effective refractive index  $n_{\text{eff}}$  and corresponding decay length of guided modes as a function of gap width in a nanowire-gap-film configuration as shown in Figure 76.

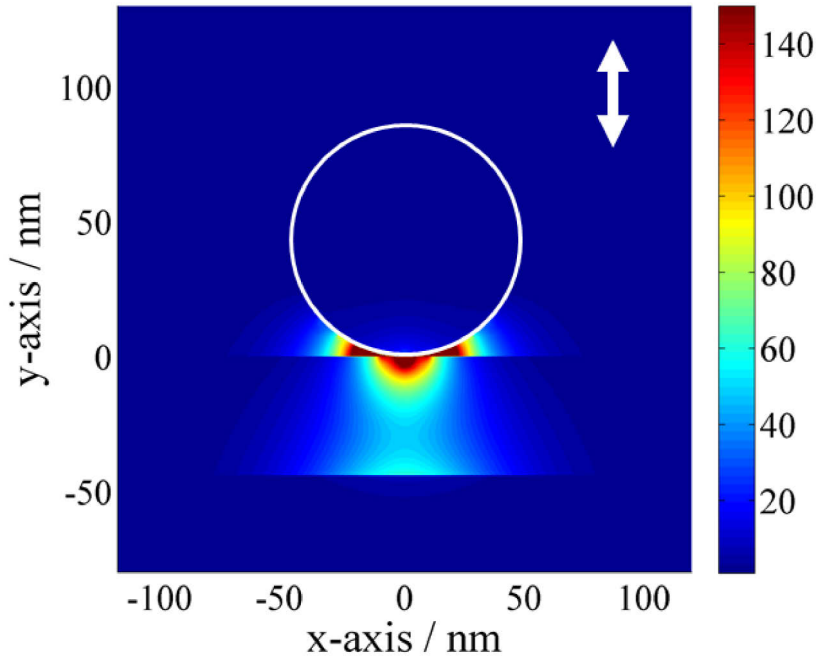


Figure 78: Purcell-effect  $\Gamma$  for the waveguide mode shown in Figure 76 as a function of emitter position in the x-y-plane for dipole emitters oriented along the y-axis at a vacuum-wavelength of 560 nm. Coupling to other dipole-orientations is significantly weaker.

Based on these simulations and on results from spin-coating (see next section), it was decided to start the work on this spaser concept with a 40 nm wide gap consisting of a 30 nm Rhodamin-doped gain medium and two 5 nm emitter-free spacing layers.

#### *Sample Fabrication and Experimental Results*

A simple production procedure was established to produce the waveguide-based spaser geometry that basically comes down to spin-coating and a few simple quality check measurements. The starting point is an ultra-flat gold film that is a commercial product (Figure 79). The gold film is deposited on a silicon wafer. Square inch glass slides are glued to the back-side of the gold film. Stripping of these glass slides leaves the thin gold film on the glass slide and the silicon wafer with a squared hole in the gold film. The now exposed gold film that was so far attached to the waver is ultra-flat and pristine: clean just like a freshly cleaved crystal. Now PMMA, PVA doped with organic laser dyes and PMMA again is spin-coated onto the gold. In between the spin-coating steps the sample quality can be checked with an optical microscope and the thickness via ellipsometry. To this end the identical spin-coating is performed on small silicon wafer pieces and then measured via ellipsometry. The main reason to do this with a

reference sample, is the stability of the fitting routine used by ellipsometry, which was found to be more unstable for the gold films as they are very thin ( $\sim 100\text{ nm}$ ) and light is partly transmitted and reflected by the sample's backside in contrast to the ordinary wafer substrates. This line of action is based on the assumption that only small differences in film thickness may originate from the differing substrates but are mainly dominated by rotation speed and viscosity of the spincoated polymer [138]. Further, it allows optimization of spincoating and solvent preparation solely with cheap silicon wafer samples.

The spincoating of different polymers (PMMA, PVA and PMMA again) was found to work out well in contrast to other combinations, where the first or second film was resolved (which is easy to detect in a microscope due to the coloring by laser dyes). This is attributed to the different solvents, which are ethanol in the case of PMMA and water in the case of PVA. Nevertheless, it cannot be excluded, that a slight mixing of the polymers takes place at the interfaces. Thus, some of the emitters might penetrate the spacing layers. The first attempt to construct the nanowire-based samples was to produce the gap via layer-by-layer deposition which should be very accurate in principle [139]. For some unknown reason the results were not satisfying as presumably already the first layer did not attach to the gold.

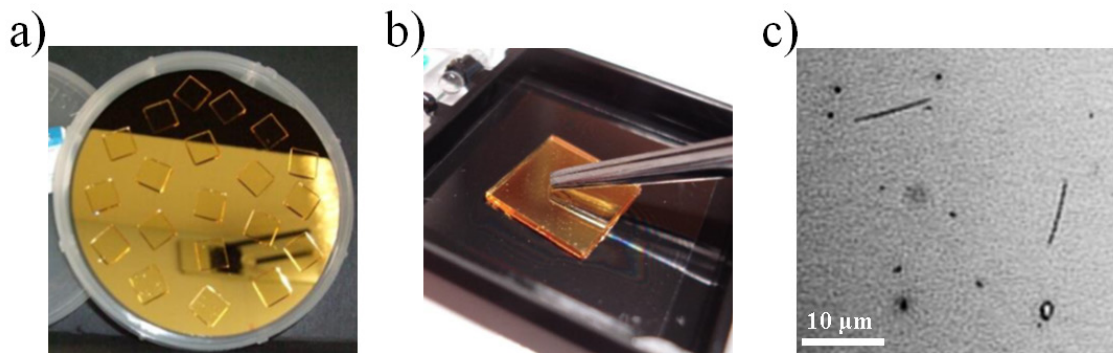


Figure 79: Sample preparation of nanowire-film cavities. Commercial Au films and Au nanowires are used. a) Silicon wafer chip coated with an Au film, glass slides are glued to the back-side of the Au-film. After stripping off the glass-slides a pristine, and atomically flat Au-surface is available. b) Contact-printing of spin-coated nanowires on glass onto a polymer coated Au-film with a tweezer. c) Microscope image of the final sample. Individual nanowires and potential contaminations can be easily identified.

In a last step the nanowires are deposited onto the layered films. Spincoating lead to a dissolving of the layers due to the specific solvent that are stabilizing the nanowires and keeping them from agglomerating. Thus the nanowires were spincoated onto an ordinary glass sample and then deposited onto the layers via contact printing as shown in Figure 79.

Only few experimental results have been acquired during the time of writing this thesis on this concept. It was found that the nanowires can be visualized by indirect illumination (dark field microscopy) very well. Thus, nanowires free of neighboring contaminations can be preselected and addressed with the pump beam quite conveniently. To pump the complete, several microns long nanowire-cavity, a collimated or weakly focused laser beam was guided to the sample from the side and the objective of the microscope object was solely used to collect luminescence. This way of excitation was also chosen, to gain a good signal to noise ratio by guiding the light directly into a spectrometer to avoid any losses by avoidable elements like beamsplitters. Essentially, this is necessary as a low repetition rate is used to avoid fast bleaching just as for the experiments on particle based lasing. In the first samples, the amount of gain medium has been too low. No signature of lasing was found but the sample was burned and a hole was left in the gold film.

Conclusively higher emitter concentrations must be used. Also emitters that emit as far as possible in the red are preferred. Probably the 532 nm laser could also pump gain media far in the red as it has been reported quite recently in random lasing experiments [140]. An even simpler sample could solve some of the difficulties that have already emerged regarding the gold nanowire cavities, i.e., the use of purely dielectric constituents. Just as for the all-dielectric nanolasers discussed earlier, these samples would not need an emitter-free spacing layer, thus allowing for more gain-medium in the gap. Further, they would not suffer so much from heating like gold, due to suppressed absorption. A corresponding cavity would consist of a high index nanowire on a low index gap and a high(er) index substrate, e.g., a silicon nanowire on ZnO with a thin PVA gap, similar to what has been reported recently [141].

## 5.6 Conclusion and Outlook

### *Fully Nanoscopic Lasers*

In this chapter a theoretical model for particle-based spasers and dielectric nanolasers has been discussed as well as experiments on core-shell particles. Both theory and experiment heavily support the following conclusions on fully-nanoscopic spasers:

- They are extremely hard to realize due to their extreme gain-media requirements,
- they have yet not been demonstrated, i.e., publications in press have misinterpreted experimental findings for spasing, and
- they would feature a very high energy consumption and heat production, if ever realized.

A main feature of the theoretical model presented in this chapter, which is completely based on Mie-theory and thus analytic, is the direct derivation of decay rates of the gain-medium without the need of dubious approximations. Specifically, the decay can be decomposed into all the channels into which the energy emitted by the gain-medium is flowing. Thereby it is revealed, that the  $\beta$ -factor of the gain-medium would be extremely poor due to quenching and consequently the laser threshold would be very large. Also it was shown here, that the energy consumption is very high for such a small laser and consequently the heat production is significant which can even lead to melting of the system in some cases. Even though this conclusion could be obvious, as strong quenching is a well-known effect in plasmonics, it seems like that this hits the heart of a wide spread misunderstanding and might be the underlying source for the differences to former spaser models. This is, that the quenching is mainly or solely attributed to coupling to the resonant cavity mode, especially for small particles that are well-suited to be described within the quasi static approximation. As it was discussed in this thesis and shown by several others before [68], this is not the case: higher order modes are contributing much stronger to the total decay rate (or quenching). This misunderstanding may stem from a main result from the quasi-static approximation, i.e., that the field outside of small metal particles is to a very good approximation dipole-like. Mathematically this means that all the scattering coefficients tend to zero and only the one coefficient for the dipolar mode survives. However, to conclude from this, that only the dipolar mode matters for the coupling to near-by emitters is not correct. In

contrast, the inner Mie coefficients (which are essential for the non-radiative decay of close-by emitters) do not show a convergence to zero. Consequently, the higher order modes dominate and the quenching is high and thus the  $\beta$ -factor is poor: a plasmonic particle does not resemble a single-mode cavity. A further fundamental issue was unraveled: as the decay rates of the gain medium speed up significantly close to metallic structures and due to the poor Q-factors, an inversion of the gain-medium might be impossible in many cases, as optical transitions compete with intraband relaxation rates that might be not affected by the plasmonic structures. Actually, it is not clear whether these rates also speed-up in the presence of a metallic structure.

Explicitly it was found that the well-known prime example of a spaser, i.e., the core-shell particle based spaser presented by Noginov et al., is not capable of spasing, as the used gain-factor is orders of magnitude too low. However, also ways to improve systems like this, have been explored here. The use of high index and low loss dielectrics and/or lower working frequencies in the NIR could potentially allow the realization of a nanolaser/ spaser that is fully nanoscopic in all three dimensions as those strategies would improve the quality factors as well as the  $\beta$ -factors.

In the experimental section it was unraveled that multiple laser-like or laser signatures can be generated by hard pumping. All of these effects could be associated to other sources than spasing. Together with the theoretical predictions it must be concluded that spasing in particle-based spasers never has been observed but that results have been misinterpreted.

### *Towards Practical Lasers*

As a consequence of these insights, new designs, that are at least larger than “nano” in one dimension have been started to be explored, namely a nanowire-based Fabry-Pérot-like cavity. Such cavities share some problems with that of particle-based cavities but they are easy to fabricate and can most importantly host more gain medium, thereby relaxing the high gain-factor requirements. These cavities potentially allow for more conclusive interpretation of experimental data, especially potentially occurring laser signatures and may enable the experimentalist to optimize the structure on basis of modified luminescence spectra (which is not known how to do for particle-based spasers).

Future approaches should focus on fully-dielectric nanowires cavities based on absolutely loss-free materials of high index to avoid any quenching, e.g. GaP. These

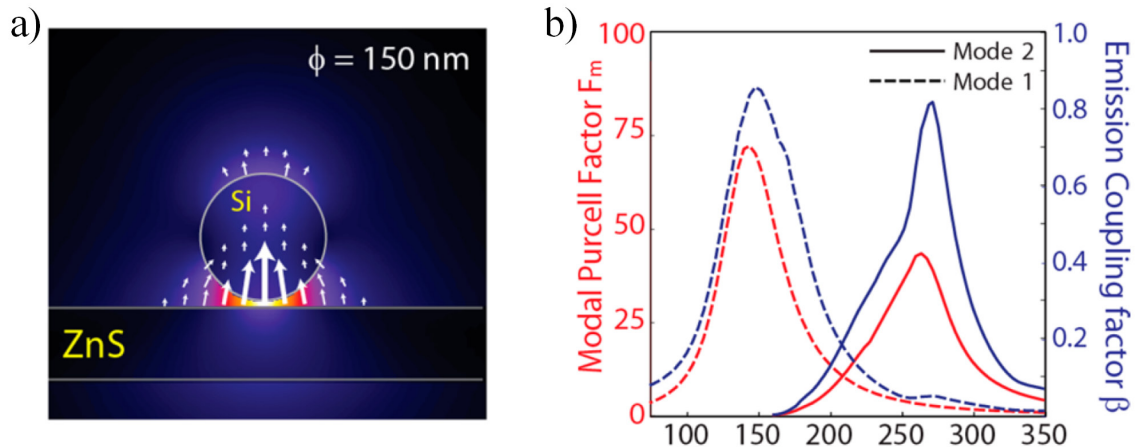


Figure 80: Guided mode properties of an all-dielectric nanowire-film waveguide. a) Absolute value and polarization of the electric field of the fundamental mode. b) Purcell-factor and  $\beta$ -factor as a function of nanowire diameter for the two lowest order modes.

lasers would be most easy to fabricate consisting of a substrate of moderate refractive index, e.g., ZnO, a thin dye-doped film made from PMMA or PVA, which is spin-coated on top and finally a high index nanowire. This approach could be improved when flakes, e.g., of hexagon shape would be used instead of nanowires. Such structures could provide better quality factors as it was demonstrated for spasers [130]. On top of that, the use of materials that have basically no absorption losses allows the use of very thin gaps without increasing propagation losses. Therefore high Purcell-factors and  $\beta$ -factors can be achieved that are comparable to plasmonic systems without the need to take care about strong quenching. Figure 80 show an analysis of such waveguides from Kolchin et al. [141] (compare with Figure 78).

Moreover, nanowire based cavities could be easily combined with a promising gain-medium, i.e., recently explored graphene-like 2D crystals. [142,143] MoSe<sub>2</sub> for instance shows relatively narrow exciton and trion PL around 760 nm [144]. It might provide as high gain-factors as other semiconductors like GaAs. Preparation of samples would be relatively easy, as such MoSe<sub>2</sub> flakes can be exfoliated onto flat substrates and observed in microscopes. This would yield well defined nanostructures.

### *Conclusions Made by Others*

Having that said, a strong claim was made, that fully nanoscopic laser systems – if ever realized - are basically of no use due to their poor performance characteristics. In order to improve the performance one has to give up some restrictions and to move towards ordinary laser physics, i.e., larger cavities, cavities made from low loss dielectrics and designs providing high  $\beta$ -factors.

This conclusion is clearly in contrast to what has been said by the Stockman and Bergman, who proposed the spaser [98,100,118]. This discrepancy arises for two reasons: firstly in the theoretical description of spasers quenching effects have been neglected so far, secondly achievable gain-factors of organics have been overestimated. Negligence of quenching is presumably explainable with a mix-up of the quasi static approximation with a dipolar approximation. For this reason the effect of higher order modes has been ignored. The overestimation of accessible gain-factors comes from a linear extrapolation of single emitter properties towards densely packed emitter ensembles. A linear extrapolation fails as effects like self-quenching set in.

Studies of Sun and Khurgin on the other hand support the findings of this thesis [58]. Their work focusses on electrical pumping of particle based spasers. A major result is, that the current-density needed to provide enough gain for the spaser is far beyond what materials can sustain. They comment on the attempts to build nanolasers: “*The threshold current of the laser decreases with the increase in  $\beta$ , that is, with the reduction in the number of modes coupled with the gain ... This is the main rationale for reducing the volume of the cavity, and ultralow thresholds as low as 4 mA (ref. 25) have been obtained for small photonic-crystal lasers. However, once the volume is reduced beyond  $(\lambda/2n)^3$ , the number of modes remains the same—at one—no matter how small the cavity, and the threshold current does not change while the threshold current density continues to increase.*” This conclusions matches the finding that larger cavities will yield relaxed gain-requirements.

Oulton, one of the authors of the first semiconductor based spasers utilizing propagating plasmonic modes [129,130], comments on quenching effects in his review on spasers [145] – a comment not given in the original spaser reports: “*Metal nanostructures introduce a further complication: emission near a metal surface strongly couples to lossy surface waves (LSWs) (ref.60,86,87). Rather than being discrete guided modes, LSWs form a continuum that rapidly dissipates energy into the*

## 5. Nanolasers & Spasers

---

*metal, essentially quenching useful emission. This drastically reduces  $\beta$  and inhibits plasmonic lasers from operating. Fig. 6 shows the Purcell effect for plasmonic nanowire lasers (ref.24) as a function of both nanowire diameter,  $d$  and insulator gap width,  $h$ . Although nanowires in contact with the metal show much larger Purcell enhancements, none of these nanowires achieved laser action. Only nanowires with an insulating gap achieved laser action, even if this gap was only 5 nm thick.”* This statement is in perfect agreement with our findings: what is called “LSWs” by Oulton is equivalent to “higher order modes” in the case of a particle based spaser.

# 6 Strategies to Probe Plasmons in Graphene and Graphene-like Materials

---

Chapter 6 considers graphene, as a material for plasmonics in the VIS. The current debate on graphene plasmons is picked up by discussing experimental findings and theoretical proposals to extend graphene's plasmonic response to the VIS (6.1). Furthermore photoluminescence studies using short pulse excitation are presented to excite transient phenomena that reveal signatures of second-harmonic generation from graphene (6.2). Some of the results discussed here are already published in Ref. [146].

## 6.1 Indications for Graphene Plasmons in the VIS

### 6.1.1 Motivation

One of the most interesting properties of graphene with respect to nanooptics would be a plasmonic response in the VIS with low losses similar to the IR and THz region. Especially as single photon emitters of high stability and quantum efficiency are available in the VIS one could strive for hybrid quantum systems enabling interesting new physics that could yet not be established due to a missing low-loss metal better than gold and silver, e.g., strong coupling of a single emitter to a plasmonic cavity [147]. On top of that, a 2D material like graphene acting as a high quality metal-sheet, could be tuned electrostatically. Besides graphene there is a zoo of potential alternative 2D materials that scientist only just begun to explore [142,143]. It is likely that one of these materials is intrinsically metallic in the VIS already without strong doping, heating or nanostructuring [148]. Interestingly, in one of the newer, recently found 2D materials, i.e., in tungsten di-selenide ( $\text{WSe}_2$ ), optically active defects where found, that behave just like quantum dots and consequently act as single photon emitters [149–153].

## 6. Graphene Plasmons

---

Attempts to study plasmonic responses of such materials in the VIS are experimentally very demanding as the localization of such plasmons will be extreme, i.e., the near-fields will be presumably located to less than 10 nm. The plasmon wavelength will be of a similar length making it almost impossible to resolve plasmonic field patterns with current technology, e.g., with SNOMs as the resolution is limited by the tip size [154].

Alternative routes to excite and to probe those extremely localized plasmons have been investigated during this thesis on graphene samples. Even though no unambiguous proof for graphene plasmons in the VIS has been reported yet, this was motivated by recent findings in the group of Prof. Rabe (with significant contributions during this thesis [146]). In this study organic chromophores (Rhodamin 6G) were brought in direct vicinity to graphene and a very strong deviation from the expected quenching was found. Quenching is expected to rise with a  $1/z^4$  distance dependence when approaching graphene (or any flat quenching surface), accordingly the chromophores should have been totally dark (well below the noise of the detection). In contrast to that, they could be easily detected and only a quenching by a factor of roughly ten was found with respect to chromophores without graphene. As studies by others confirmed the  $1/z^4$  distance dependence for larger distances ( $z > 5 \text{ nm}$ ), it was concluded, that the mechanism behind the seemingly low quenching could be a combination of an ordinary quenching plus a re-excitation, potentially provided by plasmons. It was found, that the topic is highly controversial. Thus, a goal of this part of the thesis was to search for clearer plasmonic signatures than the simple quenching and/or to enhance the plasmonic “quality” of graphene.

### 6.1.2 Graphene Plasmons in the VIS: Current Status in Literature

The current tenor in the nano optics sub-community investigating graphene plasmons is quite clear: no or only strongly damped plasmons (overdamped oscillator) can exist in the VIS without applying “tricks”. However, direct hints for graphene plasmons up to the VIS have been provided by EELS measurements in various groups. In these experiments not only the energy loss can be recorded but also the incidence angle can be controlled and the scattering angle can be analyzed. The energy loss spectra in correspondence to the scattering angles (which relate to momentum transfer) allows to plot dispersion curves of quasi-particles in an energy vs. momentum graph [155,156]. A dispersion was found that looks similar to ordinary plasmon dispersions for small momenta (square root trend) followed by an almost linear dispersion. The change of this

## 6. Graphene Plasmons

---

dispersion is even recorded for different dopings: especially higher dopings lead to a significant shift of the onset of Landau damping where plasmons are predicted to decay very fast into electron-hole pairs. Liu et al. [157] were able to trace the plasmon dispersion up to 2 eV.

These findings contradict predictions by recent theory publications that are most popular in the graphene nanooptics community. The theoretical frameworks used has been the random phase approximation (RPA) to model collective electron interactions applied on a tight binding model (TBM) description of graphene's band structure [46,47]. In this framework even loss channels like coupling to optical phonons can be studied. However, papers made use of the Dirac-cone approximation, i.e., the region where graphene's banddiagram is simply a linear function of the electron momentum. As can be seen from the banddiagram (Figure 10, chapter 2.2.3) this approximation starts to lose its validity in the near infrared (NIR).

The prediction of having no plasmons in the VIS is based on the finding that graphene does not exhibit any imaginary conductance in the VIS in that case. Frequency-resolved ellipsometry data from single graphene sheets however clearly revealed that this is not the case in the VIS where real and imaginary part are of comparable magnitude. On the other hand the ellipsometry results show that graphene behaves like an ordinary dielectric ( $\text{real}(\epsilon) > 0$  or  $\text{imag}(\sigma) > 0$ , respectively) and not metallic [43,158,159]. Especially Ref. [43] shows how the conductivity of CVD graphene is affected by doping up to 0.54 eV which shifts the metallic region almost up to telecom wavelength (Figure 81).

## 6. Graphene Plasmons

---

In contrast, theoretical simulations using density functional theory (DFT), mostly used in the EELS community, do support the plasmonic effects found by EELS measurements. To conclude, the current picture is unclear.

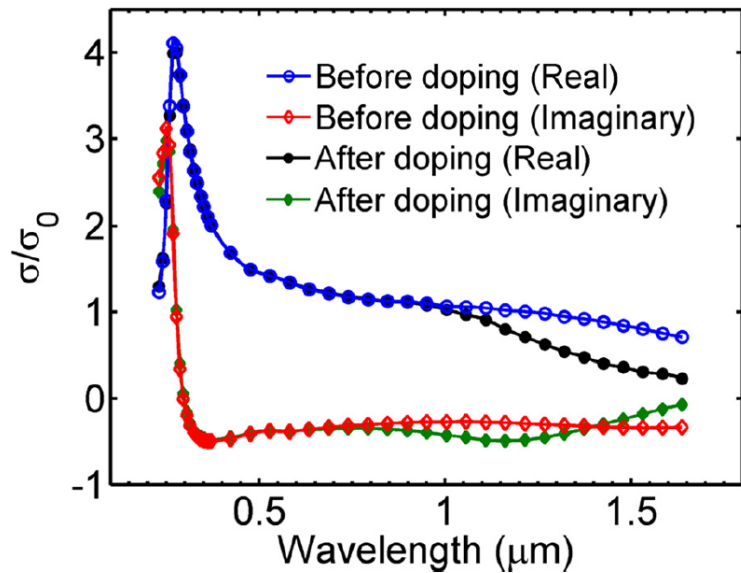


Figure 81: Conductivity (normalized to  $\sigma_0$ , the universal conductivity) of a single CVD grown graphene sheet as a function of wavelength measured by ellipsometry. Real and imaginary part of the conductivity with and without doping are shown, respectively. Plasmons can exist for an imaginary part greater than zero ( $\text{Im}(\sigma) > 0$ ). Figure taken from [43].

## 6. Graphene Plasmons

---

### *Potential reasons for the unclear situation*

One may speculate, that results depend strongly on the actual sample quality, the history of the sample preparation and the method of probing. It is very likely that CVD grown graphene contains many more defects and unwanted chemicals attached to the sample as various production steps are usually used. EELS measurements could potentially be influenced by charging of the samples, such that the signal is influenced by charge-puddles on the sample surface, effectively yielding – or just mimicking - a strong doping. Also the quenching experiments with Rhodamin feature unique sample conditions. The exfoliation of graphene onto a freshly cleaved mica substrate on which a thin Rhodamin solution was spincoated, yields together with water molecules a rather complicated structure between mica and graphene. Figure 82 shows an AFM scan of the sample used for the quenching study. Small R6G islands in a monolayer water “sea” have been found [146]. As adjacent molecules are known to provide a chemical doping to graphene [160], this configuration presumably yields a complicated fluctuating map of doping. It is however yet unclear how precisely these dopings behave and whether they can explain the weak quenching.

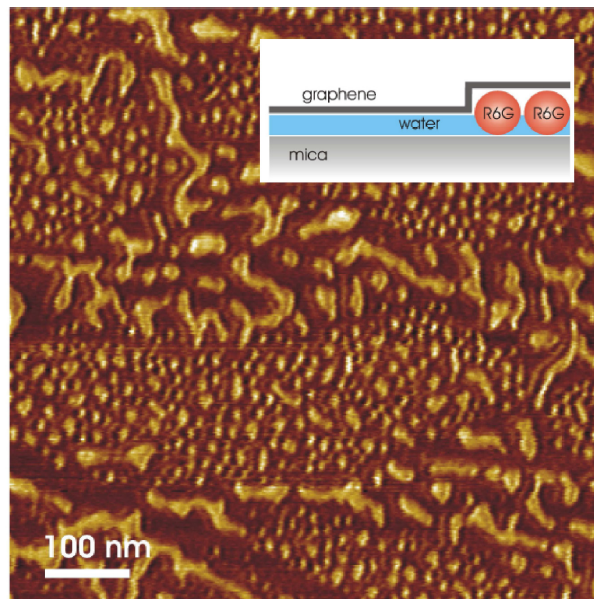


Figure 82: AFM measurement of the sample in the quenching measurement. Water stemming from ambient atmospheric humidity finds its way between graphene and mica where it forms a (sub-)monolayer [85], that is where also the R6G molecules have been deposited. Little R6G island form in the water “sea” as shown in the inset and confirmed by AFM scans at different humidities (degrees of de-wetting). Figure adapted from [146].

In summary, a potential graphene plasmon of relatively poor quality might explain the unexpected quenching results and should be considered for many experiments in which the immediate surrounding of graphene is essential, but it is not the high quality metal one strives for having interesting plasmonic applications in mind.

## 6.2 Short-pulse Excitation of Graphene

### *Motivation*

As discussed earlier it would be very attractive to extend the plasmonic activity of graphene to the VIS. Several proposals have been made on how to achieve this. They are based on either reaching a very high doping beyond what was achieved so far, or by size reduction which would yield localized plasmonic resonances [31,59]. As mentioned before (chapter 2.2.3) electrostatic doping is limited to about 1 eV. Apart from a static doping also any finite temperature of the electron-gas in graphene will result in a non-zero electron-density in the otherwise empty upper Dirac-cone, i.e., by changing the Fermi-distribution. In other words, a hot electron-gas can be regarded as being partly equivalent to a strong doping. It is thus proposed to use a strong short laser pulse to excite the electrons in graphene, [148] thereby producing an electron-gas of several thousand degrees with a correlation between doping and temperature  $\mu(T)$  according to

$$\mu(\mu_0, T) = \mu_0 + 2k_B T \cdot \log(1 + \exp(-\mu_0/k_B T)) . \quad (6.1)$$

$\mu$  is the chemical potential or doping level with respect to pristine graphene where  $\mu=0$  eV.  $\mu$  is plotted as a function of  $T$  and a possible bias electrostatic dopings  $\mu_0$  in Figure 83. In a picosecond time-window before the electrons have cooled down, the condition for a so-called “transient” plasmon would be fulfilled [148]. This section reports on the attempts to explore this proposal.

The attempt is intermixed with the possibility to probe plasmons on-the-fly, similar to a probing method for plasmons in gold nanostructures where intrinsic gold photoluminescence (PL) is employed [25,35,36]. The intrinsic PL of gold was found to be enhanced by orders of magnitude when excited in nanoparticles (compared to films). This effect was attributed to the enhanced LDOS around and inside the particles at the frequency of localized plasmon resonances. The PL was indeed found to follow spectrally and spatially the localized modes [36].

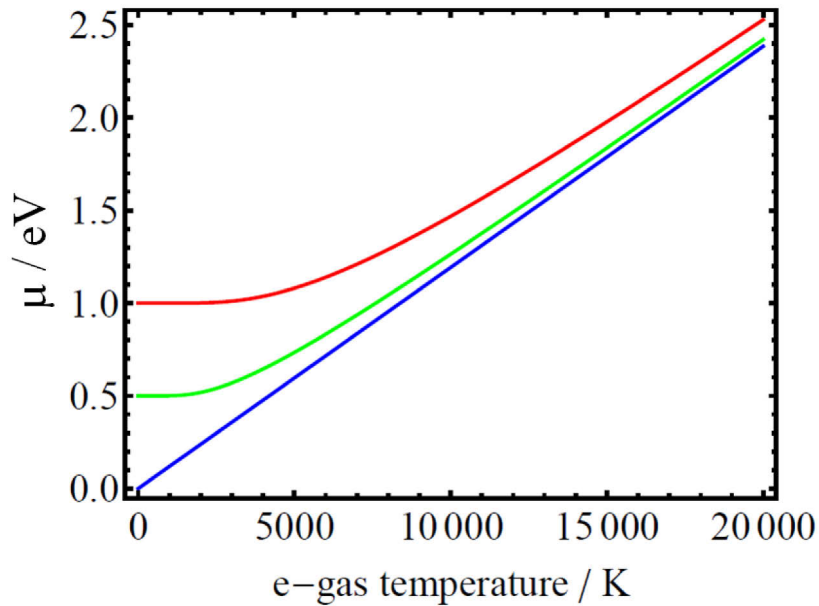


Figure 83: Chemical potential  $\mu$  (by transient doping) as a function of electron gas temperature according to Ref. [148] for three different bias electrostatic dopings of 0 eV, 0.5 eV and 1 eV (blue, green, red).

### *Experimental Results*

The experiment was thus using a relative simple setup to excite the transient doping and to probe the plamsons. As depicted in Figure 24 (section 3.2.1) the excitation was done via an Ti:Sa laser emitting at around 1  $\mu\text{m}$  with roughly 150 fs pulses and 80 MHz repetition rate. The laser was blocked with a short-pass filter and blue-shifted PL was detected. The detection was done via APD and scanning of the sample or analyzed in a spectrograph. Indeed a significant amount of PL can be excited, which obviously originates from the graphene as no PL comes from the graphene-free substrate areas. With this approach, graphene can be imaged with a good signal-to-noise ratio (Figure 84).

## 6. Graphene Plasmons

---

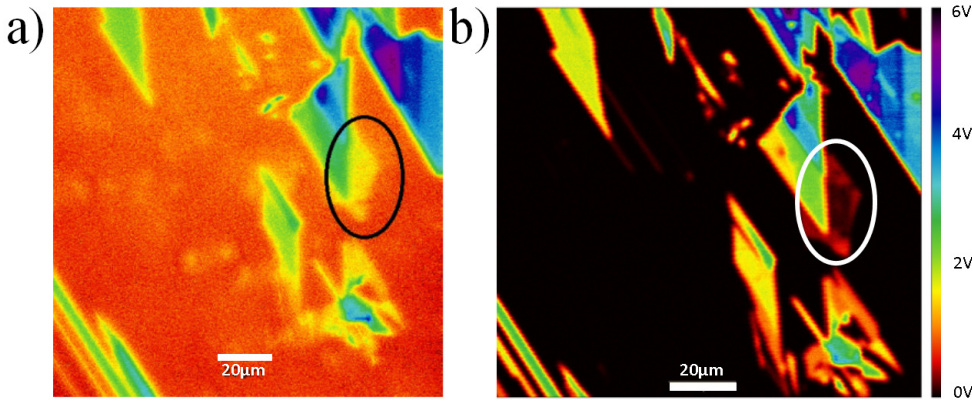


Figure 84: Graphene and graphite structures exfoliated on mica. a) Microscopy image of graphene with crossed polarizers and detected by CCD in false colors (ellipse marks a single-layer graphene region) b) Blue-shifted PL excited by short pulses of a Ti:Sa laser, detected with APD and imaged through scanning of the sample. The encircled region shows a single graphene layer that has been destroyed by the short laser pulses during repeatedly scanning this area.

Similar results were found by others [24]. No spatial modulation of the signal was detected not even at edges or tips where a modified LDOS would be expected. Furthermore, spectra have been taken that show emission like it is expected for a black-body radiator [24,161]. Spectra measured during this thesis (shown in Figure 85) also follow this distribution and similar electron-gas temperatures were found. However, associated temperatures were limited to roughly the melting temperature of graphene, i.e., roughly 4000K. Higher fluxes that have been applied to graphene in order to produce more signal lead to destruction of graphene.

This stability issue was not mentioned by others that performed similar experiments, however they also did not show spectra corresponding to hotter black-body radiators [24,161]. In fact the spectra measured in this thesis are recorded during continuously moving the sample back-and-forth to prevent destruction. This hints to a combination of fast and slow heating processes. The slow processes could be linked to chemical processes induced by hot-electrons in graphene [162–164]. Nevertheless, no spectra significantly hotter than 3000K are found and thus no high doping which would allow for plasmons in the VIS. Abajo predicts, that a temperature of 10,000K (20,000K) would yield an effective doping of 1.2 eV (2.4 eV) [148]. This temperature of the electron-gas, he further concludes, would only result in a moderate temperature increase of about 60K in the lattice of graphene. These predictions seem to be somewhat unrealistic as no higher temperatures have been reported yet. Actually 3000K correspond only to a very weak doping of maximal 0.4 eV as can be seen from Figure

## 6. Graphene Plasmons

83. This level of doping might be interesting for applications of graphene plasmon in the THz region. Lui et al. discuss, that presumably strongly coupled optical phonons cool down the hot electron-gas in the first 50 fs [161]. If so, the potential transient doping would exist much shorter than it was hoped for and thus hard to utilize for any application.

Apart from the broad PL spectrum, an interesting peak at twice the excitation frequency was detected during this thesis that could stem from second harmonic generation (SHG) like shown in Figure 86. This peak was not observed in Ref. [24,161]. The observation of this peak was found to react sensitively on the actual sample, i.e., the peak was not always reproducible. As a matter of fact in the last years several publications have reported on SHG from graphene [165,166], on other 2D-materials [167], and some found enhanced SHG signals in current-carrying graphene [168]. Interestingly, in this work excitation schemes have been used that were very similar to that used during this thesis and to those used in Ref. [24,161], i.e., excitation with a Ti:Sa laser with similar parameters. In none of the works an actual spectrum was shown, but photomultipliers were detecting the intensity at the frequency of the pretended SHG signal which was filtered by a bandpass filter. Referring to the findings during this thesis and to Ref. [24,161], this means that the SHG signals discussed in literature might either exclusively stem from the broad well-known PL or at least the SHG signal will only be a part of the detected signal besides the PL.

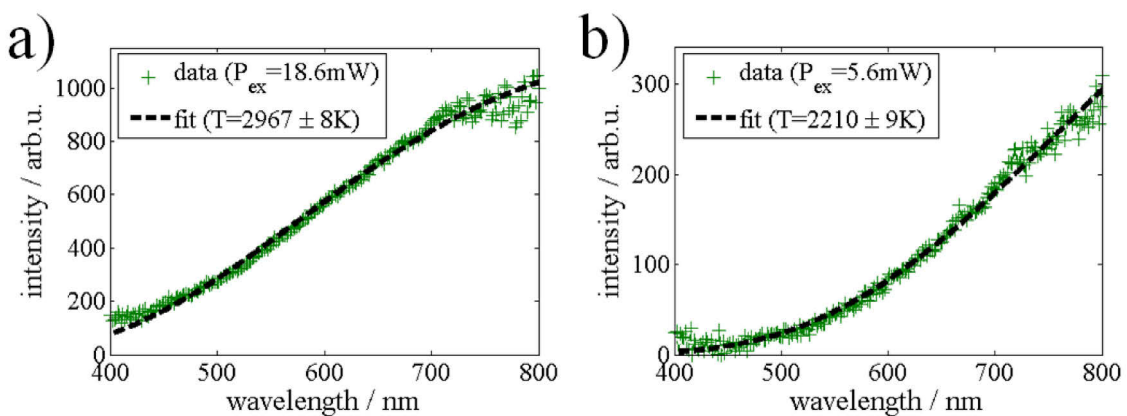


Figure 85: Broad photoluminescence spectrum of graphene after short-pulse excitation and fit with Planck's law. PL has been excited with pulses from a Ti:Sa laser at 965 nm (1.285 eV). Spectra have been corrected for the substrate and the system response of the setup. a) PL of graphene excited with 18.6 mW. The fit yields a temperature of  $T=2967 \pm 8 \text{ K}$ . b) PL spectrum when excited with 5.6 mW, yielding a temperature of  $T=2210 \pm 9 \text{ K}$ .

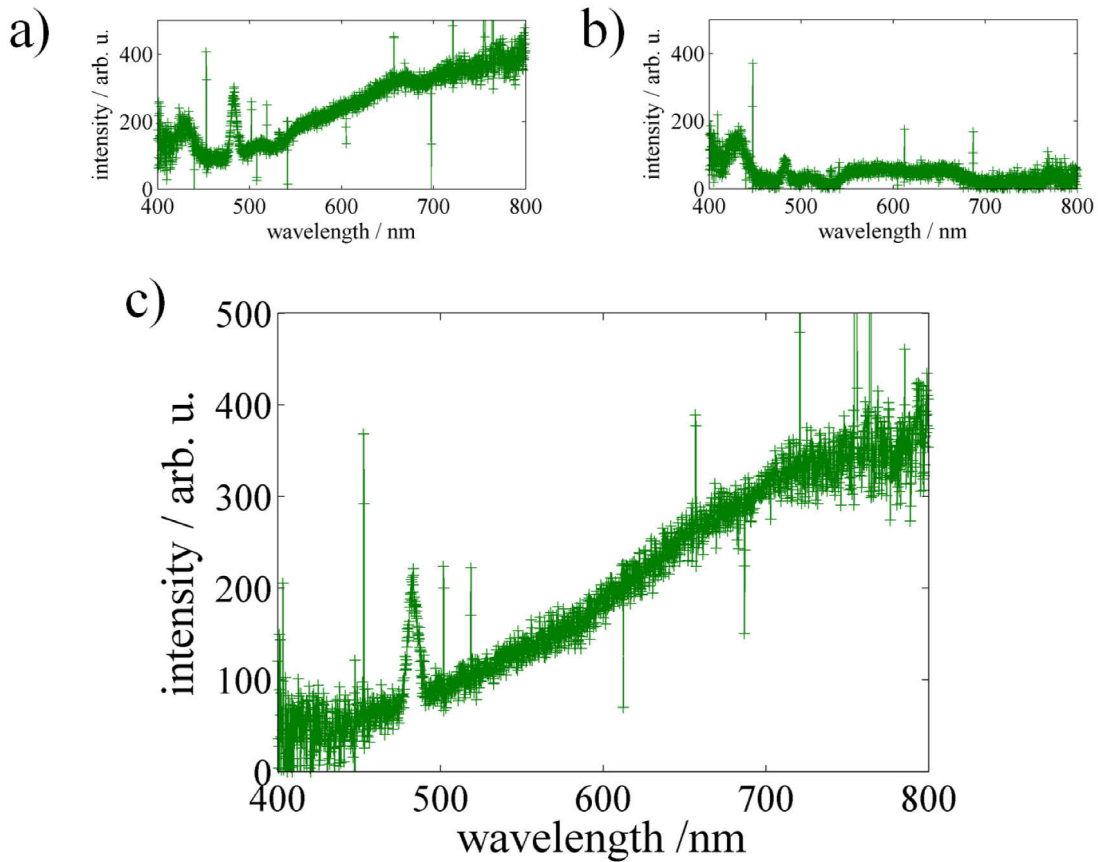


Figure 86: Broad graphene PL with a SHG-like peak at twice the excitation energy (around 490 nm). a) Raw data, b) signal of bare mica without graphene, c) background corrected signal.

SHG originates in a classical description from oscillating charges that feel perturbations from a harmonic potential, i.e., the susceptibility features a non-vanishing  $\chi^{(2)}$  value. Graphene is said to be a centro-symmetrical crystal which would in principle forbid SHG effects, however theory described SHG from graphene by taking into account a static doping and the symmetry break that is said to be induced for example by the substrate [169,170].

The findings during this thesis however also indicate alternative explanations for the SHG signal. First of all it was reported that the substrate mica can act as a nonlinear material for SHG production itself [171]. The authors found that the signal strength depends sensitively on the thickness of the substrate. Different samples used in this thesis were fabricated on freshly cleaved mica substrates, thus all substrates differed in thickness which could explain the observed changes in signal strength. Additionally, the mica samples are clean and flat on micrometer-scales but not co-planar over the whole sample. Thus, reference spectra on pure mica next to the graphene regions could potentially have been produced in mica of a different thickness, even though this seems

## 6. Graphene Plasmons

---

to be unlikely. SHG reports in literature [165,166,168] were using Si substrates with a capping  $\text{SiO}_2$ -layer. Both materials do usually not show any SHG, however, it was recently reported that stressed Si produced detectable SHG signals [172].

Secondly, the SHG-like peak could stem from a stimulated emission process including two pump photons, i.e., graphene acts as a gain medium [173]. In this thesis a weak SHG peak was detected when excitation and detection was done from below as depicted in Figure 24 (section 3.2.1). To enhance the detectable signal, a mirror was placed on top of the sample, as ordinary SHG signals, e.g., from BBO crystals follow the direction of the pump beam. Indeed more signal was detected. However, the same effect can be explained when one visualizes, that the transmitted part of the excitation pulse is reflected by the mirror and hits the excited graphene sample. In this case an emission could be stimulated by two photons of the laser. The travelling distance for the laser pulse has been in this case in the range of a millimeter which roughly corresponds to a picosecond, i.e., 6 times the pulse length. This effect can also appear without a mirror, as some reflection will appear in any sample at interfaces (steps in the refractive index), e.g., at mica-air or Si- $\text{SiO}_2$  interfaces. More experiments have to be performed to unravel the true underlying process, especially as this non-linear process in graphene is already envisioned to support non-linear functionality in silicon-based chip technology [174].

## 6.3 Conclusion and Outlook

Presumably transient graphene plasmons in the VIS – if they exist - are not practicable for several reasons. It is very likely that graphene will be destroyed before the high electron-gas temperatures are reached. Further, the lifetime of the transient regime is extremely short which will make it hard to investigate. On the other hand this feature could be an advantage as it may introduce intrinsically fast non-linearities. Finally, the efficiency to produce the transient doping is obviously very low. Even if no optical excitation via laser (in which only a poor ratio is actually absorbed, roughly 2 %) would be used, but an efficient way, a big ratio of the power will be channeled into phonons, finally just heating the sample [161]. A similar reasoning applies to attempts that want to utilize second harmonic generation as a source of non-linearity: Only a fraction of power will be transformed in a SHG or SHG-like signal while also broad PL will be excited.  $\chi^{(3)}$ -effects that naturally fit to the symmetry of graphene (even in a pristine form) have been observed with low background, e.g., four-wave mixing was demonstrated [175]. This non-linearity could potentially feature a higher efficiency and greater flexibility.

# 7 Conclusion and Outlook

---

## 7.1 Conclusion

During this thesis three different nanooptical systems have been studied: on-chip nanostructures, nanolasers and graphene. These systems have been suspected to feature non-linear responses which are attractive to develop all-optical switches with small spatial footprint and high energy efficiency. Investigations on these systems have been motivated by theoretical proposals (on-chip nanostructures: Chang et al. [51] and spasers: Stockman and Bergman [98,100]) as well as by recent findings at the Humboldt university (graphene: Lange et al. [146]).

### *Main Achievements*

Detailed discussions of the findings can be found in the “Conclusion and Outlook” sections of the corresponding chapters 4 to 6. Here only short versions of the main findings are highlighted.

- On-chip nanooptics:

Major steps towards a practical realization of Chang’s proposal [51] have been accomplished. A photon-to-plasmon coupler was designed by numerical simulations that meets the performance of subsequently fabricated on-chip structures. This underlines the quality of the numerical methods as well as the actual producibility of the on-chip structures. Further numerical studies predict that the considered organic emitters can yield the required non-linear performance when coupled to the on-chip structures.

- Spasers and nanolasers:

A novel theoretical model has been established that includes quenching effects which turn out to be extremely important. Theoretical predictions on the spaser performance are accompanied by experimental results. Both, theory and experiment state: particle-based spasers are hardly possible to fabricate and almost useless for applications due to their poor performance. Beyond pessimistic statements, clear guidelines for more efficient and easy-to-fabricate lasers with small-footprint are identified.

- Graphene:

Complementary follow-up experiments (to those performed by Lange [146]) to probe plasmons in the VIS by pulsed excitation of graphene have been performed. These studies feature rich physical phenomena like broad PL and SHG effects. Though no fully conclusive explanations have been found for all observations, these results indicate that graphene does not feature pronounced plasmonic effects in the VIS even with additional optical pumping. The potential plasmonic effects observed by Lange thus might stem from nanolocalized doping of graphene by Rhodamine islands.

## 7.2 Outlook

*Small, fast, efficient and practicable?*

In 2014 German data centers consumed roughly 10 TWh of energy according to the Borderstep Institute, 50 % of the energy is used for cooling purposes. A more efficient technology could reduce the overall power consumption and accompanied greenhouse gas production (even though achievements in speed and efficiency are often eaten up by rebound effects).

Whether new findings in research ever make their way into technology also depends on the cost, a reliable fabrication process and stability. A reliable outlook that contains all these considerations is not possible. However, some basic predictions can be made.

### *On-chip Nanooptics*

In principle hundreds of on-chip structures consisting of far-field couplers, photon-to-plasmon couplers and strongly coupled emitters can be integrated on a single inch-sized chip. Also, the non-linear behavior of the device is designated to switch extremely weak optical signals, i.e. single photons. However, various difficult tasks come into play if one strives for the interconnection of individual structures. A main difficulty will be the alignment in frequency. For a single device a laser can be easily tuned to hit the sharp resonance of the coupled emitter. To align many systems, static electrical fields could be used to induce a stark shift in the emitter. This could significantly complicate the chip design. To exploit the full potential discussed in the single-photon-transistor proposal by Chang et al. so-called  $\lambda$ -systems have to be employed [51].  $\lambda$ -systems are three-level emitters with additional internal states that can be manipulated typically via external GHz signals. Addressing individual on-chip structures with high spatial resolution, i.e., without influencing neighboring structures will be hard to realize sustaining a small overall footprint at the same time. Thus, a  $\lambda$ -system that can be fully controlled by optical means is needed. The recently found silicon vacancy center in diamond is a promising candidate [176]. Finally, emitters have to be cooled down to temperatures down to or even below 4 K to show Fourier limited emission. From these considerations one can conclude that this technology will never replace current technology but can represent at most a complementary technology which might finally enable quantum computing.

### *Nanolaser*

Guidelines to improve the laser performance have been discussed earlier in this thesis. The next step would be to check whether these guidelines turn out to be correct and to observe lasing from an individual device. Based on these prototypes and on a refinement of the theoretical framework (towards arbitrary shaped resonators - possible with the recently published work on a generalized Purcell factor [23]) further design optimization can be performed. A major step towards an actual application would be electrical pumping of the gain medium. This is presumably relatively easy to accomplish with the aforementioned graphene-like 2D materials as MoSe<sub>2</sub> which renders a direct bandgap material, which is very interesting to employ as a gain-medium.

### *Graphene*

The literature on graphene is hard to overlook. With respect to nano optics the major hope has been so far to make use of its plasmonic features in the THz or infrared frequency range. A major problem with this is however, that basically no efficient emitters are known for this region and that propagating graphene plasmons were found to be faster damped than expected.

The prospect of localized graphene plasmons in the VIS by a static nanolocalized doping is therefore very attractive. Such plasmons could be controlled via electrostatic doping that would reduce or enhance the relative doping of the nanolocalized doping islands. Next steps to gain more insight into this would therefore be a scanning probe approach (SNOM) that can resolve the sub-nanometer islands due to molecular clusters between substrate and graphene as shown in Figure 82 (chapter 6.1) and at the same time probe intensity fluctuations of the optical nearfield signals. If such localized graphene plasmons exist further control could then potentially be gained by self-assembled molecular structures.

---

## 8 Appendices

---

---

## Literature

---

1. A. Fehske, G. Fettweis, J. Malmodin, and G. Biczok, "The global footprint of mobile communications: The ecological and economic perspective," *IEEE Commun. Mag.* **49**, 55–62 (2011).
2. A. Manhart, M. Buchert, D. Bleher, and D. Pingel, "Recycling of critical metals from end-of-life electronics," *Electron. Goes Green 2012+* 1–5 (2012).
3. K. Binnemans, P. T. Jones, B. Blanpain, T. Van Gerven, Y. Yang, A. Walton, and M. Buchert, "Recycling of rare earths: a critical review," *J. Clean. Prod.* **51**, 1–22 (2013).
4. I. L. Markov, "Limits on fundamental limits to computation," *Nature* **512**, 147–154 (2014).
5. L. B. Kish, "End of Moore's law: thermal (noise) death of integration in micro and nano electronics," *Phys. Lett. A* **305**, 144–149 (2002).
6. A. A. Chien and V. Karamcheti, "Moore's Law: The First Ending and a New Beginning," *Computer (Long. Beach. Calif.)* **46**, 48–53 (2013).

## 8. Appendices

---

7. L. Novotny and B. Hecht, *Principles of Nano-Optics* (Cambridge Univ Pr, 2006).
8. S. W. Hell and J. Wichmann, "Breaking the diffraction resolution limit by stimulated emission: stimulated-emission-depletion fluorescence microscopy," *Opt. Lett.* **19**, 780 (1994).
9. D. Gevaux, "Nobel Prize in Chemistry: seeing the nanoscale.," *Nat. Nanotechnol.* **9**, 878 (2014).
10. E. Le Ru and P. Etchegoin, *Principles of Surface Enhanced Raman Spectroscopy* (Elsevier, 2009).
11. H. A. Atwater and A. Polman, "Plasmonics for improved photovoltaic devices," *Nat. Mater.* **9**, 205–213 (2010).
12. H. LIU and J. TENG, "Plasmonic Nanolithography: Towards Next Generation Nanopatterning," *J. Mol. Eng. Mater.* **01**, 1250005 (2013).
13. G. Konstantatos and E. H. Sargent, "Nanostructured materials for photon detection.," *Nat. Nanotechnol.* **5**, 391–400 (2010).
14. R. Yan, D. Gargas, and P. Yang, "Nanowire photonics," *Nat. Photonics* **3**, 569–576 (2009).
15. Y. Ma, X. Guo, X. Wu, L. Dai, and L. Tong, "Semiconductor nanowire lasers," *Adv. Opt. Photonics* **5**, 216 (2013).
16. D. Saxena, S. Mokkapati, P. Parkinson, N. Jiang, Q. Gao, H. H. Tan, and C. Jagadish, "Optically pumped room-temperature GaAs nanowire lasers," *Nat. Photonics* **7**, 963–968 (2013).
17. R.-M. Ma, R. F. Oulton, V. J. Sorger, and X. Zhang, "Plasmon lasers: coherent light source at molecular scales," *Laser Photon. Rev.* **7**, 1–21 (2013).
18. A. Poddubny, I. Iorsh, P. Belov, and Y. Kivshar, "Hyperbolic metamaterials," *Nat. Photonics* **7**, 948–957 (2013).

## 8. Appendices

---

19. C. M. Soukoulis and M. Wegener, "Past achievements and future challenges in the development of three-dimensional photonic metamaterials," *Nat. Photonics* **5**, 523–530 (2011).
20. O. Hess, J. Pendry, S. Maier, and R. Oulton, "Active nanoplasmonic metamaterials," *Nat. Mater.* **11**, 573–584 (2012).
21. T. Basché, W. E. Moerner, M. Orrit, and U. P. Wild, eds., *Single-Molecule Optical Detection, Imaging and Spectroscopy* (VCH Verlagsgesellschaft mbH, 1996).
22. W. L. Barnes, A. Dereux, and T. W. Ebbesen, "Surface plasmon subwavelength optics," *Nature* **424**, 824–830 (2003).
23. C. Sauvan, J. P. Hugonin, I. S. Maksymov, and P. Lalanne, "Theory of the Spontaneous Optical Emission of Nanosize Photonic and Plasmon Resonators," *Phys. Rev. Lett.* **110**, 237401 (2013).
24. W.-T. Liu, S. W. Wu, P. J. Schuck, M. Salmeron, Y. R. Shen, and F. Wang, "Nonlinear broadband photoluminescence of graphene induced by femtosecond laser irradiation," *Phys. Rev. B* **82**, 081408 (2010).
25. E. Dulkeith, T. Niedereichholz, T. Klar, J. Feldmann, G. von Plessen, D. Gittins, K. Mayya, and F. Caruso, "Plasmon emission in photoexcited gold nanoparticles," *Phys. Rev. B* **70**, 1–4 (2004).
26. M. Perner, P. Bost, U. Lemmer, G. von Plessen, J. Feldmann, U. Becker, M. Mennig, M. Schmitt, and H. Schmidt, "Optically Induced Damping of the Surface Plasmon Resonance in Gold Colloids," *Phys. Rev. Lett.* **78**, 2192–2195 (1997).
27. K. Sokolowski-Tinten and D. von der Linde, "Generation of dense electron-hole plasmas in silicon," *Phys. Rev. B* **61**, 2643–2650 (2000).
28. A. E. Siegman, *Lasers* (University Science Books, 1986).
29. S. A. Maier, *Plasmonics: Fundamentals and Applications* (Springer Verlag, 2007).

## 8. Appendices

---

30. K. Kolwas and A. Derkachova, "Plasmonic abilities of gold and silver spherical nanoantennas in terms of size dependent multipolar resonance frequencies and plasmon damping rates," *Opto-Electronics Rev.* **18**, 429–437 (2010).
31. A. Manjavacas, S. Thongrattanasiri, and F. J. G. de Abajo, "Plasmons driven by single electrons in graphene nanoislands," *Nanophotonics* **2**, 139–151 (2013).
32. T. Christensen, W. Wang, A.-P. Jauho, M. Wubs, and N. A. Mortensen, "Classical and quantum plasmonics in graphene nanodisks: Role of edge states," *Phys. Rev. B* **90**, 241414 (2014).
33. N. Grillet, D. Manchon, E. Cottancin, F. Bertorelle, C. Bonnet, M. Broyer, J. Lermé, and M. Pellarin, "Photo-Oxidation of Individual Silver Nanoparticles: A Real-Time Tracking of Optical and Morphological Changes," *J. Phys. Chem. C* **117**, 2274–2282 (2013).
34. P. B. Johnson and R. W. Christy, "Optical Constants of the Noble Metals," *Phys. Rev. B* **6**, 4370–4379 (1972).
35. A. Kuhlicke, S. Schietinger, C. Matyssek, K. Busch, and O. Benson, "In situ observation of plasmon tuning in a single gold nanoparticle during controlled melting.," *Nano Lett.* **13**, 2041–6 (2013).
36. S. Viarbitskaya, A. Teulle, R. Marty, J. Sharma, C. Girard, A. Arbouet, and E. Dujardin, "Tailoring and imaging the plasmonic local density of states in crystalline nanoprisms.," *Nat. Mater.* **12**, 426–32 (2013).
37. M. L. Cohen and J. R. Chelikowsky, *Electronic Structure and Optical Properties of Semiconductors*, Springer Series in Solid-State Sciences (Springer Berlin Heidelberg, 1988).
38. A. I. Kuznetsov, A. E. Miroshnichenko, Y. H. Fu, J. Zhang, and B. Luk'yanchuk, "Magnetic light.," *Sci. Rep.* **2**, 492 (2012).
39. M. Barth, N. Nüsse, J. Stingl, B. Löchel, and O. Benson, "Emission properties of high-Q silicon nitride photonic crystal heterostructure cavities," *Appl. Phys. Lett.* **93**, 021112 (2008).

## 8. Appendices

---

40. K. S. Novoselov, "Nobel Lecture: Graphene: Materials in the Flatland," *Rev. Mod. Phys.* **83**, 837–849 (2011).
41. K. J. Tielrooij, J. C. W. Song, S. A. Jensen, A. Centeno, A. Pesquera, A. Z. Elorza, M. Bonn, L. S. Levitov, and F. H. L. Koppens, "Photoexcitation cascade and multiple hot-carrier generation in graphene," *Nat. Phys.* **9**, 248–252 (2013).
42. F. H. L. Koppens, D. E. Chang, and F. J. G. de Abajo, "Graphene Plasmonics: A Platform for Strong Light-Matter Interactions," *Nano Lett.* **11**, 3370–3377 (2011).
43. Y.-C. Chang, C.-H. Liu, C.-H. Liu, Z. Zhong, and T. B. Norris, "Extracting the complex optical conductivity of mono- and bilayer graphene by ellipsometry," *Appl. Phys. Lett.* **104**, 261909 (2014).
44. J. Chen, M. Badioli, P. Alonso-González, S. Thongrattanasiri, F. Huth, J. Osmond, M. Spasenović, A. Centeno, A. Pesquera, P. Godignon, A. Z. Elorza, N. Camara, F. J. García de Abajo, R. Hillenbrand, and F. H. L. Koppens, "Optical nano-imaging of gate-tunable graphene plasmons," *Nature* **487**, 77–81 (2012).
45. A. K. Geim and K. S. Novoselov, "The rise of graphene," *Nat. Mater.* **6**, 183–191 (2007).
46. M. Jablan, H. Buljan, and M. Soljacic, "Plasmonics in graphene at infrared frequencies," *Phys. Rev. B* **80**, (2009).
47. E. H. Hwang and S. Das Sarma, "Dielectric function, screening, and plasmons in two-dimensional graphene," *Phys. Rev. B* **75**, 205418 (2007).
48. G. W. Hanson, "Dyadic Green's functions and guided surface waves for a surface conductivity model of graphene," *J. Appl. Phys.* **103**, 064302 (2008).
49. Z. Fei, A. S. Rodin, G. O. Andreev, W. Bao, A. S. Mcleod, M. Wagner, L. M. Zhang, Z. Zhao, M. Thiemens, G. Dominguez, M. M. Fogler, A. H. C. Neto, C. N. Lau, F. Keilmann, and D. N. Basov, "Gate-tuning of graphene plasmons revealed by infrared nano-imaging," *Nature* **487**, 82–85 (2012).

## 8. Appendices

---

50. L. Novotny, "Strong coupling, energy splitting, and level crossings: A classical perspective," *Am. J. Phys.* **78**, 1199 (2010).
51. D. E. Chang, A. S. Sørensen, E. A. Demler, and M. D. Lukin, "A single-photon transistor using nanoscale surface plasmons," *Nat. Phys.* **3**, 807–812 (2007).
52. J. Hwang and E. a. Hinds, "Dye molecules as single-photon sources and large optical nonlinearities on a chip," *New J. Phys.* **13**, (2011).
53. M. McGehee, R. Gupta, S. Veenstra, E. Miller, M. Díaz-García, and A. Heeger, "Amplified spontaneous emission from photopumped films of a conjugated polymer," *Phys. Rev. B* **58**, 7035–7039 (1998).
54. R. Xia, G. Heliotis, Y. Hou, and D. D. C. Bradley, "Fluorene-based conjugated polymer optical gain media," *Org. Electron.* **4**, 165–177 (2003).
55. C. F. Bohren and D. R. Huffman, *Absorption and Scattering of Light by Small Particles* (John Wiley & Sons, 2008).
56. R. Kolesov, B. Grotz, G. Balasubramanian, R. J. Stöhr, A. a. L. Nicolet, P. R. Hemmer, F. Jelezko, and J. Wrachtrup, "Wave-particle duality of single surface plasmon polaritons," *Nat. Phys.* **5**, 470–474 (2009).
57. J. S. Fakonas, H. Lee, Y. A. Kelaita, and H. A. Atwater, "Two-plasmon quantum interference," *Nat. Photonics* **8**, 317–320 (2014).
58. J. B. Khurgin and G. Sun, "Comparative analysis of spasers, vertical-cavity surface-emitting lasers and surface-plasmon-emitting diodes," *Nat. Photonics* **8**, 468–473 (2014).
59. A. Manjavacas, F. Marchesin, S. Thongrattanasiri, P. Koval, P. Nordlander, D. Sánchez-Portal, and F. J. García de Abajo, "Tunable molecular plasmons in polycyclic aromatic hydrocarbons," *ACS Nano* **7**, 3635–43 (2013).
60. A. W. Snyder and J. Love, *Optical Waveguide Theory* (Springer Science & Business Media, 2012).

## 8. Appendices

---

61. R. Zia, M. Selker, and M. Brongersma, "Leaky and bound modes of surface plasmon waveguides," *Phys. Rev. B* **71**, 165431 (2005).
62. K. J. Ebeling, *Integrated Optoelectronics - Waveguide Optics, Photonics, Semiconductors* (Springer, 1993).
63. A. Yariv and P. Yeh, *Photonics: Optical Electronics in Modern Communications* (Oxford University Press, 2007).
64. E. Vetsch, S. T. Dawkins, R. Mitsch, D. Reitz, P. Schneeweiss, and A. Rauschenbeutel, "Nanofiber-Based Optical Trapping of Cold Neutral Atoms," *IEEE J. Sel. Top. Quantum Electron.* **18**, 1763–1770 (2012).
65. D. Chang, a. Sørensen, P. Hemmer, and M. Lukin, "Strong coupling of single emitters to surface plasmons," *Phys. Rev. B* **76**, 1–26 (2007).
66. P. T. Kristensen and S. Hughes, "Modes and Mode Volumes of Leaky Optical Cavities and Plasmonic Nanoresonators," *ACS Photonics* **1**, 2–10 (2014).
67. A. F. Koenderink, "On the use of Purcell factors for plasmon antennas.," *Opt. Lett.* **35**, 4208–10 (2010).
68. A. Moroz, "Non-radiative decay of a dipole emitter close to a metallic nanoparticle: Importance of higher-order multipole contributions," *Opt. Commun.* **283**, 2277–2287 (2010).
69. R. Ruppin, "Decay of an excited molecule near a small metal sphere," *J. Chem. Phys.* **76**, 1681 (1982).
70. G. Meunier, *The Finite Element Method for Electromagnetic Modeling* (John Wiley & Sons, 2010).
71. S. Burger, L. Zschiedrich, and J. Pomplun, "Finite element method for accurate 3D simulation of plasmonic waveguides," *arXiv* (2010).
72. S. G. Johnson, "Notes on Perfectly Matched Layers ( PMLs )," Tech. Report, Massachusetts Inst. Technol. 1–18 (2010).

## 8. Appendices

---

73. F. L. Teixeira, S. Member, and W. C. Chew, "Systematic Derivation of Anisotropic PML Absorbing Media in Cylindrical and Spherical Coordinates," **7**, 371–373 (1997).
74. F. L. Teixeira and W. C. Chew, "PML-FDTD in cylindrical and spherical grids," *IEEE Microw. Guid. Wave Lett.* **7**, 285–287 (1997).
75. J. P. Dowling, "Spontaneous emission in cavities: How much more classical can you get?," *Found. Phys.* **23**, 895–905 (1993).
76. H. Tanji-Suzuki, I. D. Leroux, M. H. Schleier-Smith, M. Cetina, A. T. Grier, J. Simon, and V. Vuletic, "Interaction between Atomic Ensembles and Optical Resonators: Classical Description," arXiv **1104.3594**, 39 (2011).
77. D. Dzsotjan, A. Sørensen, and M. Fleischhauer, "Quantum emitters coupled to surface plasmons of a nanowire: A Green's function approach," *Phys. Rev. B* **82**, 1–13 (2010).
78. Y. Chen, T. R. Nielsen, N. Gregersen, P. Lodahl, and J. Mørk, "Finite-element modeling of spontaneous emission of a quantum emitter at nanoscale proximity to plasmonic waveguides," *Phys. Rev. B* **81**, 125431 (2010).
79. J. Barthes, G. Colas Des Francs, a. Bouhelier, J. C. Weeber, and a. Dereux, "Purcell factor for a point-like dipolar emitter coupled to a two-dimensional plasmonic waveguide," *Phys. Rev. B - Condens. Matter Mater. Phys.* **84**, 1–4 (2011).
80. G. Kewes, M. Schoengen, G. Mazzamuto, O. Neitzke, R.-S. Schönfeld, A. W. Schell, J. Probst, J. Wolters, B. Löchel, C. Toninelli, and O. Benson, "Key components for nano-assembled plasmon-excited single molecule non-linear devices," arXiv **1501.04788**, (2015).
81. C. Toninelli, K. Early, J. Bremi, A. Renn, S. Götzinger, and V. Sandoghdar, "Near-infrared single-photons from aligned molecules in ultrathin crystalline films at room temperature.,," *Opt. Express* **18**, 6577–82 (2010).

## 8. Appendices

---

82. J.-S. Huang, V. Callegari, P. Geisler, C. Brüning, J. Kern, J. C. Prangsma, X. Wu, T. Feichtner, J. Ziegler, P. Weinmann, M. Kamp, A. Forchel, P. Biagioni, U. Sennhauser, and B. Hecht, "Atomically flat single-crystalline gold nanostructures for plasmonic nanocircuitry.," *Nat. Commun.* **1**, 150 (2010).
83. J. Y. Kim, O. Voznyy, D. Zhitomirsky, and E. H. Sargent, "25th anniversary article: Colloidal quantum dot materials and devices: a quarter-century of advances.," *Adv. Mater.* **25**, 4986–5010 (2013).
84. M. Dorn, P. Lange, A. Chekushin, N. Severin, and J. P. Rabe, "High contrast optical detection of single graphenes on optically transparent substrates," *J. Appl. Phys.* **108**, 106101 (2010).
85. N. Severin, P. Lange, I. M. Sokolov, and J. P. Rabe, "Reversible Dewetting of a Molecularly Thin Fluid Water Film in a Soft Graphene-Mica Slit Pore," *Nano Lett.* **12**, 774–779 (2012).
86. G. Kewes, A. W. Schell, R. Henze, R. Simon Schönfeld, S. Burger, K. Busch, and O. Benson, "Design and numerical optimization of an easy-to-fabricate photon-to-plasmon coupler for quantum plasmonics," *Appl. Phys. Lett.* **102**, 051104 (2013).
87. B. D. Cobb and J. M. Clarkson, "A simple procedure for optimising the polymerase chain reaction (PCR) using modified Taguchi methods.," *Nucleic Acids Res.* **22**, 3801–5 (1994).
88. W.-P. Huang, "Coupled-mode theory for optical waveguides: an overview," *J. Opt. Soc. Am. A* **11**, 963 (1994).
89. J. Mu and W.-P. Huang, "Simulation of three-dimensional waveguide discontinuities by a full-vector mode-matching method based on finite-difference schemes," *Opt. Express* **16**, 18152 (2008).
90. P. Berini, "Plasmon-polariton waves guided by thin lossy metal films of finite width: Bound modes of asymmetric structures," *Phys. Rev. B* **63**, (2001).
91. D. Taillaert, "Grating Couplers as Interface between Optical Fibres and Nanophotonic Waveguides," (2006).

## 8. Appendices

---

92. A. W. Schell, G. Kewes, T. Schröder, J. Wolters, T. Aichele, and O. Benson, "A scanning probe-based pick-and-place procedure for assembly of integrated quantum optical hybrid devices.," *Rev. Sci. Instrum.* **82**, 073709 (2011).
93. J. Wolters, N. Sadzak, A. W. Schell, T. Schröder, and O. Benson, "Measurement of the ultrafast spectral diffusion of the optical transition of nitrogen vacancy centers in nano-size diamond using correlation interferometry.," *Phys. Rev. Lett.* **110**, 027401 (2013).
94. E. Kuramochi, H. Taniyama, T. Tanabe, K. Kawasaki, Y.-G. Roh, and M. Notomi, "Ultrahigh-Q one-dimensional photonic crystal nanocavities with modulated mode-gap barriers on SiO<sub>2</sub> claddings and on air claddings.," *Opt. Express* **18**, 15859–69 (2010).
95. S.-P. Yu, J. D. Hood, J. A. Muniz, M. J. Martin, R. Norte, C.-L. Hung, S. M. Meenehan, J. D. Cohen, O. Painter, and H. J. Kimble, "Nanowire photonic crystal waveguides for single-atom trapping and strong light-matter interactions," *Appl. Phys. Lett.* **104**, 111103 (2014).
96. G. Kewes, R. Rodríguez-Oliveros, K. Höfner, A. Kuhlicke, O. Benson, and K. Busch, "Threshold Limitations of the SPASER," *arXiv 1408.7054*, (2014).
97. G. Kewes, R. Rodriguez-Oliveros, K. Höfner, A. Kuhlicke, O. Benson, and K. Busch, "A fully nanoscopic dielectric laser," *arXiv 1412.4549*, (2014).
98. D. J. Bergman and M. I. Stockman, "Surface plasmon amplification by stimulated emission of radiation: quantum generation of coherent surface plasmons in nanosystems," *Phys. Rev. Lett.* **90**, 1–4 (2003).
99. M. A. Noginov, G. Zhu, A. M. Belgrave, R. Bakker, V. M. Shalaev, E. E. Narimanov, S. Stout, E. Herz, T. Suteewong, and U. Wiesner, "Demonstration of a spaser-based nanolaser," *Nature* **460**, 1110–1112 (2009).
100. M. I. Stockman, "The spaser as a nanoscale quantum generator and ultrafast amplifier," *J. Opt.* **12**, 024004 (2010).
101. M. I. Stockman, "Spasers explained," *Nat. Photonics* (2008).

## 8. Appendices

---

102. H. Haken, *Light, Vol. 2: Laser Light Dynamics* (Elsevier, 1985).
103. K. Kolwas, A. Derkachova, and S. Demianiuk, "The smallest free-electron sphere sustaining multipolar surface plasmon oscillation," *Comput. Mater. Sci.* **35**, 337–341 (2006).
104. H. Chew, "Transition rates of atoms near spherical surfaces," *J. Chem. Phys.* **87**, 1355 (1987).
105. Y. S. Kim, P. T. Leung, and T. F. George, "Classical decay rates for molecules in the presence of a spherical surface: A complete treatment," *Surf. Sci.* **195**, 1–14 (1988).
106. R. Carminati, J.-J. Greffet, C. Henkel, and J. M. Vigoureux, "Radiative and non-radiative decay of a single molecule close to a metallic nanoparticle," *Opt. Commun.* **261**, 368–375 (2006).
107. G. Colas des Francs, A. Bouhelier, E. Finot, J. C. Weeber, A. Dereux, C. Girard, and E. Dujardin, "Fluorescence relaxation in the near-field of a mesoscopic metallic particle: distance dependence and role of plasmon modes," *Opt. Express* **16**, 17654 (2008).
108. C. S. Yun, A. Javier, T. Jennings, M. Fisher, S. Hira, S. Peterson, B. Hopkins, N. O. Reich, and G. F. Strouse, "Nanometal surface energy transfer in optical rulers, breaking the FRET barrier.,," *J. Am. Chem. Soc.* **127**, 3115–9 (2005).
109. S. Chénais and S. Forget, "Recent advances in solid-state organic lasers," *Polym. Int.* **61**, 390–406 (2012).
110. M. C. Gather and S. H. Yun, "Bio-optimized energy transfer in densely packed fluorescent protein enables near-maximal luminescence and solid-state lasers," *Nat. Commun.* **5**, 5722 (2014).
111. F. Wang and Y. R. Shen, "General Properties of Local Plasmons in Metal Nanostructures," *Phys. Rev. Lett.* **97**, 206806 (2006).

## 8. Appendices

---

112. C. Sönnichsen, T. Franzl, T. Wilk, G. von Plessen, and J. Feldmann, "Drastic Reduction of Plasmon Damping in Gold Nanorods," *Phys. Rev. Lett.* **88**, 077402 (2002).
113. M. I. Stockman, "Spaser Action, Loss Compensation, and Stability in Plasmonic Systems with Gain," *Phys. Rev. Lett.* **106**, 156802 (2011).
114. E. I. Galanzha, R. Weingold, D. A. Nedosekin, M. Sarimollaoglu, A. S. Kuchyanov, R. G. Parkhomenko, A. I. Plekhanov, M. I. Stockman, and V. P. Zharov, "Spaser as Novel Versatile Biomedical Tool," arXiv **1501.00342**, (2015).
115. X. Meng, A. V. Kildishev, K. Fujita, K. Tanaka, and V. M. Shalaev, "Wavelength-tunable spasing in the visible.,," *Nano Lett.* **13**, 4106–12 (2013).
116. S. J. Strickler and R. A. Berg, "Relationship between Absorption Intensity and Fluorescence Lifetime of Molecules," *J. Chem. Phys.* **37**, 814 (1962).
117. A. Tagaya, T. Kobayashi, S. Nakatsuka, E. Nihei, K. Sasaki, and Y. Koike, "High Gain and High Power Organic Dye-Doped Polymer Optical Fiber Amplifiers: Absorption and Emission Cross Sections and Gain Characteristics," *Jpn. J. Appl. Phys.* **36**, 2705–2708 (1997).
118. D. Li and M. I. Stockman, "Electric Spaser in the Extreme Quantum Limit," *Phys. Rev. Lett.* **110**, 106803 (2013).
119. J. B. Khurgin and G. Sun, "Injection pumped single mode surface plasmon generators: threshold, linewidth, and coherence.,," *Opt. Express* **20**, 15309–25 (2012).
120. M. I. Tribelsky, A. E. Miroshnichenko, Y. S. Kivshar, B. S. Luk'yanchuk, and A. R. Khokhlov, "Laser Pulse Heating of Spherical Metal Particles," *Phys. Rev. X* **1**, 021024 (2011).
121. T. Coenen, J. van de Groep, and A. Polman, "Resonant modes of single silicon nanocavities excited by electron irradiation.,," *ACS Nano* **7**, 1689–98 (2013).
122. K. J. Vahala, "Optical microcavities.,," *Nature* **424**, 839–46 (2003).

## 8. Appendices

---

123. A. François, K. J. Rowland, and T. M. Monro, "Highly efficient excitation and detection of whispering gallery modes in a dye-doped microsphere using a microstructured optical fiber," *Appl. Phys. Lett.* **99**, 141111 (2011).
124. V. R. Dantham and P. B. Bisht, "Studies of whispering gallery modes of single, coated microspheres by steady-state and time-resolved laser fluorescence microscopy," *J. Phys. Conf. Ser.* **185**, 012006 (2009).
125. H. Zhu, Y. Fu, F. Meng, X. Wu, Z. Gong, Q. Ding, M. V Gustafsson, M. T. Trinh, S. Jin, and X.-Y. Zhu, "Lead halide perovskite nanowire lasers with low lasing thresholds and high quality factors.," *Nat. Mater.* **14**, 636–642 (2015).
126. A. Fu and P. Yang, "Organic–inorganic perovskites: Lower threshold for nanowire lasers," *Nat. Mater.* **14**, 557–558 (2015).
127. B. Peng, Q. Zhang, X. Liu, Y. Ji, H. V. Demir, C. H. A. Huan, T. C. Sum, and Q. Xiong, "Fluorophore-doped core-multishell spherical plasmonic nanocavities: resonant energy transfer toward a loss compensation.," *ACS Nano* **6**, 6250–9 (2012).
128. D. A. Cremers and L. J. Radziemski, *Handbook of Laser-Induced Breakdown Spectroscopy* (Wiley, 2006).
129. R. F. Oulton, V. J. Sorger, T. Zentgraf, R. Ma, C. Gladden, L. Dai, G. Bartal, and X. Zhang, "Plasmon lasers at deep subwavelength scale," *Nature* **461**, 629–632 (2009).
130. R. Ma, R. F. Oulton, V. J. Sorger, G. Bartal, and X. Zhang, "Room-temperature sub-diffraction-limited plasmon laser by total internal reflection," *10*, 2–5 (2010).
131. J. Ho, J. Tatebayashi, S. Sergent, C. F. Fong, S. Iwamoto, and Y. Arakawa, "Low-Threshold near-Infrared GaAs–AlGaAs Core–Shell Nanowire Plasmon Laser," *ACS Photonics* **2**, 165–171 (2015).
132. X. Liu, Q. Zhang, J. N. Yip, Q. Xiong, and T. C. Sum, "Wavelength tunable single nanowire lasers based on surface plasmon polariton enhanced Burstein-Moss effect.," *Nano Lett.* **13**, 5336–43 (2013).

## 8. Appendices

---

133. Y.-J. Lu, J. Kim, H.-Y. Chen, C. Wu, N. Dabidian, C. E. Sanders, C.-Y. Wang, M.-Y. Lu, B.-H. Li, X. Qiu, W.-H. Chang, L.-J. Chen, G. Shvets, C.-K. Shih, and S. Gwo, "Plasmonic nanolaser using epitaxially grown silver film.," *Science* **337**, 450–3 (2012).
134. C.-Y. Wu, C.-T. Kuo, C.-Y. Wang, C.-L. He, M.-H. Lin, H. Ahn, and S. Gwo, "Plasmonic green nanolaser based on a metal-oxide-semiconductor structure.," *Nano Lett.* **11**, 4256–60 (2011).
135. R. F. Oulton, V. J. Sorger, D. A. Genov, D. F. P. Pile, and X. Zhang, "A hybrid plasmonic waveguide for subwavelength confinement and long-range propagation," *Nat. Photonics* **2**, 496–500 (2008).
136. V. J. Sorger, N. Pholchai, E. Cubukcu, R. F. Oulton, P. Kolchin, C. Borschel, M. Gnauck, C. Ronning, and X. Zhang, "Strongly enhanced molecular fluorescence inside a nanoscale waveguide gap," *Nano Lett.* (2011).
137. K. J. Russell, T.-L. Liu, S. Cui, and E. L. Hu, "Large spontaneous emission enhancement in plasmonic nanocavities," *Nat. Photonics* **6**, 459–462 (2012).
138. D. B. Hall, P. Underhill, and J. M. Torkelson, "Spin coating of thin and ultrathin polymer films," *Polym. Eng. Sci.* **38**, 2039–2045 (1998).
139. E. W. L. Chan, D.-C. Lee, M.-K. Ng, G. Wu, K. Y. C. Lee, and L. Yu, "A Novel Layer-by-Layer Approach to Immobilization of Polymers and Nanoclusters," *J. Am. Chem. Soc.* **124**, 12238–12243 (2002).
140. J. Ziegler, M. Django, C. Vidal, C. Hrelescu, and T. A. Klar, "Gold nanostars for random lasing enhancement," *Opt. Express* **23**, 15152 (2015).
141. P. Kolchin, N. Pholchai, M. H. Mikkelsen, J. Oh, S. Ota, M. S. Islam, X. Yin, and X. Zhang, "High purcell factor due to coupling of a single emitter to a dielectric slot waveguide.," *Nano Lett.* **15**, 464–8 (2015).
142. K. S. Novoselov, D. Jiang, F. Schedin, T. J. Booth, V. V Khotkevich, S. V Morozov, and A. K. Geim, "Two-dimensional atomic crystals.," *Proc. Natl. Acad. Sci. U. S. A.* **102**, 10451–3 (2005).

## 8. Appendices

---

143. E. Gibney, "The super materials that could trump graphene," *Nature* **522**, 274–276 (2015).
144. J. S. Ross, S. Wu, H. Yu, N. J. Ghimire, A. M. Jones, G. Aivazian, J. Yan, D. G. Mandrus, D. Xiao, W. Yao, and X. Xu, "Electrical control of neutral and charged excitons in a monolayer semiconductor," *Nat. Commun.* **4**, 1474 (2013).
145. R. F. Oulton, "Surface plasmon lasers: sources of nanoscopic light," *Mater. Today* **15**, 26–34 (2012).
146. P. Lange, G. Kewes, N. Severin, O. Benson, and J. P. Rabe, "Evidence for graphene plasmons in the visible spectral range probed by molecules," *arXiv* **1404.6518**, 18 (2014).
147. A. Manjavacas, P. Nordlander, and F. J. García de Abajo, "Plasmon blockade in nanostructured graphene," *ACS Nano* **6**, 1724–31 (2012).
148. F. J. García de Abajo, "Graphene Plasmonics: Challenges and Opportunities," *ACS Photonics* **1**, 135–152 (2014).
149. A. Srivastava, M. Sidler, A. V. Allain, D. S. Lembke, A. Kis, and A. Imamoğlu, "Optically active quantum dots in monolayer WSe<sub>2</sub>," *Nat. Nanotechnol.* **10**, 491–496 (2015).
150. M. Koperski, K. Nogajewski, A. Arora, V. Cherkez, P. Mallet, J.-Y. Veuillen, J. Marcus, P. Kossacki, and M. Potemski, "Single photon emitters in exfoliated WSe<sub>2</sub> structures," *Nat. Nanotechnol.* **10**, 503–506 (2015).
151. Y.-M. He, G. Clark, J. R. Schaibley, Y. He, M.-C. Chen, Y.-J. Wei, X. Ding, Q. Zhang, W. Yao, X. Xu, C.-Y. Lu, and J.-W. Pan, "Single quantum emitters in monolayer semiconductors," *Nat. Nanotechnol.* **10**, 497–502 (2015).
152. C. Chakraborty, L. Kinnischtzke, K. M. Goodfellow, R. Beams, and A. N. Vamivakas, "Voltage-controlled quantum light from an atomically thin semiconductor," *Nat. Nanotechnol.* **10**, 507–511 (2015).

## 8. Appendices

---

153. P. Tonndorf, R. Schmidt, R. Schneider, J. Kern, M. Buscema, G. A. Steele, A. Castellanos-Gomez, H. S. J. van der Zant, S. Michaelis de Vasconcellos, and R. Bratschitsch, "Single-photon emission from localized excitons in an atomically thin semiconductor," *Optica* **2**, 347 (2015).
154. D. W. Pohl, "Near-field optics: Light for the world of NANO," *J. Vac. Sci. Technol. B Microelectron. Nanom. Struct.* **12**, 1441 (1994).
155. M. K. Kinyanjui, C. Kramberger, T. Pichler, J. C. Meyer, P. Wachsmuth, G. Benner, and U. Kaiser, "Direct probe of linearly dispersing 2D interband plasmons in a free-standing graphene monolayer," *Epl* **97**, (2012).
156. J. Lu, K. P. Loh, H. Huang, W. Chen, and A. T. S. Wee, "Plasmon dispersion on epitaxial graphene studied using high-resolution electron energy-loss spectroscopy," *Phys. Rev. B* **80**, 113410 (2009).
157. Y. Liu, R. F. Willis, K. V Emtsev, and T. Seyller, "Plasmon dispersion and damping in electrically isolated two-dimensional charge sheets," *Phys. Rev. B* **78**, 201403 (2008).
158. V. G. Kravets, A. N. Grigorenko, R. R. Nair, P. Blake, S. Anissimova, K. S. Novoselov, and A. K. Geim, "Spectroscopic ellipsometry of graphene and an exciton-shifted van Hove peak in absorption," *Phys. Rev. B* **81**, 155413 (2010).
159. J. W. Weber, V. E. Calado, and M. C. M. van de Sanden, "Optical constants of graphene measured by spectroscopic ellipsometry," *Appl. Phys. Lett.* **97**, 91904 (2010).
160. B. Guo, L. Fang, B. Zhang, and J. R. Gong, "Graphene Doping: A Review," *Insciences J.* **1**, 80–89 (2011).
161. C. H. Lui, K. F. Mak, J. Shan, and T. F. Heinz, "Ultrafast Photoluminescence from Graphene," *Phys. Rev. Lett.* **105**, 127404 (2010).
162. S. Mukherjee, F. Libisch, N. Large, O. Neumann, L. V Brown, J. Cheng, J. B. Lassiter, E. A. Carter, P. Nordlander, and N. J. Halas, "Hot electrons do the impossible: plasmon-induced dissociation of H<sub>2</sub> on Au.," *Nano Lett.* **13**, 240–7 (2013).

## 8. Appendices

---

163. K. J. Tielrooij, J. C. W. Song, S. A. Jensen, A. Centeno, A. Pesquera, A. Zurutuza Elorza, M. Bonn, L. S. Levitov, and F. H. L. Koppens, "Photoexcitation cascade and multiple hot-carrier generation in graphene," *Nat. Phys.* **9**, 248–252 (2013).
164. M. Breusing, S. Kuehn, T. Winzer, E. Malic, F. Milde, N. Severin, J. P. Rabe, C. Ropers, A. Knorr, and T. Elsaesser, "Ultrafast nonequilibrium carrier dynamics in a single graphene layer," *Phys. Rev. B* **83**, (2011).
165. J. J. Dean and H. M. van Driel, "Second harmonic generation from graphene and graphitic films," *Appl. Phys. Lett.* **95**, 261910 (2009).
166. J. J. Dean and H. M. van Driel, "Graphene and few-layer graphite probed by second-harmonic generation: Theory and experiment," *Phys. Rev. B* **82**, 125411 (2010).
167. L. M. Malard, T. V. Alencar, A. P. M. Barboza, K. F. Mak, and A. M. de Paula, "Observation of intense second harmonic generation from MoS<sub>2</sub> atomic crystals," *Phys. Rev. B* **87**, 201401 (2013).
168. Y. Q. An, F. Nelson, J. U. Lee, and A. C. Diebold, "Enhanced optical second-harmonic generation from the current-biased graphene/SiO<sub>2</sub>/Si(001) structure," *Nano Lett.* **13**, 2104–9 (2013).
169. S. A. Mikhailov, "Theory of the giant plasmon-enhanced second-harmonic generation in graphene and semiconductor two-dimensional electron systems," *Phys. Rev. B* **84**, 045432 (2011).
170. S. J. Brun and T. G. Pedersen, "Intense and tunable second-harmonic generation in biased bilayer graphene," *Phys. Rev. B* **91**, 205405 (2015).
171. A. Savoia, M. Siano, D. Paparo, and L. Marrucci, "Nonlocal optical second harmonic generation from centrosymmetric birefringent crystals: the case of muscovite mica," *J. Opt. Soc. Am. B* **28**, 679 (2011).

## 8. Appendices

---

172. M. Cazzanelli, F. Bianco, E. Borga, G. Pucker, M. Ghulinyan, E. Degoli, E. Luppi, V. Véniard, S. Ossicini, D. Modotto, S. Wabnitz, R. Pierobon, and L. Pavesi, "Second-harmonic generation in silicon waveguides strained by silicon nitride.," *Nat. Mater.* **11**, 148–54 (2012).
173. R. Jago, T. Winzer, A. Knorr, and E. Malic, "Graphene as gain medium for broadband lasers," *Phys. Rev. B* **92**, 085407 (2015).
174. C. Donnelly and D. T. H. Tan, "Ultra-large nonlinear parameter in graphene-silicon waveguide structures.," *Opt. Express* **22**, 22820–30 (2014).
175. E. Hendry, P. J. Hale, J. Moger, A. K. Savchenko, and S. A. Mikhailov, "Coherent Nonlinear Optical Response of Graphene," *Phys. Rev. Lett.* **105**, 097401 (2010).
176. L. J. Rogers, K. D. Jahnke, T. Teraji, L. Marseglia, C. Müller, B. Naydenov, H. Schauffert, C. Kranz, J. Isoya, L. P. McGuinness, and F. Jelezko, "Multiple intrinsically identical single-photon emitters in the solid state.," *Nat. Commun.* **5**, 4739 (2014).
177. R. Sundararaman, P. Narang, A. S. Jermyn, W. A. Goddard III, and H. A. Atwater, "Theoretical predictions for hot-carrier generation from surface plasmon decay," *Nat. Commun.* **5**, 5788 (2014).
178. M. Levinshtein, *Handbook Series on Semiconductor Parameters* (World Scientific Publishing Company, 1996).
179. D. Aspnes and A. Studna, "Dielectric functions and optical parameters of Si, Ge, GaP, GaAs, GaSb, InP, InAs, and InSb from 1.5 to 6.0 eV," *Phys. Rev. B* **27**, 985–1009 (1983).
180. A. H. Castro Neto, F. Guinea, N. M. R. Peres, K. S. Novoselov, and A. K. Geim, "The electronic properties of graphene," *Rev. Mod. Phys.* **81**, 109–162 (2009).
181. A. H. Castro Neto, N. M. R. Peres, K. S. Novoselov, and A. K. Geim, "The electronic properties of graphene," *Rev. Mod. Phys.* **81**, 109–162 (2009).
182. S. Forget and S. Chénais, *Organic Solid-State Lasers* (Springer, 2013).

## 8. Appendices

---

183. G. Czycholl, *Theoretische Festkörperphysik* (Springer, 2008).
184. P. B. Johnson and R. W. Christy, "Optical Constants of the Noble Metals," *Phys. Rev. B* **6**, 4370–4379 (1972).

---

## List of Publications

---

### During PhD thesis

1. O. Dietz, G. Kewes, O. Neitzke, and O. Benson, „Coupled mode approach to square gradient Bragg reflection resonances in corrugated dielectric waveguides.“, arXiv **1506:01206** (2015), and just accepted at Phys. Rev. A
2. O. Neitzke, A. Morfa, J. Wolters, A. W. Schell, G. Kewes, and O. Benson, "Investigation of Line Width Narrowing and Spectral Jumps of Single Stable Defect Centers in ZnO at Cryogenic Temperature.," Nano Lett. **15**, 3024–9 (2015).
3. R. Rajasekharan, G. Kewes, A. Djalalian-Assl, K. Ganesan, S. Tomljenovic-Hanic, J. C. McCallum, A. Roberts, O. Benson, and S. Prawer, "Micro-concave waveguide antenna for high photon extraction from nitrogen vacancy centers in nanodiamond.," Sci. Rep. **5**, 12013 (2015).
4. G. Kewes, M. Schoengen, G. Mazzamuto, O. Neitzke, R.-S. Schönfeld, A. W. Schell, J. Probst, J. Wolters, B. Löchel, C. Toninelli, and O. Benson, "Key components for nano-assembled plasmon-excited single molecule non-linear devices," arXiv **1501.04788**, (2015).
5. G. Kewes, R. Rodriguez-Oliveros, K. Höfner, A. Kuhlicke, O. Benson, and K. Busch, "A fully nanoscopic dielectric laser," arXiv **1412.4549**, (2014).
6. P. Lange, G. Kewes, N. Severin, O. Benson, and J. P. Rabe, "Evidence for graphene plasmons in the visible spectral range probed by molecules," arXiv **1404.6518**, (2014).
7. G. Kewes, R. Rodríguez-Oliveros, K. Höfner, A. Kuhlicke, O. Benson, and K. Busch, "Threshold Limitations of the SPASER," arXiv **1408.7054** (2014).

## 8. Appendices

---

8. G. Kewes, A. W. Schell, R. Henze, R. Simon Schönfeld, S. Burger, K. Busch, and O. Benson, "Design and numerical optimization of an easy-to-fabricate photon-to-plasmon coupler for quantum plasmonics," *Appl. Phys. Lett.* **102**, 051104 (2013).

### During master thesis

9. J. Wolters, G. Kewes, A. W. Schell, N. Nüsse, M. Schoengen, B. Löchel, T. Hanke, R. Bratschitsch, A. Leitenstorfer, T. Aichele, and O. Benson, "Coupling of single nitrogen-vacancy defect centers in diamond nanocrystals to optical antennas and photonic crystal cavities," *Phys. status solidi* **249**, 918–924 (2012).
10. A. W. Schell, G. Kewes, T. Schröder, J. Wolters, T. Aichele, and O. Benson, "A scanning probe-based pick-and-place procedure for assembly of integrated quantum optical hybrid devices," *Rev. Sci. Instrum.* **82**, 073709 (2011).
11. T. Schröder, A. W. Schell, G. Kewes, T. Aichele, and O. Benson, "Fiber-Integrated Diamond-Based Single Photon Source," *Nano Lett.* **11**, 198-202 (2011).
12. A. W. Schell, G. Kewes, T. Hanke, A. Leitenstorfer, R. Bratschitsch, O. Benson, and T. Aichele, "Single defect centers in diamond nanocrystals as quantum probes for plasmonic nanostructures," *Opt. Express* **19**, 7914 (2011).
13. J. Wolters, A. W. Schell, G. Kewes, N. Nüsse, M. Schoengen, H. Döscher, T. Hannappel, B. Löchel, M. Barth, and O. Benson, "Enhancement of the zero phonon line emission from a single nitrogen vacancy center in a nanodiamond via coupling to a photonic crystal cavity," *Appl. Phys. Lett.* **97**, 141108 (2010).

---

## Contributions to Conferences

---

### Talks

- “Fully Nanoscopic Laser”, Cleo, München, 2015
- “A Fully Analytic Nanolaser Model – Towards Numerical Implementation”, Matheon-Workshop: "8th Annual Meeting Photonic Devices", Berlin, 2015
- “Reversible In-Situ Plasmon Tuning of Single Gold Nanoparticles by Controlled Melting”, workshop “surface plasmon – surface chemistry”, Wien, 2013
- “Towards Synthesis and Investigation of Surface Plasmon Polariton Lasers”, DPG-Tagung, Berlin, 2012
- “Deterministic Coupling of Single Nitrogen Vacancy Centres in Diamond Nanocrystals to Bowtie Nanoantennas”, DPG-Tagung, Dresden, 2011

### Posters

- “Experiment and Theory: No Spasing from Core-Shell Spasers”, Frontiers in Nanophotonics, Monte Verità, 2015
- “Fully analytic spaser model: Understanding threshold limitations”, Nanometa, Seefeld, 2015
- “Fully analytic spaser model: Understanding threshold limitations”, TNT Conference, Barcelona, 2014 (➔ Poster-Prize)
- “Dibenzoterrylene fluorescent molecules hosted in flexible anthracene crystals: a stable organic emitter for near-infrared on-chip quantum experiments”, 20th Workshop on Single Molecule Spectroscopy, Berlin, 2014
- “Single NV-centers in Nanodiamonds as Probes for the Local Density of States”, Nanometa, Seefeld, 2013

## 8. Appendices

---

- “Towards Development and Optimization of a Surface Plasmon Polariton Laser (SPASER)”, WE-Heraeus-Seminar: “Quantum and Nano Plasmonics”, Bad Honnef, 2011
- “Single Defect Centers in Diamond Nanocrystals as Quantum Probes for Nanoantennas”, Advanced DPG Physics School on “Nanoantennas and Hybrid Quantum Systems”, Bad Honnef, 2011 (→ Poster-Prize)
- “Surface Plasmon Polaritons for Single-Photon Excitation and On-Chip Experiments/Applications”, DPG - Physics School: “Nanophotonics meets Quantum Optics”, Bad Honnef, 2010

---

## Danksagung

---

Ich möchte mich bedanken, denn die Arbeit in der Nanooptik Gruppe wird mir in absolut positiver Erinnerung bleiben. Entscheidenden Anteil daran trägt das sehr angenehme Arbeitsklima in der Gruppe, welches ganz klar auf die fantastischen Kollegen und die Leitung von Prof. Benson zurückgeführt werden muss. Prof. Benson möchte ich des Weiteren für die kompetente Betreuung und Unterstützung in allen Belangen danken. Besonders hervorheben möchte ich die Unterstützung bei der Realisierung des kurzen Forschungsaufenthalts in Australien.

Ohne die Begeisterungsfähigkeit und den ganz konkreten Einsatz vieler Kollegen wäre diese Arbeit nicht möglich gewesen. Im Besonderen möchte ich Andreas Ott, Alexander Kuhlicke, sowie den „TOPS“ Rogelio Rodríguez-Oliveros, Kathrin Höfner und Prof. Busch danken. Besonderer Dank gilt auch Oliver Neitzke, Otto Dietz und Rolf-Simon Schönenfeld. Danke auch an unsere Kooperationspartner vom HZB, Max Schöngen und Jürgen Probst und aus Florenz, Costanza Toninelli mit ihrem sympathischen Team. Danke auch an Ingo Will und seine Kollegen vom MBI für die Unterstützung beim spaser-Projekt. Besondere Freude bereitete auch die Zusammenarbeit mit den Kollegen von Prof. Rabe’s Gruppe, allen voran Philipp Lange aber auch Nikolai Severin. Ich hatte das Glück besonders clevere, engagierte und sympathische Bachelor- und Master-Studenten betreuen zu dürfen: vielen Dank an Martin Rothe, Friedemann Gädke und Thomas Kiesner.

Bedanken möchte ich mich auch bei den geduldigen Kollegen, die mir vieles während meiner Diplomarbeit und darüber hinaus beigebracht haben: Thomas Aichele (der mich für die Plasmonik begeistern konnte), Andreas Schell, Janik Wolters, Tim Schröder, Stefan Schietinger und Michael Barth. Besonders muss ich mich bei Sven Burger von JCMwave bedanken, der bei mir die Lust am (numerischen) Simulieren geweckt hat. Der oben erwähnte Forschungsaufenthalt in Australien wäre natürlich nicht ohne die

## 8. Appendices

---

australischen Kollegen möglich gewesen. Einen besseren Gastgeber kann man sich nicht wünschen. Best thanks to Snjezana, Tim, Des, Anthony, Prof. Prawer and especially to Brant Gibson and Ranjith Rajasekharan.

Besonders möchte ich mich für die permanente Unterstützung und den Zuspruch meiner Familie, von Seiten des Schwippschwagers in Spe bis hin zu meinen Eltern, bedanken. Liebe Eltern, ohne eure zumindest teilweise gelungene Erziehung wäre es mir nicht vergönnt gewesen meine Träume zu verwirklichen. Mein stärkster Halt war in den letzten Jahren meine Berliner Kleinfamilie: mein Hund und meine Freundin: Vielen Dank für Deine Geduld und Unterstützung Claudia.

---

## **Selbstständigkeitserklärung**

---

Ich erkläre hiermit, die vorliegende Arbeit selbstständig und nur unter Verwendung der angegebenen Quellen und Hilfsmittel angefertigt zu haben. Ich habe mich nicht anderweitig um einen Doktorgrad beworben und besitze einen solchen auch nicht. Die dem Verfahren zugrunde liegende Promotionsordnung der Mathematisch-Naturwissenschaftlichen Fakultät der Humboldt-Universität zu Berlin habe ich zur Kenntnis genommen.

Berlin, den 20.09.2015

Günter Kewes